GENERAL ATOMIC

GA-A14358
UC-77

GAS-COOLED FAST BREEDER REACTOR

QUARTERLY PROGRESS REPORT
FOR THE PERIOD FEBRUARY 1, 1977 THROUGH APRIL 30, 1977

by

Project Staff

NOTICE
This report was prepared as an account of work sponsored by the United States Government. Neither the United States nor the United States Energy Research and Development Administration, nor any of their employees, nor any of their contractors, subcontractors, or their employees, makes any warranty, express or implied, or assumes any legal liability or responsibility for the accuracy, completeness or usefulness of any information, apparatus, product or process disclosed, or represents that its use would not infringe privately owned rights.

Prepared under
Contract EY-76-C-03-0167
Project Agreement No. 23
for the
San Francisco Operations Office
U.S. Energy Research and Development Administration

General Atomic Project 3228

Date Published: May 1977

DISTRIBUTION OF THIS DOCUMENT IS UNLIMITED

DISCLAIMER

This report was prepared as an account of work sponsored by an agency of the United States Government. Neither the United States Government nor any agency thereof, nor any of their employees, makes any warranty, express or implied, or assumes any legal liability or responsibility for the accuracy, completeness, or usefulness of any information, apparatus, product, or process disclosed, or represents that its use would not infringe privately owned rights. Reference herein to any specific commercial product, process, or service by trade name, trademark, manufacturer, or otherwise does not necessarily constitute or imply its endorsement, recommendation, or favoring by the United States Government or any agency thereof. The views and opinions of authors expressed herein do not necessarily state or reflect those of the United States Government or any agency thereof.

DISCLAIMER

Portions of this document may be illegible in electronic image products. Images are produced from the best available original document.

PROGRESS REPORT SERIES

GA-5537	November 1, 1963 through July 31, 1964
GA-6667	August 1, 1964 through July 31, 1965
GA-7645	August 1, 1965 through July 31, 1966
GA-8107	August 1, 1966 through July 31, 1967
GA-8787	August 1, 1967 through July 31, 1968
GA-8895	August 1, 1968 through October 31, 1968
GA-9229	November 1, 1968 through January 31, 1969
GA-9359	February 1, 1969 through April 30, 1969
GA-9639	May 1, 1969 through July 31, 1969
GA-9811	August 1, 1969 through October 31, 1969
GA-9838	November 1, 1969 through January 31, 1970
GA-10517	February 1, 1970 through January 31, 1970
GA-10645	February 1, 1971 through April 30, 1971
GA-A10803	May 1, 1971 through July 31, 1971
GA-A10906	August 1, 1971 through July 31, 1971
GA-A12003	Nobember 1, 1971 through January 31, 1972
GA-A12252	May 1, 1972 through July 31, 1972
GA-A12421	August 1, 1972 through October 31, 1972
GA-A12530	November 1, 1972 through January 31, 1973
GA-A12635	February 1, 1973 through April 30, 1973
GA-A12728	May 1, 1973 through July 31, 1973
GA-A12824	August 1, 1973 through October 31, 1973
GA-A12894	November 1, 1973 through January 31, 1974
GA-A13021	February 1, 1974 through April 30, 1974
GA-A13148	May 1, 1974 through July 31, 1974
GA-A13238	August 1, 1974 through October 31, 1974
GA-A13379	November 1, 1974 through January 31, 1975
GA-A13458	February 1, 1975 through April 30, 1975
GA-A13565	May 1, 1975 through July 31, 1975

GA-A13766	August 1, 1975 through October 31, 1975
GA-A13815	November 1, 1975 through January 31, 1976
GA-A13868	February 1, 1976 through April 30, 1976
GA-A13975	May 1, 1976 through July 31, 1976
GA-A14112	August 1, 1976 through October 31, 1976
GA-A14240	November 1, 1976 through January 31, 1977

ABSTRACT

The tasks of the gas-cooled fast breeder reactor (GCFR) program which are supported by the U.S. Energy Research and Development Administration include development of GCFR fuel, blanket, and control assemblies; development of the pressure equalization system for GCFR fuel; out-of-pile loop facility test programs; fuels and materials development; fuel, blanket, and control rod analyses and development; nuclear analysis and reactor physics for GCFR core design; shielding requirements for the GCFR; reactor engineering to assess the thermal, hydraulic, and structural performance of the core and the core support structure; plant systems control; systems engineering; development of reactor components, including reactor vessel, control and locking mechanisms, fuel handling equipment, core support structure, shielding assemblies, main helium circulator, steam generator, and auxiliary circulator; development of a helium circulator test facility; reactor safety, environment, and risk analyses, including planning and support of an in-pile and out-of-pile safety test program; nuclear island engineering design; and development of a reliability data bank.

CONTENTS

FIGURES

FIGURES (Continued)

FIGURES (Continued)

TABLES

TABLES (Continued)

1. INTRODUCTION

The various tasks of the gas-cooled fast breeder reactor (GCFR) program for the period February 1, 1977 through April 30, 1977 sponsored by the U.S. Energy Research and Development Administration (ERDA) are discussed in this quarterly progress report. The GCFR utility program, which is sponsored by a large number of electric utility companies, rural electric cooperatives, and General Atomic (GA), is primarily directed toward the development of a GCFR demonstration plant. The utility-sponsored work and the ERDA-sponsored work are complementary.

Analytical, experimental, and fabrication development is being accomplished under the core assembly development task to establish the basis for the design of GCFR fuel, blanket, and control assemblies. Methods development for structural, thermal-hydraulic, and mechanical analyses is discussed, and the results of structural analysis of the fuel assembly components and thermal-hydraulic analysis of the blanket assembly during low power are presented. Current progress on rod-spacer interaction tests, fuel assembly seismic and vibration test planning, and development of assembly fabrication techniques is also presented. The various subtasks of core asembly development and the work accomplished during this reporting period are discussed in Section 2.

The technology to support the design and construction of the pressure equalization system (PES) for GCFR fuel is being developed. This includes (1) the development of analytical models and computer codes which will be verified by test programs and testing of materials and seals and (2) the development of fabrication processes for the PES. These are discussed in Section 3.

To demonstrate the ability of GCFR fuel, control, and blanket assembly designs to meet design goals and verify predictions of analytical models, a

series of out-of-pile simulation tests will be performed. The emphasis of the tests will be on obtaining thermal-structural data for steady-state, transient, and margin conditions using electrically heated rod bundles in a dynamic helium loop. These are discussed in Section 4.

In the fuels and materials development program, thermal flux and fast flux irradiation programs are being conducted to establish conditions and design features specific to GCFR fuel rods, such as vented fuel, fission product traps, and surface-roughened cladding. In addition, a test program of smooth and surface-roughened GCFR cladding specimens is being conducted to determine how materials behave under irradiation. The fuels and materials tests, the analytical studies, and the results to date are presented in Section 5.

Under the fuel rod engineering task, performance of the fuel and blanket rods under steady-state and transient conditions is being evaluated to determine performance characteristics, operating limits, and design criteria. In addition, surveillance of the fuel rod and blanket rod technology of other programs is being carried out. These studies are presented in Section 6.

The objectives of the nuclear analysis and reactor physics task are to verify and validate the nuclear design methods which will be applied to the GCFR core design. Data from a critical assembly experimental program on the ZPR-9 facility at Argonne National Laboratory (ANL) are being used for this purpose. Critical assembly design, analysis, and methods development are discussed in Section 7.

Verification of the physics and engineering analytical methods and the data for design of the GCFR shields is being conducted under the shielding requirements task along with an evaluation of the effectiveness of various shield configurations. The results of radial shield analyses and the work being done on structural analysis are presented in Section 8.

Section 9 discusses systems engineering for the GCFR. This includes systems integration; coordination of interface requirements between plant systems; development and implementation of effective documentation management; and assessment of the thermal-hydraulic performance of the core.

Section 10 presents the evaluation and development of the main components of the GCFR which are currently in progress, including reactor vessel, control and locking mechanisms, fuel handling, core support structure, shielding assemblies, main helium circulator, steam generator, auxiliary circulator, and helium processing components.

Development of control systems and assessment of seismic- and flow-induced vibration behavior for the GCFR demonstration plant are discussed in Section 11.

The reactor safety task, which is discussed in Section 12, includes (1) maintenance of liaison between GA and other organizations and integration of the overall GCFR safety analysis effort; (2) formulation and review of a GCFR safety program plan; (3) performance of detailed safety, environmental, and risk analyses of the GCFR; (4) evaluation of the postaccident fuel containment capability of the GCFR; (5) integration of the results of ERDA safety studies into the licensing reviews; and (6) evaluation of probabilistic design methods for use in the GCFR program.

Section 13 discusses the safety test program, which involves quantification of fuel and cladding behavior during accidents leading to core damage and identification of safety test information required for licensing and commercialization of the the GCFR. The GRIST-2 and duct melting and fallaway test programs are also examined.

Section 14 discusses the nuclear island. The purposes of this task are to accomplish engineering design work on the nuclear island portion of the demonstration plant and to resolve the interface requirements of major nuclear steam supply (NSSS) and balance of plant (BOP) systems.

Section 15 is concerned with the procurement, supplying, and storage of reliability data and estimates in support of probabilistic analyses of accident events being analyzed for gas-cooled reactors.

2. CORE ASSEMBLY DEVELOPMENT (189a No. 00582)

2.1. CORE ASSEMBLY THERMAL-HYDRAULIC ANALYSIS

2.1.1. Introduction

Evaluation of experimental data is being performed to develop the analytical basis for the design and development of the GCFR fuel, control, and blanket assemblies. Because complete prototype in-pile tests cannot be conducted, a strong analytical base supported by development tests is required to design the core assemblies. The current effort is devoted to the development of an adequate steady-state and transient analysis capability in the areas of thermal-hydraulic and structural analyses to provide a basis for assembly design criteria and specific test requirements. The main efforts have focused on improvement of thermal-hydraulic correlations and development of methods for applying the correlations to the design and analysis of GCFR core assemblies.

2.1.2. Fuel Assembly Analysis

2.1.2.1. Nondimensional Analysis. The heat transfer and friction factor correlations used for thermal-hydraulic analysis of roughened rod bundles are derived from basic single-rod experiments. In order to plan these experiments and correctly transform the raw data, it is essential to know the basic nondimensional parameters influencing the friction factor and Stanton number. To determine the relationship between the friction factor/heat transfer coefficient and the independent variable, the Buckingham π theorem (Ref. 2-1) was used. According to this theorem, the total number of nondimensional groups is equal to n - m, where n is the number of physical quantities (e.g., heat transfer coefficient, rib height, velocity, etc.) and m is equal to the primary dimensions (mass, length, time, and temperature).

For heat transfer from roughened rods, the physical quantities are

Quantity	Symbol	Dimension*
Rib height	h	L
Rib width	w	L
Rib pitch	p	L
Rod diameter	d_R	L
Hydraulic diameter	d_H	L
Thermal conductivity of fluid	k_f	ML/θ^3T
Velocity of fluid	V	L/θ
Density of fluid	ρ	M/L^3
Specific heat of fluid	C_p	L^2/θ^2T
Viscosity of fluid	μ	$M/L\theta$
Thermal conductivity of cladding	k_c	ML/θ^3T
Ratio of average wall temperature to bulk temperature	T_W/T_B	--
Heat transfer coefficient	h_c	M/θ^3T

*L = length, M = mass, θ = time, T = temperature.

There are thirteen physical quantities and four primary variables; hence, the number of dimensionless groups will be n - m = 13 - 4 = 9. To find the dimensionless groups, π (dimensionless) is made equal to a product of the variables raised to an unknown power.

$$\pi = (h)^{n_1}(w)^{n_2}(p)^{n_3}(d_R)^{n_4}(d_H)^{n_5}(k_f)^{n_6}(V)^{n_7}(\rho)^{n_8}(C_p)^{n_9}$$

$$(\mu)^{n_{10}}(k_c)^{n_{11}}(T_w/T_B)^{n_{12}}(h_c)^{n_{13}} \quad . \qquad (2\text{-}1)$$

When the condition of dimensional equality is applied to Eq. 2-1, the following nondimensional groups are obtained:

$$St = \phi\left(Re, Pr, Bi, \theta_R, \epsilon_1, \epsilon_2, \frac{w}{h}, \frac{p}{h}\right) \quad , \qquad (2\text{-}2)$$

where Stanton number $= St = \frac{h_c}{C_p \rho V}$,

Reynolds number $= Re = \frac{\rho V d_H}{\mu}$,

Prandtl number $= Pr = \frac{\mu c_p}{K_f}$,

Biot number $= Bi = \frac{h_c h}{K_c}$,

Temperature ratio $= \theta_R = T_W/T_B$,

Relative roughness $= \varepsilon_1 = h/d_H$,

Geometry factor $= \varepsilon_2 = h/d_R$.

For a given roughness configuration (i.e., constant W/h and p/h), Eq. 2-2 reduces to

$$St = \phi(Re, Pr, Bi, \theta_R, \varepsilon_1, \varepsilon_2) \quad . \tag{2-3}$$

A table similar to that for the heat transfer correlation can be prepared for the friction factor of roughened rods. In the case of the friction factor, the thermal conductivity of the fluid (k_f), specific heat of the fluid (c_p), and thermal conductivity of the cladding (k_c) are not relevant. Hence, the number of physical quantities is reduced to ten, and according to the Buckingham π theorem, the number of independent dimensionless groups is $n - m = 10 - 3 = 7$. Using a procedure similar to that for the heat transfer correlation, the following relationship is obtained:

$$f = \phi\left(Re, \theta_R, \varepsilon_1, \varepsilon_2, \frac{w}{h}, \frac{p}{h}\right) \quad . \tag{2-4}$$

For a given roughness configuration, Eq. 2-4 reduces to

$$f = \phi(Re, \theta_R, \varepsilon_1, \varepsilon_2) \quad . \tag{2-5}$$

In order to transform single rod experiments into rod bundles, Eqs. 2-2 and 2-4 clearly require that the roughness configuration (rib width to rib height ratio and rib pitch to rib height ratio) be identical in the single-rod experiment and the GCFR fuel rod. In general, two roughness parameters are necessary to correlate the heat transfer and friction factor data. However, if the roughness configuration and the rib height to rod diameter ratio (ε_2) are kept constant, only one roughness parameter $\varepsilon_1 = h/d_H$ will be required to correlate the data. Note that the h/d_R value used for current GCFR correlations is 10.7% larger than the h/d_R ratio for GCFR rods. This effect has not been accounted for in the transformations and correlations currently used for GCFR analysis.

Another important point which should be considered relates to the difference between the relative roughness $\varepsilon_1 = h/d_H$ and the roughness parameter $\varepsilon_3 = h/\hat{y}$ (where $\hat{y} = r_o - r_1$, r_o = radius of zero shear, and r_1 = radius of rod). The following relations exist:

$$d_H = \frac{2(r_o^2 - r_1^2)}{r_1} \quad , \tag{2-6}$$

$$\hat{y} = (r_o - r_1) \quad . \tag{2-7}$$

Hence,

$$d_H = 2\hat{y}\left(\frac{\hat{y}}{r_1} + 2\right) \quad , \tag{2-8}$$

so that for a given rib height and rod diameter, there is a one-to-one relationship between relative roughness (h/d_H) and roughness parameter ($h/\hat{y}$), and either parameter can be used to correlate the data. However, whenever the diameters of the rods in the single-rod experiment and the fuel bundle are different, the ratio h/d_R must be constant (this is the parameter ε_2 in Eqs. 2-2 and 2-4). If this condition is satisfied

according to Eq. 2-8, there will be a one-to-one correspondence between h/d_H and $h/\hat{y}$. The use of either parameter is then just a matter of convenience.

It can be concluded from the above analysis that the ratio of rib height to rod diameter used in the single-rod experiments should be maintained equal to the value for GCFR fuel rods. Once this condition is satisfied, the friction factor and heat transfer correlations used for the roughened fuel rod bundle will be in the following form:

$$f = \phi(Re, \theta_R, \varepsilon) \quad , \tag{2-9}$$

$$St = \phi(Re, Pr, Bi, \theta_R, \varepsilon) \quad , \tag{2-10}$$

where ε can be either h/d or $h/\hat{y}$.

2.1.2.2. Edge Channel Analysis. Utilization of experimental sincle-rod data in rod bundle analysis involves transformation of the raw data, correlation of the transformed data into a form which can be used in subchannel analysis computer codes, and application of the correlations to specific subchannel configurations. When edge subchannels having rough (rod) and smooth (duct wall) surfaces are analyzed, it is generally necessary to perform an additional step, i.e., an inverse transformation, to arrive at friction factor and Stanton number values for the subchannel. The transformation-correlation-application procedure at GA used the Warburton-Pirie transformation (Ref. 2-2), empirical curve fitting for correlation, equivalent annulus representation of subchannels, and an inverse of the Warburton-Pirie transformation for edge subchannels. Each procedure is subject to uncertainties because there is no theory which completely describes flow in channels with combined smooth and rough surfaces.

However, if the ratio of the roughness rib height to the rod diameter is the same for the single-rod test and the rod bundle being analyzed, then a direct correlation of the raw annulus data can be used in place of the

transformation-correlation-inverse transformation procedure for the edge channels. As discussed in Section 2.1.2.1, the friction factor is a function of the following dimensionless groups:

$$f = \phi\left(Re, \frac{Tw}{T_b}, \frac{h}{d_H}, \frac{h}{d_R}, \frac{w}{h}, \frac{p}{h}\right) \quad .$$

If the single rod and bundle rod have the same roughness configuration (w/h and p/h) and rib height to rod diameter ratio (h/d_R) and the single-rod tests are performed at the same temperature ratio (T_w/T_b), then the correlation reduces to

$$f = \phi\left(Re, \frac{h}{d_H}\right) \quad .$$

Therefore, a simple correlation of the single-rod test data as a function of Reynolds number and relative roughness is sufficient for use in edge subchannel analysis.

2.1.2.3. Edge Channel Parameter Study. GCFR fuel assemblies consist of two different types of flow channels: (1) interior channels where the entire perimeter is rough and (2) edge channels where the perimeter is partly rough and partly smooth. Because of the different thermal-hydraulic properties of these channels, selection of the proper edge spacing to minimize temperature gradients across rods and keep the hot spot cladding temperature within limits during all flow conditions poses a difficult problem. The effect of edge spacing on the pressure gradient across the edge rods during full-power operation was analyzed for the peak-power fuel assembly. The friction factor used for the edge channel was derived from the following approximation:

$$\bar{f} = \frac{f_R \cdot P_R + f_S \cdot P_S}{P_R + P_S} \quad , \qquad (2\text{-}11)$$

where $\bar{f}$ = friction factor for edge channel,

f_R = friction factor for rough channel,

f_S = friction factor for smooth channel,

P_S = smooth perimeter of edge channel,

P_R = rough perimeter of edge channel.

The results are shown in Fig. 2-1, which depicts the ΔT value across the edge rods as a function of edge spacing. The edge spacing is expressed in percent of rod spacing and is calculated as follows:

$$\% \text{ edge spacing} = \left(\frac{\ell - d_o/2}{p - d_o} \right) * 100 \quad , \tag{2-12}$$

where ℓ = distance between duct wall and center of edge rod,

d_o = root diameter of rod,

p = pitch of rod.

The results shown in Fig. 2-1 indicate that the edge spacing should be larger than 37% to avoid having the edge channels run hotter than the internal channels. The fabrication tolerances are +20% and -10% of the nominal spacing between rods. To avoid overheating of any edge channel during normal operation, a nominal edge spacing of about 47% has been selected for this fuel assembly design, which yields temperature gradients across the edge rods ranging from 0° to 68°C. Methods of reducing the temperature gradient range are being investigated.

2.1.2.4. SCEPTIC/COBRA IIIc Analysis. The SCEPTIC subchannel thermal-hydraulic analysis computer program (Ref. 2-3) has been obtained and is presently operational on the UNIVAC 1110. The principal advantage of this code is that it models circumferential conduction in the fuel rod cladding and radiation between surfaces in the bundle. This capability is particularly important during off-normal operating conditions, where high temperatures and large temperature gradients may occur.

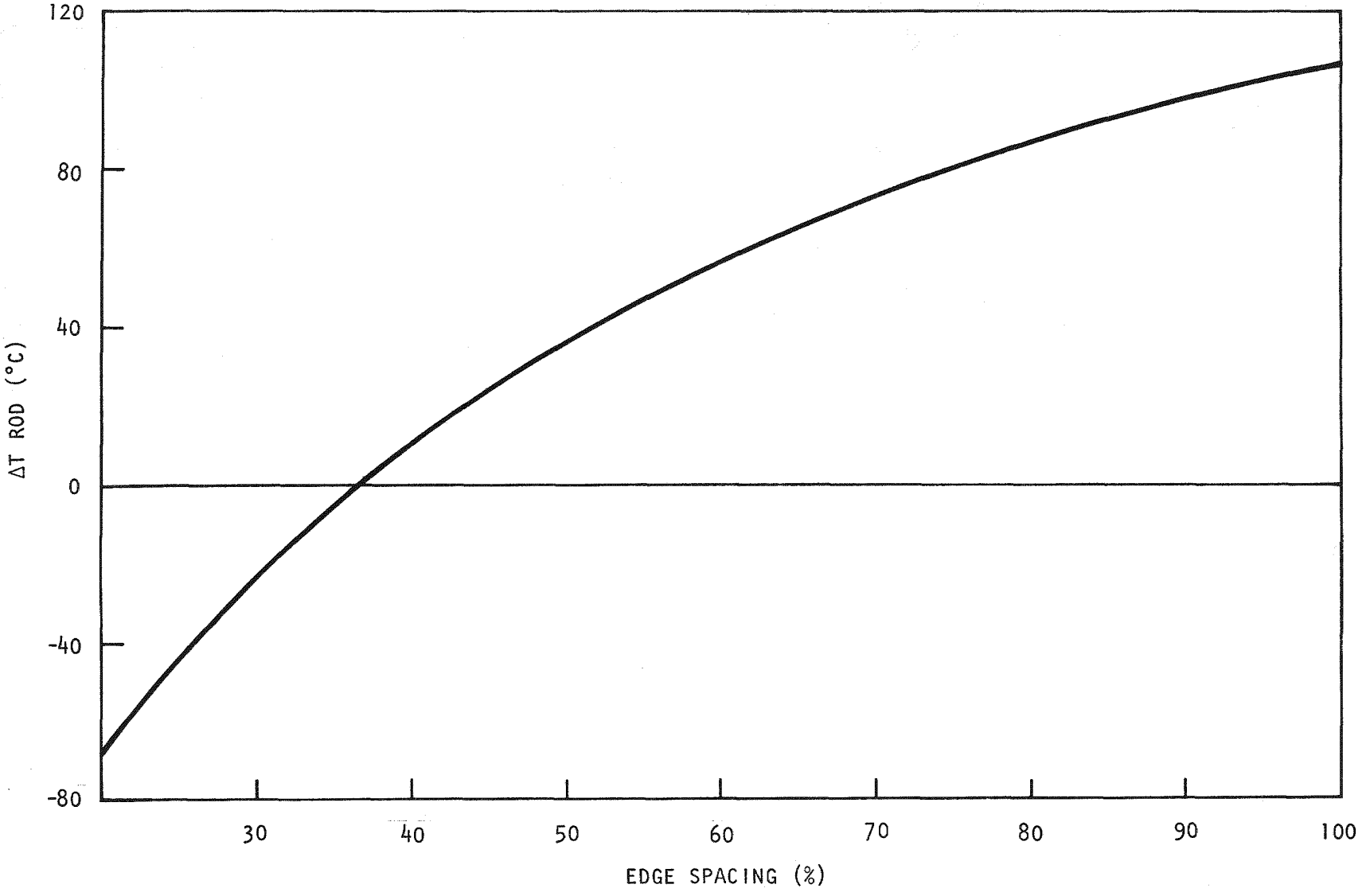

Fig. 2-1. Peak temperature difference across the edge rod vs edge spacing (100% spacing = 3.875 mm)

To evaluate the SCEPTIC code and investigate the effect on surface temperatures of adding conduction and radiation to the model, the results of a series of SCEPTIC and COBRA (Ref. 2-4) runs were compared. A strip model representing five rod rows at the edge of a GCFR fuel assembly was prepared, and runs were made at power levels ranging from 100% to 2%, with a large power-to-flow mismatch at 4%. At the higher power levels, the coolant and surface temperatures predicted by the two codes were in good agreement. Slight cladding temperature deviations were due to differences in the manner in which subchannel mixing is modeled. Since the circumferential cladding temperature differences were small, the addition of conduction to the model had little effect on the results. For the power flow mismatch case, where the power and flow levels were 10% and 4%, respectively, the addition of conduction resulted in a 50% reduction in the maximum cladding differential temperature in the edge rod. When radiation was added to the model, large increases in the duct wall temperature were experienced, particularly in the upper smooth section of the rod. In general, the absolute cladding temperature decreased and the edge rod differential temperature rose slightly.

2.1.3. Control Assembly Analysis

The design of the 300-MW(e) GCFR control assembly consists of a single rod contained in a guide tube. A thermal-hydraulic analysis was conducted to check and improve this design concept. Two configurations were considered. The configuration shown in Fig. 2-2 has a circular guide tube with a fluted inner duct; the duct limits the temperature gradient across the rods. In the second configuration, shown in Fig. 2-3, the inner duct and guide tube are hexagonal. The configuration in Fig. 2-3 is more desirable from a fabrication and design viewpoint. The COBRA code has been used to determine the edge spacing which would limit the temperature difference across the control rod to less than 20°C. The new control cluster geometry parameters are listed below.

Rod diameter	14.06 mm
Bundle length	1130 mm

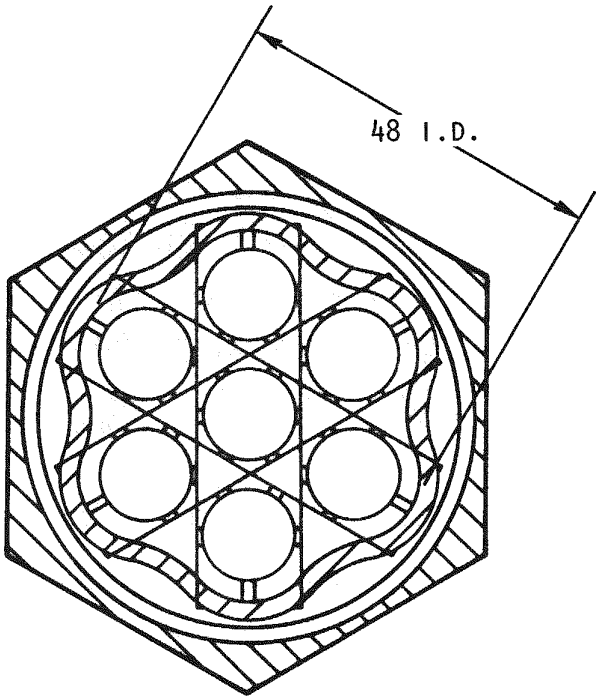

Fig. 2-2. Control assembly configuration with fluted inner duct and circular guide tube

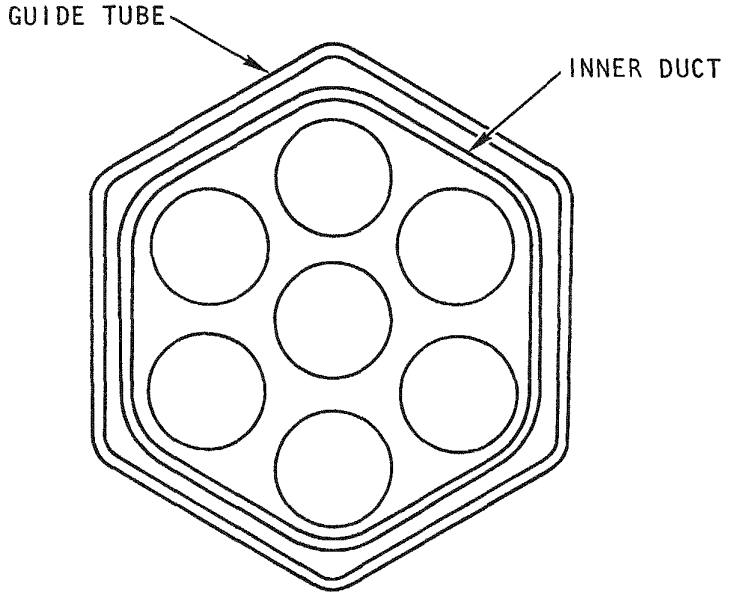

Fig. 2-3. Control assembly configuration with hexagonal guide tube and inner duct

Number of rods	7
Pitch/diameter ratio	1.26
Ratio of total pellet area to guide tube area	0.30
Ratio of rod-wall gap to rod-rod gap	0.73

2.1.4. Blanket Assembly Analysis

2.1.4.1. COBRA IV Code Development. The COBRA IV code (Ref. 2-4) received from Battelle Northwest Laboratory (BNWL) in late 1976 has been modified to make it compatible with the UNIVAC 1110. With the use of overlays, the program storage requirements have been significantly reduced, allowing expansion of the data bank, which permits analysis of larger rod bundles. By taking advantage of peripheral data storage, a full radial blanket assembly with 61 rods, 126 subchannels, and 186 gap connections has been modeled. Six sets of updated programs have been received from BNWL, and five have been incorporated into the code. Three sample problems supplied by BNW have been successfully executed, and the results compare well with those obtained by BNWL with an earlier version of the code. A closer comparison will be made with current BNWL results when the most recent revisions are incorporated.

The general COBRA IV program contains a number of features which are not pertinent to GCFR analysis. Therefore, a helium coolant version of the code which eliminates the routines which calculate coolant quality, void fraction, critical heat flux, and two-phase effects has been produced. A new subroutine which provides the properties of helium gas based on correlations taken from Ref. 2-6 has also been added. To check out this version of the code, the full blanket assembly model described above will be run and the results compared with those of COBRA IIIc. Wire wrap effects are simulated by a turbulent mixing coefficient. Experimental data for wire-wrapped rod bundles will be used to evaluate the program.

2.1.4.2. Thermal-Hydraulic Analysis. Based on the revised GCFR plant performance parameters and the new assembly duct dimensions, the radial

blanket assembly geometry has been recalculated. The current design retains the 61-rod configuration with the as-built dimensions shown in Table 2-1. Taking into account the spacing between assemblies in the blanket region, the overall blanket fuel volume fraction is 0.59. This assumes an edge spacing of 100%, which is the most convenient value for a wire-wrapped bundle. Edge subchannel analyses will be performed to check the validity of this assumption.

A half-bundle model of the radial blanket assembly has been prepared for analysis with COBRA IIIc. Since the GA version of this code does not contain the wire-wrap modeling capability, the wrap-induced flow around the periphery of the bundle cannot be simulated. Therefore, a half-bundle model is sufficient with regard to geometric symmetry. Based on the most recent information on radial power gradients in the blanket region and the revised geometry, new normalized power distributions have been calculated in the first and second blanket rows for the beginning and end of the first four operating cycles. Average power values have been obtained from the most recent power splits, and an assembly coolant mass flow rate estimate has been determined based on the assumption of 60% overcooling (ΔT blanket/ΔT fuel). The Novendstern equation (Ref. 2-7) for wire-wrapped bundles was used to develop a correlation for friction factor as a function of Reynolds number to input to the code. A Stanton number correlation (Ref. 2-8) for flow in a smooth rod bundle was used to predict cladding temperatures. Revised hot spot factors of 1.241 for the coolant and 2.386 for the film have been included.

The initial runs for the end-of-cycle No. 4 condition indicate that the maximum cladding temperature occurs on the inside of the edge rod located at the center of the duct flat nearest the center of the core. For the specified input conditions, the maximum hot spot temperature exceeded the 700°C limit by 28°C. Calculations which include the effects of cladding conduction are required to determine the actual cladding differential temperature and maximum hot spot temperature.

TABLE 2-1
RADIAL BLANKET ASSEMBLY GEOMETRY

Rod diameter	21.4 mm
Rod pitch	22.8 mm
Rod pitch to diameter	1.07 mm
Wire diameter	1.40 mm
Wire pitch	300 mm
Duct inside dimension	183 mm
Cladding thickness	0.5 mm
Duct wall thickness	2.5 mm
Edge spacing	1.4 mm

2.2. CORE ASSEMBLY MECHANICAL ANALYSIS

During this quarter, analyses were performed to evaluate the bending stiffness of the fuel assembly hexagonal flow duct and to assess potential thermal downshocking of the core assemblies.

2.2.1. Core Static Analysis of Fuel Assembly Duct Stiffness

A formula for calculating fuel assembly duct deflection due to end loads has been developed using simple beam theory. The model of the duct which was analyzed is illustrated in Fig. 2-4. To determine the effect of possible duct rotation at the conical seat on duct end displacement, it was assumed that the cylindrical nozzle of the duct was pinned to the top and bottom of the grid plate and the grid plate offered no other rotational restraint or flexibility. A lower bound to the effect of duct rotation (i.e., no rotation whatever) can be obtained from this model simply by assuming that the cylindrical portion of the duct is completely rigid.

The formula derived for calculating duct deflection, including the effect of rotation at the grid plate, is

$$\delta = \frac{P}{3}\left[\frac{\ell_a^3 + 3\ell_a\ell_b^2 + 3\ell_b\ell_a^2}{(EI)_a} + \frac{\ell_b^3}{(EI)_b} + \frac{(\ell_a + \ell_b)^2\ell_c}{(EI)_c}\right] ,$$

where δ = duct end deflection,

P = end load,

ℓ = length,

E = Young's modulus,

I = moment of inertia,

a = duct upper hex,

b = duct lower hex,

c = duct cylindrical neck.

Any consistent set of units may be used with this formula.

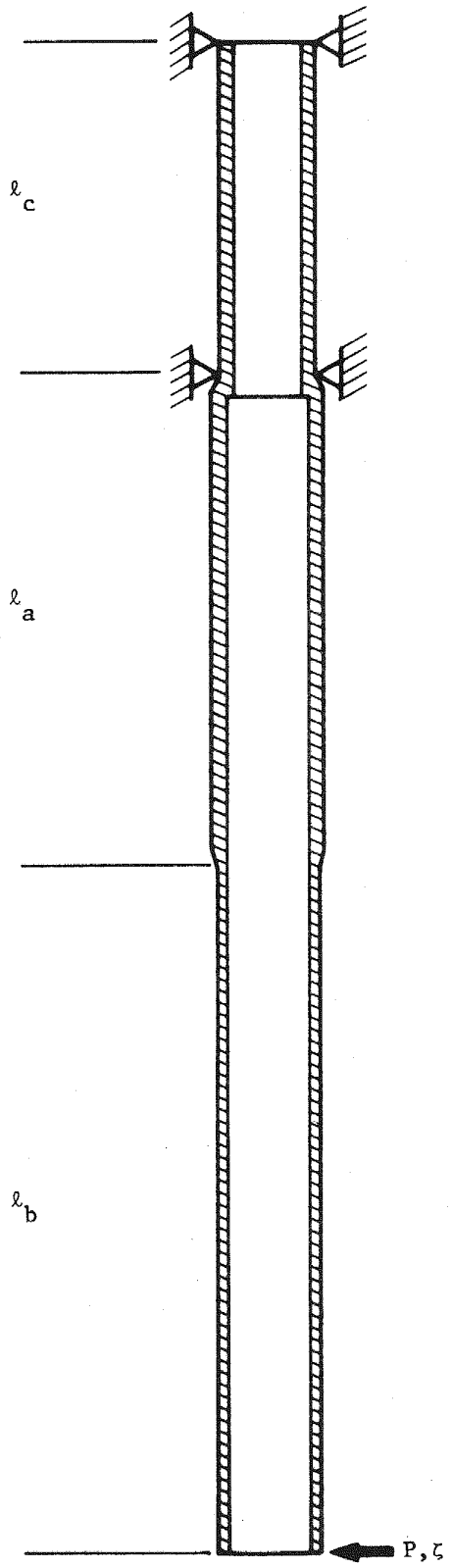

Fig. 2-4. Duct model

Deflection for the case where the assembly is completely restrained from rotation at the grid plate may be obtained from the formula by deleting the last term in the equation. To illustrate the use of the formula, consider the following parameters which are representative of the current duct design:

ℓ_a = 1.060 m, I_a = 11.92E-6 m^4, E_a = 193.1 GPa,
ℓ_b = 1.870 m, I_b = 7.68E-6 m^4, E_b = 193.1 GPa,
ℓ_c = 0.610 m, I_c = 8.46E-6 m^4, E_c = 193.1 GPa.

Substituting these values into the formula, the case of full grid plate rotation can be found:

$$k_{rot} = P/\delta = 1.91E\text{-}5 \text{ N/m} = 191 \text{ N/mm} \quad .$$

Neglecting the last term in the formula yields the following equation for the case of no grid plate rotation:

$$k_{no\ rot} = P/\delta = 2.40E\text{-}5 \text{ N/m} = 240 \text{ N/mm} \quad .$$

From these results, it can be seen that

$$k_{rot} = 0.80 \cdot k_{no\ rot} \quad .$$

The force required to straighten a bowed duct may be determined from the k values; e.g., for a typical worst-case deflection,

	δ_{max} (mm)	k = P/δ (N/mm)	P (kN)
No grid plate rotation	50	240	12.0
Full grid plate rotation	50	191	9.6

2.2.2. Core Dynamic Analysis of Thermal Downshocking of Core Assemblies

A concern which has recently been raised is possible thermal downshocking of the core during reactor trips in the event that coolant flow rate reduction did not keep pace with power reduction. It has been postulated that for such an event, the fuel rod cladding might be cooled more rapidly than the fuel, potentially leading to large, irrecoverable strains in the cladding as a result of fuel-cladding mechanical interaction. Subsequent detailed transient thermal analyses have confirmed that this is correct for the lower blanket region of the rod. This is not correct in the active core regions of the rod because fuel temperatures in these regions always fall much more rapidly than cladding temperatures. Because blanket pellets are expected to swell much less than fuel pellets, it is believed that pellet-cladding interactions will not pose significant problems for this transient.

A two-step approach was taken to determine the transient temperature distribution in a GCFR fuel rod undergoing scram without flow reduction. The ROD*SIM code (Ref. 2-9) was used to determine the transient local coolant temperature at the point of interest. This information was in turn fed into a detailed transient TAC2D (Ref. 2-10) thermal model as a boundary condition for a section of a fuel rod at the axial location of interest. It was found that the fuel temperatures in the powered regions of the core dropped much faster than the cladding temperatures.

In order to study this further, a simple model was set up to represent a fuel rod:

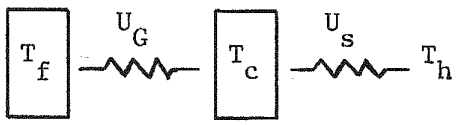

T_f and T_c represent the fuel and cladding temperatures, respectively, which can be determined from the following coupled first-order linear differential equations:

$$(\rho Vc_p)_f \frac{dT_f}{dt} = U_G \cdot (T_c - T_f) + Q \quad ,$$

$$(\rho Vc_p)_c \frac{dT_c}{dt} = U_G(T_f - T_c) + U_s \cdot (T_h - T_c) \quad ,$$

where $(\rho Vc_p)_f$ = fuel heat capacity J/K,
$(\rho Vc_p)_c$ = cladding heat capacity J/K,
U_G = gap conductance W/K,
U_s = surface film conductance W/K,
Q = power generated in the fuel section W,
T_h = local coolant temperature K.

An analytic solution to these equations was attempted using LaPlace transforms. However, this led to cumbersome algebraic equations, so this approach was abandoned in favor of directly solving the equations using the SYSL simulation code (Ref. 2-11). Parameter studies were performed with SYSL to determine the nature of the transient local rod response as a function of parameters such as gap conductance and axial location for a wide variety of transients. The behavior of the rod during a hypothetical transient consisting of a scram without flow reduction was of particular interest, since it was felt that such a transient could lead to a rapid reduction in cladding temperature while the fuel temperature remained high, which would result in possible overstraining of the cladding. This transient has been examined, and the results are given below.

Three cases were considered. The first case consisted of a section of a maximum powered rod at midcore undergoing a transient during which rod power is instantaneously reduced to zero and coolant flow rate and temperature are held constant. Figure 2-5 shows the fuel and cladding temperatures as a function of time. As can be seen, the fuel temperature drops much faster than the cladding temperature in such a way that the temperature difference between the fuel and cladding is a monotonic decreasing function of time

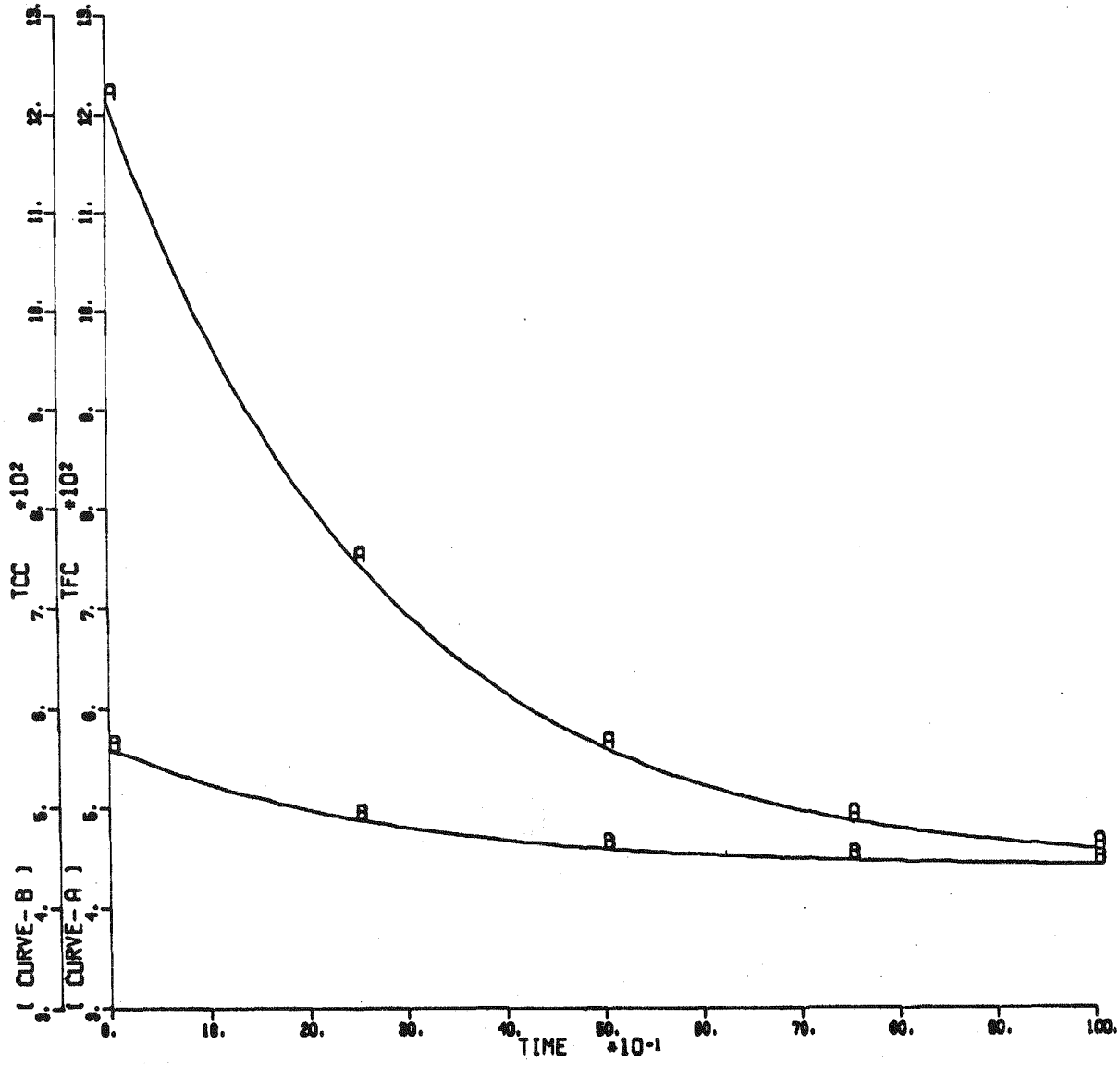

Fig. 2-5. Trip without flow reduction, midcore response: pellet and cladding temperatures (°C) vs time (s)

(Fig. 2-6). Thus, because of the loss of internal heat generation, the fuel rod cools from the inside out, in contrast to a hot ingot placed in a cool bath, which cools from the outside in.

An important effect missing from the first case is the decrease in local coolant temperature which would occur during a scram without flow reduction. This effect was accounted for in the second case, which considered a portion of the maximum-powered rod near the core outlet; the decrease in local coolant temperature is greatest in this region. When power was cut, the local coolant temperature was assumed to decrease exponentially from its initial value to the value of the core inlet temperature with a time constant of 3.8 s (a reasonable value chosen on the basis of previous analyses). Once again, it was found that the fuel temperature always decreased faster than the cladding temperature in such a way that the fuel-cladding temperature difference is a monotonic decreasing function of time. This is illustrated in Figs. 2-7 and 2-8.

The third case consisted of the lower axial blanket portion of the maximum-powered fuel rod. This case is different from the first two cases because little power generation occurs in this portion of the rod. It was assumed that no power generation was occurring in this part of the rod, and thus the pellet and cladding temperatures initially equalled the local coolant temperature. Upon initiation of the transient, the local coolant temperatures decreased as in case 2. As expected, the rod cooled from the outside in, and the temperature difference between the pellet and cladding, which initially was zero, rapidly increased to a maximum value and then slowly decayed to zero. For parameter values typical of GCFR fuel rods, this transient could cause the cladding in the blanket region of the rod to be overcooled by about 48°C (Figs. 2-9, 2-10). Whether this is sufficient to cause significant over-straining of the cladding will be determined by stress analyses which are in progress.

The results of this analysis indicate that in the event of a power trip without flow reduction, fuel temperatures in the active core region of a fuel rod always decrease at a faster rate than corresponding cladding

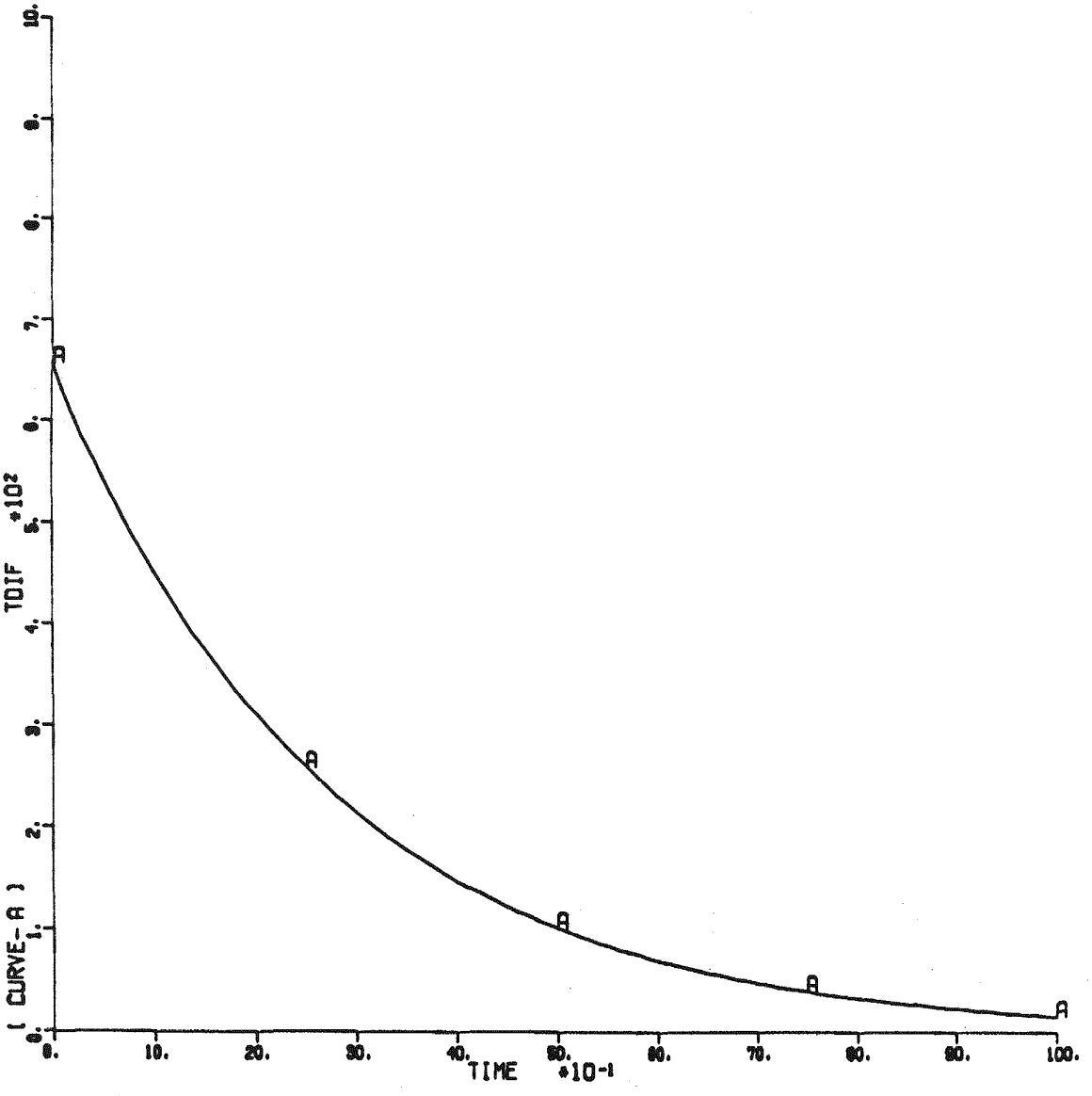

Fig. 2-6. Trip without flow reduction, midcore response: pellet-cladding temperature difference (°C) vs time (s)

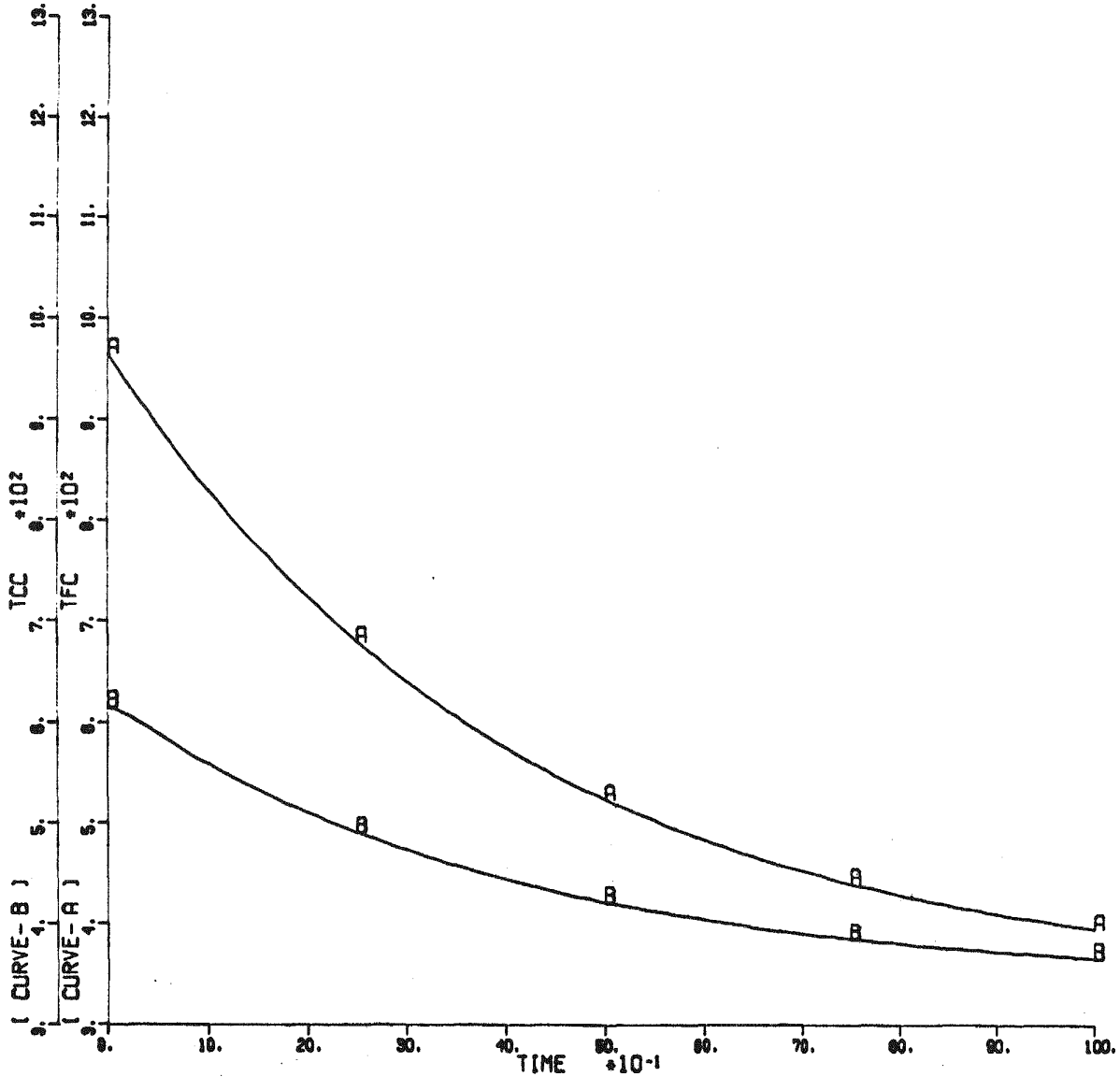

Fig. 2-7. Trip without flow reduction, lower core response: pellet and cladding temperatures (°C) vs time (s)

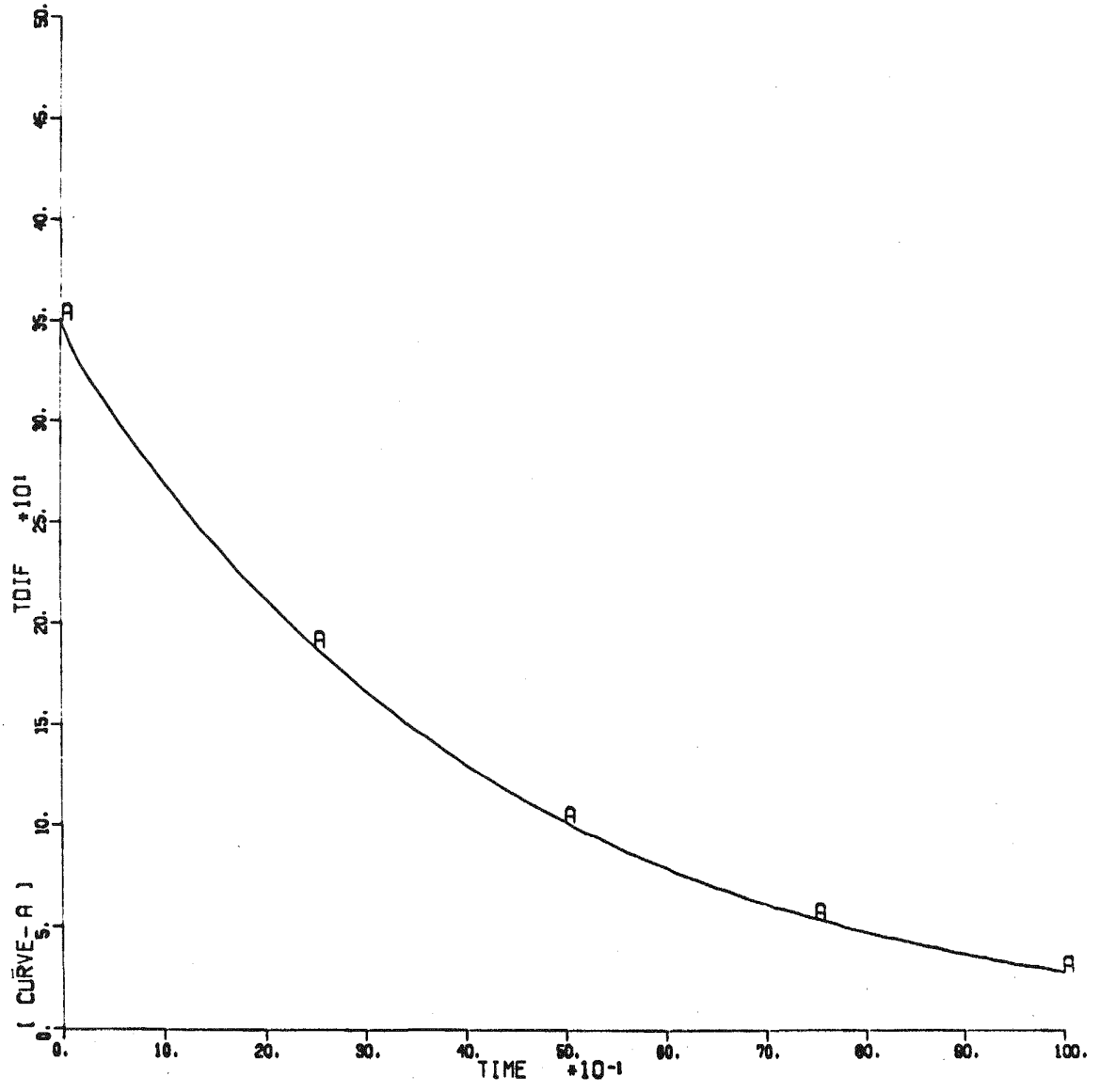

Fig. 2-8. Trip without flow reduction, lower core response: pellet-cladding temperature difference (°C) vs time

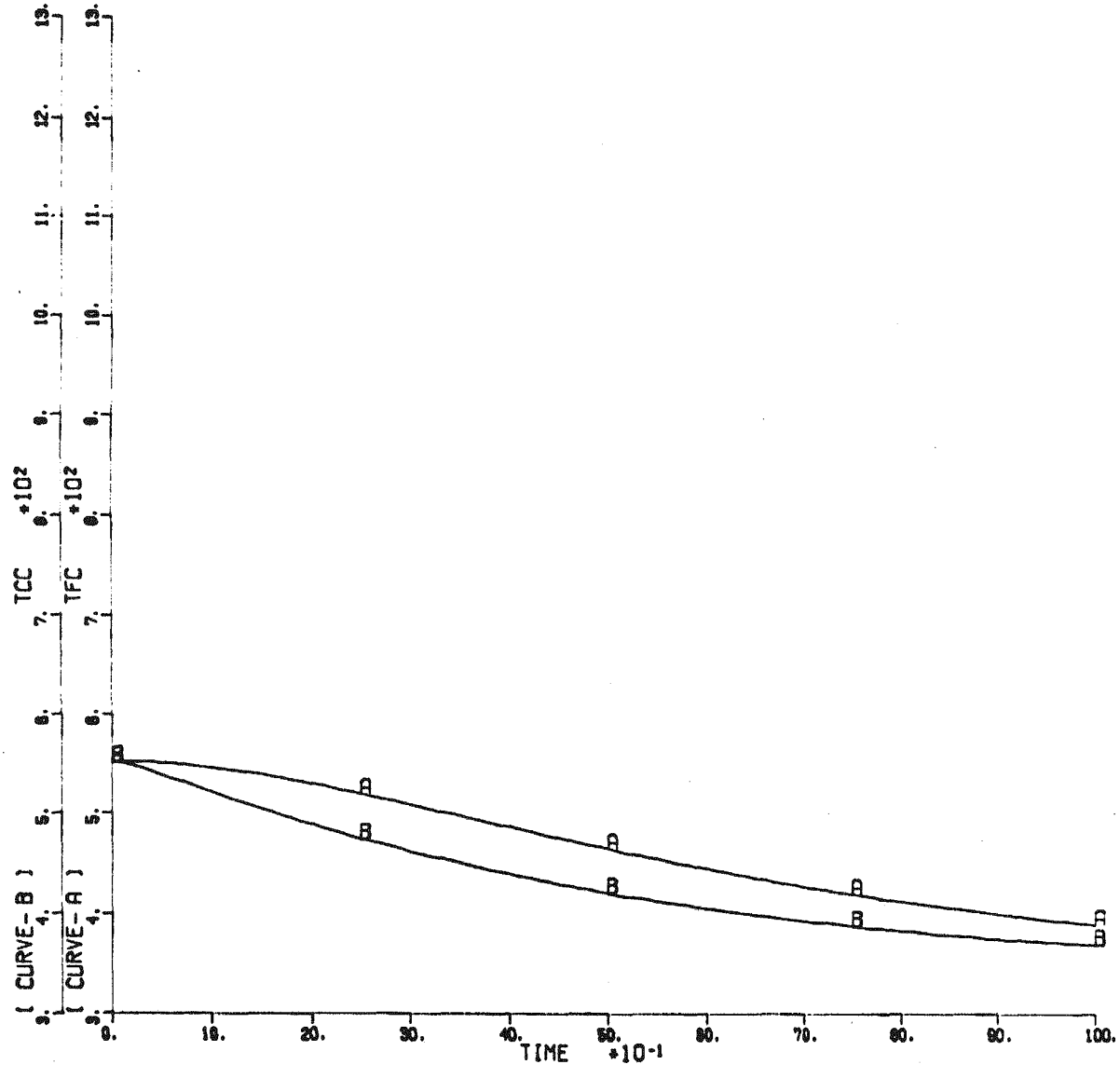

Fig. 2-9. Trip without flow reduction, lower blanket response: pellet and cladding temperatures (°C) vs time (s)

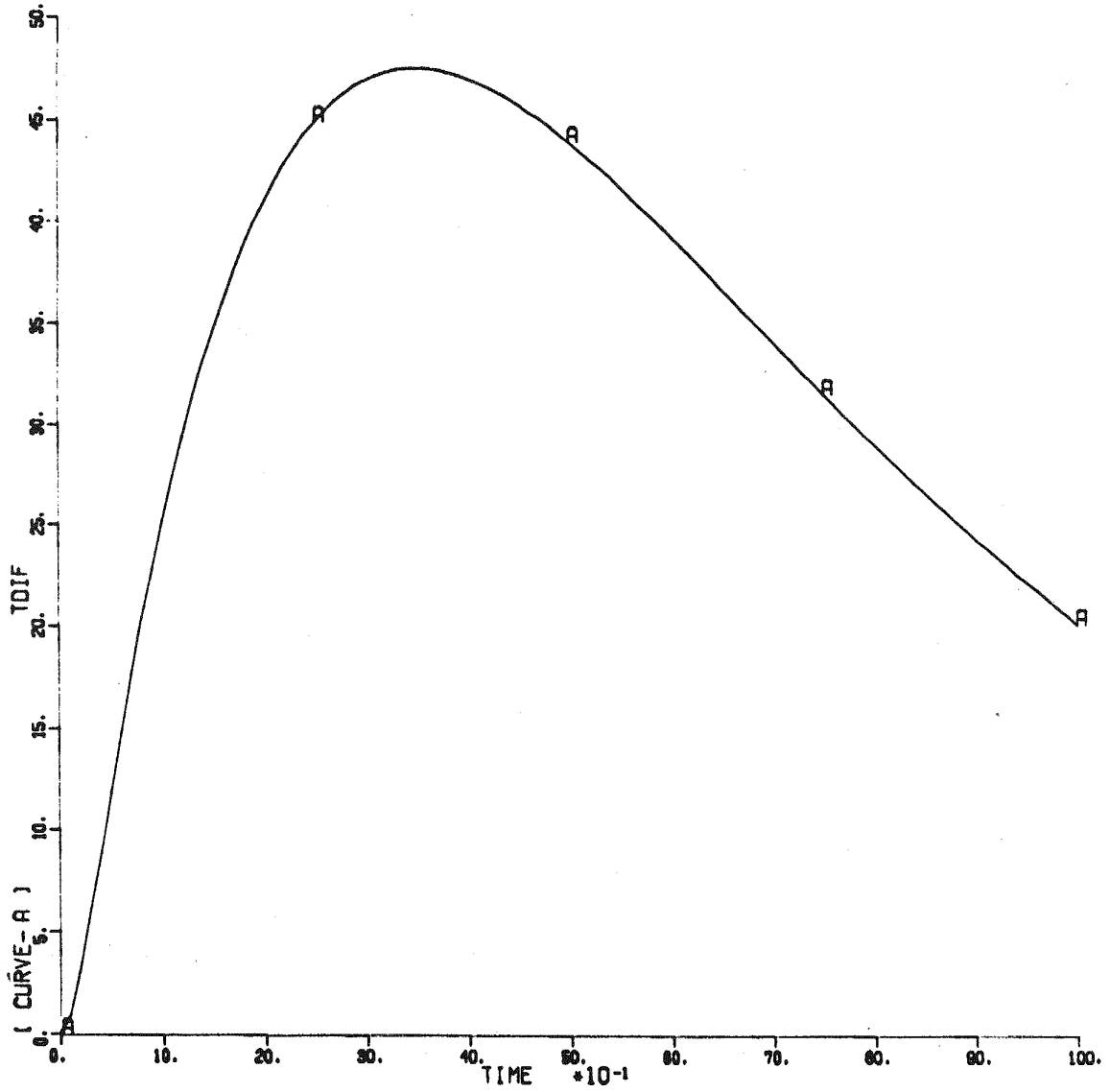

Fig. 2-10. Trip without flow reduction, lower blanket response: pellet-cladding temperature difference (°C) vs time (s)

temperatures. Thus, overstraining of the fuel rod cladding will not occur in this region for such a transient. It was also shown however, that in the lower blanket region of the core, the cladding temperatures decrease at a faster rate than the corresponding pellet temperatures. Thus, there is a potential for cladding overstraining in the lower blanket region of the rod for this transient. Ongoing stress analyses are addressing this question and will be the sujbect of a future report.

2.3. CORE ASSEMBLY STRUCTURAL DESIGN CRITERIA

Work continued on the development of the core consumable design criteria. In order to justify the selection of these criteria and verify their adequacy for ensuring structural integrity, a trial application program has been undertaken. During this quarter, the design criteria guidelines were applied to previous analyses of fuel rod bowing and fuel assembly bowing and dilation.

In order to perform the structural evaluations, it was necessary to modify some of the structural analysis codes to allow output of various quantities required for application of the criteria. This was done, and the revised codes were checked to verify their correctness. Once the codes were modified, the application of the criteria was successfully carried out. It was found that all stress and strain quantities necessary for comparison with their limit quantities could be computed. All primary and secondary stress limits and thermal creep damage and thermal creep strain limits were met. Fatigue and brittle fracture considerations have been deferred until the next phase of trial application. The structural evaluation has been summarized and presented to the National Structural Design Criteria Working Group.

2.4. CORE ASSEMBLY MECHANICAL TESTING

The objective of this task is to conduct mechanical tests of core assembly components and subassemblies to simulate the mechanical loads expected during normal and abnormal reactor operating conditions. The current phase of the assembly mechanical testing program involves testing

of fuel assembly components. The preliminary fuel rod/spacer interaction test using single spacer cells and rods was conducted during FY 76. The reproducibility testing of the hexagonal spacer cells was completed, and testing of a new modified hex design is continuing. The design and procurement of blanket assembly components for testing was initiated. Further tests on grid spacers are being planned and designed, and flow-induced vibration test planning is in progress.

2.4.1. Rod-Spacer Interaction Tests

The purpose of prior rod-spacer interaction tests was to evaluate the effect of interacting forces between the fuel rod and the spacers under the mechanical and environmental operating conditions expected in the GCFR. The simulated forces are primarily caused by bowing induced by temperature gradients and irradiation-induced swelling. Reactor operational transients cause relative motion of the rod and spacer, which results in frictional forces. The frictional forces and relative motion cause wear of the rod and spacer pad surfaces. The interaction force is simulated by a deadweight load on a spacer cell resting on a fuel rod. The calculated loads due to rod bowing have always been predicted to be of the order of 5 N. The results of the reproducibility tests using a reference design hexagonal rod spacer indicated there was no problem due to these loads. The bowing load simulation tests are being continued to investigate an advanced design called the modified hexagonal spacer. Because of some spurious test results (Ref. 2-12), cell dimensions during processing have been measured. Measurements were made after electrodischarge machining (EDM) of the grid, stress relieving, and final cutting of each of seven cells from the 37-rod grid spacer. The seven cells are presently being cut from the grid by EDM wire cutting. The measurements made to date indicate that the cell diameters and perpendicularity have not changed. These measurements will be repeated after cutting and during assembly of the cells in the test rig. The cells will be tested against ribbed rods using a long stroke (3.8 mm) and a 1-hr dwell time between strokes for a total of 100 strokes.

A second phase of rod-spacer testing is being planned. During this phase, tests will simulate interactions due to misalignments between adjacent spacers occuring as a result of tolerances or distortions. This requires at least three adjacent spacers with a provision for misalignment of the center spacer. The No. 3 test rig has the largest furnace and will be modified for this test. Misalignments of up to 0.5 mm of one spacer to another spacer will be allowed in the test rig design. It is calculated that the interaction loads due to a 0.5-mm misalignment will be about 50 N. Interacting normal loads between rod and spacer cannot be directly measured, but the frictional forces will be measured by a load cell installed on the push rod which pushes the fuel rod during its simulated expansion and contraction linear movements. The length of the test piece is 300 mm, or the pitch of three spacers, which is the length of the uniform heating zone of the present furnace. For future spacer tests which might involve multiple spacers, more axial spacers, and increased spacer pitch, a larger furnace will be required. A furnace with a 150-mm diameter and a 600-mm-long uniform heating zone is being procured.

2.4.2. Spacer-Grid Mechanical Tests

Tests of the 37-rod AGATHE spacer will be conducted on the INSTRON universal testing machine. This machine has been received, and arrangements for laboratory installation are in progress.

2.4.3. Flow-Induced Vibration

Design of a small, room-temperature helium loop (at high pressure) for flow-induced vibration testing has continued. This loop will also be used for flow and pressure drop testing of core assembly components. The blower and loop requirements are being established.

2.5. HEAT TRANSFER AND FLUID FLOW TESTING

During this quarter, correlation of the test data from the initial inlet nozzle test was completed along with the design of two new component

flow tests. The test data are from tests discussed in Ref. 2-12 and shown in Table 2-2. The layout of the test assembly is shown in Fig. 2-11. The data shown in Table 2-2 are the pressure loss coefficients for each component predicted analytically and calculated from measured data. The loss coefficient is defined as follows:

$$\Delta P_{loss} = K\frac{\rho V^2}{2g} \quad ,$$

where ΔP_{loss} = pressure loss,
K = loss coefficient (constant),
ρ = fluid density,
V = fluid velocity in the fuel assembly,
g = gravitational constant.

The measured loss coefficients differ considerably from the predicted coefficients, although the overall sum is very close. The only close correlation is in the fission product trap region, where there are parallel flow paths. The reason for the large discrepancy at the inlet is believed to be due to flow energy being converted to acoustical energy (Ref. 2-12). The higher coefficients across the manifold were unexpected. Further tests will be conducted on the manifold and inlet nozzle. It is believed that these tests will result in data which will explain the discrepancies of the test.

The design of new test model components for simulating the new inlet nozzle design is continuing, and the detail drawings have been reviewed, approved, and released for fabrication. The design layout is shown in Fig. 2-12. A test model assembly of the blanket low-flow control device has been designed, and the drawings are being reviewed.

REFERENCES

2-1. Kreith, F., Principles of Heat Transfer, International Textbook Company, Scranton, 1967.

TABLE 2-2
INLET NOZZLE FLOW TEST DATA CORRELATION

	Loss Coefficient K		
	Predicted		Measured
Inlet (sharp edge)	1.117		0.215
Expansion into inlet struts	0.09		
Expansion into nozzle section	0.141	0.24	0.478
Friction in nozzle section	0.009		
Across fission gas trap	0.191		0.193
Center shield	0.152		-0.174
Annular shield	0.132		0.607
	ΣK_p = 1.83		ΣK_m = 1.32
Manifold	0.24		0.94
Total	2.07		2.26

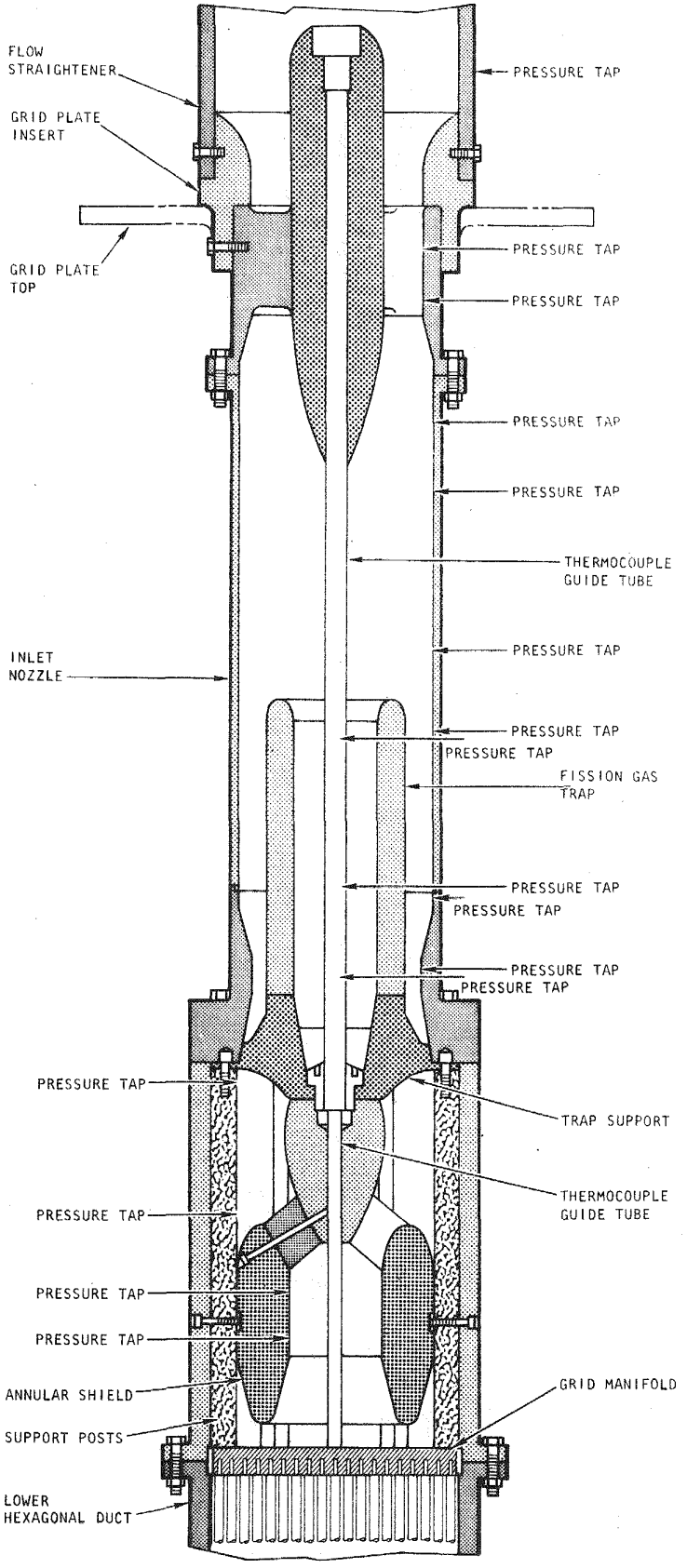

Fig. 2-11. Inlet nozzle test assembly for test data correlation

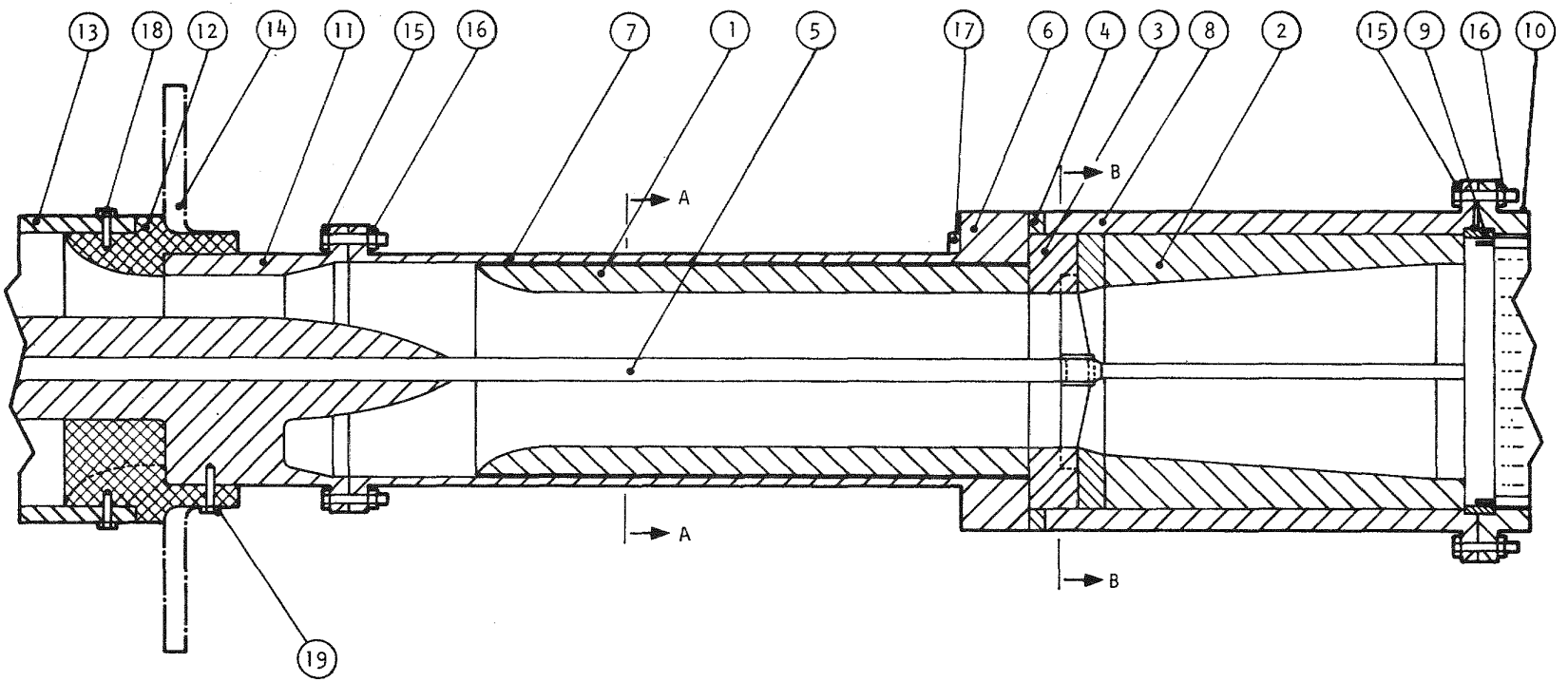

1	TRAP AND SHIELDING	11	UPPER INLET NOZZLE FITTING
2	ANNULAR SHIELD ASSEMBLY	12	GRID PLATE INSERT SIMULATOR
3	THERMOCOUPLE SUPPORT ASSEMBLY	13	INLET SIMULATOR
4	FLANGE	14	INLET FITTING
5	TUBE ASSEMBLY	15	HEX CAP SCREW 5/16-18 UNC X 1.5 LG
6	LOWER INLET NOZZLE FITTING	16	HEX NUT 5/16-18 UNC
7	INLET NOZZLE CYLINDER	17	HEX CAP SCREW 3/8-16 UNC X 3.0 LG
8	UPPER FLOW DUCT	18	HEX CAP SCREW 1/4-20 UNC X 0.75 LG
9	MANIFOLD ASSEMBLY	19	HEX CAP SCREW 1/4-20 UNC X 1.0 LG
10	LOWER FLOW DUCT		

Fig. 2-12. Inlet nozzle flow test assembly

2-2. Langhaar, H. L., Dimensional Analysis and Theory of Models, John Wiley & Sons, New York, 1951.

2-3. Eriksson, S. O., "SCEPTIC, a Fortran IV Computer Program for Temperature Analysis of Gas or Liquid Cooled Flow Passages With Heated Smooth or Roughened Surfaces, A User's Guide," Swiss Federal Institute for Reactor Research Report TM-IN-479, July 16, 1971.

2-4. Rowe, D. S., "COBRA IIIc: A Digital Computer Program for Steady State and Transient Thermal-Hydraulic Analysis of Rod Bundle Nuclear Fuel Elements," Battelle Northwest Laboratory Report BNWL-1695, March 1973.

2-5. Wheeler, C. L., et al., "COBRA-IV-I: An Interim Version of COBRA for Thermal-Hydraulic Analysis of Rod Bundle Nuclear Fuel Elements and Cores," Battelle Northwest Laboratory Report BNWL-1962, March 1976.

2-6. Goodman, J., et al., "The Thermodynamic and Transport Properties of Helium," General Atomic Report GA-A13400, October 1975.

2-7. Novendstern, E. H., "Pressure Drop Model for Wire-Wrapped Assemblies," Trans. Am. Nucl. Soc. 14, 660-661 (1971).

2-8. Deissler, R. G., and M. F. Taylor, in Reactor Heat Transfer Conference of 1956, part 1, J. E. Viscardi (compiler), 1957, p. 416 (TID-7529).

2-9. Lee, G. E., "User's Manual for 'ROD*SIM'," General Atomic, unpublished data.

2-10. Boonstra, R. H., "TAC2D: A General Purpose Two-Dimensional Heat Transfer Computer Code, User's Manual," General Atomic Report GA-A14032, July 15, 1976.

2-11. Estrine, E. A., "SYSL Users Guide," General Atomic, to be published.

2-12. "Gas-Cooled Fast Breeder Reactor Quarterly Progress Report for the Period November 1, 1976 Through January 31, 1977," ERDA Report GA-A14240, General Atomic, February 1977.

3. PRESSURE EQUALIZATION SYSTEM FOR FUEL (189a No. 00582)

3.1. CORE ASSEMBLY AND PES SEALS

The core assemblies (fuel, control, and blanket) in the GCFR are clamped at the conical surfaces of the assemblies to the matching surfaces in the grid plate with a force sufficient to support the assembly against side loading. The assemblies are cantilevered downward and must be sealed to the grid plate to limit the coolant flow bypassing the assemblies. The assembly vents must be connected and sealed to matching gas passages in the grid plate, and the seals must function at the coolant pressure difference between the reactor core inlet and exit plenums. The effectiveness of the seals over the life of the core is uncertain, not only because each assembly may be rotated several times over its useful life, but also because the seals must be effective in a high-purity, high-temperature helium environment while subject to mechanical, vibrational, and thermal effects. Most of the uncertainties are expected to be resolved in a two-part program: (1) a materials screening test program for the study of static adhesion of simulated fuel assembly and grid plate parts clamped together and (2) leakage tests of fuel assembly and vent connection seals to the grid plate. Current progress in these activities is described below.

3.1.1. Static Adhesion Tests

The first set of static adhesion tests was conducted in FY 75 on 316 and 304 stainless steel at various matching cone angles, contact loadings, and surface finishes. This was followed in FY 76 by a second set of tests using materials including couples of Inconel 718 - 316 stainless steel, Inconel 718 - 304 stainless steel, and 304 - 316 stainless steel. Preliminary planning of tests for FY 77 is in progress. The third test phase will

include adhesion tests of metal samples coated with hardened surface materials. The simulated grid plate materials will be type 316 or type 304 stainless steel and Stellite-6B tested against simulated fuel assembly samples of type 316 stainless steel, Stellite-6B, and coatings of chromium carbide, chromium oxide, and Stellite-6. The conical surface angle will be limited to a 60-deg included angle (30 deg plus cone angle), and the static load will be 1,333 N (simulating a 13,330-N clamping load for a full-size assembly). The assembly combinations are listed in Table 3-1. The substrate samples for coating have been machined.*

3.1.2. Fuel Assembly Ring Seal Leakage Tests

An alternative to the conical metal-to-metal core assembly seal design being developed uses piston rings as static sealing members. The test equipment, test grid parts, and core subassembly parts from the conical seal test have been modified, and ring seal tests are in progress. These tests include two ring designs provided by U.S. vendors (Stein Company and Dover Corporation) and one German design [Kraftwerk Union (KWU)]. The KWU design is being fabricated by KWU and two U.S. vendors for performance test comparisons. The piston ring designs and the room temperature test data for the U.S. vendor designs are described in Ref. 3-1.

During this quarter, preparations were made for temperature testing of the U.S. vendor design piston ring autoclave. This involved adding installation heaters and more electrical power for the longer test assembly. Temperature testing of the piston rings will be conducted during the next quarter.

The piston rings designed by KWU and manufactured by KWU and Dover Corporation were received. The as-built designs appear to have different dimensions, and they are being inspected to determine the discrepancies. The drawings for the piston ring test apparatus were changed to accommodate

*The Coatings Service Department of the Linde Division of Union Carbide Corporation will apply the coatings using its proprietary D-gun method. A quotation and delivery date are being prepared. Other coating vendors have been asked for quotes for their plasma gun methods.

TABLE 3-1
GRID PLATE AND FUEL ASSEMBLY MATERIALS

Grid Plate	Fuel Assembly	No. of Samples
316 stainless steel	Chromium carbide coating	2
316 stainless steel	Chromium oxide coating	2
316 stainless steel	Stellite-6 coating	2
316 stainless steel	Stellite-6B sample	2
304 stainless steel	Chromium carbide coating	2
304 stainless steel	Chromium oxide coating	2
304 stainless steel	Stellite-6 coating	2
304 stainless steel	Stellite-6B sample	2
Stellite-6B	316 stainless steel	4
Stellite-6B	Chromium carbide coating	4
Stellite-6B	Chromium oxide coating	4
Stellite-6B	Stellite-6 coating	4
Stellite-6B	Stellite-6B sample	4

the KWU piston rings. The second set of parts will be modified, and the first set will be used for continued testing of the U.S. vendor designs.

3.1.3. Vent Assembly Seals

The vent assembly design concept being developed for connecting the GCFR core assembly vents to the PES passages in the grid plate is described in Refs. 3-1 and 3-2. The vent assembly devices were laboratory performance tested with helium at room temperature and elevated temperatures to 300°C. The four test conditions are shown in Fig. 3-1 and listed below.

1. Condition 1: the fuel assembly is out of the reactor grid plate; the port seal valve is closed; the pressure outside the fuel assembly is higher than that inside; and leakage is into the fuel assembly.

2. Condition 2: the fuel assembly is in position, clamped to the grid plate; the port seal valve is open; and leakage is across the metal-to-metal torus seal.

3. Condition 3: the fuel assembly is in position, clamped to the grid plate; the port seal valve is open; and flow is from the fuel assembly through the vent connection to the PES vent.

4. Condition 4: the fuel assembly is out of the reactor grid plate; the port seal valve is closed; the pressure inside the fuel assembly is higher than that outside; and leakage is out of the fuel assembly.

These tests differ in several details from those described in Ref. 3-1. In order to obtain a higher creep strength at high temperatures, the belleville springs are made of 17-7 ph material rather than 310 stainless steel, which was used for the tests described in Ref. 3-1. In addition, the port seal valve is a flat metal-to-metal surface rather than mismatched conical surfaces, as in Ref. 3-1.

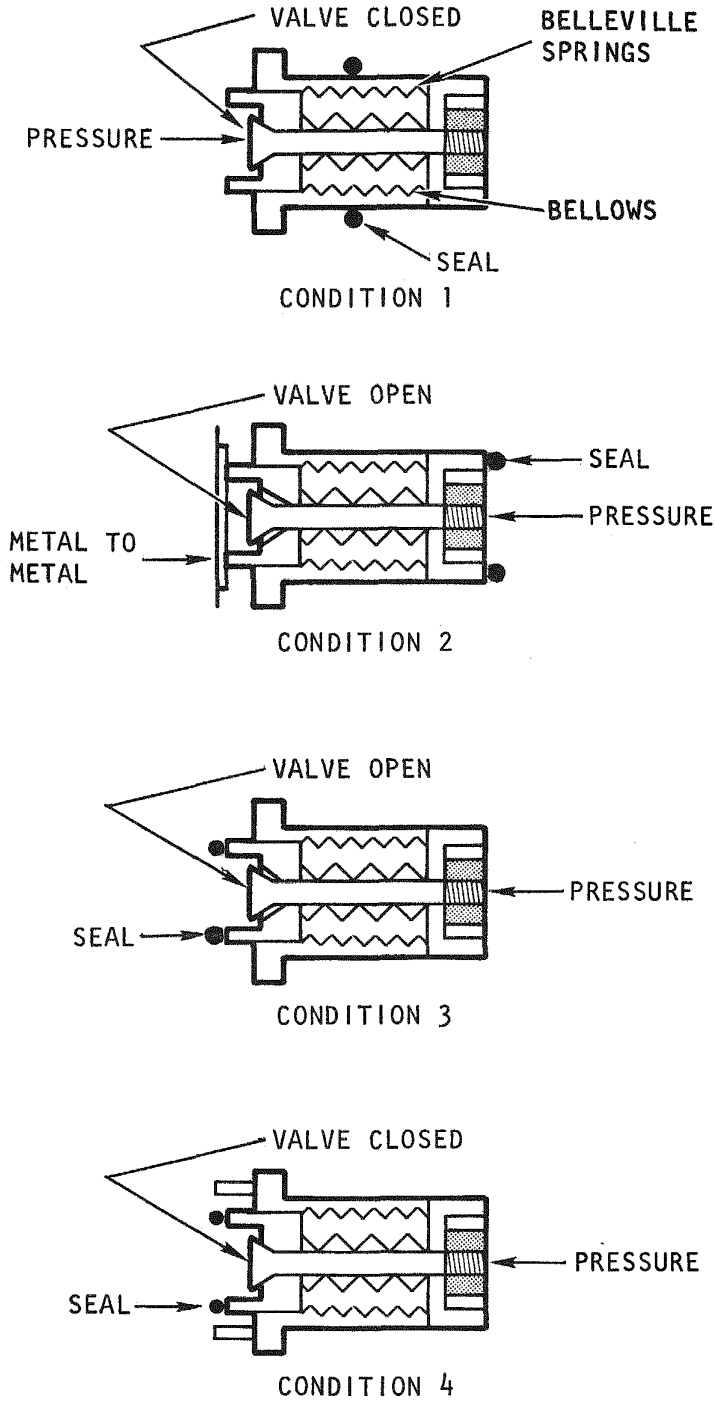

Fig. 3-1. Test conditions

The test results indicate a general performance improvement over that of the previous vent assembly. The vent connection leakage shown in Fig. 3-2 is well within the specified limit of 135 cm^3/min at a pressure differential of 21 MPa. There are no established criteria for leakage in conditions 1, 3, and 4 at this time; however, the flow in condition 3 (Fig. 3-3) may be too low, although it can be increased by redesigning the valve seat to increase the flow area. The leakage of the port seal in either direction, as shown in Figs. 3-4 and 3-5, is low, but it may not be low enough to seal off fission products. A criterion for port seal leakage has not been established.

3.2. ANALYSIS, MODELS, AND CODE DEVELOPMENT

During this quarter, detailed modeling of a fuel rod was initiated. This modeling requires the description of the flow in particle beds (e.g., the fuel pellets and the charcoal trap) connected by flow lines. Two activities are in progress: determination of the time constants for the core components and spatial integration of the one-dimensional compressible flow equations.

To determine the time constants, the isentropic depressurization of a volume of gas, V, was considered. This volume was initially at a pressure and temperature of P_o and T_o, respectively, exhausting to a vacuum through a flow line with area A and loss coefficient K. The conservation of mass and energy for the volume are

$$V \frac{d\rho}{dt} = -\rho A u \quad , \tag{3-1}$$

$$V \frac{dP}{dt} = -\gamma R T \rho A u \quad . \tag{3-2}$$

The equation of state and the flow resistance equation are

$$P = \rho R T \quad , \tag{3-3}$$

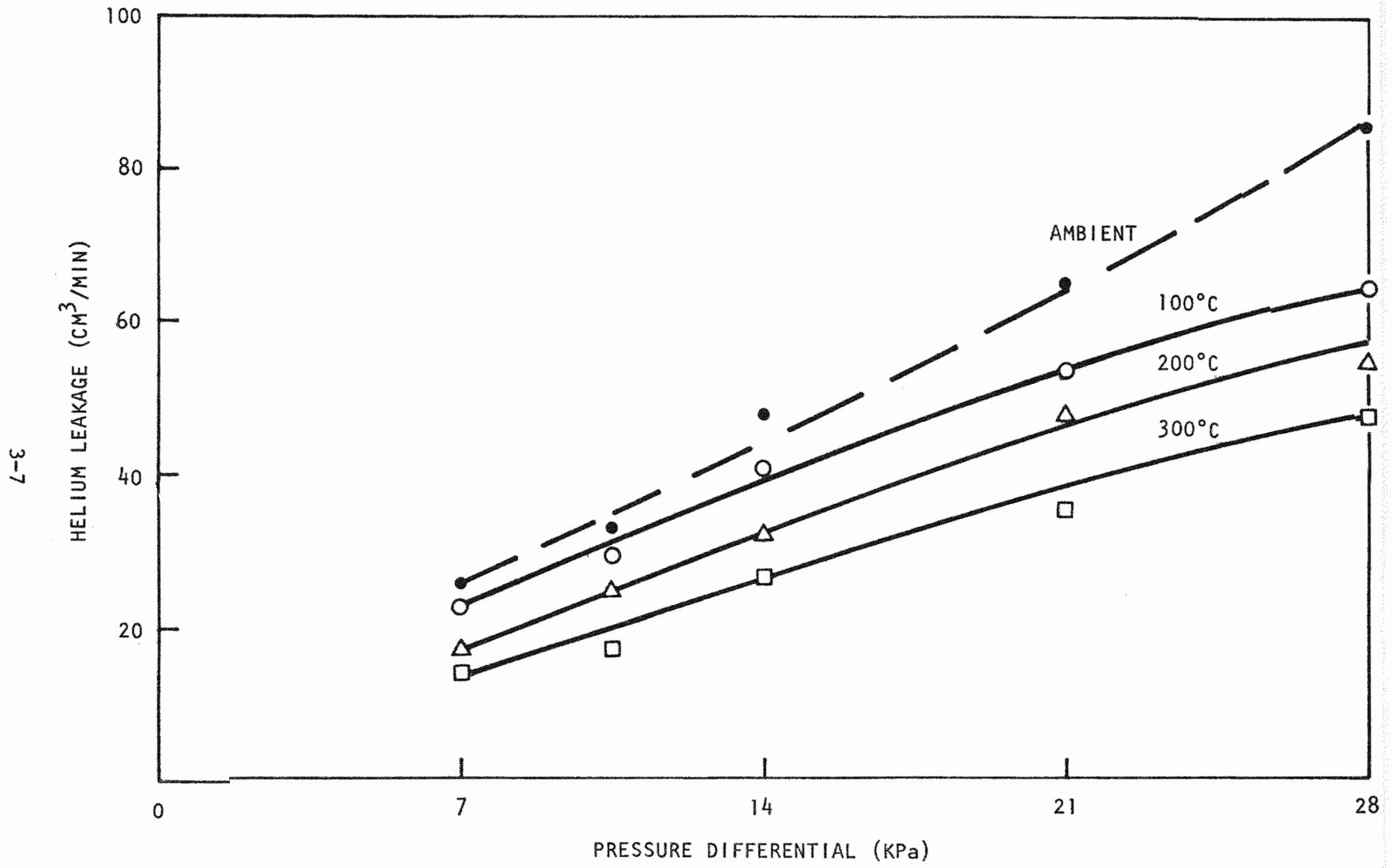

Fig. 3-2. PES vent connection, condition 2

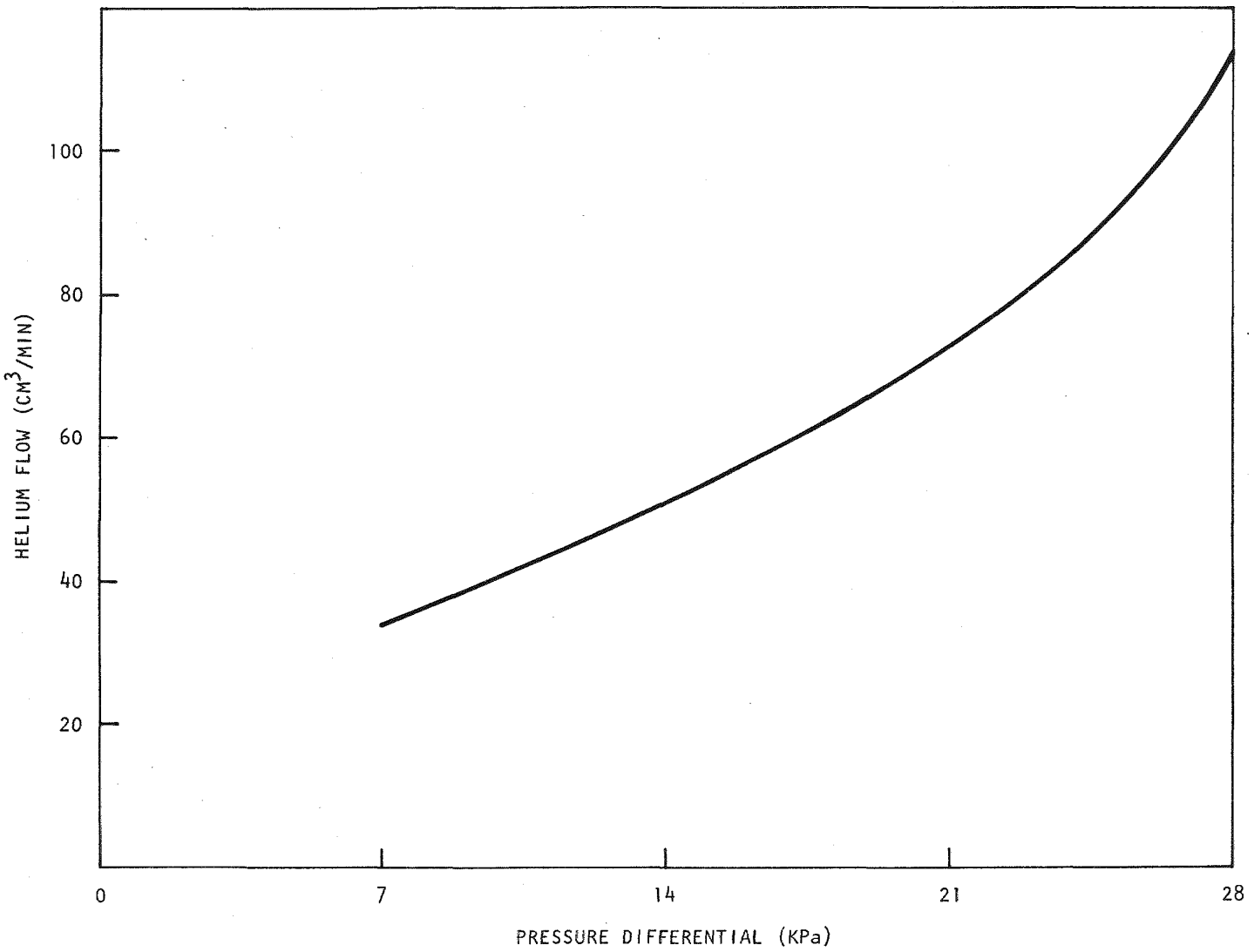

Fig. 3-3. PES port seal, condition 3

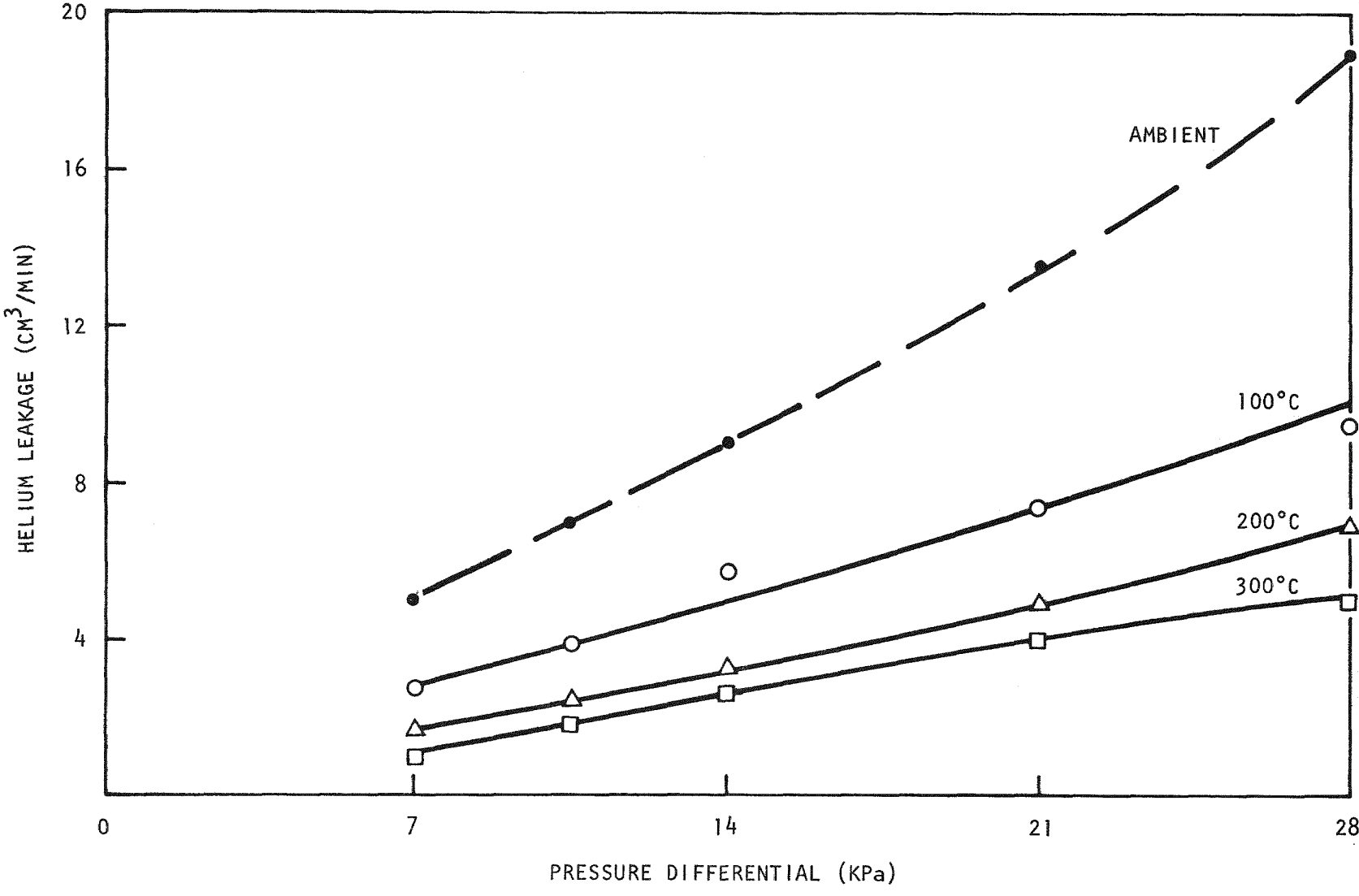

Fig. 3-4. Port seal valve, condition 1

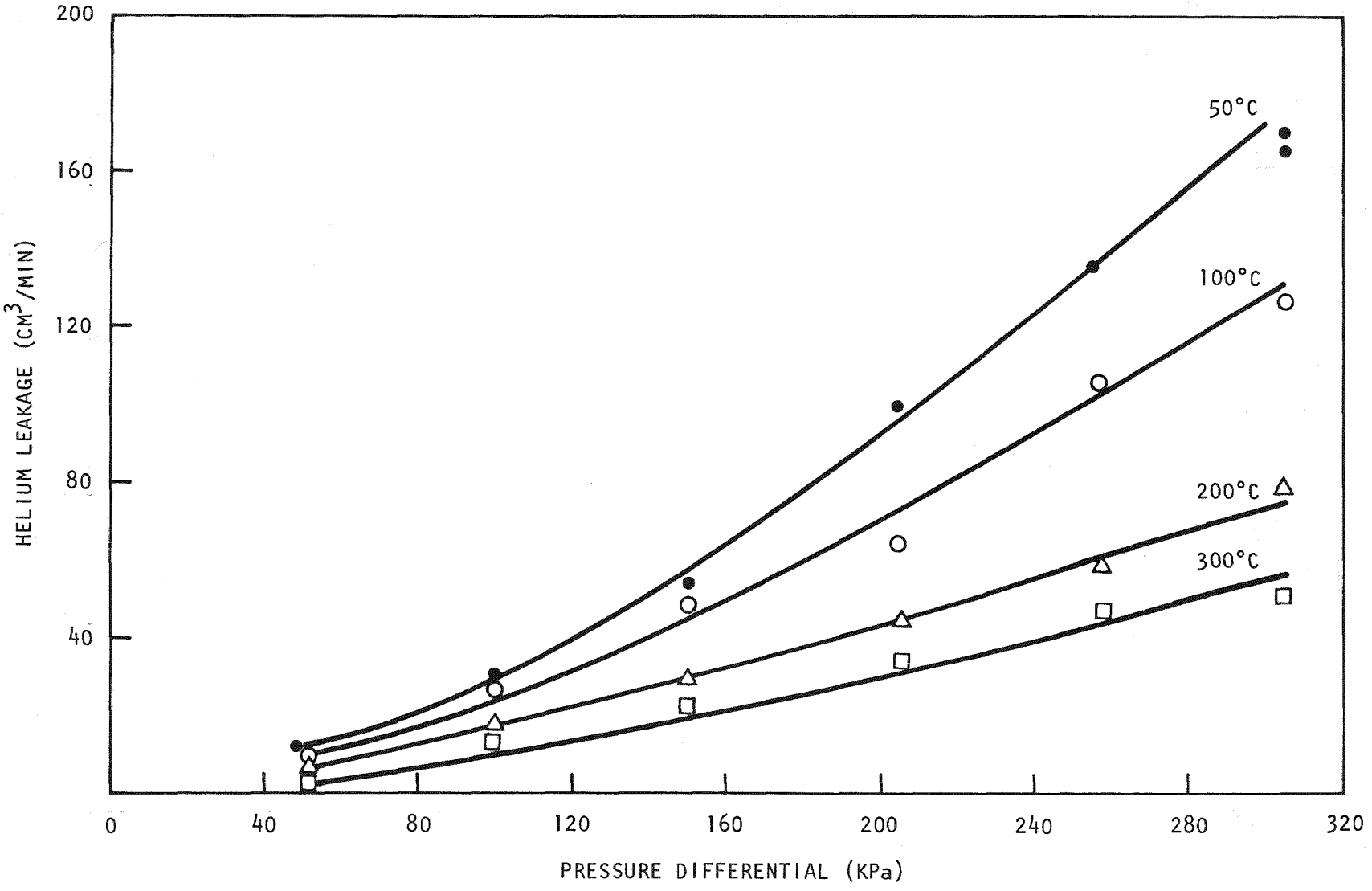

Fig. 3-5. Port seal valve, condition 4

$$P = \frac{1}{2} \rho u^2 K \quad , \tag{3-4}$$

respectively, where t, ρ, u, P, γ, R, and T are the time, density, velocity, pressure, specific heat ratio, gas constant, and temperature variables, respectively. By combining Eqs. 3-1 through 3-3, the isentropic relations are obtained:

$$\frac{\rho(t)}{\rho_o} = \left[\frac{P(t)}{P_o}\right]^{\frac{1}{\gamma}} \quad , \tag{3-5}$$

$$\frac{T(t)}{T_o} = \left[\frac{P(t)}{P_o}\right]^{(\gamma-1)/\gamma} \quad , \tag{3-6}$$

and Eq. 3-4 is solved for u:

$$u = \min(\sqrt{2P/\rho K},\ c) \quad , \tag{3-7}$$

where the speed of sound is $c = \sqrt{\gamma RT}$, and min(a,b) denotes the minimum of a and b. Substituting Eqs. 3-5 through 3-7 into Eq. 3-2 yields a single differential equation in P, which is integrated to give

$$P'(t') = \left(1 + \frac{\gamma - 1}{\sqrt{2\gamma}} mt'\right)^{-2\gamma/(\gamma-1)} \quad , \tag{3-8}$$

where $P' = P/P_o$,

$t' = t/(V\sqrt{K}/Ac_o)$,

$m = \min(1, \sqrt{\gamma K/2})$.

Setting $P' = e^{-1}$ at $t' = \tau'$, the dimensionless time constant is

$$\tau' = \frac{\sqrt{2\gamma}}{m(\gamma - 1)}\left[\exp\left(\frac{\gamma - 1}{2\gamma}\right) - 1\right] \quad ,$$

or, for helium with $\gamma = 1.67$,

$$\tau' = 0.606/m \quad .$$

In physical variables this corresponds to the time constant

$$\tau = \frac{0.606}{m} \frac{V\sqrt{K}}{Ac_o} \quad , \tag{3-9}$$

where $c_o = \sqrt{\gamma RT_o}$. In Eq. 3-9, m = 1 corresponds to a line loss coefficient $K > 2/\gamma$ which prevents choking, and τ is proportional to $V\sqrt{K}/Ac_o$; the other value, $m = \sqrt{\gamma K/2}$, corresponds to choking in the line and $K < 2/\gamma$, in which case τ is proportional to V/Ac_o and there is sonic velocity in the line [u(t) = c(t)].

Figure 3-6 shows the network analyzed in Ref. 3-1. Using Eq. 3-9, the time constants were calculated for each of the volume-line pairs as if they existed separately. The results are summarized below.

Volume	Line	A ($m^2 \times 10^3$)	K	τ (s)
N_1 (1.02 m^3)	K_2	0.45	137	9.46
	K_3	0.45	137	9.46
N_2 (0.02 m^3)	K_1	0.51	5.5	0.033
	K_2	0.45	137	0.185
	K_4	1.16	24.2	0.030
N_3 (3.46 m^3)	K_4	1.16	24.2	5.22
	K_5	1.96	225	9.41

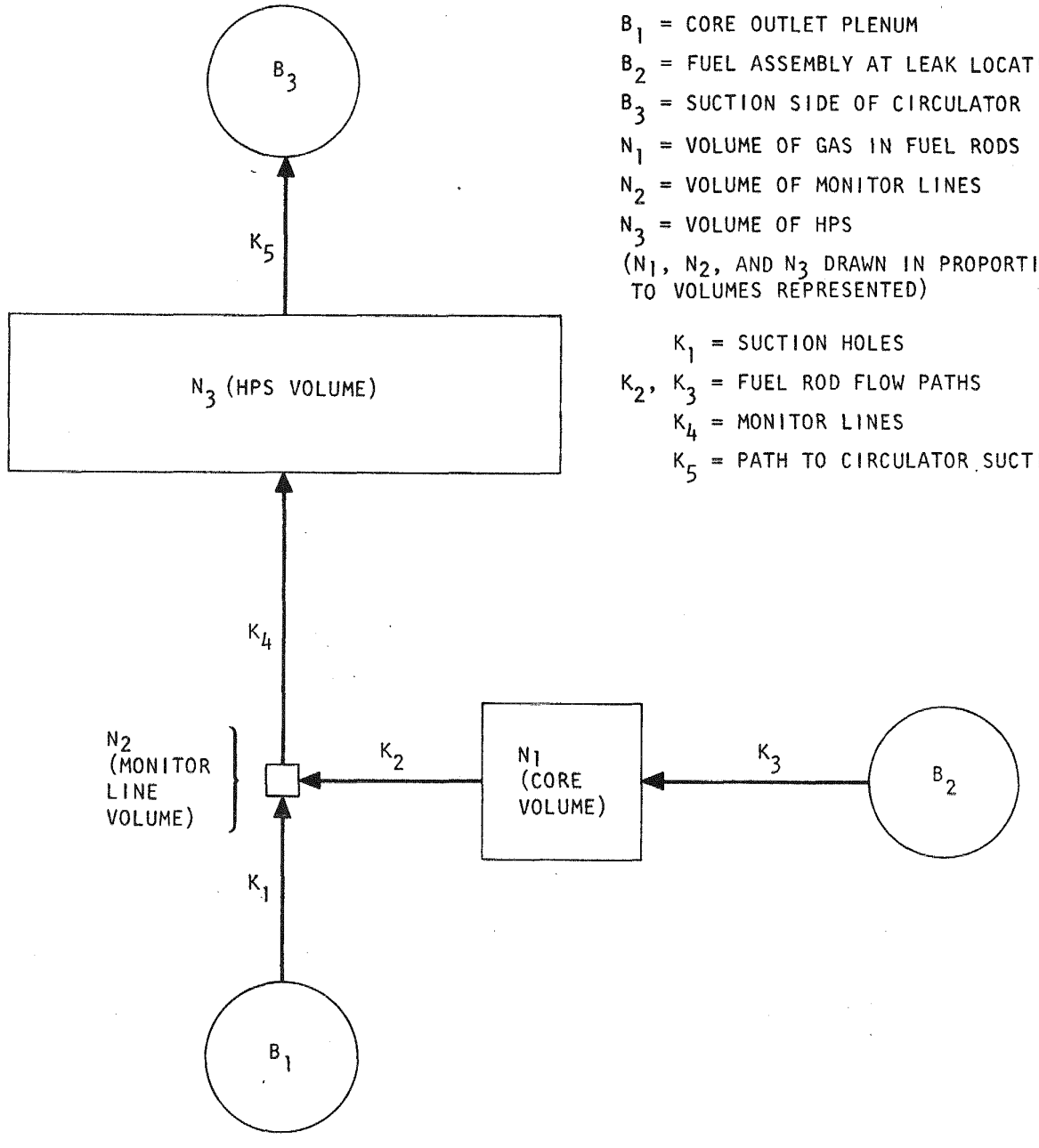

Fig. 3-6. Three-node lumped parameter model of the PES

From these values, it can be seen that core volume N_1 has the largest time constant, so this volume would be expected to depressurize most slowly. The helium purification system (HPS) volume N_3 has the next smaller time constants and thus depressurizes a little faster. The time constants for volume N_2 are two orders of magnitude smaller than those for N_1 or N_2, so if N_2 were not fed from volumes N_1 and N_2, it would depressurize very fast. The 9.46-s time constant for the core volume was based on all the gas volumes in the core being modeled as one volume. However, the gas stored in the many separate fuel rods does not behave as a single volume of gas. Therefore, these results are very tentative. An effort is now under way to determine the time constants of a single fuel rod using Eq. 3-9.

Derivation of the one-dimensional compressible flow equations was accomplished as follows (see Fig. 3-7):

Conservation of mass

$$\frac{\partial \rho}{\partial t} + \frac{\partial (\rho u)}{\partial x} = 0 \quad ; \tag{3-10}$$

Conservation of axial momentum

$$\frac{\partial (\rho u)}{\partial t} + \frac{\partial (\rho u^2)}{\partial x} = - \frac{\partial p}{\partial x} - F + \rho g \cos \theta \quad ; \tag{3-11}$$

Conservation of energy

$$C_p \left(\frac{\partial (\rho T)}{\partial t} + \frac{\partial (\rho u T)}{\partial x} \right) = \frac{4 q_w}{D_h} + \frac{\partial p}{\partial t} + u \frac{\partial p}{\partial x} + uF - \rho u g \cos \theta \quad ; \tag{3-12}$$

Equation of state

$$p = R \rho T \quad ; \tag{3-13}$$

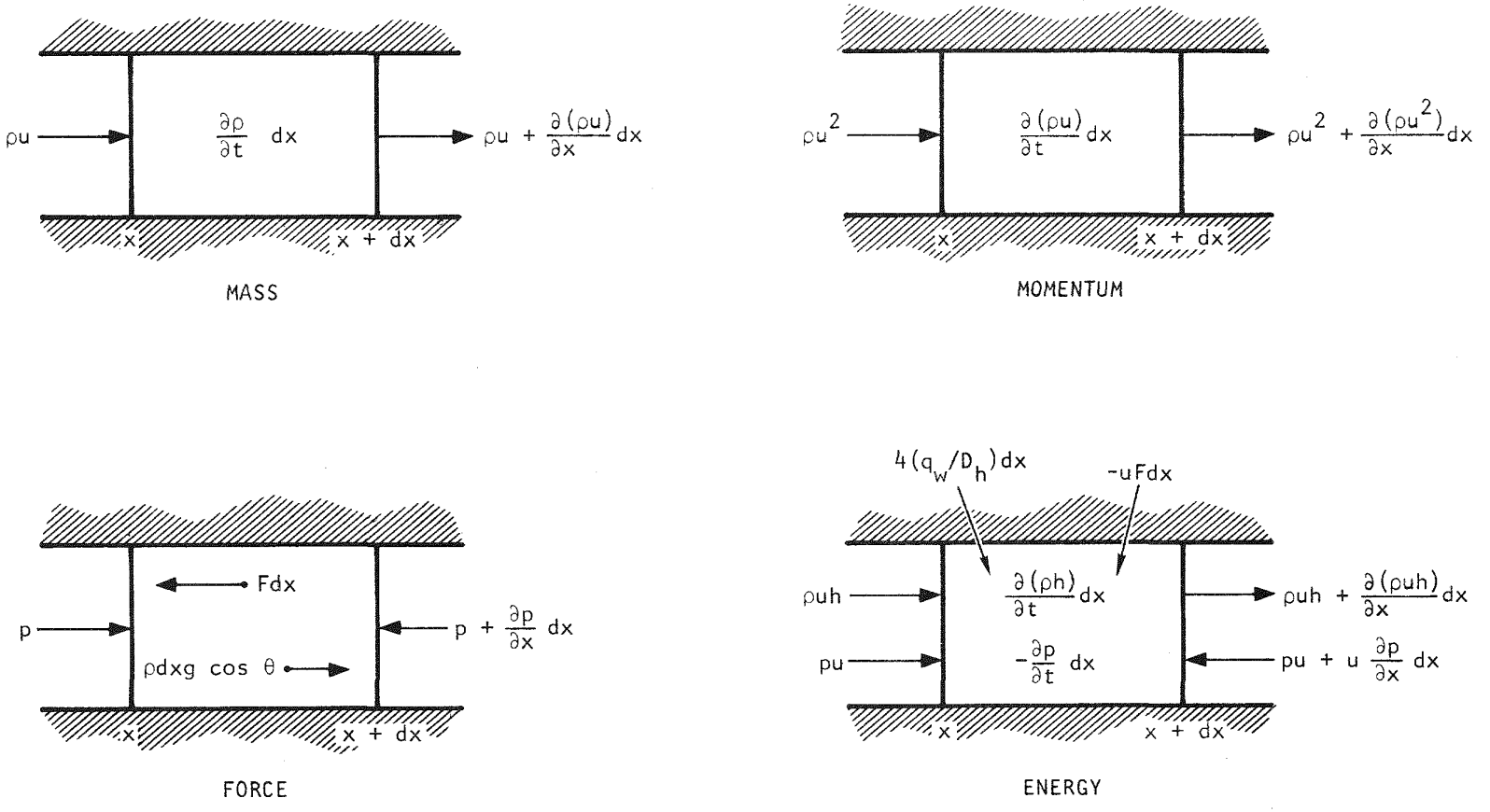

Fig. 3-7. Control volumes for derivation of one-dimensional, compressible flow descriptive equations (flows and forces are per unit area and axial diffusion is neglected)

where the enthalpy is

$$h = C_p T \quad .$$

Equation 3-10 states that the time rate of increase of mass must balance the net outflow of mass, and Eq. 3-11 equates the net rate of change of axial momentum with the forces acting on the fluid. The first force is the axial pressure gradient; the second force is the drag per unit volume, F, which is due to the shear stress at the wall in the case of a monitor line and the resistance of the particles in the case of a bed of granular solids. In the first case, F is related to the Darcy friction factor λ_s:

$$F = \frac{\rho u^2}{2D_h} \lambda_s(Re, r_s) \quad , \tag{3-14}$$

where $Re = \rho u D_h/\mu$ is the Reynolds number and $r_s = k_s/D_h$ is the relative surface roughness. In the second case, F is related to the particle-bed friction factor λ_p:

$$F = \frac{\rho u^2}{2D_h} \lambda_p(Re, r_p, \pi, \phi) \quad , \tag{3-15}$$

where $r_p = D_p/D_h$ is the relative particle diameter, π is the porosity or volume fraction, and $\phi = A_{sphere}/A_{particle}$ is the particle surface shape factor.

The particle-bed friction factor is

$$\lambda_p(Re, r_p, \pi, \phi) = \frac{4f_m}{r_p \pi^2} \left(\frac{1 - \pi}{\phi}\right)^{3-n} \quad , \tag{3-16}$$

where the modified friction factor f_m and the exponent n are functions of the modified Reynolds number $Re_m = r_p Re$:

$$f_m = \frac{100}{Re_m} + f_t \quad ,$$

$$n = 1.5 + 0.5 \tanh[2 \log_{10}(Re_m/60)] \quad ,$$

$$(1 \leq n \leq 2) \quad ,$$

where f_t is the fully turbulent value of f_m ($0.7 \leq f_t \leq 2.0$). In Eqs. 3-10 through 3-16, for the case of flow in a granular bed, $\rho = \pi\rho_g$ is the effective density, where ρ_g is the gas density; $u = G/\rho_g$ is the effective velocity; and G is the superficial mass flux based on the total duct area. For a normal duct without granules or particles, $\rho = \rho_g$ is the usual gas density.

In Eq. 3-12, the rate of change of enthalpy is equated to the contributions of the heat flux at the wall, q_w, the pressure work on the gas, the dissipation work due to F, and the gravitational work. If q_w is large, thermal choking is possible (the Rayleigh-Line process), and if uF is large, frictional choking is possible (the Fanno-Line process); however, these terms will be small for the PES application.

Equations 3-10 through 3-12 were also derived from the fundamental three-dimensional equations. Only the axial diffusion terms have been neglected, so the one-dimension equations are applicable to all significant flow phenomena in a single fluid line, including choking. For application to the PES network, it is necessary to integrate the equations over the axial coordinate x, resulting in a system of ordinary differential equations which can be numerically integrated over the time t.

In the PES application where there is heat transfer to the gas in the line, it is usually the temperature at the wall, T_w, and not the heat flux,

q_w, which is a known function of time (e.g., the fuel temperature); i.e.,

$$q_w = h(t - T_w) = C_p \rho u St(T - T_w) \quad ,$$

where h is the heat transfer coefficient and St is the Stanton number. For subsequent calculations, it is adequate to use Reynolds' analogy and take $St = \lambda/8$ ($\lambda = \lambda_s$ or λ_p). Therefore, the heat flux in Eq. 3-3 is related to the wall temperature by

$$q_w = \frac{1}{8} C_p \rho u \lambda (T - T_w) \quad . \tag{3-17}$$

The heat flux may also be specified; e.g., $q_w = 0$ for an adiabatic monitor line.

For the steady-state where the $\partial(\ )/\partial t$ terms are zero, Eqs. 3-10 through 3-13 have exact solutions when either $F = 0$ (the Rayleigh-Line process) or $q_w = 0$ (the Fanno-Line process). However, there is no exact solution for the unsteady problem, Eqs. 3-10 through 3-13. The various terms in Eqs. 3-10 through 3-13 are being evaluated to see which terms are negligible, which will lead to an approximate integration over the length of the line. This will result in ordinary differential equations in time which will be incorporated into the network code and numerically integrated.

3.3. PLATEOUT AND PLUGGING

Volatile fission products, particularly cesium and iodine, vented from the core assemblies and produced by gaseous precursor decay of fission products vented from the core assemblies may plate out on the walls of the monitor lines. These fission products are swept through the monitor lines into the HPS traps by helium entering at the core subassembly vent connections. Accumulation of deposited material may constrict the sweep gas flow passages and could potentially lead to plugging of the lines. The conditions under which plateout and plugging could occur in the GCFR, the means of

minimizing or eliminating it, and the methods for removing deposits are being investigated. A small high-pressure loop has been built and is being used for this purpose. Development of components for injection, control, and measurement of impurities in the helium (i.e., H_2 and H_2O) and sources for simulating venting of the volatile fission products and their compounds is being examined.

3.3.1. High-Pressure Loop

A mass spectrometer leak detector was used to isolate several leaks in the loop. The leaking components were removed from the system, and where necessary, weld seals were made to replace mechanical tube fittings. The loop is now ready for final checkout prior to admission of cesium vapor into the test segment.

3.3.2. Oxygen Potential Analyzer

The ZrO_2 cell with the GA-fabricated reference gas sleeve is continuing to function well. A new reference sleeve for a second oxygen analyzer was fabricated and is currently undergoing calibration.

3.4. FISSION PRODUCT RELEASE AND TRANSPORT

The purpose of the work on this subtask is to obtain experimental data on the interdiffusion and gas phase and the surface back diffusion of gaseous and volatile fission products. The diffusion coefficient data will be used to validate or improve the SLIDER code (Ref. 3-3), a one-dimensional model for fission gas diffusion transport (including radioactivity decay). Surface transport and back diffusion data will be used to establish a model for predicting the importance of these mechanisms to contamination of the reactor coolant system.

Adequate thermal performance and leak-tightness of the apparatus were verified. The background count rate of the detector system was reduced to

~45 counts/min by judicious use of lead shielding. The single-channel analyzer being used was calibrated for the Kr-85 gamma peak at 515 keV using a 100-keV window. Several Kr-85 diffusion experiments have been performed at a temperature of 308 K in helium having pressures of 0.51, 3.55, and 8.72 MPa. The data are being evaluated to verify that they agree with the literature values and that the SLIDER code can be adequately applied to the current geometry of the apparatus.

3.5. MONITOR STATION AND INSTRUMENTATION

3.5.1. Monitor Station Layout Studies

Some valve vendors have questioned the use of valves requiring all-metal construction, including sealing surfaces for the high-temperature (≤400°C) service needed in the monitor station application. The leak-tightness and life of the valves are not believed to be adequate during measurement of the radioactivity flowing through one open line manifolded with 23 closed lines (see diverter flow concept in Fig. 3-8). Consequently, an alternative concept in which line scanning by the radiation detector would be used to replace flow diversion (Fig. 3-9) was conceived. A first attempt at the initial monitor station layouts has been made for each concept, and changes and improvements are being made. The envelope dimensions of the PCRV cavities required for the stations are 1.5 x 1.5 x 1.3 m for the diverter and a diameter of 1.4 m and a length of 3.0 m for the scanner.

3.5.2. Flow Diversion Components

The potential leakage of the diverter valves referred to in Section 3.5.1 led to consideration of fluidic (Coanda effect) flip-flop devices. Fluidic diverters are attractive because they have no moving parts (except for the fluid), are very temperature and radiation tolerant, and their controls can be remotely located so that maintenance, repair, and replacement can be easily performed. However, discussions with vendors revealed that fluidic devices have a high inherent pressure drop in their nozzles, which

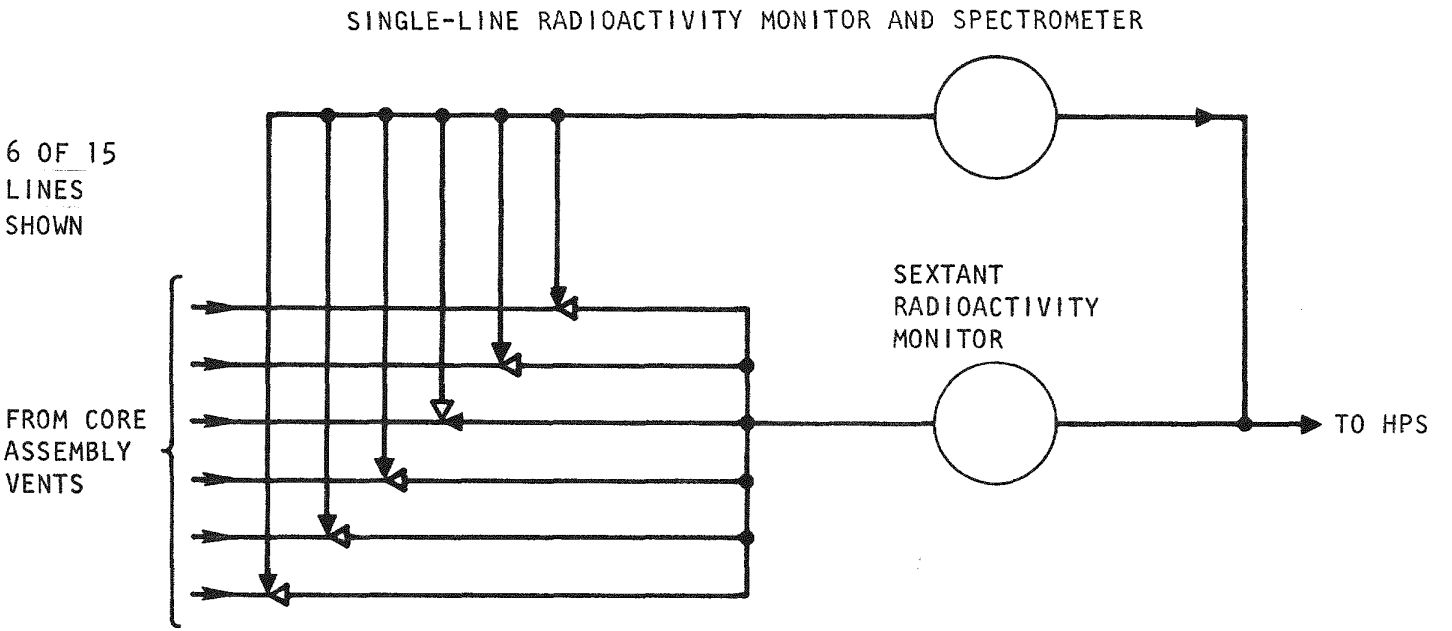

Fig. 3-8. Diverter flow concept

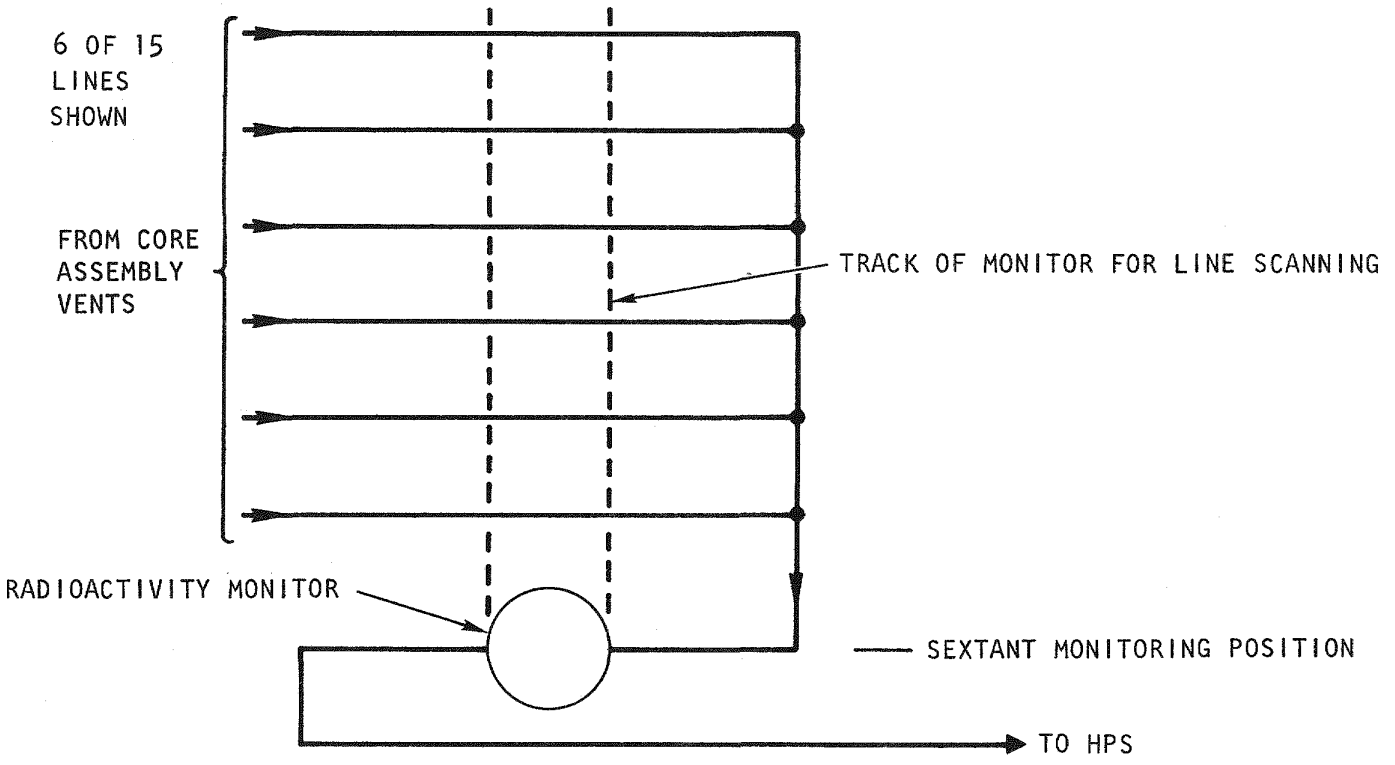

Fig. 3-9. Line scanning concept

is necessary to produce the Coanda effect, and only a fraction (less than half) of the input flow would appear in the outlet lines; the remainder would be the sum of the undiverted flow and that exiting from the dormant signal line. Thus, it is clear that Coanda-effect fluidic diverters are not useful for monitor station application.

A pneumatic approach which retains the advantages cited above for fluidic diverters was investigated. A simple network representing flow switching from a single monitor line was analyzed for the pressure conditions for which switching was possible. Parametric calculations showed that the flow in the simple network could be switched or diverted. However, when more branches, representing the other monitor lines, were added to the network, control of the switching was lost. Thus, pneumatic control diversion is not useful for this application, and further efforts with conventional valves are warranted.

3.6. PES PROGRAM PLANNING

Updating and revision of the PES design criteria and development plan were undertaken during this quarter and are expected to be completed during the next quarter. The design criteria revisions are about 25% complete, and the development plan is about 15% complete.

REFERENCES

3-1. "Gas-Cooled Fast Breeder Reactor Quarterly Progress Report for the Period November 1, 1976 Through January 31, 1977," ERDA Report GA-A14240, General Atomic, February 1977.

3-2. "Gas-Cooled Fast Breeder Reactor Quarterly Progress Report for the Period August 1, 1976 Through October 31, 1976," ERDA Report GA-A14112, General Atomic, November 1976.

3-3. Jadhov, K. B., and B. W. Roos, "SLIDER, A Fortran-V Program for the Computation of Release of Fission Products From One-Dimensional Multi-Layered Fuel Configurations," USAEC Report GA-8566, Gulf General Atomic, August 1969.

4. CORE FLOW TEST LOOP PROGRAM (189a No. 00582)

A series of out-of-pile simulation tests will be performed to (1) demonstrate the ability of the GCFR fuel, control, and blanket assembly designs to meet design goals and (2) verify predictions of analytical models which describe design operation and accident behavior. The emphasis of the tests will be on obtaining thermal-structural data for steady-state, transient, and marginal conditions using electrically heated rod bundles in a dynamic helium loop. Final margin tests will be progressively extended to the highest possible temperature until the heater elements fail. The core flow test loop (CFTL) program plan (Ref. 4-1) describes the requirements for the test program to be conducted in the CFTL, which will be constructed and operated by Oak Ridge National Laboratory (ORNL). The principal work accomplished during this quarter was as follows:

1. The CFTL network diagram was updated, and associated planning information was provided for the Resource Evaluation and Control System (RECS) (Ref. 4-2).

2. A set of performance predictions covering the preliminary test series was completed and issued.

3. Design drawings of the conceptual details of the 37-, 61-, and 91-rod bundles for the fuel model tests were completed and issued.

4. One CFTL and three fuel failure mock-up (FFM) fuel rod simulators (heaters) were received from ORNL, and trial roughening procedures are being developed.

5. Planning of the CFTL analysis was discussed by GA and ORNL. Specific goals and objectives were reviewed, and the status of the GA analysis was presented.

6. Liaison and loop evaluation for the prototype assembly tests are being considered as part of the European program. This represents a shift in the previous position that the EBOR facility be the testing site.

4.1. PROGRAM PLANNING

4.1.1. RECS Planning

General Atomic has selected RECS (Ref. 4-2) to integrate the planning, scheduling, and cost control and priority identification for the GCFR program. The previously developed PERT summary planning for the CFTL program has been updated to provide current input for RECS which covers activities at GA and ORNL. A principal source of current information is the FY 77 program and budget proposal. An initial CFTL network diagram (Fig. 4-1) covering the total program was prepared and logic diagrams were developed for the work item schedule, cost, and manpower requirements; these will be input into RECS. When complete, RECS will improve the efficiency of resource allocation to the CFTL and other tasks.

4.1.2. Alternate Test Program

The test program specified in the CFTL program plan (Ref. 4-1) requires testing of 12 CFTL rod bundles in 15 months. ORNL feels it cannot meet this schedule, based on its experience with sodium and light water reactor (LWR) tests. Since acquisition of CFTL test data is on the critical path for GCFR core development, it is important to obtain CFTL information in a timely fashion. This problem has been discussed, and ORNL has agreed to suggest an achievable CFTL test program for 15 and 36 months which is based on fulfilment of the test functions presented in Table 10-1 of Ref. 4-1. An initial draft of an alternate test program has been received from ORNL and is in review. Table 4-1 lists the top priority test bundles and the alternate test bundles proposed by ORNL; Table 4-2 is a checklist of the required test information and the top priority test bundles. The degree to which the alternate test bundle series will fulfill the top priority requirements is being studied.

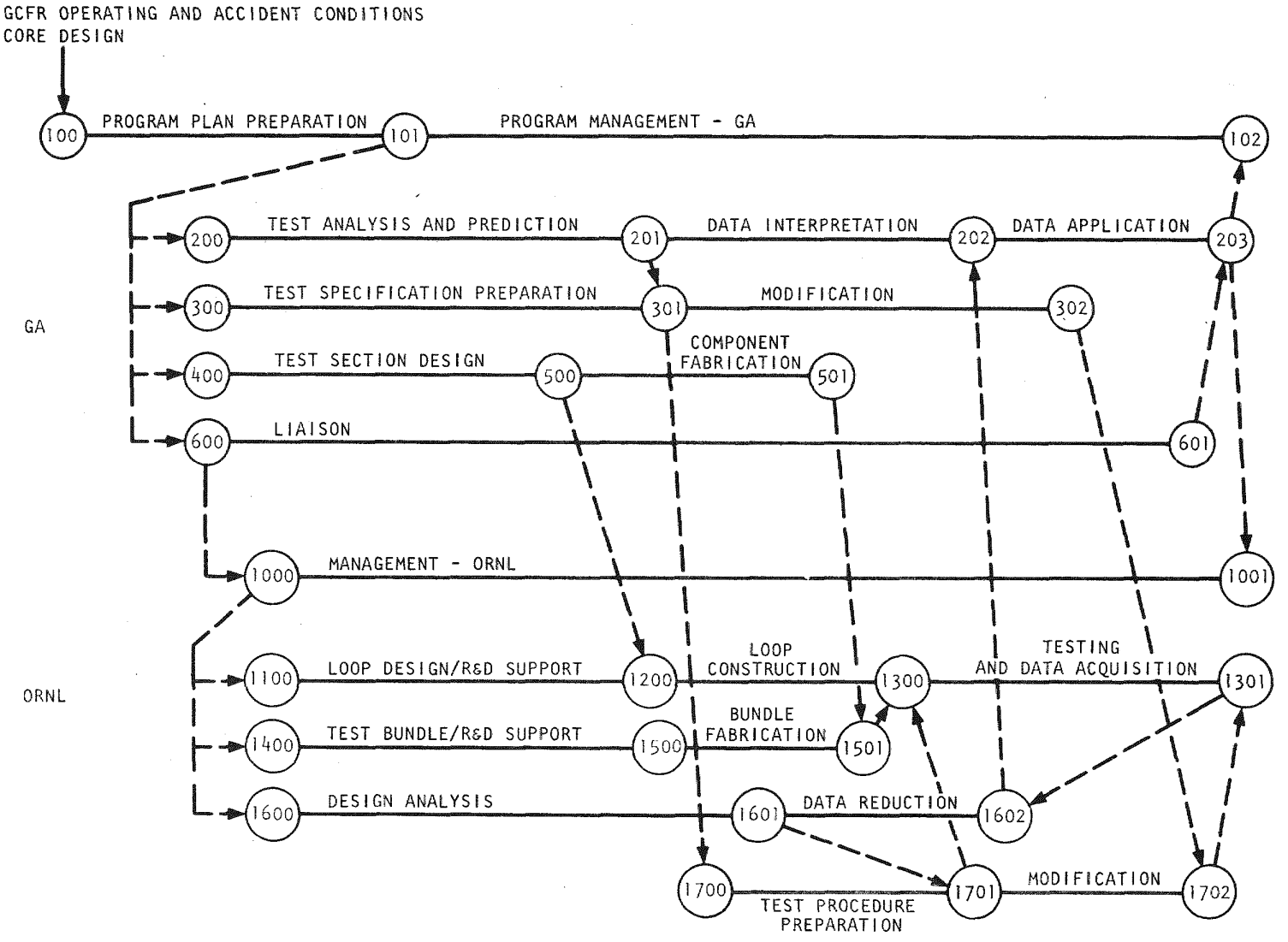

Fig. 4-1. CFTL network

TABLE 4-1
COMPARISON OF GA AND ORNL CFTL TEST BUNDLE PLANS

Type	Test Series	Bundle	Total No. of Rods	Test Range
		GA Program Plan		
Fuel	P-2	C	37	Plant conditions
Fuel	P-2	D	37	Steady-state margin
Fuel	P-2	E	37	Transient margin
Fuel	F-1	H	61	Plant conditions
Control	C-1	A	54	Plant conditions
Blanket	B-1	A	61	Plant conditions
Fuel	F-2	K	91	Plant conditions
Fuel	F-2	M	91	Transient margin
Fuel	F-3	S	91	Faulted
Control	C-1	B	54	Transient margin
Blanket	B-1	B	61	Transient margin
Control	C-2	F	90	Faulted
		Alternate ORNL Proposal		
Fuel	1	F1	37	(a)
Fuel	2	F2	61	
Control	3	C1	54	
Blanket	4	B1	61	
Control	5	C2	90	
Fuel	6	F3	91	

(a) Plant conditions and margin tests will be performed with the same bundles. Faulted test will be performed by bundle modification after some testing.

TABLE 4-2
TOP PRIORITY TEST MATRIX FOR CFTL BUNDLES[a]

Information Required	Fuel Assembly	Control Assembly	Blanket Assembly
Facility checkout			
Loop performance verification, cold flow	C	A	A
Instrumentation check	C	A	A
Thermal performance			
Swiss and German result verification	H		
Size extrapolation verification	C,H,K	A	
Small distortion analyses verification			
Skewed power effects	C,H,K	A	A
Transient analyses verification	C,H,K	A	A
Low flow effects	C,H,K	A	A
Local flow blockage		F	
Structural-thermal-flow interaction			
Effects of normal transients	C,H,K	A,F	A
Effects of upset transients	C,H,K	A,F	A
Reactor trip			
Reactor trip with one-loop isolation			
Accident behavior			
Effect of emergency and DBA transients	C,H,K	A	A
Shutdown with helium valve failure			
Rod withdrawal with high-flux trip			
Shutdown with two auxiliary loops			
Slow depressurization			
Design basis accident depressurization			
Local flow blockage and transients		F	
Design and safety margins			
Steady-state undercooling	D,H		A
Transient undercooling	E	B,F	B
Transient overcooling	M	F	B
Depressurization	C,K	S,A	
Component tests (orifice, sensors, control rod)		A,B,F	A

[a]Each bundle is assigned a letter designation.

4.2. TEST ANALYSIS AND PREDICTION

Three problems were studied during this quarter: (1) simplified performance prediction for test series P-1 and P-2; (2) potential value of studying bundle mixing using single heated rod experiments; and (3) internal bundle flow distribution resulting from the structure modeling requirement for an inlet section which is as short as possible and above the inlet grid mock-up.

4.2.1. Predictions for Test Series P-1 and P-2

A set of simplified predictions for test series P-1 and P-2 (Ref. 4-3) was completed using the computer code TSPEC (Ref. 4-4). A sample prediction, for the simulation of the fast margin trip is presented in Table 4-3. This table illustrates the expected scram performance of initial overcooling followed by a slow return to steady-state temperatures. The principal dynamic structural interaction occurs within a few seconds of scram as the fuel rod simulators (heater) rapidly contract relative to the spacer support rods and sliding friction load forces are generated between the rods and the spacers. There are two major reasons for providing these predictions to ORNL at this time:

1. The prediction package complements the test specification by providing estimates of dependent test parameters which are required to define the test loop operating conditions. These estimates may be extended to other size fuel and fuel control bundles by factoring the ratio of the number of rods. The results should be used to improve the definition of the loop operating envelope.

2. The large mass of data, particularly for the thermal flow area, is clearly illustrated, and the need for early initiation of planning to handle these data is apparent. ORNL should use the predictive data to start planning its data acquisition and reduction. The emphasis on determining the structural integrity and/or faults of the core assemblies should not be subverted because of the massive amounts of thermal data which may readily be generated.

TABLE 4-3
CFTL SPECIFICATION FOR TEST P-2-5-1-2, BUNDLE C

BUNDLE DESIGN
BUNDLE TYPE - FUEL
BUNDLE IDENTIFICATION - C

BUNDLE DATA
RODS PER BUNDLE = 37. HEATED = 31. UNHEATED = 6.
BUNDLE OD = 83.4 MM
DUCT WALL THICHNESS = 2.500 MM
BUNDLE FLOW AREA = 2393. MM**2
DUCT PERIMETER = 235.20 MM
AVG BUNDLE HYDRAULIC DIAMETER = 8.67 MM

ROD DATA
ROD DIAMETER = 7.48 MM
ROD PITCH = 11.20 MM
HEIGHT OF ROUGHENING = .140 MM
PITCH OF ROUGHENING = 1.68 MM
FLOW AREA PER ROD = 64.69 MM**2
H T PERIMETER PER ROD = 23.50 MM
LOCAL HYDRAULIC DIAMETER = 11.01 MM
UPPER BLANKET LENGTH = 655.0 MM
HEATED LENGTH = 1130.0 MM
LOWER BLANKET LENGTH = 450.0 MM
TOTAL LENGTH = 2235.0 MM

ROUGHENING DATA
ROUGHENED FRACTION OF HEATED LENGTH = .765
ROUGHENED LENGTH = 864.4 MM
FRICTION FACTOR MULTIPLIER = 4.40
HEAT TRANSFER MULTIPLIER = 2.30
REFERENCE REYNOLDS NO = 100000.

SPACER AND FLOW COEFFICIENT DATA
NUMBER OF SPACER = 10.
SPACER COEFFICIENT = 1.372
SPACER SOLIDITY = .145
INLET COEFFICIENT = 1.000
OUTLET COEFFICIENT = .500

HEATER AXIAL POWER PROFILE
AXIAL QMAX/QAVG = 1.210
QX/QMAX = COS(1.049*(2*X/L - 1))

X/L	QX/QMAX
.000	.4984
.100	.6681
.200	.8084
.300	.9133
.400	.9781
.500	1.0000
.600	.9781
.700	.9133
.800	.8084
.900	.6681
1.000	.4984

TABLE 4-3 (Continued)

UPSET TR. FAST MARGIN TRIP UNIF POWER
TRANSIENT TEST SERIES RUN NO. - 1
LINEAR POWER AND FLOW RAMP

	FRACTION (1)	FRACTION (2)	FRACTION (3)	START TIME (S)	DECAY TIME (S) (2)-(1)	DECAY TIME (S) (3)-(2)
POWER	1.000	.400	.100	.2	.7	2.2
FLOW	1.000	.290	.100	2.0	3.4	20.0

	INITIAL CONDITIONS	FINAL CONDITIONS
INPUT PARAMETERS		
TOTAL BUNDLE HEAT INPUT, KW	868.000	86.800
AVG POWER PER ROD, KW	28.000	2.800
MAX POWER PER ROD, KW	28.000	2.800
MIN POWER PER ROD, KW	28.000	2.800
FLOW PER BUNDLE =, KG/SEC	.860	.086
HELIUM INLET TEMPERATURE, C	350.0	350.0
HELIUM INLET PRESSURE, MPA	9.000	9.000
THERMAL OUTPUT PARAMETERS		
AVERAGE BUNDLE OUTLET TEMPERATURE, C	544.4	544.4
AVERAGE BUNDLE TEMPERATURE RISE, C	194.4	194.4
OUTLET TEMPERATURE - AVG POWER ROD, C	582.1	582.1
TEMPERATURE RISE - AVG POWER ROD, C	232.1	232.1
OUTLET TEMPERATURE - MAX POWER ROD, C	582.1	582.1
TEMPERATURE RISE - MAX POWER ROD, C	232.1	232.1
OUTLET TEMPERATURE - MIN POWER ROD, C	582.1	582.1
TEMPERATURE RISE - MIN POWER ROD, C	232.1	232.1
MAX SURFACE TEMPERATURE, C (AT X/L =)	635.7 (.920)	635.1 (.930)
FILM DROP AT MAX SURFACE, C	66.4	64.1
MAX POWER DENSITY, W/CM	299.8	30.0
SMOOTH H. T. COEF, W/M*M/C	12370.	1248.
ROUGTH H. T. COEF, W/M*M/C	12693.	1281.
FLOW OUTPUT PARAMETERS		
BUNDLE AVG. RE	86945.	8695.
LOCAL RE	98368.	9837.
TOTAL BUNDLE PRESSURE DROP, KPA	177.855	1.580
INLET, KPA	9.878	.099
UPPER BLANKET, KPA	13.852	.220
SMOOTH CORE LENGTH, KPA	6.666	.105
ROUGHENED CORE LENGTH, KPA	93.123	.545
LOWER BLANKET, KPA	13.211	.205
ACCELERATION LOSS, KPA	3.113	.031
SPACERS LOSS, KPA	31.383	.311
OUTLET LOSS, KPA	6.610	.065

THERMAL EXPANSION PARAMETERS THERMAL INPUT AS FABRICATED		TEST TEMPERATURE DUCT	TEST TEMPERATURE ROD	TEST TEMPERATURE DIF	TEST TEMPERATURE DUCT	TEST TEMPERATURE ROD	TEST TEMPERATURE DIF
AVERAGE, MM	2235.0	2252.3	2254.0	1.7	2252.3	2254.0	1.7
HOTTEST, MM	2235.0	2252.3	2254.0	1.7	2252.3	2254.0	1.7
COLDEST, MM	2235.0	2252.3	2254.0	1.7	2252.3	2254.0	1.7
MAX BOW DISPLACEMENT, MM			.0			.0	

TABLE 4-3 (Continued)

UPSET TR. FAST MARGIN TRIP UNIF POWER

INITIAL AXIAL PRESSURE, POWER, AND TEMPERATURE VALUES

LOCATION	X MM	X/L	DP KPA	AVERAGE POWER W/CM	AVERAGE HELIUM C	AVERAGE CLAD C	MAXIMUM POWER W/CM	MAXIMUM HELIUM C	MAXIMUM CLAD C	MINIMUM POWER W/CM	MINIMUM HELIUM C	MINIMUM CLAD C
INLET	.0		9.878	.0	350.0	350.0	.0	350.0	350.0	.0	350.0	350.0
CORE INLET	655.0	.000	32.927	149.4	350.0	476.2	149.4	350.0	476.2	149.4	350.0	476.2
SMOOTH	796.2	.125	38.267	211.7	371.3	556.0	211.7	371.3	556.0	211.7	371.3	556.0
SMOOTH	936.4	.249	43.564	259.2	398.8	491.4	259.2	398.8	491.4	259.2	398.8	491.4
ROUGH	938.6	.251	43.564	259.8	399.2	492.1	259.8	399.2	492.1	259.8	399.2	492.1
ROUGH	1220.0	.500	78.473	299.8	466.0	573.5	299.8	466.0	573.5	299.8	466.0	573.5
ROUGH	1333.0	.600	92.492	293.2	493.9	598.6	293.2	493.9	598.6	293.2	493.9	598.6
ROUGH	1446.0	.700	106.512	273.8	520.5	617.8	273.8	520.5	617.8	273.8	520.5	617.8
ROUGH	1559.0	.800	120.532	242.4	544.8	630.2	242.4	544.8	630.2	242.4	544.8	630.2
ROUGH	1672.0	.900	134.551	200.3	565.6	635.5	200.3	565.6	635.5	200.3	565.6	635.5
ROUGH	1728.5	.950	141.561	175.8	574.4	635.5	175.8	574.4	635.5	175.8	574.4	635.5
CORE OUTLET	1785.0	1.000	148.571	149.4	582.0	633.7	149.4	582.0	633.7	149.4	582.0	633.7
OUTLET	2235.0		177.855	.0	582.0	582.0	.0	582.0	582.0	.0	582.0	582.0

FINAL AXIAL PRESSURE, POWER, AND TEMPERATURE VALUES

LOCATION	X MM	X/L	DP KPA	AVERAGE POWER W/CM	AVERAGE HELIUM C	AVERAGE CLAD C	MAXIMUM POWER W/CM	MAXIMUM HELIUM C	MAXIMUM CLAD C	MINIMUM POWER W/CM	MINIMUM HELIUM C	MINIMUM CLAD C
INLET	.0		.099	.0	350.0	350.0	.0	350.0	350.0	.0	350.0	350.0
CORE INLET	655.0	.000	.409	14.9	350.0	423.4	14.9	350.0	423.4	14.9	350.0	423.4
SMOOTH	796.2	.125	.482	21.2	371.3	477.3	21.2	371.3	477.3	21.2	371.3	477.3
SMOOTH	936.4	.249	.553	25.9	398.8	490.6	25.9	398.8	490.6	25.9	398.8	490.6
ROUGH	938.6	.251	.553	26.0	399.2	491.3	26.0	399.2	491.3	26.0	399.2	491.3
ROUGH	1220.0	.500	.774	30.0	466.0	572.6	30.0	466.0	572.6	30.0	466.0	572.6
ROUGH	1333.0	.600	.862	29.3	493.9	597.7	29.3	493.9	597.7	29.3	493.9	597.7
ROUGH	1446.0	.700	.951	27.4	520.5	616.9	27.4	520.5	616.9	27.4	520.5	616.9
ROUGH	1559.0	.800	1.039	24.2	544.8	629.4	24.2	544.8	629.4	24.2	544.8	629.4
ROUGH	1672.0	.900	1.128	20.0	565.6	634.9	20.0	565.6	634.9	20.0	565.6	634.9
ROUGH	1728.5	.950	1.172	17.6	574.4	635.0	17.6	574.4	635.0	17.6	574.4	635.0
CORE OUTLET	1785.0	1.000	1.216	14.9	582.0	633.2	14.9	582.0	633.2	14.9	582.0	633.2
OUTLET	2235.0		1.580	.0	582.0	582.0	.0	582.0	582.0	.0	582.0	582.0

TABLE 4-3 (Continued)

UPSET TR. FAST MARGIN TRIP UNIF POWER
TRANSIENT TEST SERIES RUN NO. - 1

INITIAL AXIAL VALUE FOR AVERAGE ROD

AVG POWER PER ROD = 28.000 KW
STORED ENERGY BASE TEMPERATURE = 350.0 C
AVG STORED ENERGY PER ROD = 87.845 KW-S
STORED ENERGY/POWER FOR AVG ROD = 3.1 S

LOCATION	X MM	X/L	POWER W/CM	STORED ENERGY W*S/CM	ENERGY/POWER S	HELIUM C	CLAD C	WALL DT C	HT*A/L W/CM/C	TEMP/TIME C/S	ROD CENTER C
INLET	.0		.0	.0	.0	350.0	350.0	.0	1.29	.0	350.0
CORE INLET	655.0	.000	149.4	342.0	2.3	350.0	476.2	126.2	1.18	84.9	658.7
SMOOTH	796.2	.125	211.7	532.5	2.5	371.3	556.0	184.7	1.15	120.3	814.5
SMOOTH	936.4	.249	259.2	456.7	1.8	398.8	491.4	92.6	2.80	147.3	808.0
ROUGH	938.6	.251	259.8	458.4	1.8	399.2	492.1	92.9	2.80	147.6	809.5
ROUGH	1220.0	.500	299.8	633.9	2.1	466.0	573.5	107.5	2.79	170.4	939.7
ROUGH	1333.0	.600	293.2	672.9	2.3	493.9	598.6	104.7	2.80	166.6	956.8
ROUGH	1446.0	.700	273.8	691.1	2.5	520.5	617.8	97.2	2.82	155.6	952.2
ROUGH	1559.0	.800	242.4	687.8	2.8	544.8	630.2	85.4	2.84	137.7	926.2
ROUGH	1672.0	.900	200.3	663.5	3.3	565.6	635.5	69.9	2.87	113.8	880.1
ROUGH	1728.5	.950	175.8	643.9	3.7	574.4	635.5	61.1	2.88	99.9	850.2
CORE OUTLET	1785.0	1.000	149.4	619.6	4.1	582.0	633.7	51.6	2.90	84.9	816.2
OUTLET	2235.0		.0	477.5	.0	582.0	582.0	.0	1.29	.0	582.0

FINAL AXIAL VALUES FOR AVERAGE ROD

AVG POWER PER ROD = 2.800 KW
STORED ENERGY BASE TEMPERATURE = 350.0 C
AVG STORED ENERGY PER ROD = 65.133 KW-S
STORED ENERGY/POWER FOR AVG ROD = 23.3 S

LOCATION	X MM	X/L	POWER W/CM	STORED ENERGY W*S/CM	ENERGY/POWER S	HELIUM C	CLAD C	WALL DT C	HT*A/L W/CM/C	TEMP/TIME C/S	ROD CENTER C
INLET	.0		.0	.0	.0	350.0	350.0	.0	.21	.0	350.0
CORE INLET	655.0	.000	14.9	141.3	9.5	350.0	423.4	73.4	.20	8.5	441.7
SMOOTH	796.2	.125	21.2	241.4	11.4	371.3	477.3	106.1	.20	12.0	503.2
SMOOTH	936.4	.249	25.9	268.5	10.4	398.8	490.6	91.8	.28	14.7	522.2
ROUGH	938.6	.251	26.0	269.9	10.4	399.2	491.3	92.1	.28	14.8	523.0
ROUGH	1220.0	.500	30.0	416.3	13.9	466.0	572.6	106.6	.28	17.0	609.2
ROUGH	1333.0	.600	29.3	460.1	15.7	493.9	597.7	103.8	.28	16.7	633.5
ROUGH	1446.0	.700	27.4	492.4	18.0	520.5	616.9	96.4	.28	15.6	650.4
ROUGH	1559.0	.800	24.2	512.0	21.1	544.8	629.4	84.6	.29	13.8	659.0
ROUGH	1672.0	.900	20.0	518.2	25.9	565.6	634.9	69.3	.29	11.4	659.4
ROUGH	1728.5	.950	17.6	516.4	29.4	574.4	635.0	60.5	.29	10.0	656.4
CORE OUTLET	1785.0	1.000	14.9	511.2	34.2	582.0	633.2	51.2	.29	8.5	651.5
OUTLET	2235.0		.0	477.5	.0	582.0	582.0	.0	.21	.0	582.0

TABLE 4-3 (Continued)

TRANSIENT TEST SERIES RUN NO. - 1

LINEAR POWER AND FLOW RAMP

	FRACTION (1)	FRACTION (2)	FRACTION (3)	START TIME (S)	DECAY TIME (S) (2)-(1)	DECAY TIME (S) (3)-(2)
POWER	1.000	.400	.100	.2	.7	2.2
FLOW	1.000	.290	.100	2.0	3.4	20.0

APPROXIMATE TRANSIENT HISTORY

TIME	AVG POWER PER ROD	FLOW	EQ. STORED Q PER ROD	EQ. STORED Q CHANGE/T	TIME CONSTANT	OUTLET TEMPERATURE EQ.	OUTLET TEMPERATURE ACT.	CLAD TEMPERATUPE, AVG EQ. AVG.	CLAD TEMPERATUPE, AVG ACT. AVG.	CLAD TEMPERATUPE, AVG ACT. MAX.
S	KW	KG/S	KW-S	KW	S	C	C	C	C	C
.0	28.000	.860	87.847	.000	3.1	582.	582.	509.	509.	634.
1.6	8.647	.860	27.015	-38.942	3.1	422.	519.	399.	466.	557.
3.1	2.800	.657	10.598	-8.675	3.8	380.	464.	370.	428.	490.
5.0	2.800	.317	18.891	2.458	6.7	413.	444.	390.	413.	464.
8.4	2.800	.225	25.810	1.501	9.2	439.	442.	407.	411.	461.
13.0	2.800	.187	30.628	.881	10.9	457.	448.	419.	414.	468.
18.5	2.800	.143	39.710	1.281	14.2	490.	464.	440.	424.	488.
25.6	2.800	.086	65.135	2.186	23.3	582.	511.	502.	455.	545.
37.2	2.800	.086	65.135	.000	23.3	582.	539.	502.	473.	580.
48.8	2.800	.086	65.135	.000	23.3	582.	556.	502.	485.	601.
60.5	2.800	.086	65.135	.000	23.3	582.	566.	502.	491.	614.
72.1	2.800	.086	65.135	.000	23.3	582.	572.	502.	496.	621.
83.7	2.800	.086	65.135	.000	23.3	582.	576.	502.	498.	626.
95.4	2.800	.086	65.135	.000	23.3	582.	579.	502.	500.	629.
107.0	2.800	.086	65.135	.000	23.3	582.	580.	502.	500.	631.
118.6	2.800	.086	65.135	.000	23.3	582.	581.	502.	501.	632.
130.2	2.800	.086	65.135	.000	23.3	582.	581.	502.	501.	632.
141.9	2.800	.086	65.135	.000	23.3	582.	582.	502.	502.	633.

4.2.2. Thermal-Hydraulic Performance of the CFTL 37-Rod Bundle With One Powered Rod

The mixing correlation of Ref. 4-5 for a square lattice has been used for the triangular lattice of the GCFR, and a test has been proposed for the CFTL 37-rod bundle to determine the validity of this correlation for a triangular geometry. This will be done by having only one rod heated in the entire bundle and measuring the temperature of the coolant at various distances from the rod. A half-section of the assembly (Fig. 4-2) was analyzed using COBRA (Ref. 4-6) with 100% flow and only one rod heated (No. 1). It can be seen from Fig. 4-3 that it is probably impossible to determine from heater surface temperature measurements whether there was any mixing, since the zero mixing and nominal mixing predictions were within the $\pm 2\sigma$ uncertainty band. It is concluded that with the predicted uncertainty band, little information about mixing could be obtained using single heated rod experiments. Similarly, transverse exit temperature measurements are of questionable value. The maximum temperature difference between coolant from different subchannels at the exit is only about 45°C (Fig. 4-4). In addition, four of the six subchannels shown have temperatures very close to the inlet temperature. Considering the $\pm 2\sigma$ band of uncertainty, the temperature differences are not measureable. To obtain larger differences between subchannels, two rows of heated rods may be required (Fig. 4-5).

4.2.3. Inlet Velocity Distribution to the CFTL 37-Rod Assembly

The inlet to the 37-rod assembly is a plenum around a bundle of tubes. The coolant has to work its way across the bundle and at the same time turn 90 deg to enter the test section through the inlet grid. The velocity at the inlet to the test section is not uniform, but as the coolant moves down the bundle, there is a cross flow between subchannels to equalize the pressure at different axial positions. This is true even if the inlet velocity is uniform across the bundle. Thus, it is essential to compare the flow distribution for these two cases at the axial location just before the heated section of the bundle.

PITCH = 11.288 MM

d_{ROOT} = 7.26 MM

d_{ROUGH} = 7.52 MM

$d_{HANGER\ ROD}$ = 11.20 MM

ROUGHENING STARTS = 918 MM

HEATING STARTS = 645 MM

ROUGH LENGTH = 868 MM

HEATED LENGTH = 1140 MM

TOTAL LENGTH = 2240 MM

AXIAL POWER PROFILE = $\cos\left[1.049\left(\frac{2x}{\ell} - 1\right)\right]$

$\frac{x}{\ell}$ = 0 TO 1.0

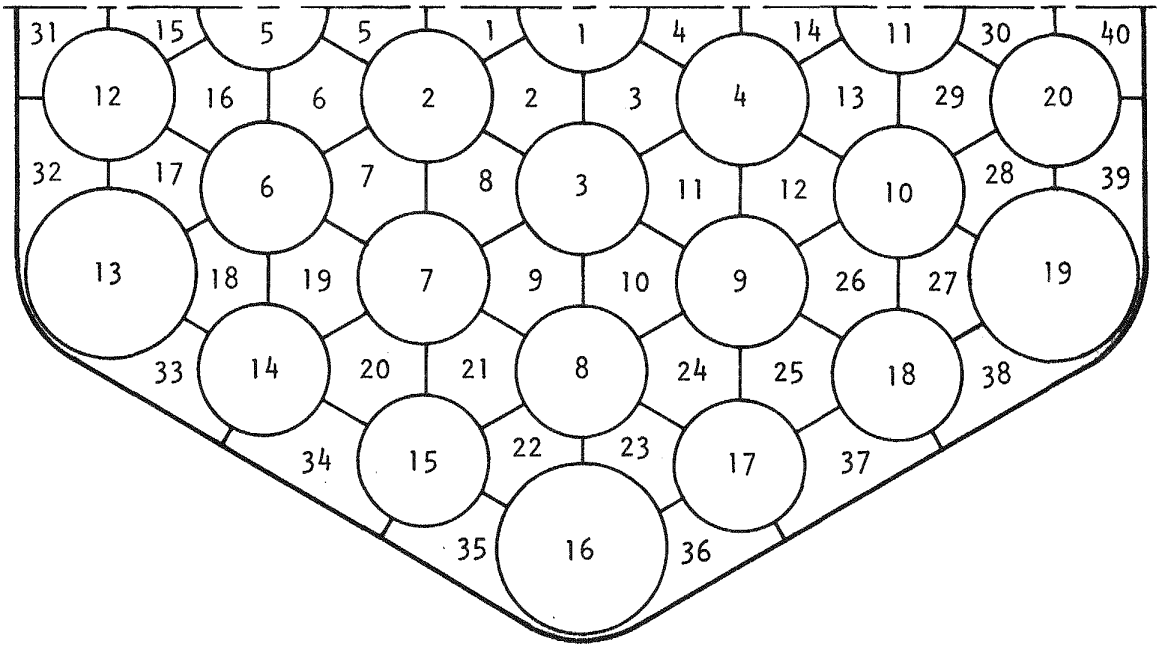

Fig. 4-2. COBRA model of CFTL 37-rod assembly

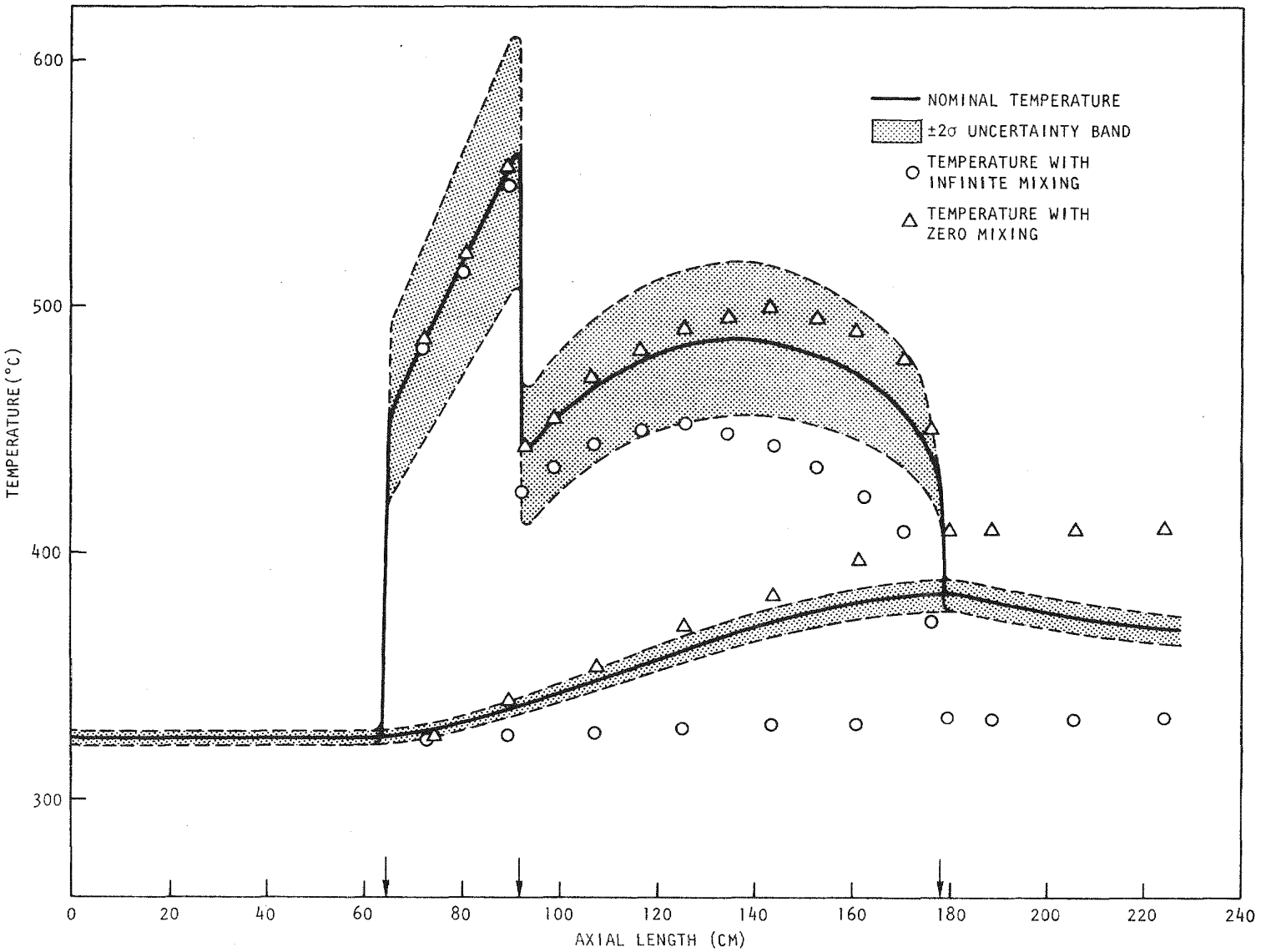

Fig. 4-3. Temperature of heated rod and its neighboring subchannel

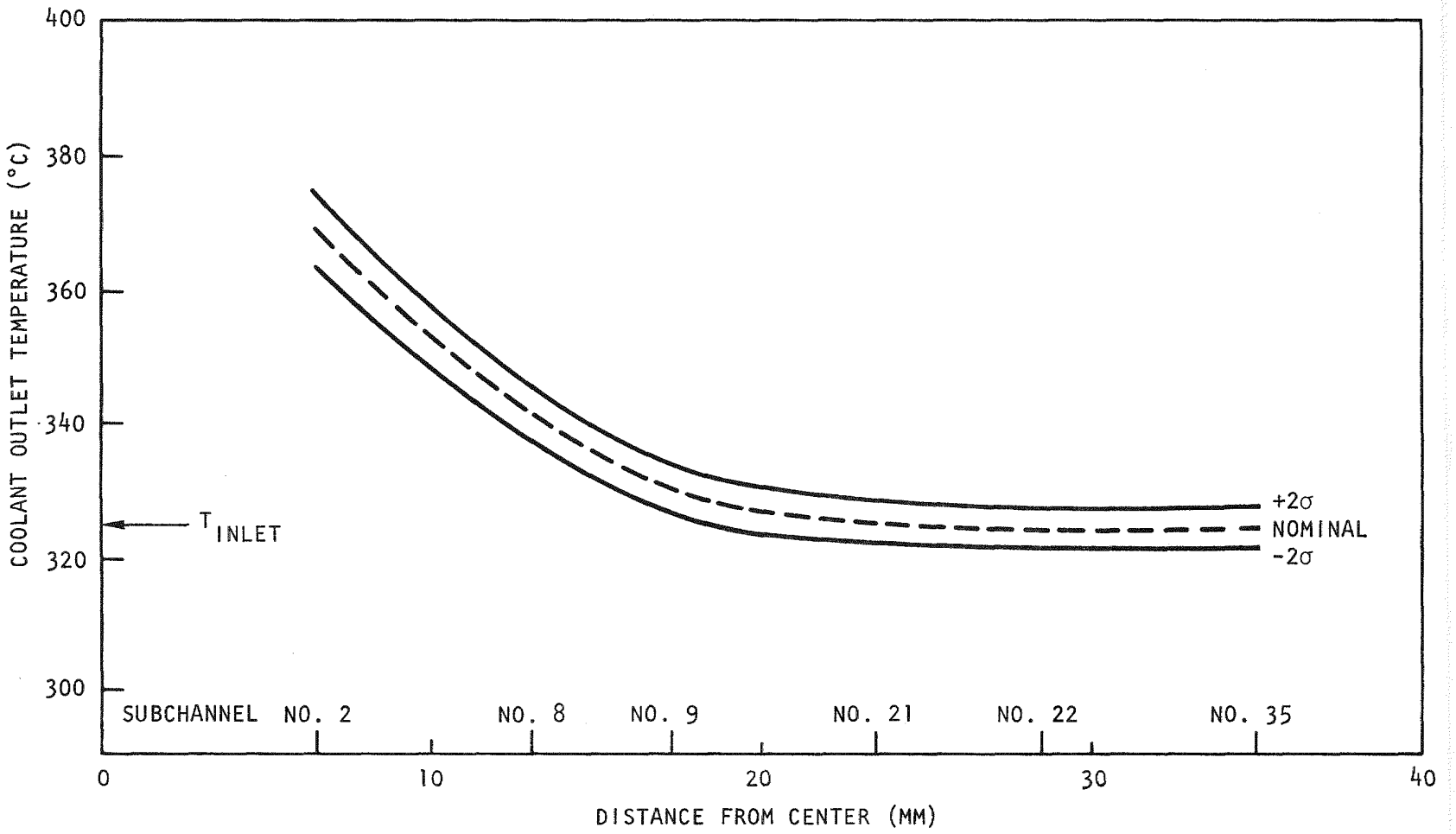

Fig. 4-4. Coolant temperature and 2σ uncertainty band at bundle exit, central rod heated (subchannels as shown in Fig. 4-2)

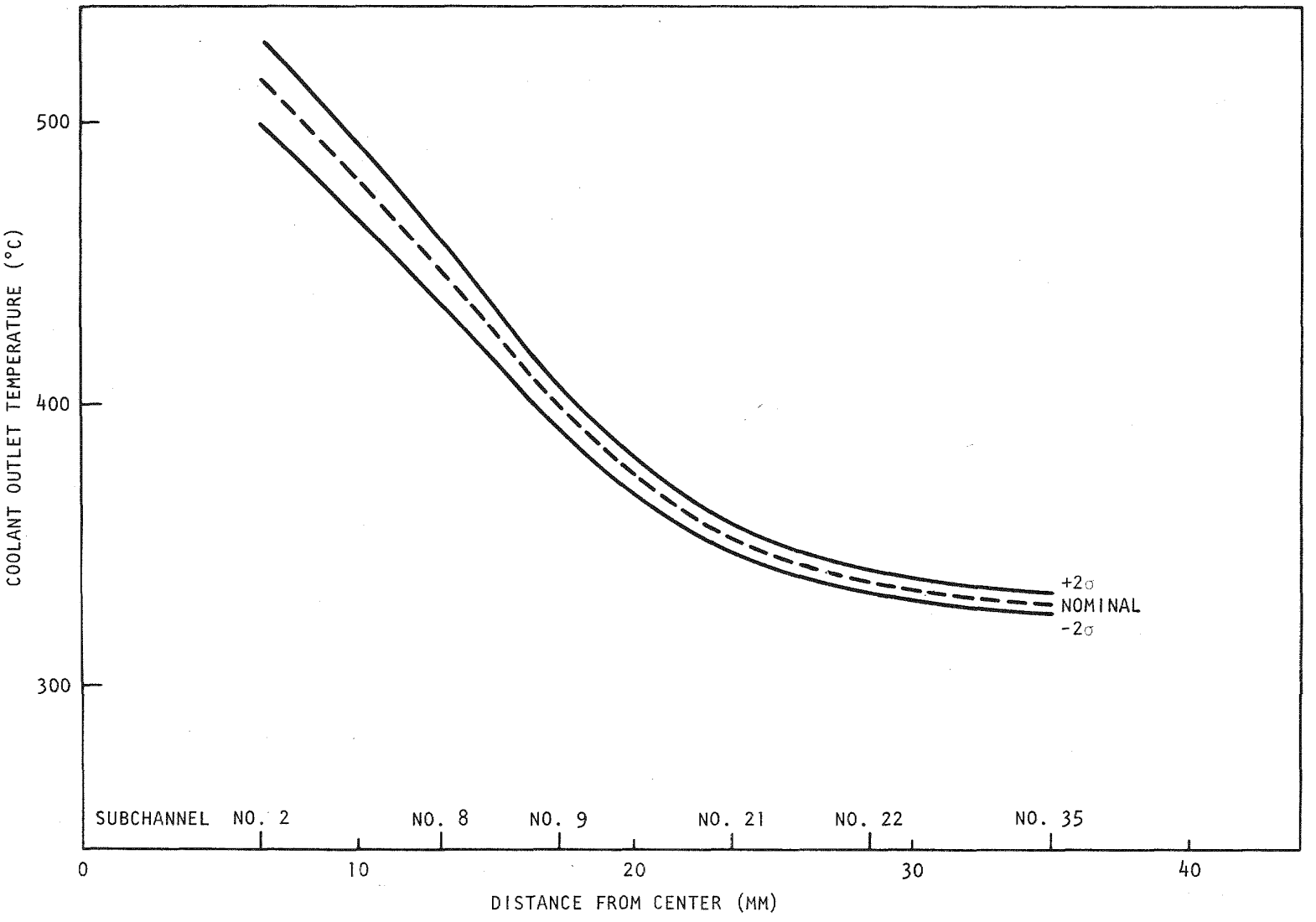

Fig. 4-5. Coolant temperature and 2σ uncertainty band at bundle exit, two rows heated (subchannels as shown in Fig. 4-2)

The flow network code FLAC (Ref. 4-7) was used to analyze the coolant flow through the inlet section, past the inlet grid, and into the test section up to the first spacer. The velocity distribution obtained was used in a subchannel analysis of the test assembly using COBRA, and the flow distribution along the axial length was compared to the flow distribution obtained with uniform velocity ($V/V_{uniform}$) at the inlet. The results are shown in Figs. 4-6 and 4-7. The flow distribution considered for both cases was just before the heated section and within ±4% of that obtained with the uniform inlet. The uncertainty (due to engineering tolerances at this point) was ±2% of the flow, and the pressure drops in the bundle were 0.11% higher than that with the uniform inlet. To obtain uniform inlet flow, a large resistance is required at the inlet grid, which may result in a pressure drop four to five times higher than that obtained with the current grid design. Therefore, an inlet section of 15.25 to 28 cm is adequate for the test.

4.3. TEST SPECIFICATION

4.3.1. Requirement Change

Initiation of cladding melting tests has been downgraded by GA as a requirement for the CFTL test program based on the status of heater element and thermocouple development, which currently indicates unfavorable technical cost factors. In addition, the Los Alamos Scientific Laboratory (LASL) duct melting and fallaway tests and the Idaho Nuclear Engineering Laboratories (INEL) GRIST-2 test conditions are being designed to exceed initiation of cladding melting temperatures. Therefore, required information in the temperature range beyond that for CFTL operation may be obtained during either or both test programs; accordingly, changes in the test specification for the GCFR CFTL preliminary series P-1 and P-2 are being made. Tests will be executed to the maximum temperature capability of the heaters, and the most extreme test will be limited only by heater failure.

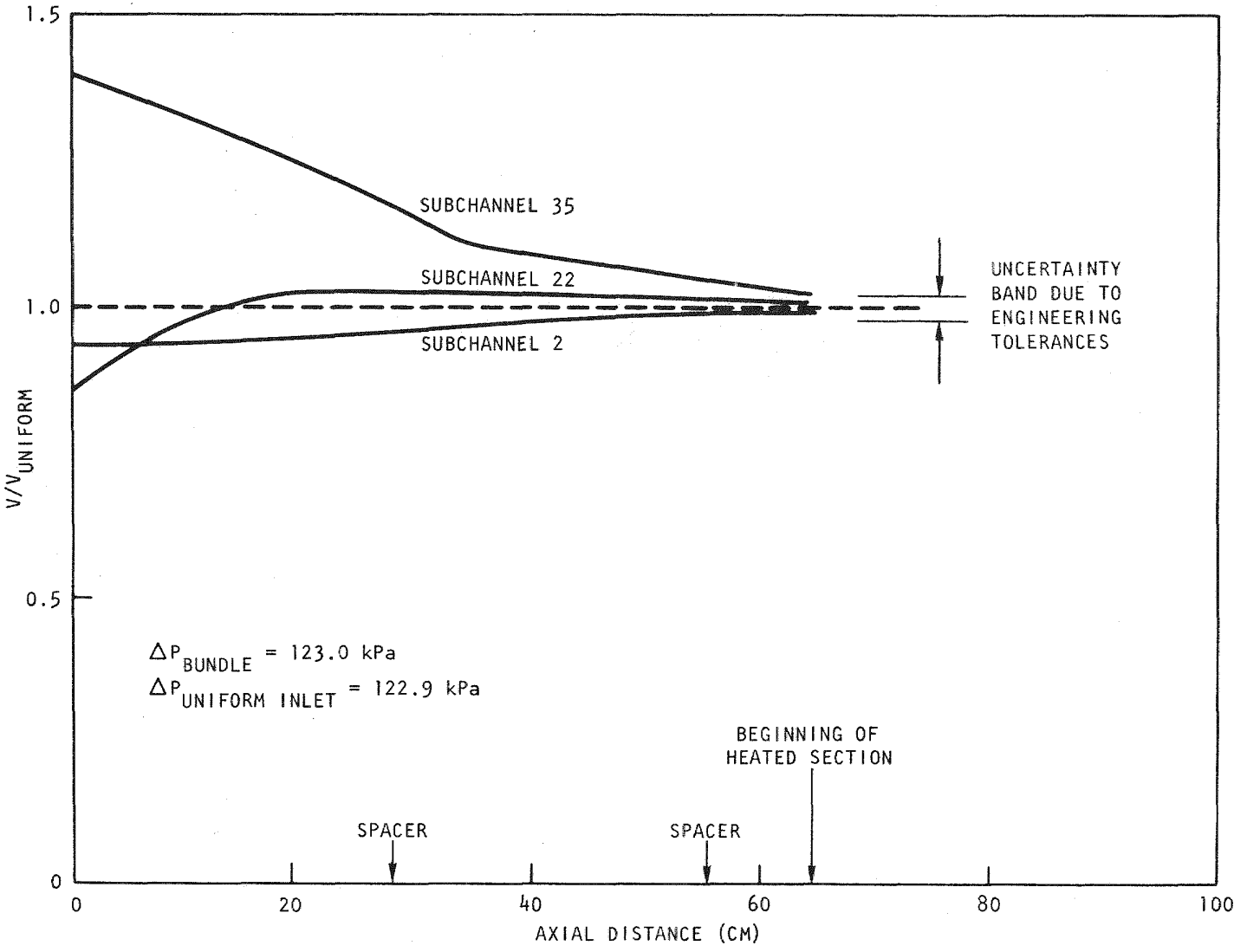

Fig. 4-6. Axial velocity distribution for 28-cm inlet section

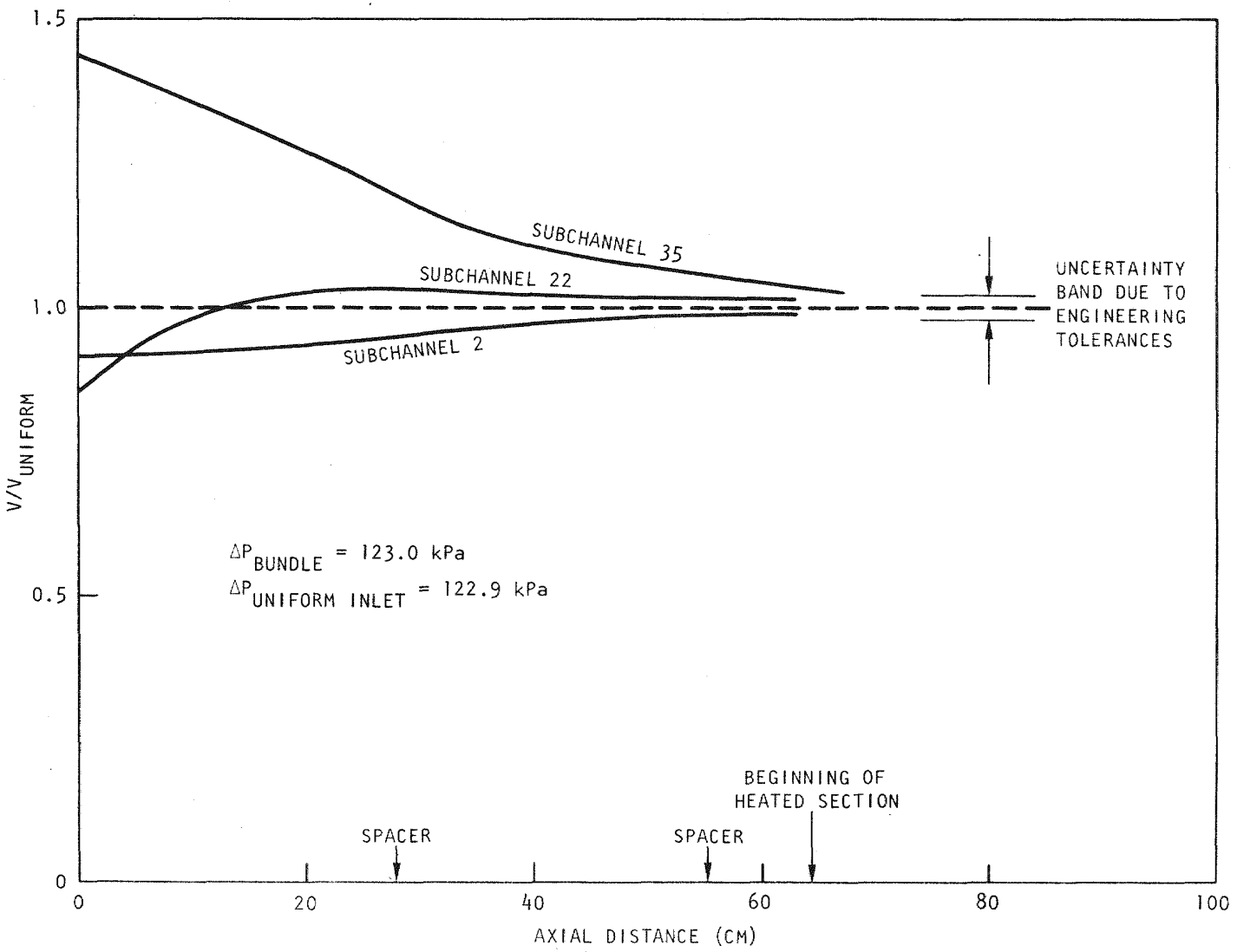

Fig. 4-7. Axial velocity distribution for 15.25-cm inlet section

4.3.2. Structural Measurements

Test bundle structural measurements, requirements for which will be detailed in the test specifications or other requirement documentation, were reviewed by the fuel designers. The five in-place measurements being considered are

1. Edge rod bowing.
2. Axial differential expansion between fuel rod simulators and bundle duct.
3. Hanger rod axial loads.
4. Duct bowing.
5. Acoustical surveillance.

Consideration is being given to the purpose of each measurement, alternatives to the measurement, measurement sensors and location, and GCFR fuel assembly design changes which could be contemplated if the test results indicate that they are warranted. Changes could be made on the rod diameter, space between the duct and the rods, and number of spacer grids.

4.3.3. Interim Inspection

Inspection and determination of test bundle geometry before initiation of testing and after heater failure will provide information on structural performance. Interim inspection during testing is being considered, and ORNL is reviewing the LOFT fuel module interim inspection program to see if it can be applied to CFTL.

4.4. TEST BUNDLE DESIGN AND FABRICATION

4.4.1. Fuel Rod Simulator (Heater)

Two major design decisions have been made for the fuel rod simulators:

1. A uniform outside diameter (the smooth diameter is the same as the crest diameter of the roughened length).

2. A maximum of two thermocouples in a fuel rod simulator (attached to the cladding inner surface.

The use of a uniform diameter fuel rod simulator has been favored by ORNL for easier bundle assembly and replacement of damaged simulators, if necessary. General Atomic has reviewed the fuel rod design, and preliminary analysis indicates a minimal degradation of GCFR plant performance if uniform-diameter rods are used. The cost of grinding the smooth inlet length of the fuel rods to the root diameter of the roughened length has been estimated to equal or exceed the cost of grinding the roughened length. The economic advantages of eliminating the reduced diameter of the smooth inlet length appear to outweigh the disadvantage of a core outlet temperature reduction of $\sim 5^{\circ}C$. Since it has been recommended that the GCFR fuel rod have a uniform diameter, this change has been incorporated into the design of the CFTL fuel rod simulators (Fig. 4-8). A result of this change is the need for only one size spacer grid (Fig. 4-9).

The CFTL program plan (Ref. 4-1) indicates a maximum of four thermocouples per fuel rod simulator and a maximum of 100 thermocouples per test bundle. Development of boron nitride insulation preforms (tubularceramic pieces) by ORNL allows for 4 thermocouples located 90 deg apart [Fig. 4-10(a)]. If rod thermocouple data are treated statistically, less than 2 thermocouples per rod is the cost effective optimum. A decision was made by GA to change to a maximum of 2 thermocouples per fuel rod simulator while maintaining the 100-thermocouple measurement maximum per bundle, which allows spare

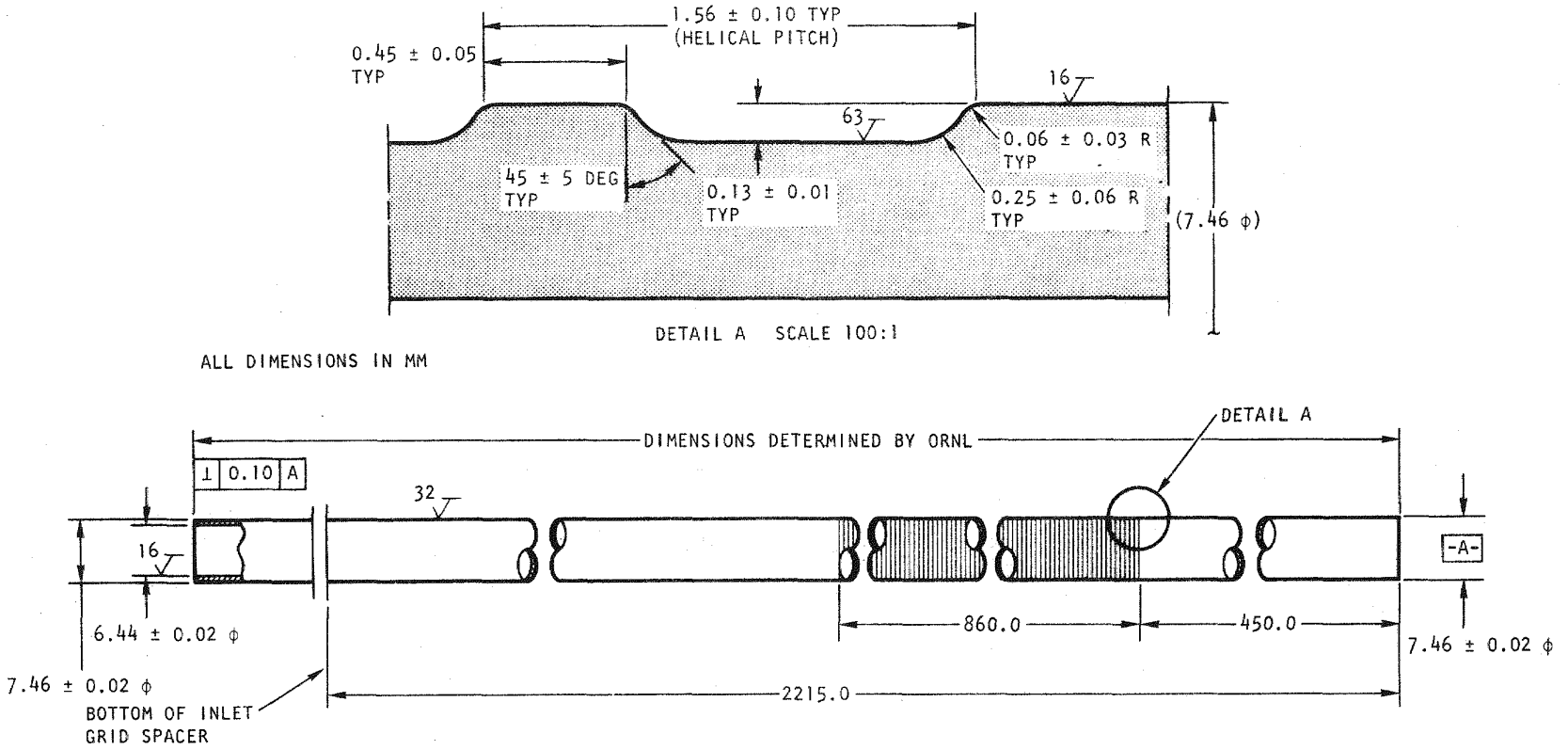

Fig. 4-8. Fuel rod simulator with roughening

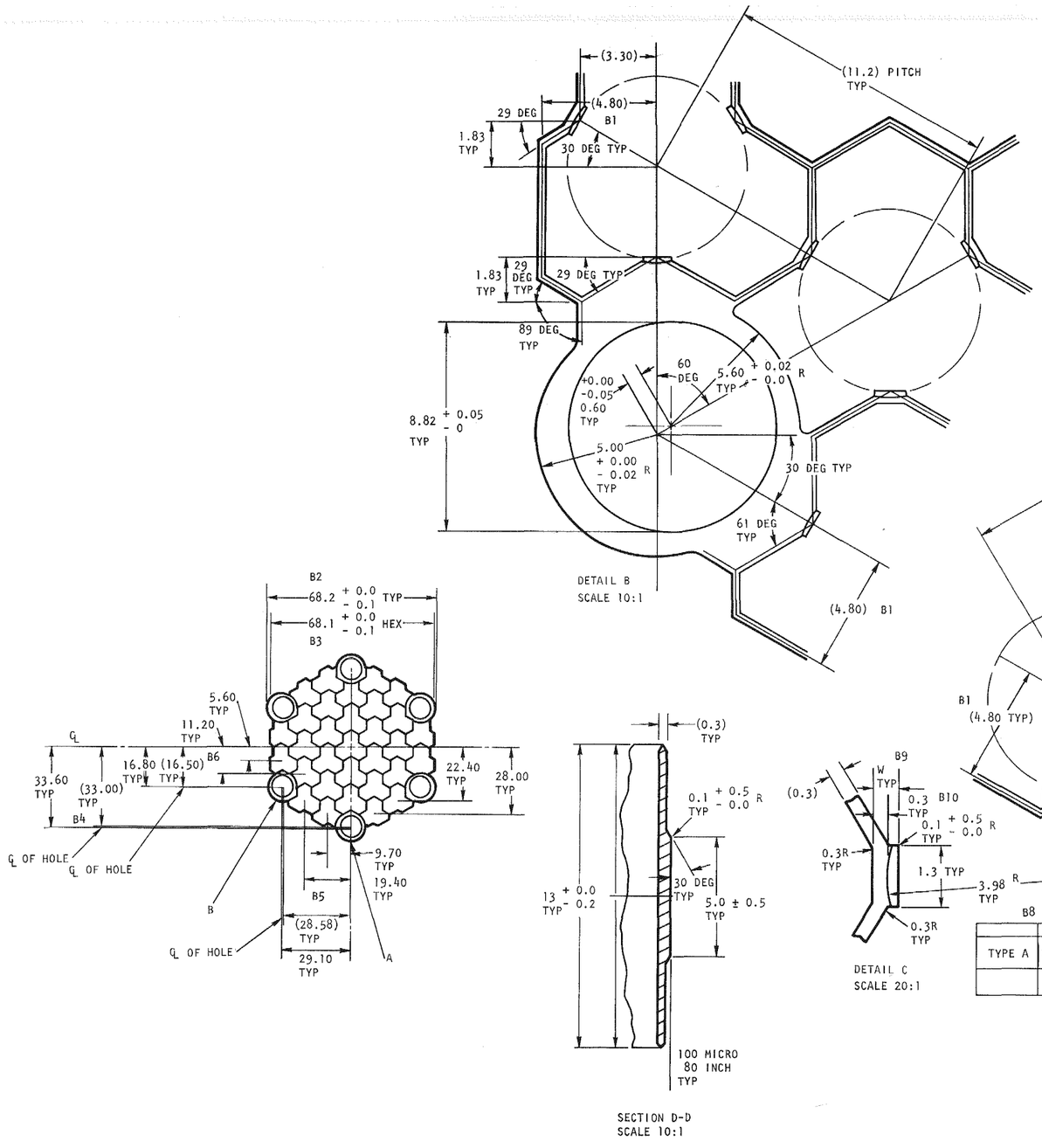

Fig. 4-9. Spacer grid, type A

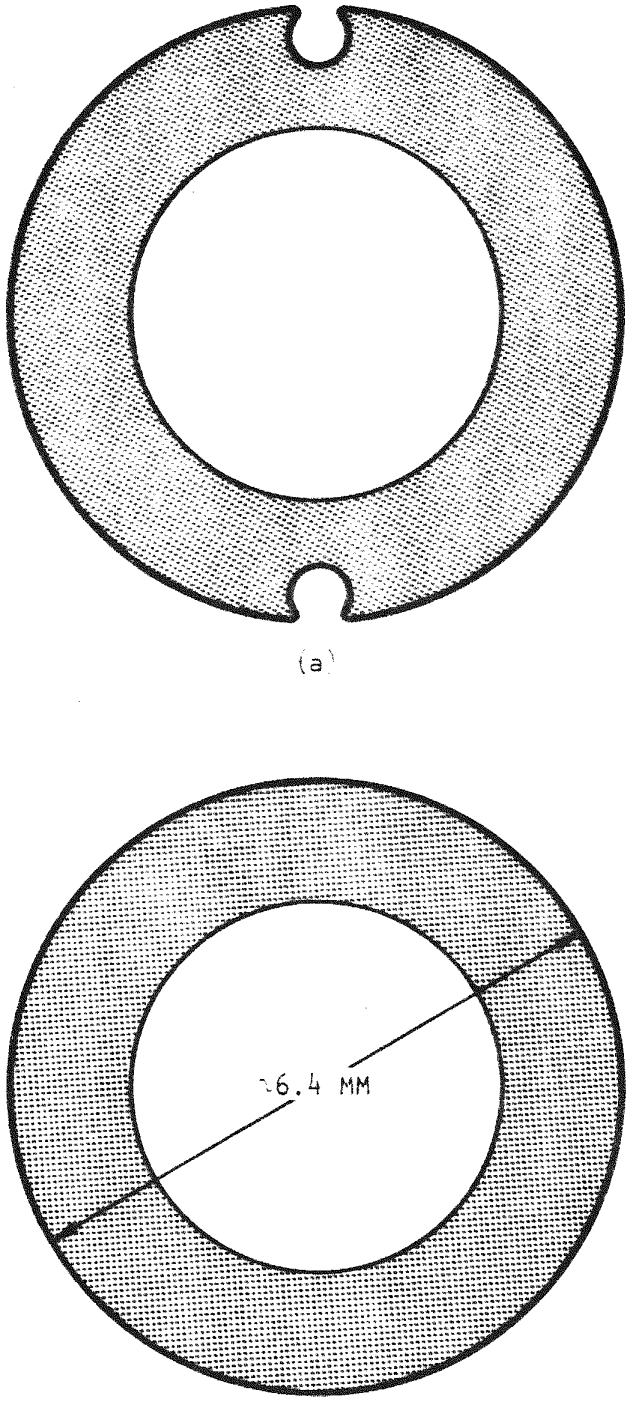

Fig. 4-10. Boron nitride preform cross sections (a) with axial grooves for 0.5-mm-diameter metal-sheathed thermocouple wires (b) without grooves

thermocouples to replace any failures. The required boron nitride preforms will have cross sections similar to those shown in Fig. 4-10.

4.4.2. Test Section Designs

Drawings of the test sections and test section components for the 61-and 91-rod fuel assembly test bundles were issued during this quarter, and drawings for the 37-rod bundle were updated and reissued. Figure 4-11 shows the revised locations for the spacer grids which resulted from changes in the GCFR design to minimize rod bending in the heated zone.

4.4.3. Rod Roughening

Four fuel rod simulators which were rejects from the thermal-hydraulic out-of-reactor safety facility (THORS) (previously FFM) and CFTL test programs have been received from ORNL for trial roughening of the cladding. The simulators were requested by GA for initial use in determining the effects of the mechanical grinding operation on the integrity of the simulators. Dimensional measurements of the units were made along with electrical resistance measurements of the heater elements and thermocouples for comparison with values obtained after roughening is completed. Drawings of the two types of simulators were prepared for use in negotiations with WMC Grinding Company of Downey, California, on the trial roughening of the simulators.

4.5. LIAISON WITH ORNL

During this quarter, a coordination and review meeting was held at ORNL covering progress during the first quarter of FY 77; a CFTL analysis planning meeting was also held at GA. The decisions made at the ORNL meeting included

1. The reference design thermocouple shall be type K.

2. Nichrome V shall be an acceptable fallback material for the heater elements.

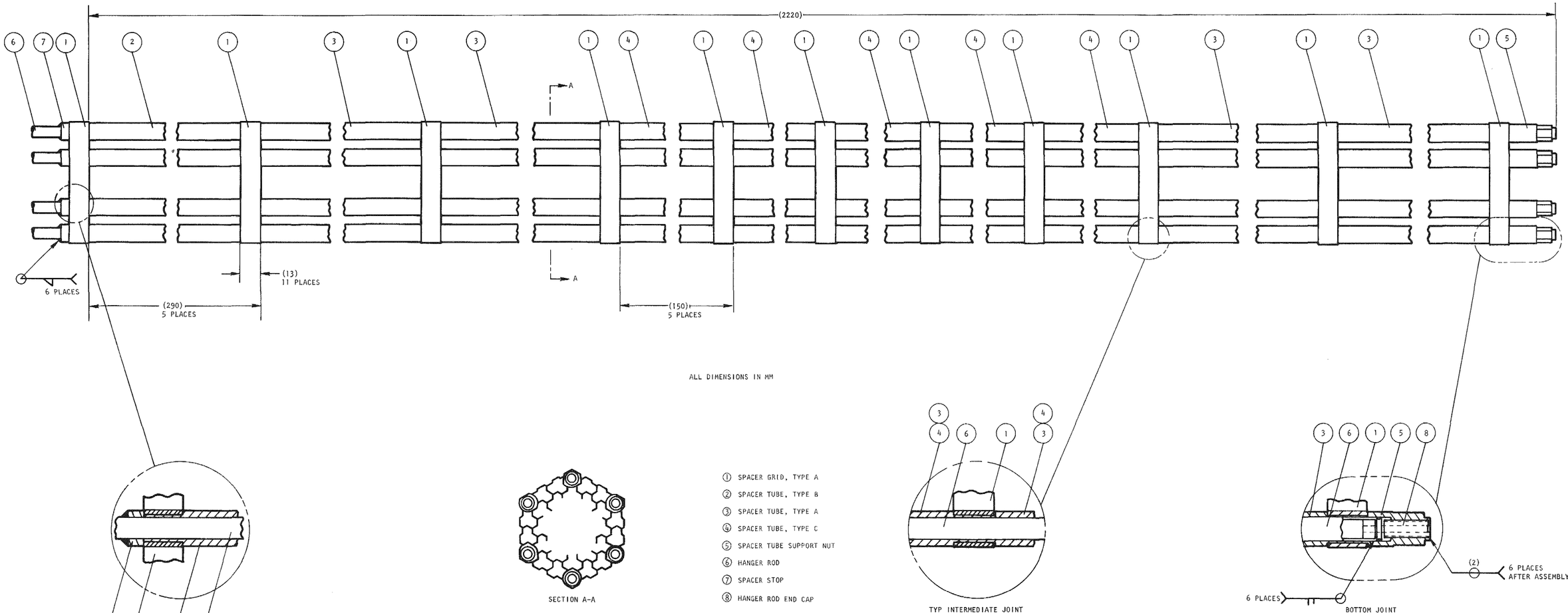

Fig. 4-11. Bundle skeleton, 37-rod test bundle

3. The priority of the initiation of cladding melting tests was lowered.

4. The proposed outline of CFTL analysis responsibilities was accepted as a starting basis.

5. ORNL will suggest an alternate, achievable test program.

The conclusions of the GA meeting were

1. A set of CFTL analysis goals and ORNL analysis objectives was prepared and discussed and is in review.

2. ORNL agreed to prepare a CFTL analysis and data reduction plan.

3. The relevant GCFR computer code activity was summarized.

4.6. GCFR PROTOTYPE ASSEMBLY TEST PLANNING

Program planning (Ref. 4-8) for testing of the full-size prototype core assemblies is continuing. These tests will provide assurance that the core assemblies will meet design qualification requirements prior to fabrication of the GCFR demonstration plant initial core. The full-size GCFR core assemblies will be subjected to maximum GCFR helium flow conditions under a close simulation of the reactor core environment, but without radiation. One assembly of each type (fuel, control, and blanket) will be subjected to the equivalent of approximately one year of reactor operation in a hot helium test loop. The helium test loop temperature will be maintained external to the test section, since fuel rod heating will not be simulated in these tests.

The test loop facility options for the prototype tests are being reviewed. The options being evaluated include a modification of the EBOR loop at INEL, the CARMEN 2 loop at Saclay, France, and a new facility which will most likely be sited in Germany. As pointed out in Ref. 4-9, EG&G has completed a preliminary proposal to conduct the prototype tests in the

modified EBOR loop. Included in the proposal is the suggestion that the EBOR main blower, which failed during the last operation of the loop in 1966, be inspected, refurbished, and checked out by the blower manufacturer. Lack of funding has prevented this effort. Early determination of the adequacy of the EBOR blower is needed to permit a meaningful evaluation of the EBOR facility option, since the blower is a major component of the facility.

Prototype testing in Europe was discussed with representatives of Kernforschungsanlage (KFA) and KWU in Germany and with Commissariat à L'Energie Atomique (CEA) representatives in Saclay, France. The German representatives have indicated that they may be interested in building and operating a new loop especially designed for prototype testing. By the end of 1977, KFA plans to complete a draft report on a study of a new prototype fuel test facility. This study will be used as the basis for the decision on the prototype test facility. The French representatives have indicated that with modifications, the CARMEN 2 loop at Saclay could be utilized for prototype testing. The modifications would include a larger reheater-recuperator and a larger cooler and would permit concurrent operation of the prototype assemblies in parallel at temperatures approaching 550°C while allowing operation of the blowers at a low temperature of approximately 80°C in order to obtain the required flow and ΔP. An information package defining the prototype test conditions has been sent to CEA to enable preparation of a loop feasibility plan by mid-1977.

An analysis has been made to determine whether conducting the prototype tests at 450° rather than 550°C would satisfy test objectives. This reduction in operating temperature would result in considerable cost savings during the facility construction, modification, and testing phases. The initial analysis indicates that from an acoustical and vibration standpoint, the test objectives would be satisfied; this is also true from a material standpoint. Additional analysis of this reduction in temperature will be made prior to final commitment to a test section inlet temperature.

REFERENCES

4-1. Hopkins, H. C., Jr., "Program Plan for GCFR Core Flow Test Loop," USAEC Report GA-A13080, General Atomic, August 9, 1977.

4-2. Yensuang, P. K., "Users Guide for Integrated Scheduling Management: RECS - Resource Evaluation and Control System," General Atomic Report GA-A13805, March 1976.

4-3. "Gas-Cooled Fast Breeder Reactor Quarterly Progress Report for the Period May 1, 1976 Through July 31, 1976," ERDA Report GA-A13975, General Atomic, August 31, 1976.

4-4. Hopkins, H. C., Jr., "TSPEC - A Computer Program to Predict Approximate Model Performance in the Core Flow Test Loop," ERDA Report GA-A14057, General Atomic, November 1976.

4-5. Castallana, F. S., W. T. Adams, and J. E. Casterline, "Single Phase Subchannel Mixing in a Simulated Nuclear Fuel Assembly," Nucl. Eng. Design 26, 242-249 (1974).

4-6. Rowe, D. S., "COBRA IIIc: A Digital Computer Program for Steady State and Transient Thermal-Hydraulic Analysis of Rod Bundle Nuclear Fuel Elements," Battelle Northwest Laboratory Report BNWL-1695, March 1973.

4-7. Marksberry, C. L., "FLAC 73: 1973 Status of FLAC, A Flow Network Analysis Code," General Atomic Report GA-D12942, March 1974.

4-8. Strong, W. R., "Outline Plan for GCFR Prototype Core-Element Test Program," General Atomic, unpublished data.

4-9. "Gas-Cooled Fast Breeder Reactor Quarterly Progress Report for the Period November 1, 1976 Through January 31, 1977," ERDA Report GA-A14240, General Atomic, February 1977.

5. FUELS AND MATERIAL ENGINEERING (189a No. 00583)

5.1. OXIDE FUEL, BLANKET, AND GRID PLATE SHIELDING MATERIALS TECHNOLOGY

This subtask is concerned with oxide fuel and blanket technology. As a result of the decision to replace ThO_2 with UO_2 as a candidate radial blanket material, differentiation of the axial and radial blanket material has been suspended.

During this quarter, efforts were directed at reviewing and summarizing fuel-cladding chemical attack data from GCFR fuel rod irradiation experiments F-1 and F-3. Data are being prepared in fulfillment of the GA commitment to the Fuel-Cladding Chemical Interaction (FCCI) committee. As part of the design effort for the modified fuel-blanket interface for the F-5 experiment, a review of cesium transport phenomena in F-1 series fuel rods was also carried out in conjunction with ANL; the conclusions from this review are discussed in Section 5.5.

5.2. CLADDING TECHNOLOGY

5.2.1. Mechanical Testing Program at Argonne National Laboratory

The objectives of the ANL test program are to determine the effects of the following factors on the behavior and mechanical properties of GCFR ribbed and smooth cladding:

1. Ribs, rib geometry, and fabrication technique.

2. Helium impurity levels typical of the environment expected in the GCFR demonstration plant.

These tests are biaxial creep rupture tests with a loop to axial tensile stress ratio of 2. Two tests at 650°C and a loop stress of ∿238 MPa in purified helium atmosphere using smooth and ribbed cladding fabricated by various techniques have been completed. In general, the ribs increased the load-carrying ability of the cladding.

During this quarter, the water saturator system and the impurity monitoring systems were made operational, and the third test (ANL test 3) was initiated; the test matrix is shown in Table 5-1. The specimens were mounted on two separate flanges, and one flange was tested at a time. When one flange was removed to obtain the creep strain curve, the specimens in the other flange were tested. Four major types of specimens were included in this test: (1) mechanically ground smooth, (2) mechanically ground ribbed (KWU), (3) electrochemically ground ribbed [Swiss Federal Institute for Reactor Research (EIR)], and (4) as-received smooth. An assortment of other specimens was also included. These tests are being performed at 667°C in helium containing 300 Pa of H_2 and 30 Pa of H_2O. Only chromium is expected to oxidize under these conditions.

Three specimens have failed to date: two mechanically ground smooth and one electrochemically ground ribbed specimens. These specimens were loaded such that the hoop stress was ∿268 MPa based on the root dimensions. The failure times were in the lower portion of the expected range of lifetimes.

5.2.2. Helium Loop Test Program at Pacific Northwest Laboratory

The primary objective of the helium loop test program is to compare the mechanical properties in recirculating helium determined at Pacific Northwest Laboratory (PNL) with those in quasistatic helium determined at ANL. The work scope has been defined, and the loop has been modified for unattended operation. An impurity monitoring system has been installed, and the first test has been initiated. The first 100 hr of testing indicated many significant problems, and efforts to solve these problems are under way.

TABLE 5-1
TEST MATRIX FOR ANL TEST 3[a]

Specimen Type[b]	Number of Specimens	Hoop Stress (Mpa)	Remarks
MG smooth	6	262	These specimens are in flange A
ECG ribbed	5	262	
MG ribbed	5	262	
MG smooth	6	238	
ECG ribbed	5	238	
MG ribbed	5	238	
ECG ribbed	2	∿281[c]	These specimens are in a separate flange, B
Etched ribbed	2	∿281	
MG ribbed	2	∿281	
As-received smooth	6	238	
ECG ribbed	2	∿315[c]	Assorted types of specimens were included in the test.
Etched ribbed	1	∿315	
MG ribbed	3	∿315	
As-received smooth	6	∿262	

[a] All tests performed at 667°C.

[b] MG = mechanically ground; ECG = electrochemically ground.

[c] These specimens are pressurized by the same source as the smooth specimens. Stress computation for the ribbed specimens is based on the root diameter.

A calibration setup for the calibration and checkout of the Thermox ZrO_2 cell and the checkout of the EG&G dew point hygrometer is being assembled. An EG&G model 440 hygrometer, a water saturator, and a multicool refrigeration unit have been loaned to PNL for use in calibrating and operating the loop. The calibration will be done external to the loop, and the EG&G dew point hygrometer sensor will be installed between the helium circulator outlet and the inlet. The performance of the loop without the test specimens will be monitored for some time prior to the continuation of the test program.

5.3. F-1 FAST FLUX IRRADIATION EXPERIMENT

Postirradiation examination of the encapsulated seven-fuel-rod F-1 (X094) experiment (Ref. 5-1), which received a maximum burnup exposure of ∿13.0 at. % [∿121 MWd/kg (8×10^{22} n/cm^2, 6.1×10^{22} E > 0.1 m/cm^2)], is continuing at Argonne National Laboratory East (ANL-E). All seven fuel rods in the final F-1 assembly have been de-encapsulated and are in excellent condition.

Profilometry results from F-1 rods G-4, G-8, and G-9 through G-13 are given in Table 5-2. The largest diameteral strains (0.07 mm, or 0.9% at 97 MWd/kg exposure) are in rod G-8, and an increase of 0.05 mm, or 0.7%, occurred in rod G-4, which achieved the 121 MWd/kg exposure. The rod from thermal irradiation capsule GB-10 is shown for comparison (zero strain). No difference was found between the strain in the ribbed and the smooth rods in rods which achieved 75 MWd/kg exposure. Figure 5-1 shows the relationship between the cesium peaks at the ends of the fuel column and the diametral strain in rod G-4.

Photomicrographs of transverse and longitudinal sections cut from G-4 have been received from ANL. The specimens were examined in the polished, unetched condition. At about the fuel midplane and above, fission product migration to the fuel cladding gap and cladding reaction to the extent of

TABLE 5-2
SUMMARY OF PROFILOMETRY RESULTS FOR F-1 RODS IN FINAL PORTION OF X094 IRRADIATION AND GB-10

Fuel Rod Capsule Identification (Cladding Surface)	Nominal Cladding Temperature, I.D. Surface (°C)	Burnup [at. % (MWd/kg)]	Total Fluence [$n/cm^2 \times 10^{22}$ (E > 0.1 MeV)]	Oxygen-to-Metal Ratio	Smear Density (% of Theoretical Density)	Power (kW/m)	Original Diameter (mm)	Change in Diameter (mm)	Diameter Increase (%)
G-4 (smooth)	680	13.0 (121)	8.2 (6.7)	1.983	82.5	45.6	7.62	0.05	0.7
G-8 (smooth)	672	10.3 (97)	6.8 (5.6)	1.985	86.1	48.6	7.62	0.07	0.9
G-9 (smooth)	727	7.7 (73)	5.1 (4.2)	1.947	84.6	50.4	7.62	0.03	0.4
G-10 (ribbed)	727	7.7 (73)	5.1 (4.2)	1.968	84.2	48.0	7.82	0.03	0.4
G-11 (ribbed)	729	7.7 (73)	5.1 (4.2)	1.968	84.3	48.0	7.82	0.04	0.5
G-12 (smooth)	735	7.7 (73)	5.1 (4.2)	1.976	84.3	45.4	7.62	0.04	0.5
G-13 (smooth)	758	7.7 (73)	5.1 (4.2)	1.973	84.4	50.4	7.62	0.05	0.6
GB-10 (ribbed)	700	12.3 (112)	0.01	1.977 to 1.986	84.2	39.3[a] 44.3[a] 49.2[a]	9.18	0	0

[a] GB-10 operated at three power levels during reactor exposure. No measurable diameter increase was noted, but at one location in the upper one-third of the fuel rod, a very localized increase of 0.01 mm was noted.

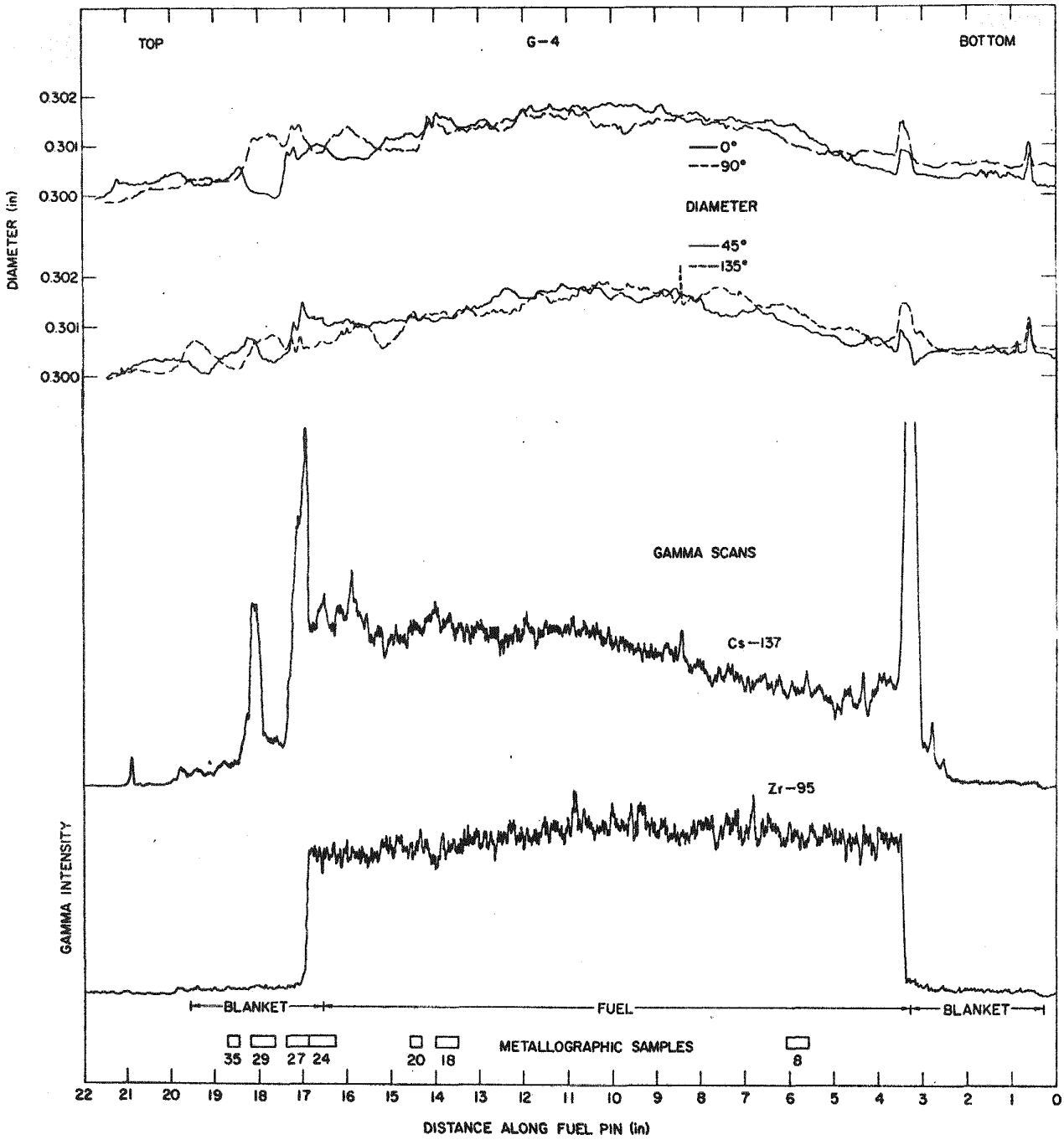

(a)

Fig. 5-1. Diametral strains and gamma scans showing cesium peaking in rods (a) G-4 and (b) G-9 (sheet 1 of 2)

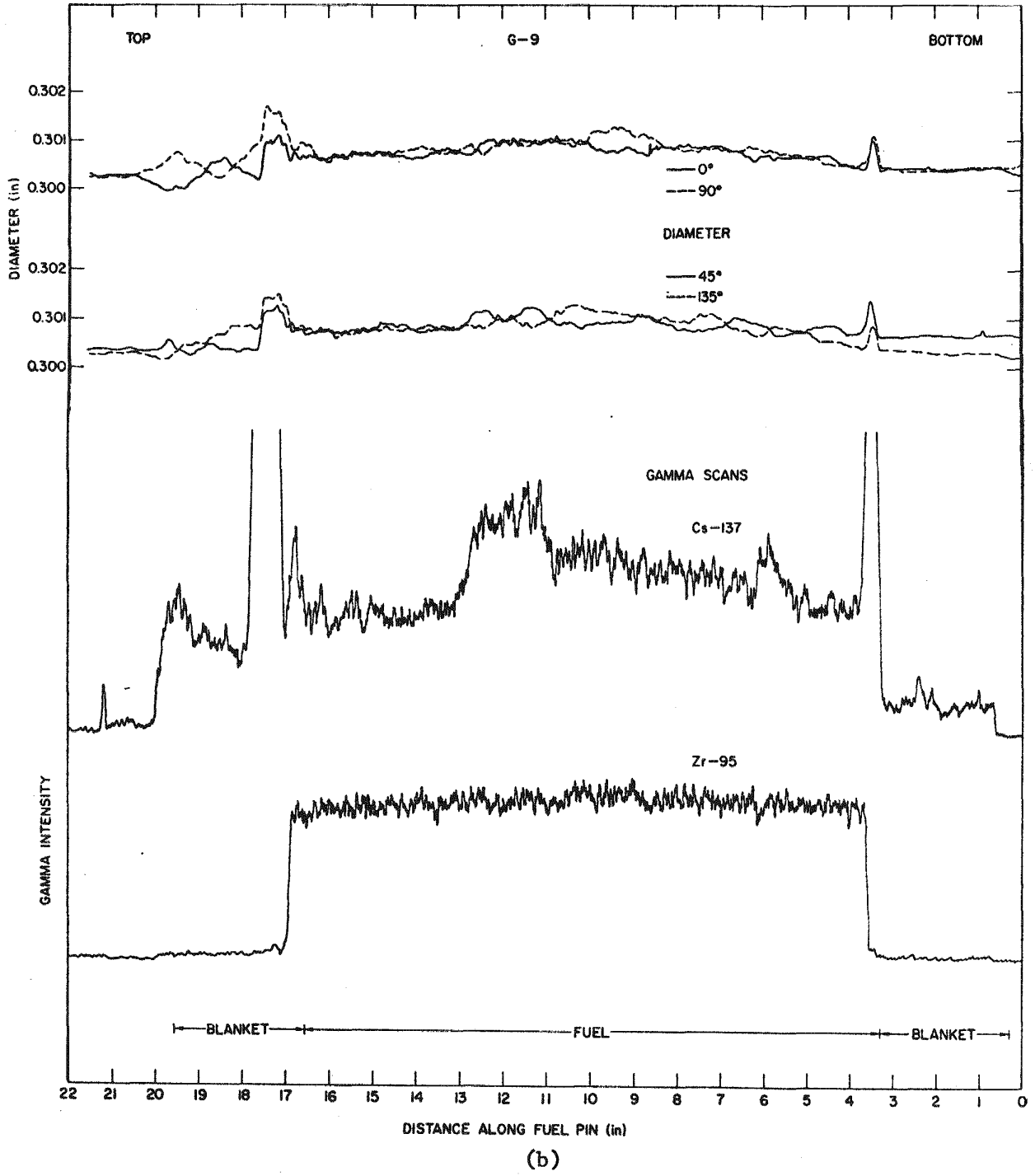

(b)

Fig. 5-1. Diametral strains and gamma scans showing cesium peaking in rods (a) G-4 and (b) G-9 (sheet 2 of 2)

∿0.06 mm maximum are evident (see Figs. 5-2 through 5-5). The nature of the reaction is a general or matrix attack. More precise measurements will be made by ANL after the samples are etched; etching will follow electron microprobe examination of the samples. Less fission product migration and minimal or no cladding attack is present below the fuel midplane (Figs. 5-6 through 5-10).

Cesium reaction has caused cracking of the first axial blanket pellet at the fuel-blanket interfaces at both ends of the rod (see Figs. 5-5 and 5-10). Beyond the first blanket pellet, the UO_2 pellets are relatively unaffected (see Fig. 5-11).

5.4. F-3 FAST FLUX IRRADIATION EXPERIMENT

The F-3 experiment was irradiated in location 4B3 in EBR-II to an exposure of 4.9 at. % (∿46 MWd/kg); the burnup goal was 100 MWd/kg. The experiment reached an exposure of 46 MWd/kg on February 11, 1976, at which time it was removed from the core for a planned interim examination. It was discovered that nine of the ten rods had failed, apparently owing to inadequate capsule sodium bonds.

Work at ANL on the F-3 experiment has been stopped because of the higher priority of work on G-4 from the F-1 experiment. However, X-radiography on the spare capsule G-27 indicated defects in the sodium bond, although eddy current measurements indicated a satisfactory bond. This result demonstrates that eddy current bond testing is not satisfactory when ribbed rods are present. ANL has stated that it is "highly probable" that the cause of the failure of the F-3 fuel rods was the inadequate sodium bonds in the capsules rather than anything related to fuel rod design.

Density measurements made at GA on the BeO axial neutron shield samples (Be, BeO, and ZrH_x) from F-3 have been rechecked on a new, more sensitive balance which recently became available. These data are being reduced.

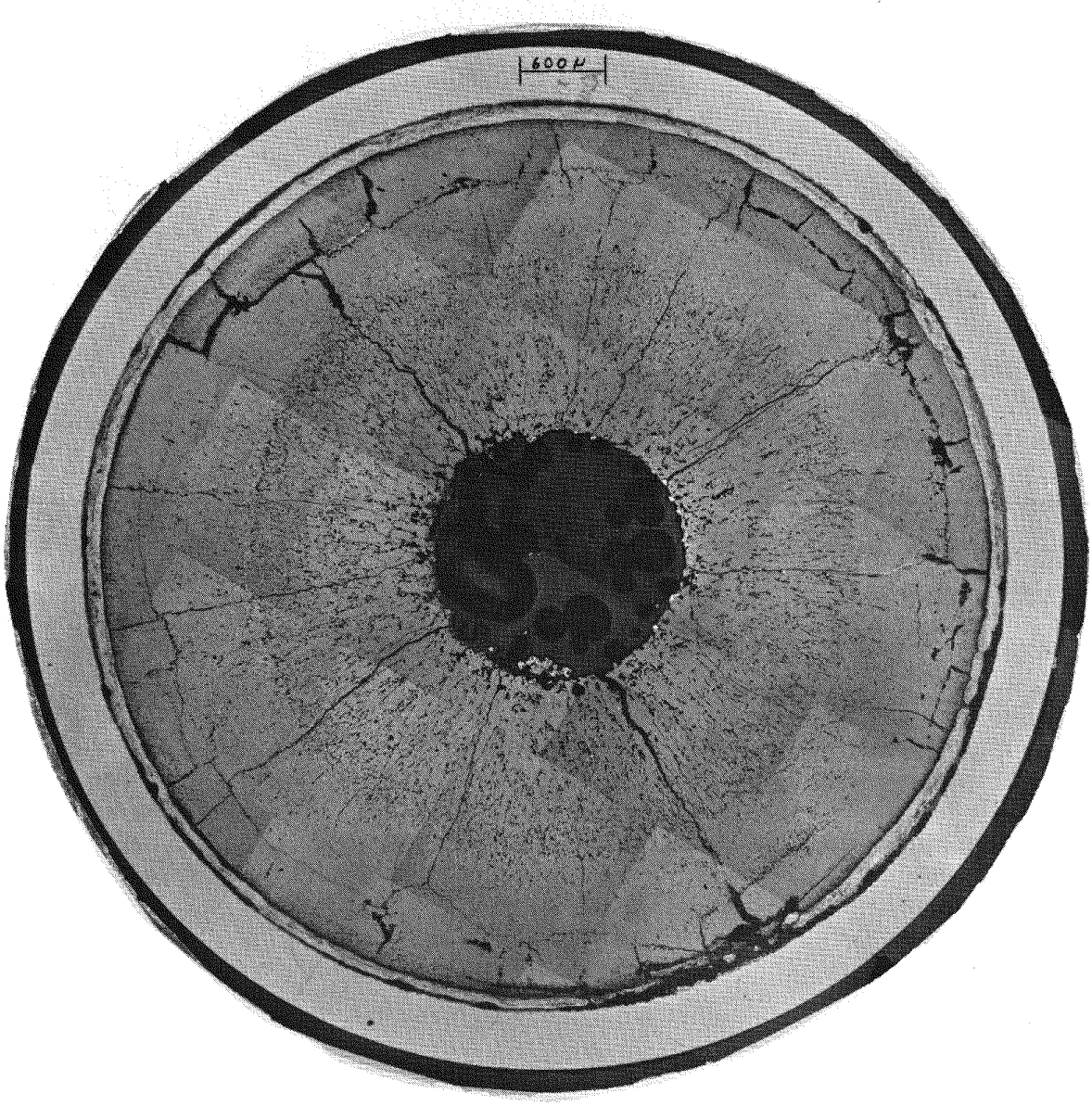

MSD 189454

Fig. 5-2. Composite of photomicrographs of section at midlength of the fuel column in rod G-4. Note large amount of fission products in the fuel–cladding gap and small amount of cladding attack.

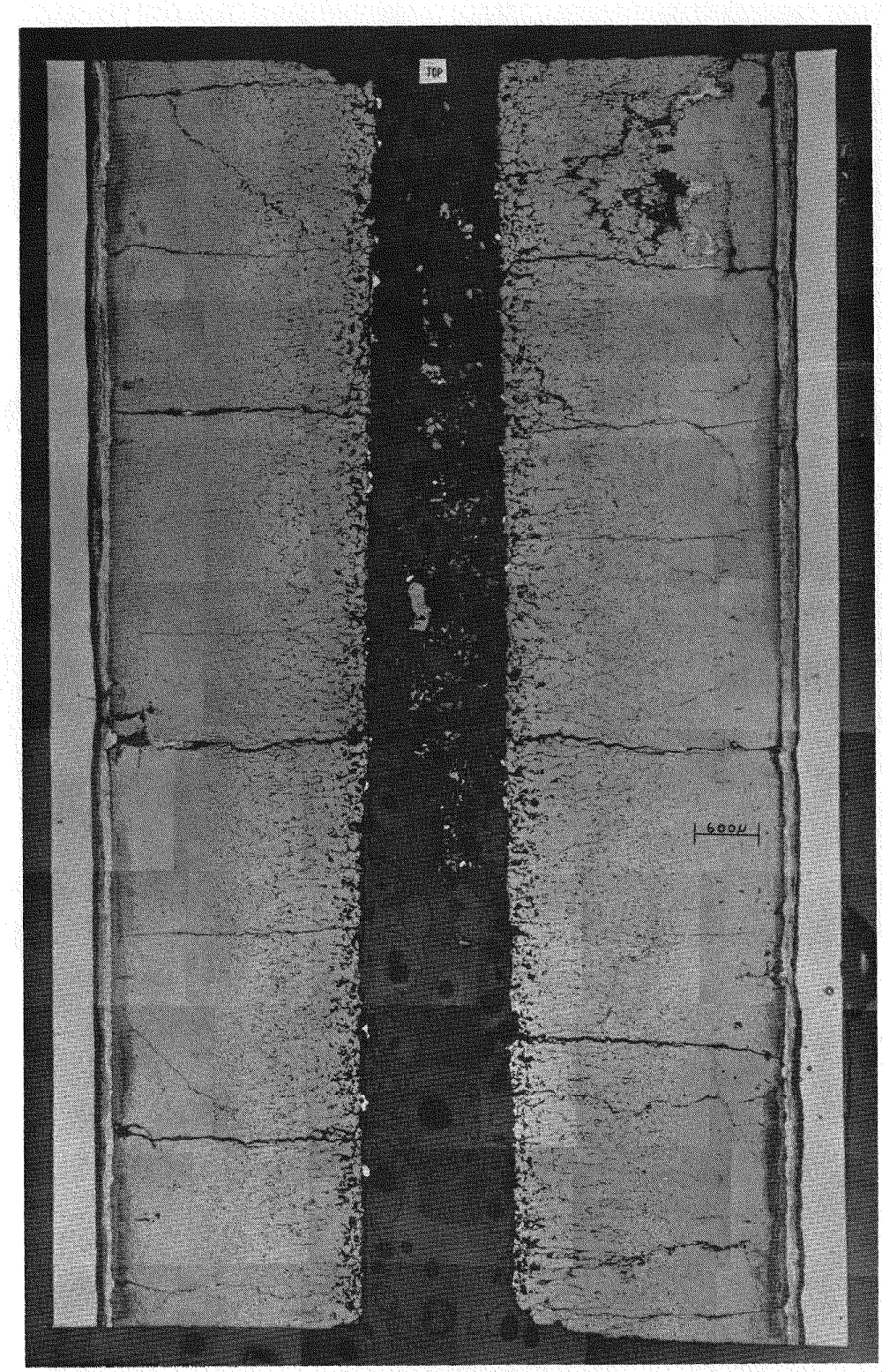

MSD 189443

Fig. 5-3. Composite of photomicrographs of rod G-4, 254 to 266 mm above the bottom of the fuel column. Note large amount of fission products in the fuel-cladding gap and nonuniform general cladding attack.

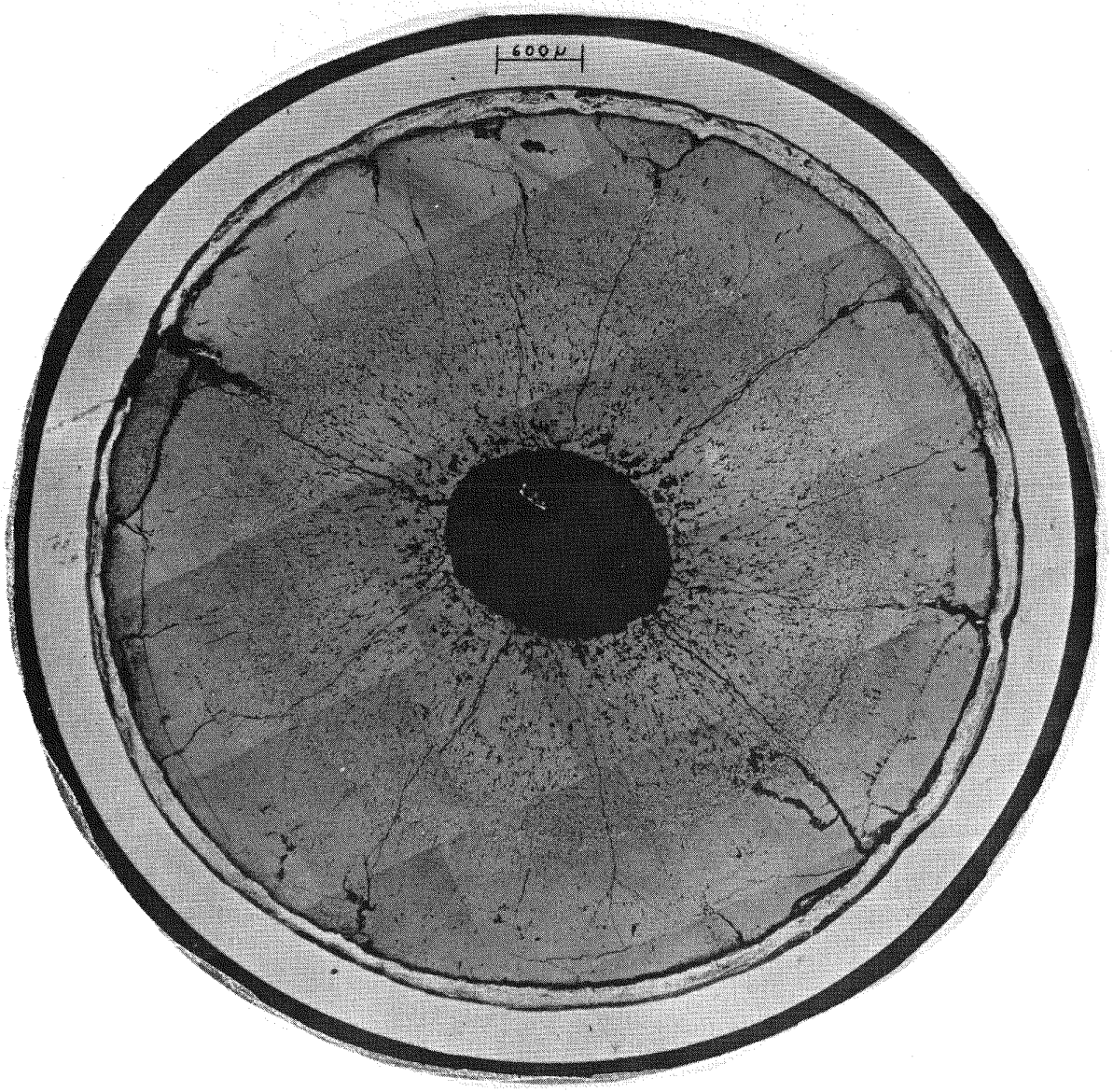

MSD 189455

Fig. 5-4. Composite of photomicrographs of rod G-4, 280 to 286 mm above the bottom of the fuel column. Note very large amount of fission and reaction products in the fuel-cladding gap and nonuniform general cladding attack.

MSD 189482

Fig. 5-5. Composite of photomicrographs of rod G-4 in near-upper fuel blanket interface. Note (1) closure of central hole in the fuel at the interface, (2) fission and reaction products in the fuel-cladding gap, and (3) disintegration of blanket pellet, apparently from reactions with cesium.

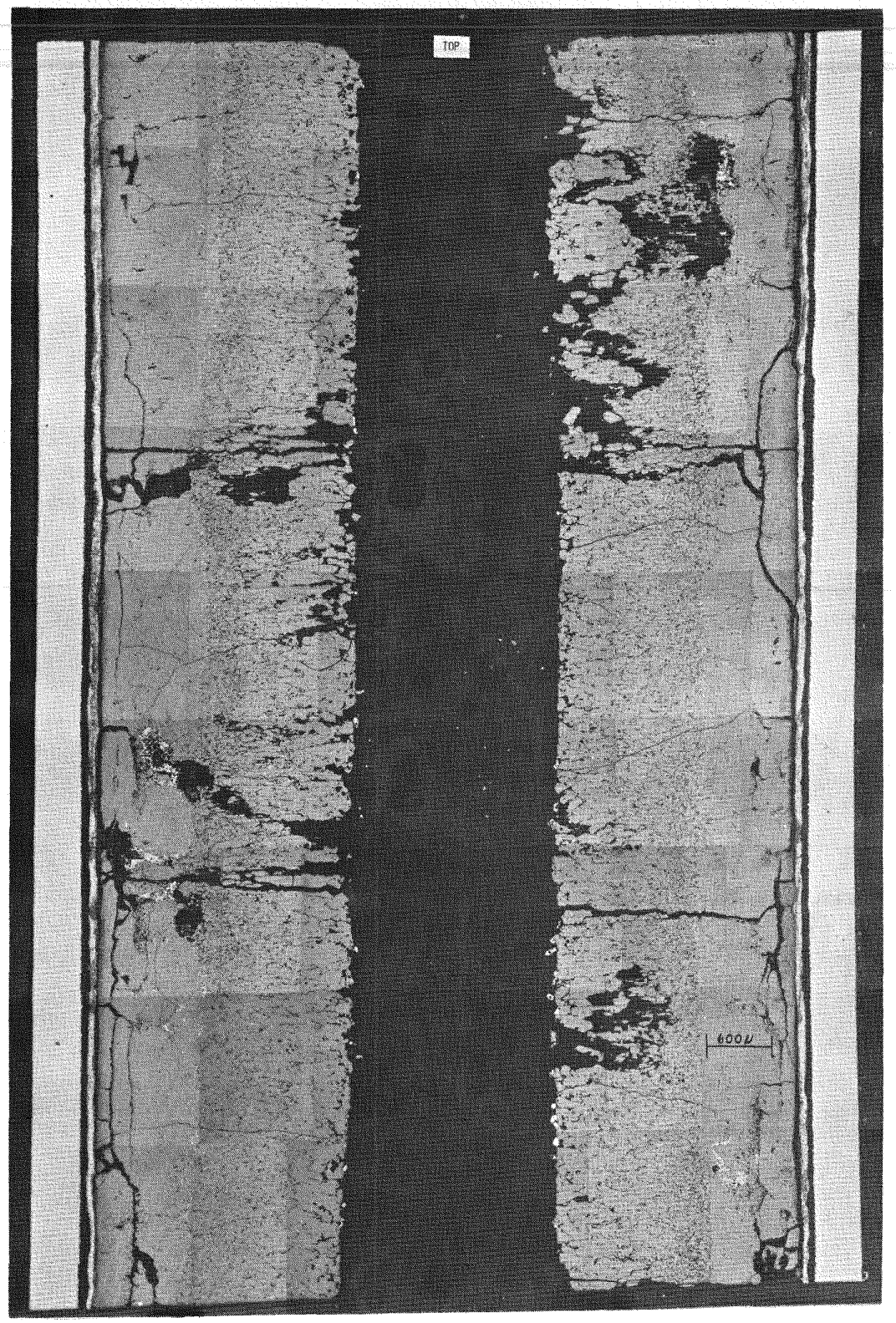

MSD 189446

Fig. 5-6. Minimal and relatively uniform general cladding attack 150 to 162 mm above the bottom of the fuel in rod G-4. Note progressively increasing amount of fission products in the fuel-cladding gap from the bottom to the top of this longitudinal section.

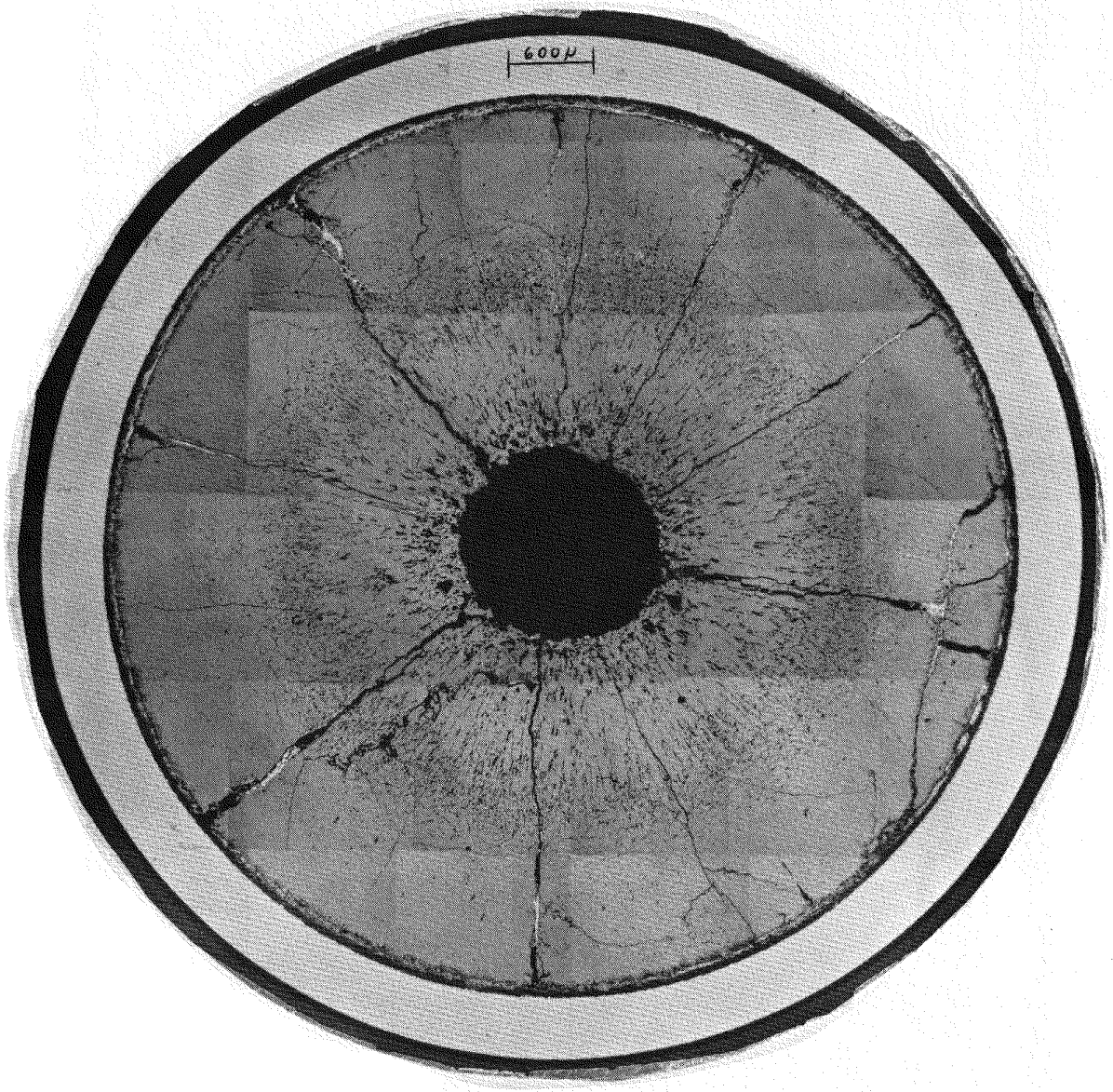

MSD 189453

Fig. 5-7. Fission products in radial cracks in the fuel and the fuel-cladding gap, 75 to 80 mm above the bottom of the fuel column in rod G-4

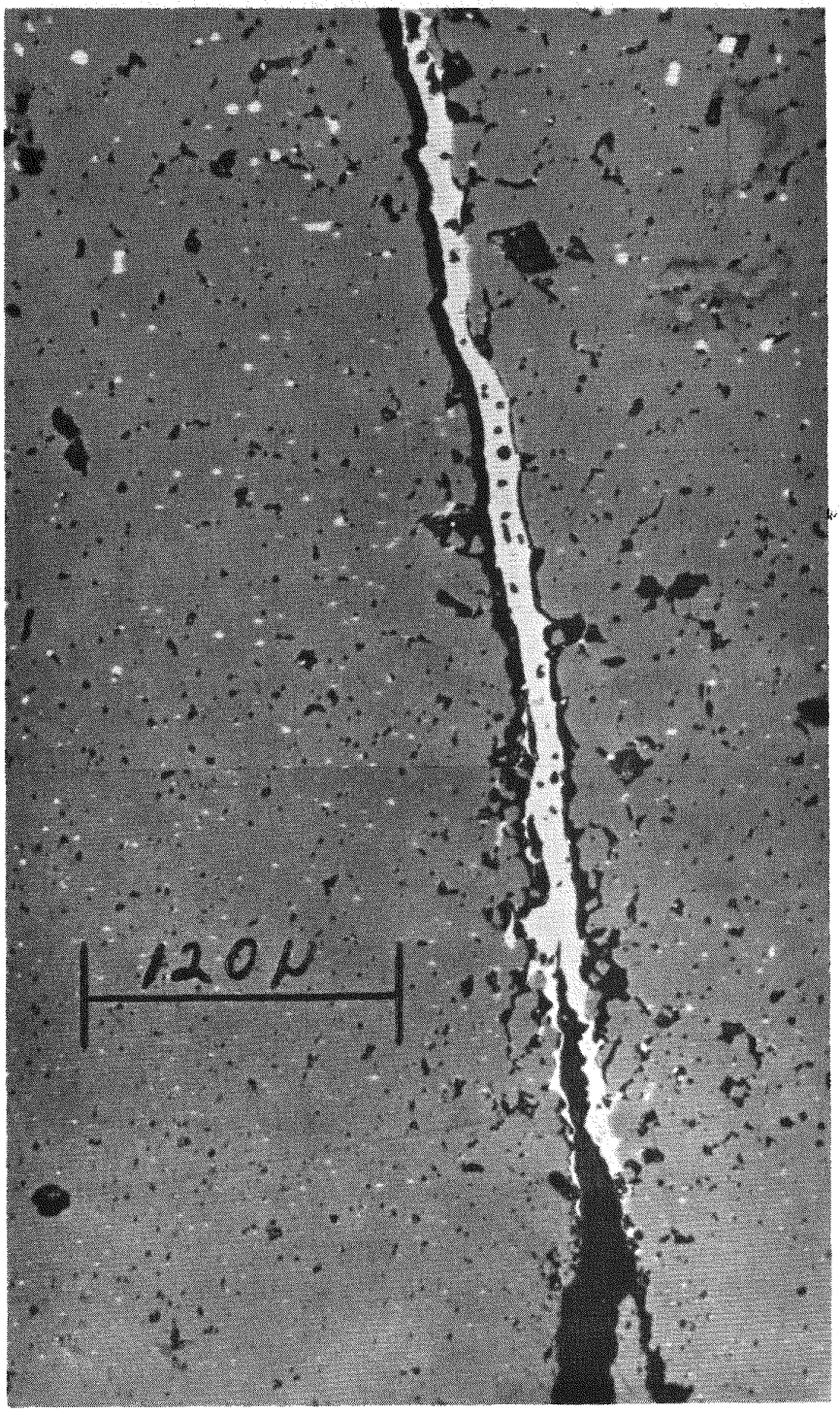

MSD 189452

Fig. 5-8. Fission products in cracks in the fuel, 75 to 80 mm above the bottom of the fuel column in rod G-4

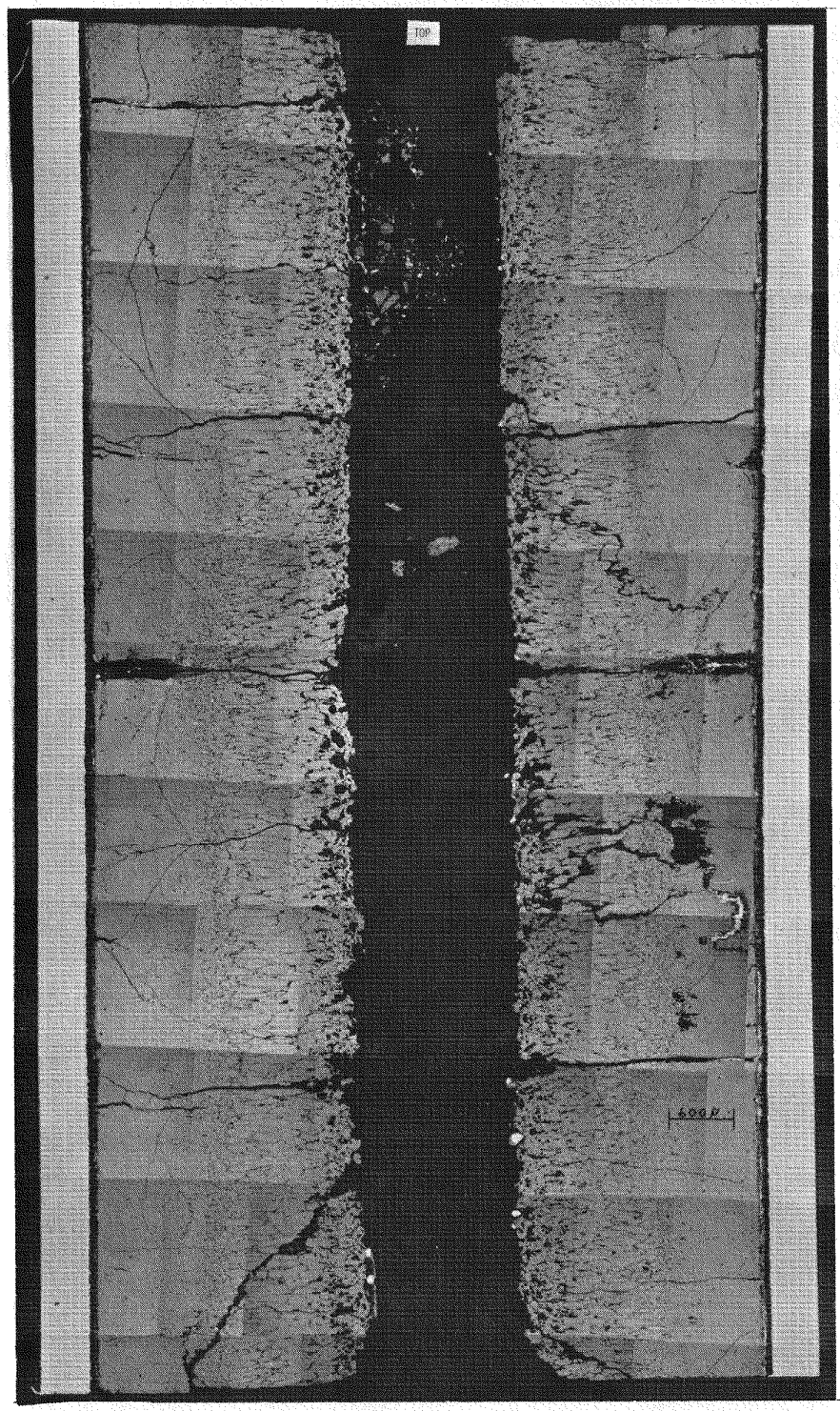

MSD 189449

Fig. 5-9. Composite of photomicrographs of longitudinal section of rod G-4, 50 to 60 mm above the bottom of the fuel column (colder end). Note apparent absence of cladding attack and relatively small amount of fission products in the fuel-cladding gap compared with regions at the fuel midplane and above.

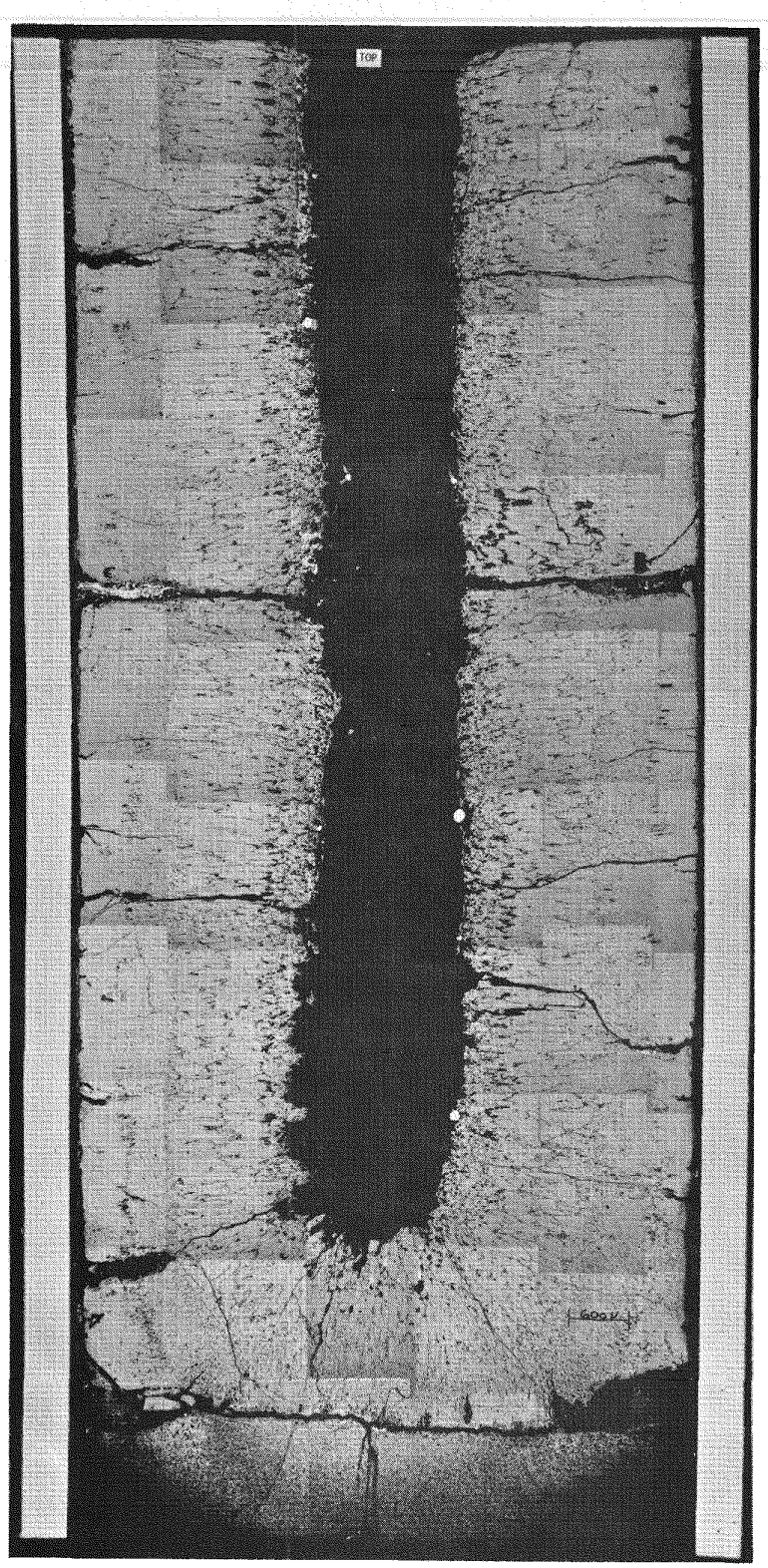

MSD 189485

Fig. 5-10. Composite of photomicrographs of bottom end region of fuel column in rod G-4. Note the closure of the central hole near the fuel-blanket interface.

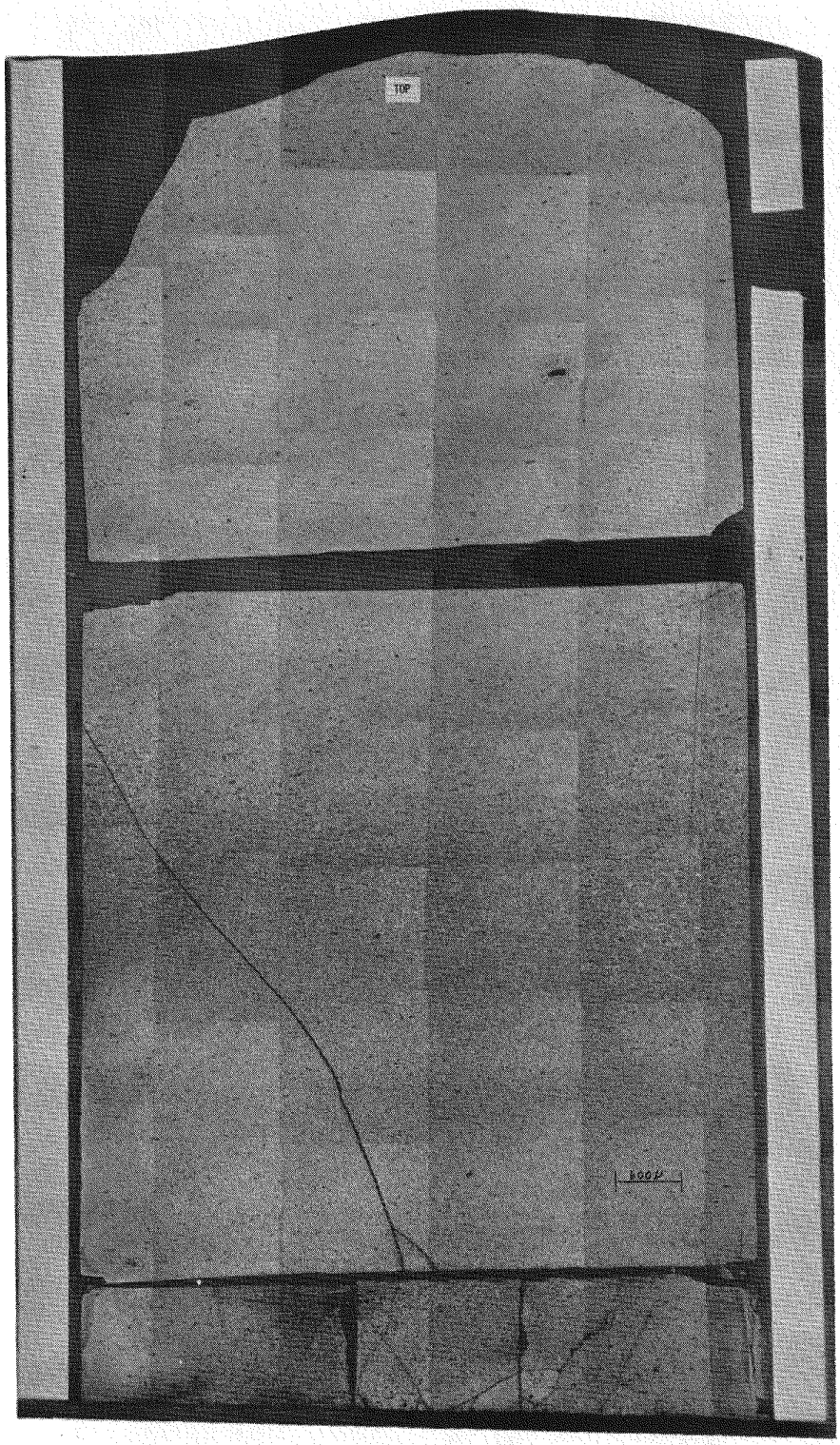

MSD 189346

Fig. 5-11. Condition of UO_2 blanket pellets 1, 2, 3 on the top end of the rod. Pellet 1 has been attacked by cesium, but pellets 2 and 3 are relatively unaffected.

5.5. F-5 PROTOTYPE IRRADIATION EXPERIMENT

Design work continued during this quarter, and fabrication of special components for the F-5 prototype design fuel rod experiment was initiated. As previously reported (Ref. 5-2), the F-5 experiment for the study of the performance of fuel rods irradiated under simulated GCFR conditions to high burnups will (1) determine the reliability of the GCFR fuel rod design, (2) discover the failure modes which may exist, and (3) study the effect of a step power increase which simulates the 180-deg rotation of a subassembly at the core-blanket interface in the proposed GCFR demonstration plant.

In response to the addendum to the F-5 Request for Approval In Principal in which it was proposed that F-5 be designed for use of two 19-rod subassemblies rather than a single 33-rod subassembly, the EBR-II project has stated that a reactivity crunch exists in EBR-II, and all the row four positions for which F-5 has been designed are taken up by high priority liquid metal fast breeder reactor (LMFBR) experiments. This results in the need for getting the priority raised for F-5 from priority five to priority one or two. Alternate positions in rows five and six are also being considered.

Row 5 locations have tentatively been selected for nuclear analysis, and the EBR-II project has recommended run 87 as a good representation of the core environment for the next 1-1/2 to 2 yr. They have also pointed out that two fueled subassemblies have been tested in row eight and that row eight could be utilized for the step power change portion of the experiment. Analysis of enrichment requirements for the row five locations has been initiated.

The special blanket pellet (for use at the fuel-blanket interface to accommodate cesium) smear density has been set at 82% and the pellet length at 7 mm. Fabrication of the dosimeters for the F-5 fuel rods has been initiated. After a weather-related plant shutdown, delivery of the F-5 cladding from Superior Tube Company is scheduled to be on about May 10, 1977.

5.6. GB-10 VENTED FUEL ROD EXPERIMENT

During this quarter, nondestructive examination of the GB-10 experiment GA-21 vented fuel rod which achieved an exposure of ∿112 MWd/kg in the Oak Ridge Reactor (ORR) was completed at ANL, and destructive examination has been initiated. Flow testing will be performed to determine the location of the apparent flow restriction in the fuel rod. Following the flow tests, sectioning of the rod for metallographic examination, microprobe scanning, and burnup analyses will be accomplished, and the charcoal trap will be shipped to GA for analysis. A sectioning diagram and a detailed postirradiation examination plan have been prepared and agreed upon by GA and ANL.

5.7. HEDL CLADDING IRRADIATIONS

Planning continued at ANL for a GCFR cladding irradiation test to be conducted in EBR-II. Although the initial loading of the experiment will contain smooth and ribbed cladding samples of 20% cold-worked 316 stainless steel, GA has requested that samples of advanced alloy cladding be inserted into the experiment on a replacement basis as the 316 stainless steel samples achieve their goal exposures. Selection of the advanced alloys to be inserted will be made in FY 78, when additional data from the national advanced alloy cladding program have been generated.

Some ribbed and smooth GCFR cladding specimens have already been irradiated (Table 5-3), and the specimens have been shipped from Hanford Engineering Development Laboratory (HEDL) to ANL Material Sciences Division (ANL-MSD) for postirradiation testing. Some specimens are continuing to be irradiated as part of the HEDL cladding irradiation test capsules. The actual conditions under which the samples were irradiated are shown in Figs. 5-12 through 5-14. The temperature profiles were established using thermal expansion difference (TED) monitors located at three positions in each subcapsule. These profiles represent the peak temperatures attained during the early cycles of the irradiations. The fluence profiles for subcapsule B-139 are based on the analysis of flux monitors irradiated in

TABLE 5-3
GCFR CLADDING SPECIMENS WHICH HAVE COMPLETED IRRADIATION

Desired Irradiation Temperature (°C)	Fluence (n/cm^2)	Type of Specimen	Date of Removal from EBR-II	Postirradiation Tests	
				Temperature (°C) and Environment	Stress,[a] Root of Rib (MPa)
700	2.6 to 3.6×10^{22}	5 smooth, 5 ribbed by etching	9/75	700 (1.013×10^5 Pa static helium)	138
700	4.2 to 6×10^{22}	2 smooth, 3 ribbed by etching	3/76	700 (1.013×10^5 Pa static helium)	138

[a] The hoop stress to axial stress ratio is equal to one.

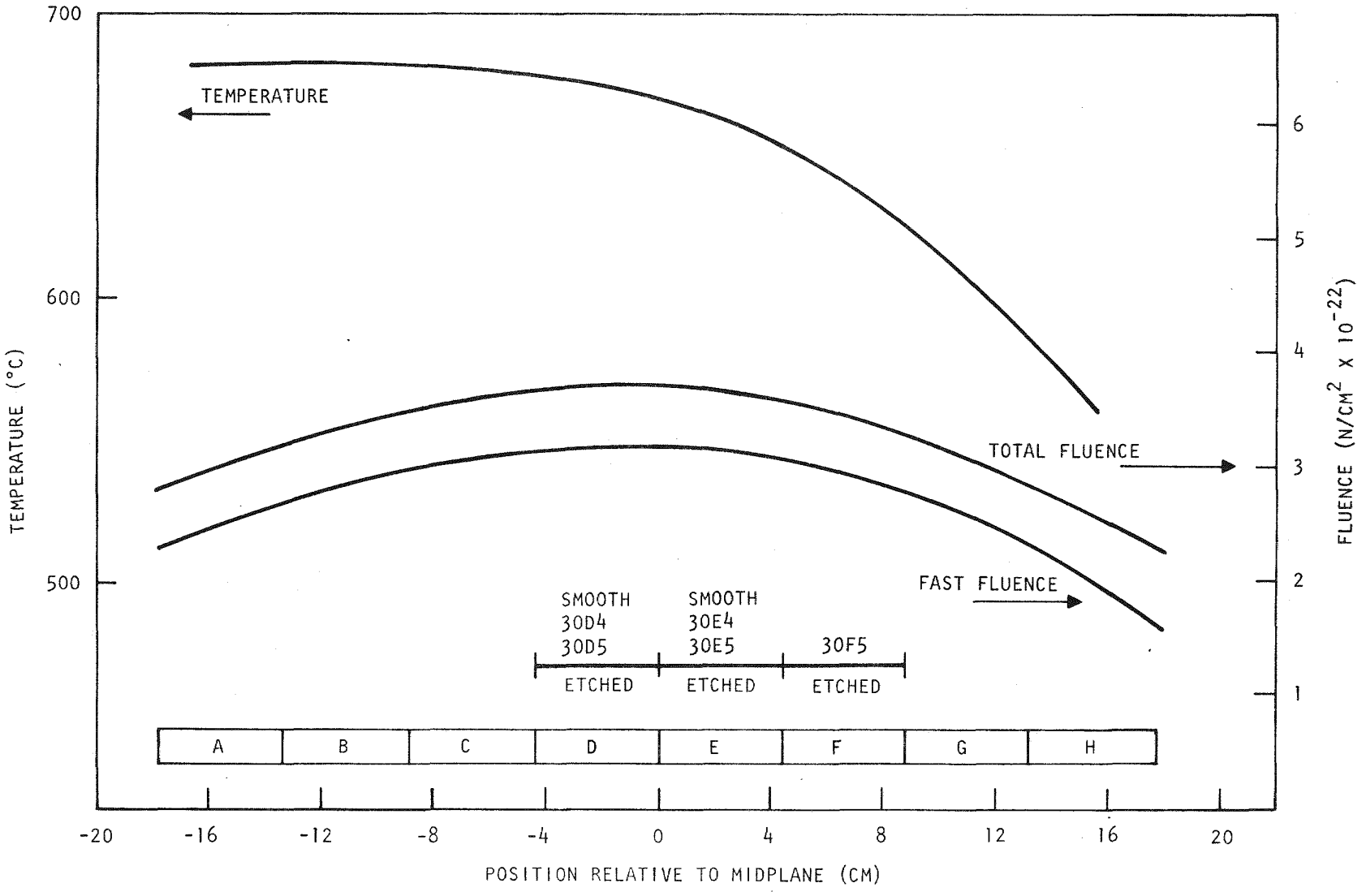

Fig. 5-12. Irradiation conditions for B-130

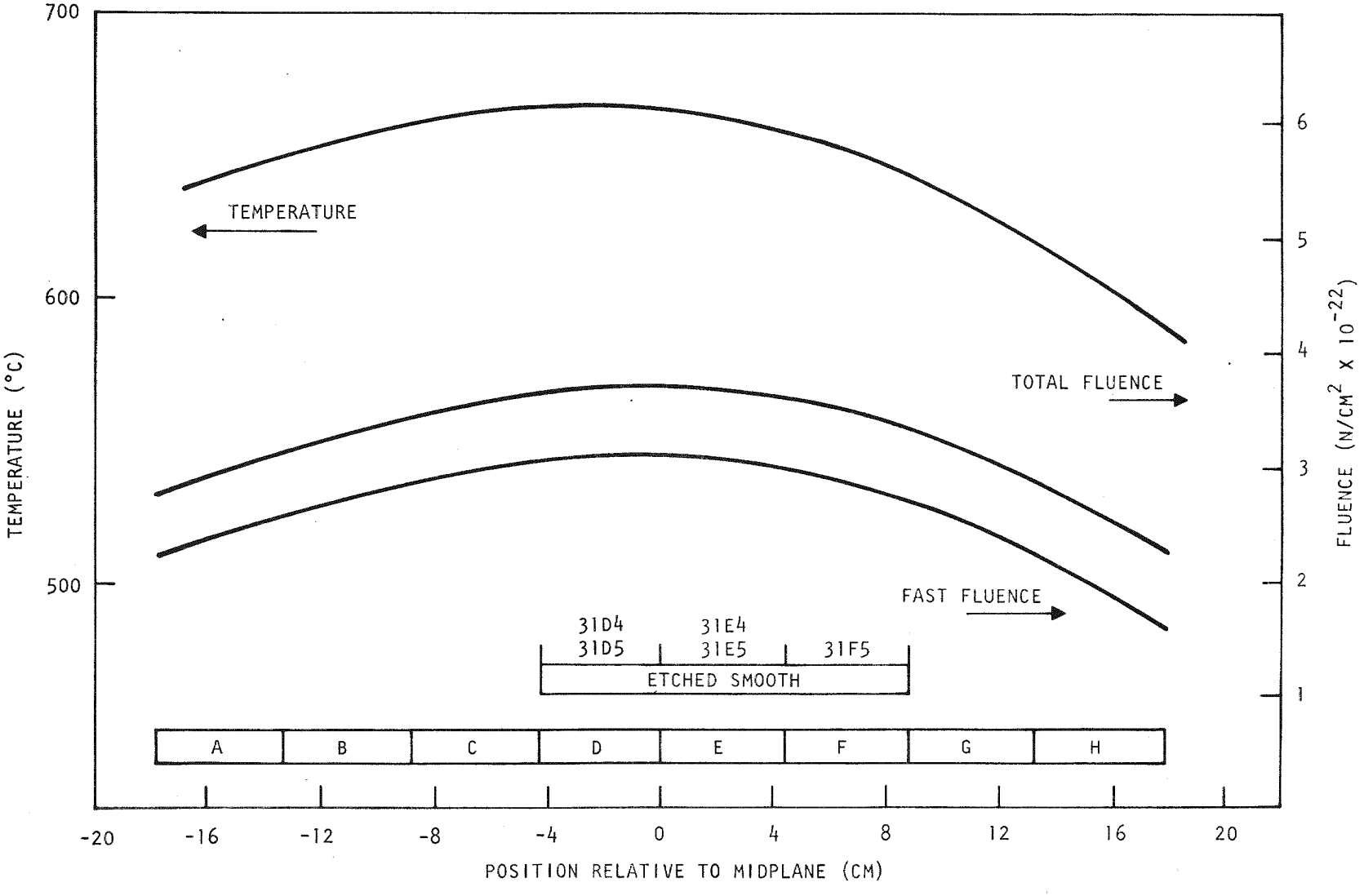

Fig. 5-13. Irradiation conditions for B-131

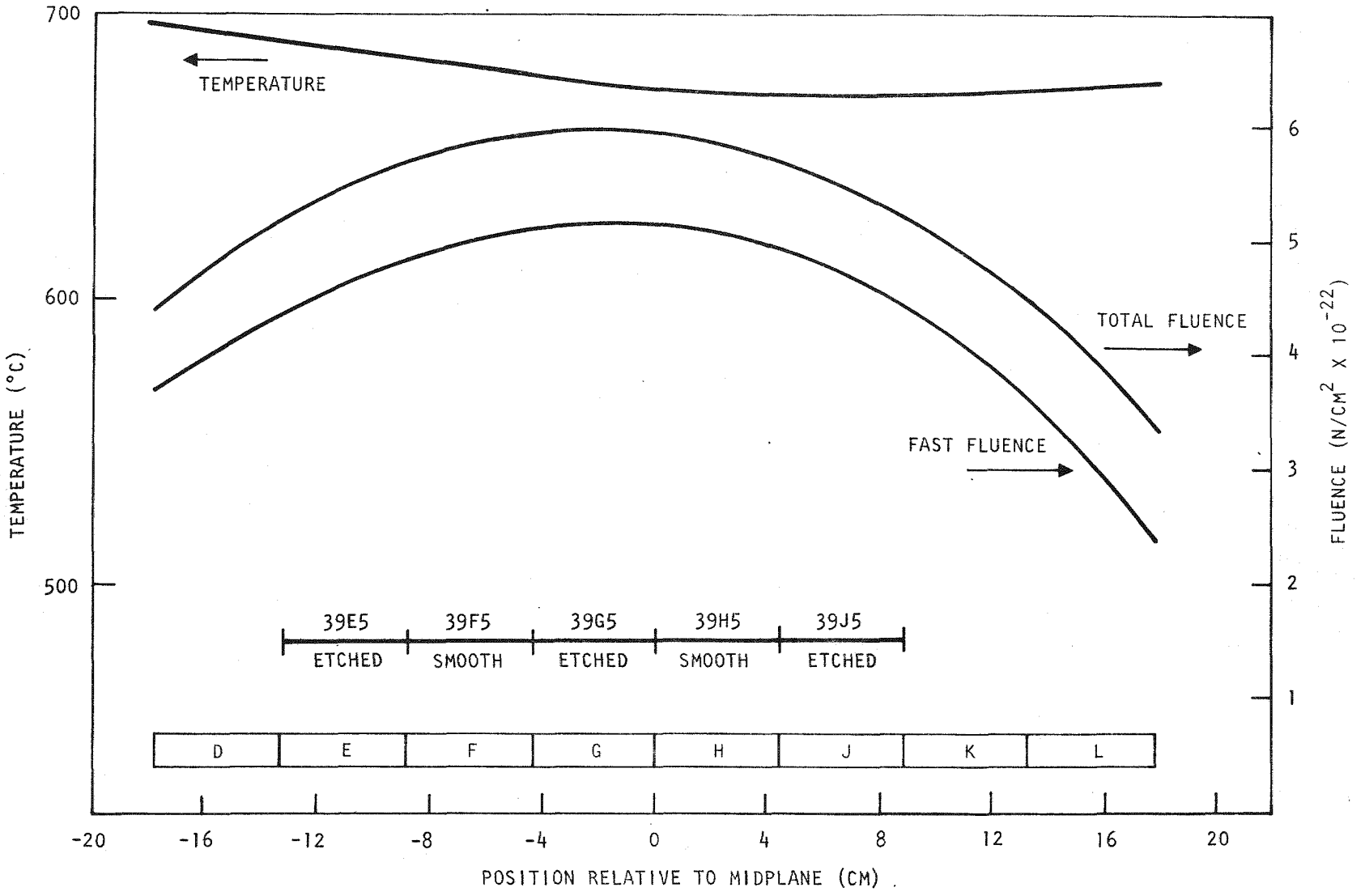

Fig. 5-14. Irradiation conditions for B-139

the same subassembly. Neutron dosimetry is not yet available for subcapsules B-130 and B-131, and the fluence profiles presented for these two subcapsules are therefore based on the dosimetry from the companion subassembly scaled to a peak fluence value of 3.2×10^{22} n/cm^2 ($E > 0.1$ MeV).

REFERENCES

5-1. "Gas-Cooled Fast Breeder Reactor Quarterly Progress Report for the Period November 1, 1976 Through January 31, 1977," ERDA Report GA-A14240, General Atomic, February 1977.

5-2. "Gas-Cooled Fast Breeder Reactor Quarterly Progress Report for the Period August 1, 1976 Through October 31, 1976," ERDA Report GA-A14112, General Atomic, November 1976.

6. FUEL ROD ENGINEERING (189a No. 00583)

The objective of this task is to evaluate the steady-state and transient performance of the fuel, blanket, and control rods for the determination of performance characteristics, operating limits, and design criteria. To this end, analytical tools [such as the LIFE-III code (Ref. 6-1)] are being adapted and/or developed and applied to the analysis of GCFR prototypical rods and experimental rods. In addition, continuous surveillance of the LMFBR fuels and materials development program and technology is maintained to maximize the use of development technology and material properties. Support is also given for the planning and designing of irradiation experiments.

6.1. FUEL, BLANKET, AND CONTROL ROD ANALYTICAL METHODS

The current work plan has been revised to maximize the effort to develop the analytical capability for predicting GCFR vented rod irradiation performance. This revision is based on the fact that the analytical methods for LMFBR fuel and blanket rods developed by the National LIFE Working Group are generally applicable to GCFR rod analysis. Therefore, the GA effort will concentrate on modeling the special features of the GCFR rod design and environment.

One of the two primary, unique characteristics of the GCFR fuel rod design which distinguishes it from the LMFBR design is its utilization of the pressure-equalized vented concept. During steady-power operation, released fission gases are continuously vented off, and during power changes, the rod breathes (inhales helium at power decreases and exhales during power increases). In addition, the fuel rod internal pressure is held constant at the reactor core outlet coolant pressure. These effects result in a rod internal atmosphere which differs somewhat from that of the LMFBR rod and

has some impact upon the pellet-to-cladding gap conductance. A second consideration related to rod internal atmosphere effects concerns internal rod voids. The LMFBR rods have a large internal fission gas plenum, and as a result, the voids associated with pellet porosity, pellet-to-cladding gap, and center holes represent a very small fraction of the total and are simplistically treated in the LIFE code. In the GCFR rod design, there is no large plenum, and the pellet porosity (fuel and blanket), pellet-to-cladding gap, and center hole (if any) voids are more significant and should be treated somewhat more carefully.

The second area in which the GCFR rod design differs from the LMFBR rod design is in the use of roughened cladding. For thermomechanical behavior studies, the roughened cladding leads to the need for expanded capabilities in LIFE to handle additional axial zones and zones of differing length. Since ANL is also interested in investigation of GCFR fuel rod performance behavior, a discussion was held with representatives of ANL and GA, and a joint GA-ANL effort initiated to modify the LIFE code for GCFR fuel rod performance analysis.

6.2. ANALYSIS OF IRRADIATION TESTS

Modeling of the GCFR vented rod internal atmosphere will be derived using a semi-empirical approach; i.e., the fundamental physical principles and measured data from the GB-9 and GB-10 capsule tests will be combined. All documents related to both capsule tests are being reviewed. The GB-9 and GB-10 tests were instrumented thermal-flux capsule experiments performed at ORNL to simulate the performance characteristics of the GCFR vented fuel rod. Furthermore, they were specifically designed with sweep gas lines to generate basic information on fission product transport and release phenomena. The LIFE code will be employed to analyze the data collected from the GB-9 and GB-10 capsule tests, and a new fission gas release model will be developed to account for release of individual radioactive isotopic species. As a first approximation, classical diffusion theory will be used to describe

fission gas release from a spherical fuel particle with a finite radius (as described in Ref. 6-2). The fuel sphere will be treated as a homogeneous medium, and no account will be taken of bubbles, pores, dislocations, grain boundaries, or irradiation-produced defects which may impede gas atom migration. The effect of these trapping centers will be included in the diffusion coefficient, which will be determined by matching the analytical prediction to the experimental data from both capsule tests. Therefore, the diffusion coefficient will be an apparent diffusivity for the heterogeneous medium.

6.3. ROD ANALYSIS AND PERFORMANCE

During the previous quarter, the transient pellet-cladding mechanical interaction model described in Ref. 6-3 was modified to account for cladding plasticity. Several test problems were run to assure that the code operated properly. Previous to the model modifications, studies were initiated to select a method for representing the constituitive equations for 20% cold-worked 316 stainless steel. It was decided that the cladding would initially be modeled as an elastic, perfectly plastic material, although it is recognized that at a later date, bilinear representations of the stress-strain curves should be developed in accordance with the procedures recommended in Ref. 6-4. A number of test problems have been run with this model. These problems typically considered the plastic strain of the cladding which would result from rapid power rises in the event that the pellet and cladding were initially in contact. The performance of the code appears satisfactory.

6.4. ROD MECHANICAL TESTING

Test specifications for the fuel rod mechanical testing program are being formulated. Arrangements to fabricate ribbed cladding by mechanical grinding have been made, and fabrication will begin upon delivery of cladding from Superior Tubing Company. An Instron universal testing machine has been purchased, and an environmental furnace with an averaging extensometer has been ordered. Installation and checkout of the Instron machine has been delayed pending authorization for the required laboratory space.

REFERENCES

6-1. Billone, M. C., et al., "The LIFE-III Fuel-Element Performance Code User's Manual," Argonne National Laboratory Revised Draft, September 1976.

6-2. Booth, A. H., "A Suggested Method for Calculating Diffusion of Radioactive Rare Fission Gas Products From UO_2 Fuel Elements and a Discussion of Proposed In-Reactor Experiments That May Be Used to Test Its Validity," Atomic Energy of Canada Report DCI-27, 1957.

6-3. "Gas-Cooled Fast Breeder Reactor Quarterly Progress Report for the Period November 1, 1976 Through January 31, 1977," ERDA Report GA-A14240, General Atomic, February 1977.

6-4. Corum, J. M., et al., "Interim Guidelines for Detailed Inelastic Analysis of High-Temperature Reactor System Components," Oak Ridge National Laboratory Report ORNL-5014, December 1974.

7. NUCLEAR ANALYSIS AND REACTOR PHYSICS (189a No. 00584)

The scope of activities planned under this subtask encompasses the validation and verification of the nuclear design methods which will be applied to the GCFR core design. This will primarily be done by evaluating the methods using a critical assembly experimental program specifically directed toward GCFR development. Program planning and coordination activities, critical assembly design and analysis, and the necessary methods development will be carried out during the course of this program.

The major effort during the previous quarter was concentrated on post-analysis of the phase II assembly experiments. Kinetics parameters were generated, and the effect of the reflector and steam entry upon central reactivity worths was investigated. Selected configurations were recalculated for the steam entry experiment using the new methodology for shielding of resonance cross sections; this methodology was compared with earlier methods. Calculation of the Doppler experiment was initiated.

During this quarter, the Doppler experiment calculations were completed in 10 and 28 groups using the upgraded methodology. Control rod modeling and self-shielding analyses were begun for the B_4C columnar control rod mock-ups, and a study of the adequacy of various forms of the $P_\ell S_n$ equations for representation of the plate format of the ZPR cells was undertaken.

7.1. PHASE II GCFR CRITICAL ASSEMBLY ANALYSIS

7.1.1. Analysis of U-238 Doppler Coefficient

7.1.1.1. Summary of Experiment. Experimental determination of the U-238 Doppler worth in the GCFR phase II critical assembly was accomplished by ANL using the N-1 Doppler sample at the center of the phase II core. This sample

consisted of 12 natural UO_2 cylindrical pellets stacked in a column 30.48 cm high and 2.54 cm in diameter. The total UO_2 weight was 1266.29 g. The UO_2 sample was surrounded by an Inconel capsule placed in the oscillator drawer and inserted into the empty central matrix position. The sample-oscillation reactivity-difference technique was then used to measure the Doppler reactivity at five temperatures of the Doppler sample, including 298 and 1095 K. To eliminate the Doppler effect of the Inconel capsule as it changed temperature, another sample with a similar capsule, but without the UO_2 column, was heated to three temperatures, and the Inconel Doppler effect was again determined by the sample-oscillation reactivity-difference technique. Both sets of reactivity-temperature data were fitted (in a least squares sense) to the integral of the theoretical Doppler coefficient expression:

$$\frac{1}{K}\frac{dK}{dT} = \frac{\alpha}{T^{\gamma}} \quad .$$

Using these fitted parameters, the Doppler worth for the UO_2 sample plus capsule and for the empty capsule could be calculated for a temperature rise from 300 to 100 K. Subtracting the empty capsule Doppler worth from the UO_2 sample plus capsule Doppler worth yields the Doppler worth of the UO_2 sample as its temperature rises, with the capsule remaining at a constant temperature. The resulting value is 0.623 ±0.009 Ih/kg U-238. Details of the ANL experiment and analysis and Doppler worth calculation are given in Ref. 7-1.

7.1.1.2. Cross Sections for the Doppler Calculation. In order to include the UO_2 sample core resonance interaction, two GGC-5 spectrum codes (Ref. 7-2) were run for the central seven matrix drawers, i.e., the central Doppler sample drawer plus the surrounding six drawers. Region 1 of the two-region cylindrical GGC codes was the UO_2 column with a 2.54-cm diameter. Region 2 was the homogenized remainder of the central seven matrix drawer (capsule plus central drawer plus surrounding six core drawers). One GGC-5 code had the U-238 in the UO_2 sample (region 1) at 300 K in the GAROL (Ref. 7-3) resolved resonance calculation and the GANDY (Ref. 7-4) unresolved resonance calculation. The other GGC-5 code had the region 1 U-238 at 1100 K in the GAROL and GANDY calculations. Both GGC codes had the U-235 and oxygen in region 1 and all nuclides in region 2 at 300 K.

ENDF/B-4 data and shielded GAROL resonance parameters were used for the cross section preparation. Atom densities used in GGC-5 (Table 7-1) were calculated from data in Ref. 1. To simulate leakage effects in GGC-5 for the central seven drawers, 28-group B^2 values were input to be used in the variable buckling calculation of the 999-group flux. These B^2 values were calculated from a 2DB (Ref. 7-5) flux calculation of the phase II core without the Doppler sample, since the phase II core with the Doppler sample had not been calculated. These B^2 values are listed in Table 7-2 along with the "second iteration" B^2 values from a phase II core with a Doppler sample for the same central seven drawers. Evidently, the "first iteration" B^2 values used in GGC-5 were not very accurate, although the inaccuracy had little effect upon the flux (Table 7-3) or the Doppler worth, since the 10- and 28-group worths were so close, i.e., -0.591 and -0.599 Ih/kg, respectively.

Table 7-4 compares the differences in the U-238 capture cross section between 300 and 1100 K. These differences are given for the UO_2 sample and the surrounding six core drawers. These core drawers remained at 300 K, so that their U-238 capture cross sections changed because of the resonance interaction with the UO_2 sample as the sample temperature changed. General Atomic cross sections for groups 12 through 15 were calculated by the GANDY unresolved resonance option in GGC-5, and groups 16 through 28 were calculated by the GAROL resolved resonance option of GGC-5. ANL cross sections for groups 13 through 17 were calculated using equivalence theory in MC^2-2/SDX, and groups 18 through 27 were calculated using integral transport theory in MC^2-2. If the ANL U-238 capture cross section values were used in the GA PERT (Ref. 7-6) exact-order perturbation calculation of the Doppler worth, the GA 28-group worth would change from -0.599 to -0.560 Ih/kg. The ANL calculated Doppler worth was -0.515 Ih/kg, so there evidently are other significant differences between methods.

7.1.1.3. Shielding Factors for Doppler Sample. The two-region GAROL calculation in GGC-5 includes shielding effects in the Doppler sample over the resolved resonance energy range below 7500 ev. To calculate shielding factors for the Doppler sample above this energy, a DTFX (Ref. 7-7) one-dimensional transport calculation of the phase II core and radial blanket

TABLE 7-1
ATOM DENSITIES USED IN CROSS-SECTION CALCULATIONS[a]

Nuclide	Region 1	Region 2	Cell Average
H	0.00000	0.00000	0.0000
B-10	0.00000	0.00000	0.0000
B-11	0.00000	0.00000	0.0000
C	0.00000	0.00000	0.0000
O	3.71533-02[b]	1.18010-02	1.2402-02
Cr	0.00000	3.20560-03	3.1296-03
Mn	0.00000	2.44200-04	2.3841-04
Fe	0.00000	1.55539-02	1.5185-02
Ni	0.00000	1.86200-03	1.8178-03
Mo	0.00000	2.74000-04	2.6750-04
U-235	1.34700-04	1.07000-05	1.3641-05
U-238F	1.84412-02	0.00000	4.3743-04
U-238O	0.00000	4.86540-03	4.7500-03
Pu-239	0.00000	1.03870-03	1.0141-03
Pu-240	0.00000	1.37700-04	1.3443-04
Pu-241	0.00000	1.43100-05	1.3971-05
Pu-242	0.00000	2.02000-06	1.9721-06
Am-241	0.00000	8.16000-06	7.9664-06

[a] Dimensions (cm): region 1 = 1.27000; region 2 = 8.24600.
Volume fractions: region 1 = 0.02372; region 2 = 0.97628.

[b] 3.71533-02 = 3.71533×10^{-2}.

TABLE 7-2
COMPARISON OF 28-GROUP BUCKLING

Group	Buckling Used in GGC-5	Buckling Recalculated Using 2DB-PERT
1	1.42471-03	3.65952-04
2	1.42504-03	3.28043-04
3	1.42513-03	2.89861-04
4	1.42375-03	4.75763-04
5	1.42942-03	7.02101-04
6	1.45337-03	9.24285-04
7	1.45947-03	1.14058-03
8	1.50702-03	1.23566-03
9	1.49446-03	1.19815-03
10	1.49142-03	1.29686-03
11	1.48786-03	1.30269-03
12	1.47145-03	1.32767-03
13	1.47902-03	1.18766-03
14	1.40535-03	1.18057-03
15	1.37571-03	1.31228-03
16	1.37829-03	2.14464-03
17	1.34576-03	1.35460-03
18	1.32815-03	1.75936-03
19	1.29628-03	1.76851-03
20	1.27311-03	1.00838-03
21	1.23935-03	2.61082-04
22	1.22055-03	-2.34210-03
23	1.17801-03	-7.04219-03
24	1.14088-03	-1.02218-02
25	1.04970-03	-5.72282-02
26	9.78770-04	-5.72865-02
27	5.64000-04	-1.32299-02
28	1.16133-03	-0.15813

TABLE 7-3
28-GROUP DATA COMPARISON

Group	Real Flux for Central Seven Drawers With Hot Doppler Sample		2DB Flux for Hot UO_2 Sample (GA Values)		Doppler Worth for UO_2 Sample (Ih/kg U-238)	
	From GGC-5	From 2DB	Real Flux	Adjoint Flux[a]	GA Calculation	ANL Calculation
1	0.025	0.024	0.023	1.557	0.0	0.0
2	0.339	0.330	0.316	1.338	0.0	0.0
3	1.37	1.32	1.26	1.163	0.0	0.0
4	3.51	3.42	3.30	1.174	0.0	0.0
5	5.05	4.90	4.76	1.086	0.0	0.0
6	6.93	6.76	6.64	0.981	0.0	0.0
7	13.38	13.19	13.16	0.956	0.0	0.0
8	10.35	10.27	10.23	0.947	0.0	0.0
9	12.06	12.08	12.13	0.919	0.0	0.0
10	11.56	11.65	11.69	0.896	0.0	0.0
11	9.43	9.56	9.61	0.865	0.0	0.0
12	7.61	7.75	7.83	0.826	-0.00760	0.0
13	4.78	4.90	4.97	0.800	-0.0159	-0.190
14	5.06	5.23	5.15	0.786	-0.0326	-0.0358
15	3.24	3.34	3.46	0.802	-0.0451	-0.0482
16	1.70	1.71	1.77	0.829	-0.0652	-0.0462
17	1.41	1.41	1.44	0.869	-0.0833	-0.0730
18	0.948	0.938	0.977	0.909	-0.0908	-0.0801
19	0.665	0.646	0.670	0.947	-0.0792	-0.0740
20	0.325	0.313	0.331	0.994	-0.0684	-0.0593
21	0.168	0.163	0.173	1.041	-0.0457	-0.0434
22	0.0645	0.0645	0.0697	1.093	-0.0199	-0.0178
23	0.0392	0.0435	0.0492	1.139	-0.0159	-0.0147
24	0.00332	0.00400	0.00466	1.449	-0.00164	-0.00100
25	1.27-04	2.74-04	2.77-04	0.637	-3.29-05	-2.10-05
26	4.12-06	1.74-05	1.68-05	1.271	-4.18-06	-7.91-08
27	9.99-07	3.12-06	3.04-06	1.025	-2.82-08	2.87-09
28	6.73-07	6.59-07	7.09-07	0.702	-1.21-09	
Total	100.0	100.0	100.0		-0.5713	-0.5125

[a] Group average adjoint = 1.00.

TABLE 7-4
U-238 CAPTURE CROSS SECTION DIFFERENCES (300 to 1100 K)
FOR THE UO_2 SAMPLE AND SIX CELLS
SURROUNDING THE DOPPLER CELL

GA Group	Lower Energy Limit (eV)	GA Cross Sections		ANL Cross Sections	
		UO_2 Sample	Six Cells	UO_2 Sample	Six Cells
12	4.09+04	0.00163	-6.0-07		
13	248+04	0.00554	-4.0-07	0.00593	
14	1.50+04	0.01122	-1.4-06	0.01148	
15	9.12+03	0.02260	-2.8-06	0.02367	
16	5.53+03	0.06195	3.4-04	0.04472	
17	3.36+03	0.09276	8.0-04	0.08075	
18	2.04+03	0.1421	0.00112	0.1322	0.00043
19	1.23+03	0.1734	0.00059	0.1731	0.00017
20	748	0.2880	0.00063	0.2790	0.0001
21	454	0.3524	0.00007	0.3593	-0.0002
22	275	0.3619	0.00060	0.3591	0.0000
23	101	0.3935	-0.00207	0.4357	-0.0019
24	37.3	0.3382	-0.00195	0.3443	-0.0018
25	13.7	0.2582	-0.00385	0.4429	-0.0096
26	5.04	0.2747	-0.00037	0.02267	-0.0014
27	1.86	0.01233	-0.00113	-0.00221	-0.00073
28	0.414	0.00728	-0.00008		

in cylindrical geometry was set up. The Doppler sample had 5 radial intervals, the capsule had 3, the remainder of the core had 15, and the radial blanket had 4. Since it was planned to have only 1 radial interval in the UO_2 sample in the R-Z diffusion theory model used in 2DB, the most appropriate shielding factors which could be obtained from DTFX would be the ratio of the average flux in the sample to the flux at the midpoint (interval 3) of the sample. For each group,

$$g = \frac{\bar{\phi}}{\phi_3} = \frac{1}{\phi_3} \quad \frac{\sum_1^5 \phi_j V_j}{\sum_1^5 V_j} \quad ,$$

where j is the interval number, from 1 to 5. The results of this calculation are given in Table 7-5. Since the shielding factors were so small, their effect on the Doppler worth should be less than 1%. Therefore, they were not used in later calculations.

7.1.1.4. Flux Calculations. Ten- and 28-group flux calculations for the phase II assembly with the Doppler sample were done in R-Z geometry using the diffusion theory code 2DB. A real flux calculation was done for the hot sample (1100 K), and an adjoint flux calculation was done for the cold sample (300 K), so that the Doppler worth could be calculated by exact-order perturbation theory using PERT. The cross sections discussed previously were used for the UO_2 sample, capsule, and surrounding six core drawers. Separate cross sections generated using GGC-5 were used for the core, radial blanket, axial blanket, and matrix regions. The Doppler extension into the core and axial blanket used cross sections generated for the core.

Atom densities unique to this Doppler calculation are given in Table 7-6. Atom densities for the Doppler extension were based on a composition (Ref. 7-8) of 16% U_3O_8, 5% nickel, 15% 304 stainless steel, and 69% void. Radial and axial direction diffusion modifiers, as calculated by the code PLADIF (Ref. 7-9), were used in 2DB and PERT. Modifiers calculated for the core were used for the Doppler sample.

TABLE 7-5
DOPPLER SAMPLE SHIELDING FACTORS CALCULATED BY DTFX

Group	Shielding Factor (g)
1	1.0030
2	1.0055
3	1.0024
4	0.9995
5	0.9993
6	0.9959
7	1.0017
8	0.9989
9	1.0012
10	0.9997

TABLE 7-6
ATOM DENSITIES FOR DOPPLER CALCULATION

Nuclide	Doppler Sample UO_2	Doppler Capsule + Cell	Six Core Cells Around Doppler Cell	Doppler Extension Into Core and Axial Blankets
O	3.71533-2		1.34423-2	7.17-03
Cr		5.526-3	2.8828-3	2.44-03
Mn		3.749-4	2.260-4	2.01-04
Fe		1.69776-2	1.5356-2	8.62-03
Ni		5.6984-3	1.3281-3	5.66-03
Mo			3.121-4	1.08-05
U-235	1.347-4		1.22-5	5.74-06
U-238	1.84412-2		5.5421-3	2.69-03
Pu-239			1.1832-3	
Pu-240			1.569-4	
Pu-241			1.63-5	
Pu-242			2.30-6	
Am-241			9.30-6	
Outer radius (cm)	1.270	3.117	8.246	3.117
Radial mesh intervals	1	1	2	2

7.1.1.5. Results of Calculation. Table 7-7 lists the K_{eff} for each of the 2DB runs. The K_{eff} convergence was inadequate for calculating the Doppler worth by eigenvalue difference, but the flux convergence was more than adequate for calculating the Doppler worth by perturbation theory. The exact-order perturbation worths (from PERT) are given in Table 7-8 for 10 and 28 groups for each region. They were calculated considering the cross section changes for all nuclides and for only U-238, as ANL did in its calculation. Obviously, considering only U-238 cross section changes introduces a negligible error in the total Doppler worth. Very good agreement was also obtained between 10- and 28-group calculations. Only about 5% of the total calculated Doppler worth (-0.599 Ih/kg) came from regions outside the UO_2 sample. The capsule and the central drawer stainless steel made a negligible contribution because of the relatively few resonances in the structural nuclides which interact with the U-238 resonances in the resolved energy range.

Table 7-9 lists the component (fission, absorption, or downscatter) of the Doppler worth for each region. The leakage component is not listed because it was extremely small, since the sample was at the center of the core. 99.9% of the UO_2 sample worth was due to changes in the absorption cross section, with the fission and downscatter components being negligibly small. The fission and downscatter components were larger for the six-drawer region because fissionable nuclides were present there. Table 7-3 lists the group dependence of the real and adjoint flux and the UO_2 sample Doppler worth. The ANL Doppler worths by group were calculated from the 28-group data in Ref. 7-10 and normalized to the ANL Doppler worth for the UO_2 sample (-0.5125 Ih/kg).

7.1.2. Studies of Heterogeneity Corrections

As a prelude to the cell calculations with TWOTRAN (Ref. 7-11) for the phase II control rod shielding factors, a number of TWOTRAN and DTFX calculations were run for comparison. Simple models of the unrodded, 1 x 3 drawer phase 2 core cell were used to ascertain the geometric mesh, scattering order, and quadrature parameters which are sufficient for providing the hetrogeneity correction factors for the cross sections.

TABLE 7-7
2DB RESULTS

Group	Temperature of Doppler Sample (K)	Type of Calculation	Convergence ($k_i - k_{i-1}$)	k_{eff}
10	1100	Real	1.6-06	0.9939632
10	300	Adjoint	2.1-06	0.9939658
28	1100	Real	6.0-05	0.9935749
28	300	Adjoint	1.7-05	0.9934995

TABLE 7-8
REGION CONTRIBUTIONS TO DOPPLER WORTH FOR 300 TO 1100 K
(Ih/kg U-238)

Region	10 Groups[a]	28 Groups[a]	28 Groups[b]
UO_2 sample	-0.5450	-0.5713	-0.5747
Doppler capsule + central drawer (stainless steel)	-0.0014	-0.0010	--
Six drawers surrounding Doppler drawer	-0.0446	-0.0272	-0.0235
Total Ih/kg U-238	-0.591	-0.599	-0.598
Calculated-to-experimental ratio	0.949	0.962	0.960

[a] Including cross section changes for all nuclides.

[b] Cross section changes for U-238 only.

TABLE 7-9
COMPONENTS OF DOPPLER WORTH

Component	10 Groups			28 Groups		
	UO_2 Sample	Capsule	Six Drawers	UO_2 Sample	Capsule	Six Drawers
Fission	-0.00065	0.0	-0.0382	-0.00048	0.0	0.0081
Absorption	-0.5438	0.0002	0.0088	-0.5706	-0.0004	-0.0301
Downscatter	-0.00051	-0.0016	-0.0152	-0.00017	-0.0006	-0.0050
Total	-0.5450	-0.0014	-0.0446	-0.5713	-0.0010	-0.0272

In the past analyses, the cell calculations for the complex plate loadings of the ZPR-9 drawers have been carried out with DTFX using P_3 anisotropic scattering, S_{16}-double P_n quadrature, and a fine spatial mesh with the fuel and fertile plates represented by six spatial intervals each. In the DTFX runs of this study, three-drawer models with three and six intervals for the fuel were used. P_1 and P_3 runs were compared, and several optional quadrature sets were used (as provided by the code and input separately). For the TWOTRAN model, a 10 x 50 mesh with 3 x 9 intervals in the fuel plates was adopted. Only P_1 cross sections were employed for TWOTRAN, but four different quadrature schemes were studied. A 2DB case was run to provide a starting flux guess for the TWOTRAN problems.

Table 7-10 compares the eigenvalues provided by the DTFX and TWOTRAN runs using the same set of group-dependent leakage parameters (DB^2 pseudo-absorber) provided uniformly throughout the cell. For a given code and model, Table 7-10 shows how the quadrature parameters influence the heterogeneity effect which results from using the output shielding factors. Comparing the results obtained from diffusion theory (with essentially a flat cell flux) and the P_3-S_{16} DP_n run of DTFX, the overall heterogeneity correction amounts to about 1.2% $\Delta k/k$. Comparison of the 70- and 104-mesh DTFX cases indicates that the coarser mesh with three intervals through the fuel plates is adequate. As expected, the double-P_n quadratures are preferable for slab geometry and give considerable differences (0.5% k for S_{16}) from the built-in DTFX quadratures.

Table 7-11 compares the groupwise flux factors provided by several different calculations for the Pu-U-Mo plate in the cell (ratio of plate-average flux to cell-average flux). The factors for the first few groups illustrate the fast-fission multiplication effect, which is the predominant source of the heterogeneity effect in these plate cells. The inadequacy of the DTFX built-in quadratures is again evident, and double-P_n sets provide asymptotic results at a relatively low order; DTFX runs (not shown) with S_{16}, S_{24}, and S_{32} double P_n sets provided essentially identical results for the same model and scattering order. For future cell calculations, S_{16} or even

TABLE 7-10
COMPARISON OF EIGENVALUES GIVEN BY CELL CALCULATIONS
FOR PHASE II CORE

Scattering Order/ Quadrature	Slab Geometry (DTFX)		XY-Geometry 2DB/TWOTRAN
	70-Mesh Intervals	104-Mesh Intervals	10 x 50 Mesh Intervals
Diffusion theory	--	--	0.98214
P_1/S_4 [a]	0.98594	--	0.98570
P_1/S_8 [a]	0.98764	--	0.98794
P_1/S_{12} [a]	--	--	0.98919
P_1/S_{16} [a]	0.98970	--	--
P_1/S_8-double P_n	--	--	0.99314 [b]
P_1/S_{12}-double P_n	0.99463	0.99468	--
P_1/S_{16}-double P_n	0.99450	0.99456	--
P_1/S_{24}-double P_n	0.99447	--	--
P_1/S_{32}-double P_n	--	0.99457	--
P_3/S_{16}-double P_n	0.99473	--	--

[a] Quadrature sets provided internally by the DTFX and TWOTRAN codes.

[b] Calculated using a double-P_n quadrature in the Z direction cosines coupled with Tschebyscheff coefficients for the XY plane.

TABLE 7-11
COMPARISON OF CELL CALCULATIONS OF HETEROGENEITY FACTORS FOR PHASE II
CORE FUEL PLATE CROSS SECTIONS (10-GROUP SET)

	Code/Problem								
	DTFX 2	DTFX 3	DTFX 5	DTFX 7	DTFX 8	DTFX 9	TWOTRAN A	TWOTRAN C	TWOTRAN D
Pu Δx mesh (cm)	0.170	0.170	0.170	0.170	0.085	0.085	0.170	0.170	0.170
Scattering order	P_1	P_1	P_1	P_3	P_1	P_1	P_1	P_1	P_1
Quadrature	S_8	S_{16}	$S_{16}DP_n$	$S_{16}DP_n$	$S_{12}DP_n$	$S_{16}DP_n$	S_4	S_{12}	S_8DP_n
Calculated k	0.9876	0.9898	0.9945	0.9947	0.9947	0.9946	0.9857	0.9892	0.9931
Flux factor 1	1.0713	1.0971	1.1556	1.1588	1.1580	1.1564	1.0742	1.1227	1.1731
Flux factor 2	1.0381	1.0500	1.0813	1.0828	1.0827	1.0817	1.0364	1.0609	1.0829
Flux factor 3	1.0152	1.0168	1.0263	1.0268	1.0266	1.0264	1.0119	1.0198	1.0283
Flux factor 4	1.0082	1.0070	1.0101	1.0102	1.0100	1.0100	1.0050	1.0080	1.0106
Flux factor 5	1.0003	0.9977	0.9974	0.9974	0.9972	0.9973	0.9983	0.9974	0.9970
Flux factor 6	0.9941	0.9940	0.9934	0.9934	0.9932	0.9932	0.9958	0.9941	0.9936
Flux factor 7	0.9891	0.9880	0.9847	0.9847	0.9843	0.9843	0.9910	0.9867	0.9841
Flux factor 8	0.9697	0.9757	0.9727	0.9727	0.9722	0.9722	0.9804	0.9749	0.9736
Flux factor 9	0.9515	0.9555	0.9505	0.9505	0.9498	0.9498	0.9627	0.9519	0.9494
Flux factor 10	0.9022	0.8901	0.8834	0.8834	0.8818	0.8818	0.9018	0.8848	0.8838

S_{12} double-P_n sets using P_1 cross sections and three intervals in the fuel plate should suffice, with little loss of accuracy for a considerable savings in running time from using a higher scattering order (P_3) or a higher spatial and angular mesh.

Comparison of the DTFX and TWOTRAN flux factors shows that the built-in TWOTRAN quadrature sets are not as good for the low orders as the special input sets. It is not clear why higher group one factors are found with the two-dimensional calculation than with the more approximate one-dimensional slab approximation in DTFX. The rodded cell (3 x 3 drawer model) calculations with TWOTRAN will use the S_8 special quadrature (DP_n-T_n) in 10 groups.

REFERENCES

7-1. Pond, R. B., "^{238}U Doppler Effect Measurement in GCFR-II," Argonne National Laboratory Report ZPR-TM-243, June 10, 1976.

7-2. Mathews, D. R., et al., "GGC-5, A Computer Program for Calculating Neutron Spectra and Group Constants," Gulf General Atomic Report GA-8871, September 27, 1971.

7-3. Stevens, C. A., and C. V. Smith, "GAROL, A Computer Program for Evaluating Resonance Absorption Including Resonance Overlap," General Dynamics, General Atomic Division Report GA-6637, August 24, 1965.

7-4. Cohen, S. C., and P. K. Koch, "GANDY, A Computer Program for the Evaluation of Effective Cross Sections in the Unresolved Resonance Region," USAEC Report GA-8003, General Dynamics, General Atomic Division, May 22, 1967.

7-5. Little, W. W., Jr., and R. W. Hardie, "2DB, A Two-Dimensional Diffusion-Burnup Code for Fast Reactor Analysis," USAEC Report BNWL-640, Battelle Northwest Laboratory Report, January 1968.

7-6. Hardie, R. W., and W. W. Little, Jr., "PERT-IV, A Two-Dimensional Perturbation Code in Fortran-IV," USAEC Report BNWL-409, Battelle Northwest Laboratory, 1967.

7-7. Mathews, D. R., General Atomic, private communication.

7-8. Pond, R. B., Argonne National Laboratory, private communication.

7-9. Tsoulfanidis, N., General Atomic, private communication.

7-10. Mathews, D., and R. Moore, General Atomic, private communication.

7-11. Lathrop, K. D., and F. W. Brinkley, "Theory and Use of the General-Geometry TWOTRAN Program," USAEC Report LA-4432, Los Alamos Scientific Laboratory, May 1970.

8. SHIELDING REQUIREMENTS (189a No. 00584)

The purposes of the shielding task are to verify the adequacy of the methods and data (physics and engineering) for the design of GCFR shields and to evaluate the effectiveness of various shield configurations. This task also coordinates and provides liaison with the analytical and experimental GCFR shielding activities at ORNL.

During the last quarter, a topical report summarizing the GCFR shielding benchmark calculations performed by GA and ORNL was completed (Ref. 8-1). New shielding cross section sets were generated which included self-shielding and new weighting function techniques. During this quarter, studies of the revised upper axial shield assembly were continued, and the DOT II (Ref. 8-2) two-dimensional neutron transport calculations were completed. The candidate grid plate shielding materials were compared, and a report summarizing the grid plate design confirmation experiment requirements was written (Ref. 8-3). A method for evaluating irradation exposure for damage to graphite was adopted, and an auxiliary computer program was written for performing sensitivity analyses of ex-core or in-core damage or detector response to the core and blanket source distribution.

8.1. REVISED UPPER AXIAL SHIELD

The initial analysis of the revised upper axial shield is presented in Ref. 8-4. During this quarter, neutron damage and gamma ray heating studies were initiated.

The revised upper plenum region is shown in Fig. 8-1. In this revised configuration, the fuel assembly locking mechanism extensions and the central plug of the reference upper shield assembly have been removed. This revised

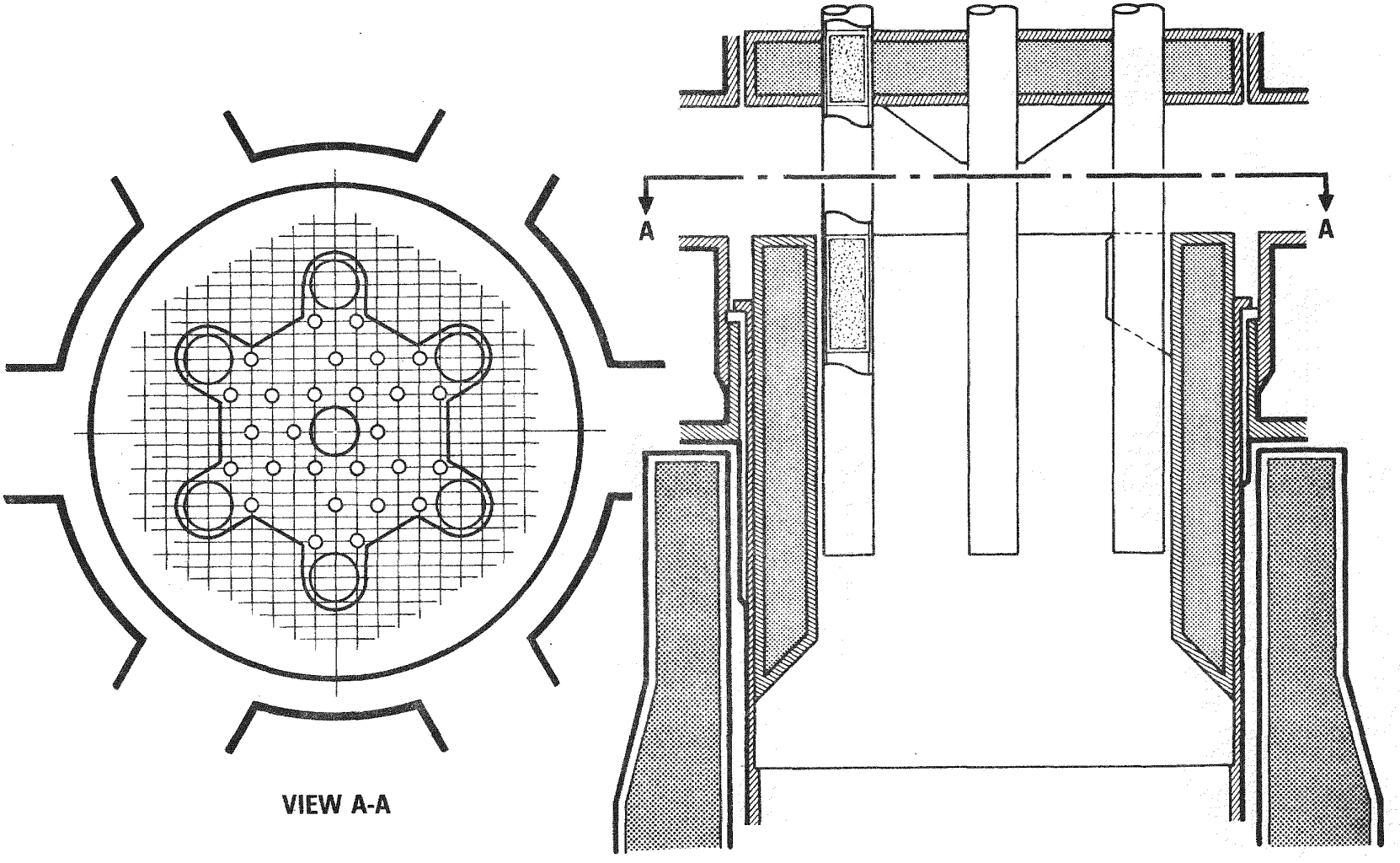

Fig. 8-1. Revised upper axial shield for 300-MW(e) GCFR

configuration provides the physical advantage of reducing the pressure drop in this region and is less difficult to analyze, but it still requires extensive two- and three-dimensional transport calculations. The shield materials shown in Fig. 8-1 are stainless steel and graphite. B_4C may be required in critical areas which may be revealed in the two-dimensional neutron transport calculations. The seven penetrations from above are access ports for the fuel locking mechanism. Each sleeve contains shielding material plugs which remain in place during reactor operation.

Given the proposed upper shield assembly shown in Fig. 8-1, the next step in the analysis is to develop a model for calculational purposes. The model initially used is shown in R-Z two-dimensional geometry in Fig. 8-2. Only the central penetration of the seven locking mechanism penetrations can be handled, and the radial shield at the lower level of the inlet ducts must be made continuous. At the level of the inlet ducts, the total area open to the six ducts is about equal to the closed area of the cavity wall between ducts. Therefore, an open configuration was used at the level of the ducts in the R-Z calculations in order to obtain the upper bound on the streaming neutron flux source for use in subsequent duct streaming calculations.

A source is needed for the neutrons which stream up through the grid plate openings into the upper cavity plenum. This source was generated from one of the grid plate shielding configurations described in Ref. 8-5. The actual configuration used was close to MOD 4 of Fig. 6 of Ref. 8-5 without the control rod guide tube. Starting with the S_8 cylindrical angular fluxes at each radial interval along the top of the grid plate, the fluxes were averaged in space at each angle for a central angular source (only the fluxes directed toward the upper axial shield are needed for the surface source). Since using the central flux as a constant surface source along the entire radius at the top of the grid plate would have been much too conservative for the upper axial shielding studies, a radial dependence of the source was approximated. This was done by scaling the variation in the neutron flux calculated by ORNL at the level of the grid plate in the two-dimensional calculations of the GCFR reactor cavity. In all, eight scale factors were used between r = 0 and r = 212.5 cm.

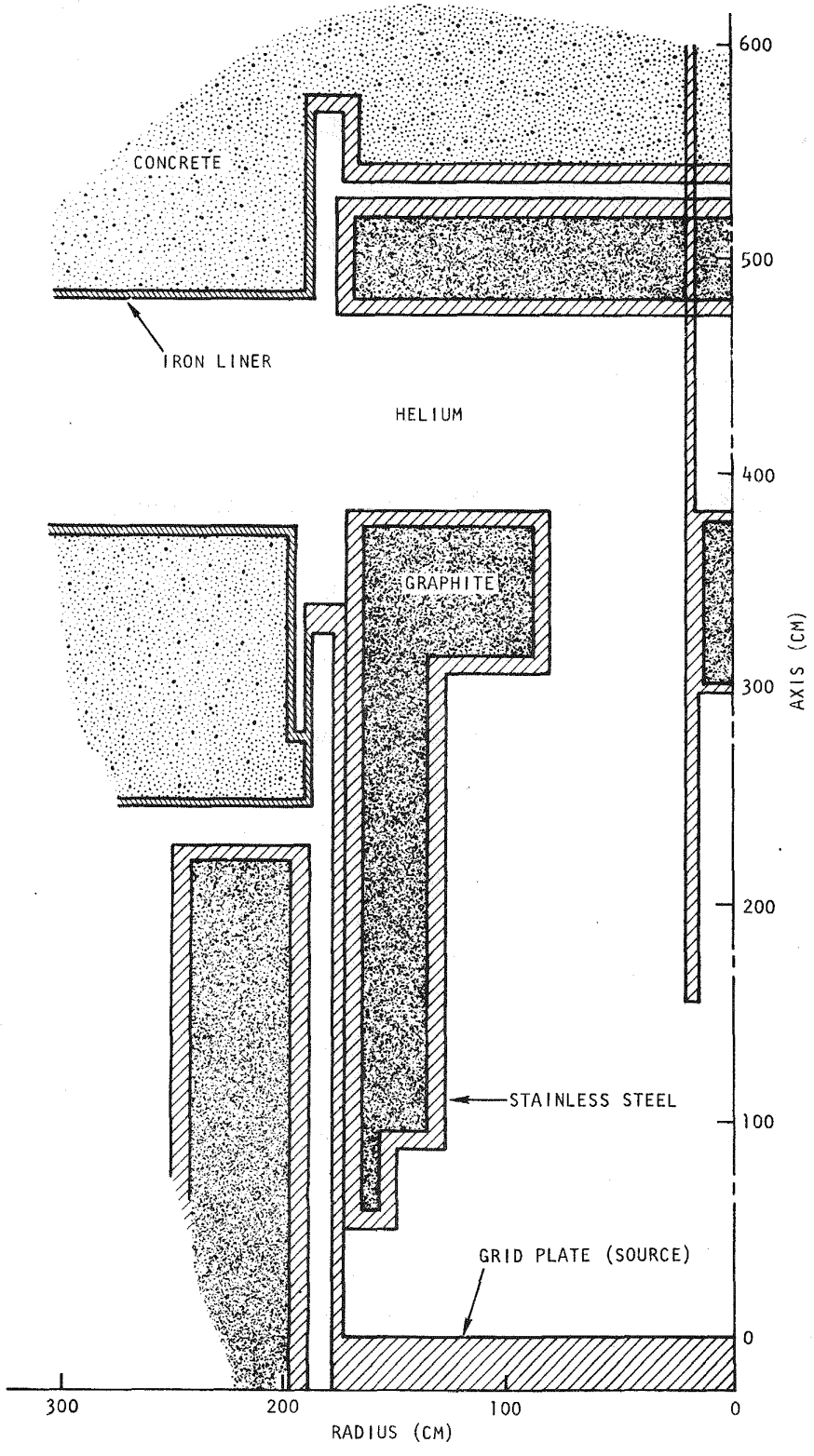

Fig. 8-2. Configuration of upper axial shield

The neutron transport calculations were performed with 10 neutron groups in symmetric S_8 angular quadrature and P_3 anisotropic scattering. The problem was calculated in two parts: part one covered the transport between z = 0 in Fig. 8-2 to z = 420 cm; part two covered the region between z ∿ 400 cm to z ∿ 520 cm. The calculations were performed with the DOT II computer program (Ref. 8-2), which was modified to utilize the extended core capability of the UNIVAC 1110.

8.1.1. Neutron Damage and Gamma Ray Heating Results

Neutron damage and gamma ray heating studies were initiated using the DOT II results described above. The preliminary neutron damage results are discussed in Section 8.1.2, and the gamma ray heating results are discussed in Section 8.1.3. The two neutron damage mechanisms considered are (1) a change in the uniform elongation (UE) and (2) the nil ductility temperature shift (NDTS).

8.1.2. Uniform Elongation and Nil Ductility Temperature Shift Damage Fluence Limits

The 5% and 10% UE and 75°C NDTS limits were calculated at several points in the region of the upper axial shield. The semiempirical method used in the damage function analysis is described in Refs. 8-6 through 8-8, and the damage functions used are given in Ref. 8-7. For the broad groups used in the present analysis, a code was written to collapse the fine groups of Ref. 8-6 with any desired weighting function. The resulting damage functions for 5% and 10% UE, nominal and upper-bound, are given in Table 8-1. The 75°C NDTS damage function and a response calculation are given in Table 8-2. The response calculation is discussed later in this section. The points at which the 5% and 10% UE nominal and upper-bound fluence limits were calculated are shown in Fig. 8-3. The least conservative point for the 10% UE upper bound is point A along the central penetrations in Fig. 8-3; the fluence limit is about seven times the fluence at this point. Consequently,

TABLE 8-1
BROAD-GROUP DAMAGE FUNCTIONS USED FOR UPPER SHIELD
UNIFORM ELONGATION CALCULATIONS

Group n	Lower Energy Bound (MeV)	Nominal Damage Function		Upper-Bound Damage Function	
		5% UE $[(n/cm^2)^{-1} \times 10^{22}]$	10% UE $[(n/cm^2)^{-1} \times 10^{22}]$	5% UE $[(n/cm^2)^{-1} \times 10^{22}]$	10% UE $[(n/cm^2)^{-1} \times 10^{22}]$
1	6.72+00[a]	3.00+00	4.05+00	9.29+00	1.26+01
2	3.01+00	2.01+00	2.71+00	4.75+00	6.43+00
3	1.00+00	1.10+00	2.49+00	1.42+00	1.92+00
4	2.47-01	5.08-01	6.92-01	6.97-01	9.50-01
5	5.25-02	2.64-01	3.60-01	5.63-01	7.68-01
6	1.17-02	1.23-01	1.70-01	3.31-01	4.54-01
7	1.23-03	2.82-02	3.89-02	1.08-01	1.48-01
8	6.14-05	2.81-03	2.79-03	1.67-02	2.16-02
9	2.38-06	6.58-04	9.14-04	1.73-02	2.41-02
10	1.00-10	2.42-03	3.37-03	7.78-02	1.07-01

[a] Read as 6.72×10^0.

TABLE 8-2
BROAD-GROUP DAMAGE FUNCTION USED FOR THE UPPER SHIELD 75°C NIL DUCTILITY TEMPERATURE SHIFT AND THE DAMAGE RESPONSE CALCULATION AT THE INLET DUCT

Group n	Lower Energy Bound (MeV)	Nominal Damage Function 75°C NDTS $[n/cm^2)^{-1}]$	Flux[a]	Response	Percent of Total Response
1	6.72+00[b]	2.14-17	5.22-06	1.12-22	0.093
2	3.01+00	1.80-17	4.75-05	8.55-22	0.147
3	1.00+00	1.27-17	5.09-04	6.44-21	1.11
4	2.47-01	5.86-18	1.72-02	1.01-19	17.4
5	5.25-02	3.80-18	6.50-02	2.47-19	42.6
6	1.17-02	9.61-19	1.02-01	9.76-20	16.8
7	1.23-03	9.13-21	1.92-01	1.76-21	0.303
8	6.14-05	1.12-20	2.47-01	2.76-21	0.476
9	2.38-06	4.16-20	2.04-01	8.48-21	1.46
10	1.00-10	6.62-19	1.72-01	1.14-19	19.6
	Total		6.85+10	5.80-19[c]	

[a] Normalized to 1.0 for the 10 groups. The total is the total scalar flux in n/cm^2-s; the total fluence is 5.19+19 n/cm^2.

[b] Read as 6.72×10^0.

[c] The total fluence limit is 1.29+20 n/cm^2.

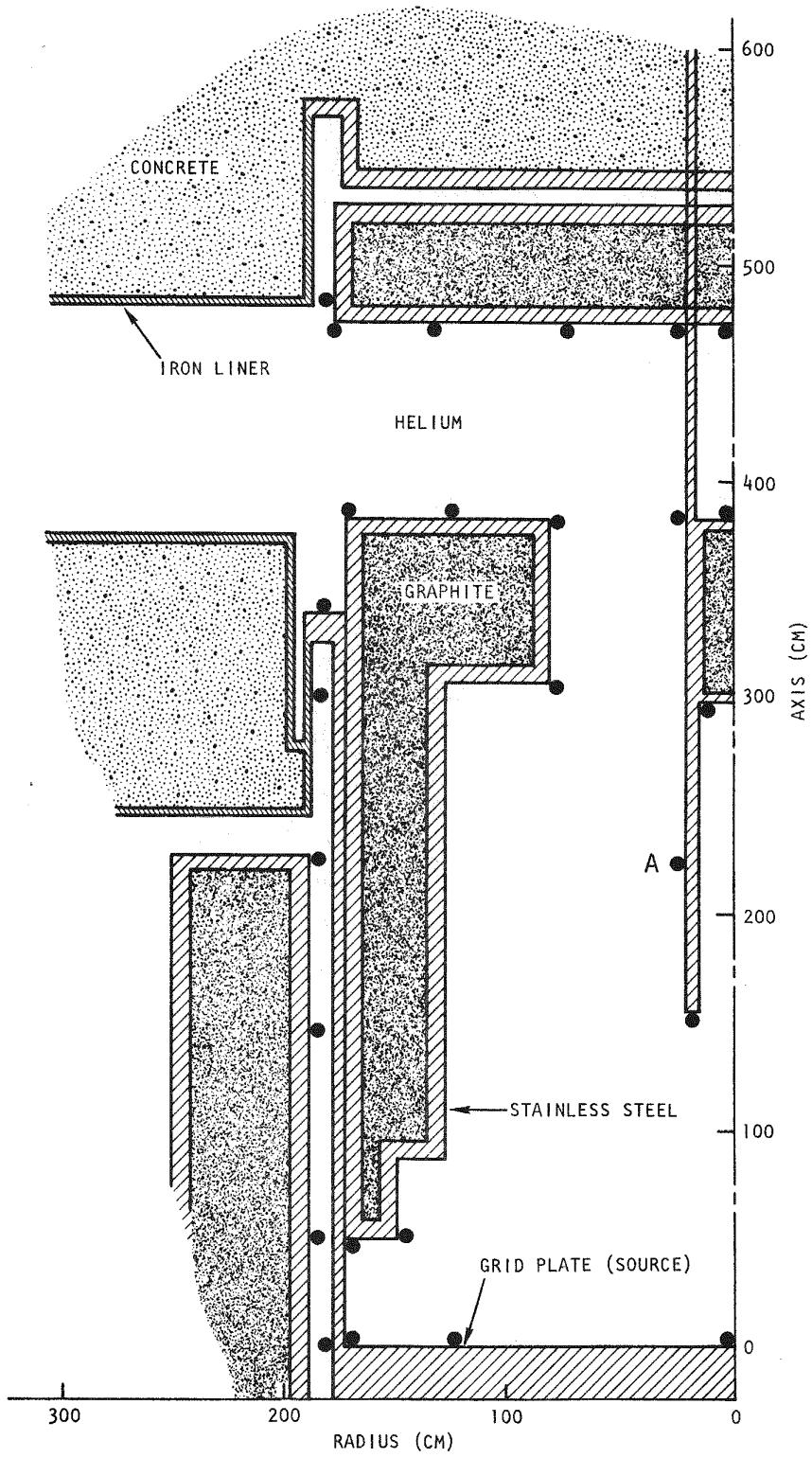

Fig. 8-3. Configuration of upper axial shield showing the points where the uniform elongation damage responses of the stainless steel were calculated

no problem is indicated for the stainless steel in this revised upper shield configuration. However, this did not turn out to be true for the NDTS damage to the liner.

The points on the liner where the 75°C NDTS responses were calculated are shown in Fig. 8-4. The least conservative point is point A at the level of the inlet duct penetration to the upper plenum. The 75°C NDTS response at this point is presented in Table 8-2, which indicates that the fluence limit is only about twice the calculated fluence. About 77% of the 75°C NDTS response is due to neutrons with energies between 12 keV and 1 MeV and about 20% to thermal neutrons.

If the above factor of two conservatism were the sole problem, then only a more accurate neutron transport calculation of the revised upper shield assembly would be indicated. However, if the 75°C NDTS damage function for A212-B and A302-B steel given in Ref. 8-6 were applied as outlined in Appendix E of Ref. 8-6, then point A would have a fluence limit about a factor of 30 less than the calculated fluence. It was necessary to multiply the damage function fluence limit by a factor of 75 to bring the results into approximate agreement with similar applications (Ref. 8-8). Further investigations revealed that a liner steel with a 75°C NDTS had not been qualified for the GCFR liner. Therefore, it is necessary to use the same steel (A537-B) which is employed in the HTGR liner, but with, at most, an 85°F (47.2°C) NDTS. Consequently, an 85°F (47.2°C) NDTS would mean that instead of a factor of two conservatism, the liner at the level of the inlet ducts would be marginal. This would require additional shielding.

8.1.3. Gamma Ray Heating

The methods used for gamma ray heating calculations are described in Refs. 8-1, 8-9, and 8-10. In order to perform an approximate gamma ray heating calculation for the initial assessment of the concrete gamma ray

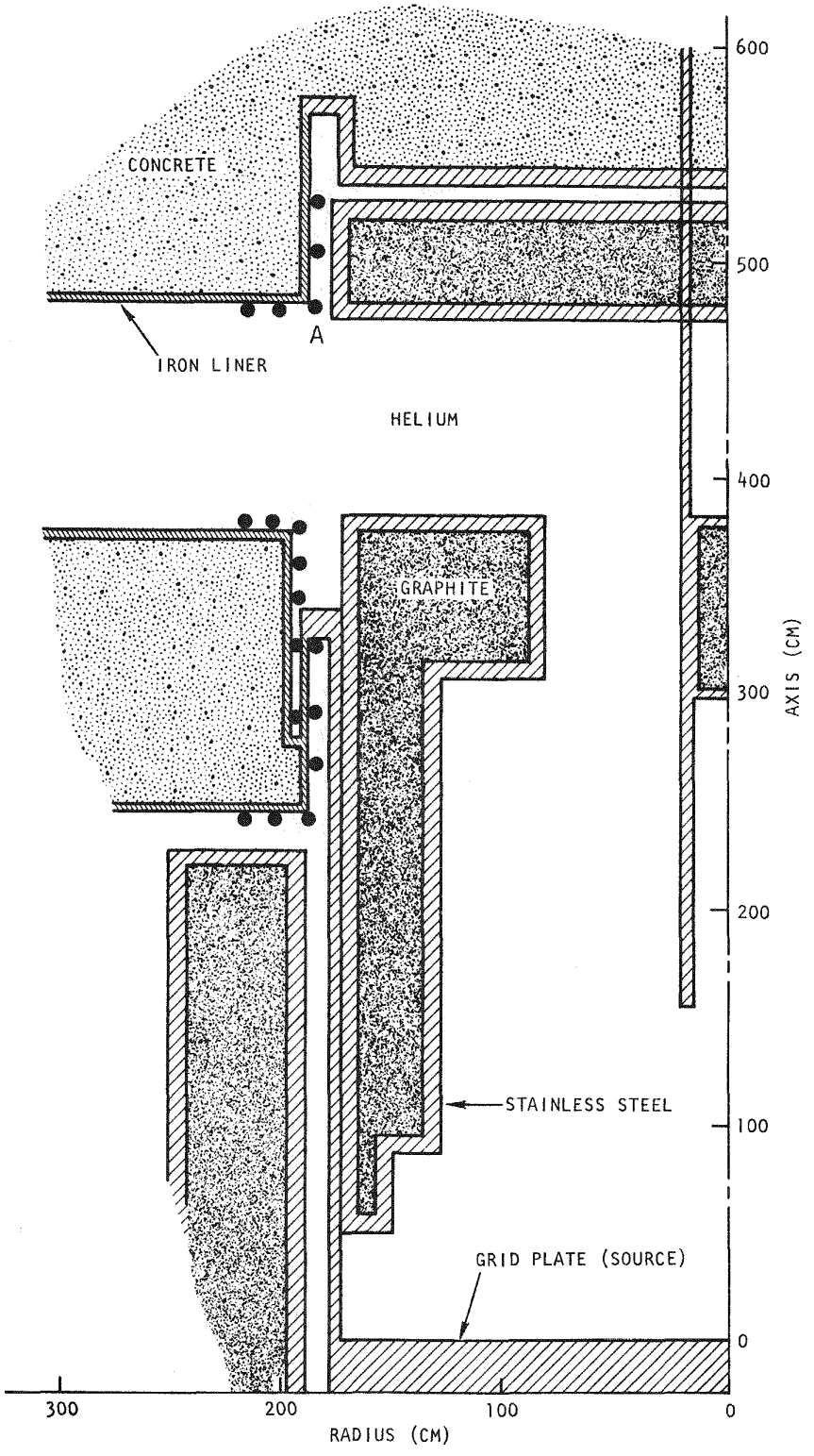

Fig. 8-4. Configuration of upper axial shield showing the points where the 75°C nil ductility temperature shift liner damage responses were calculated

heating rate, a one-dimensional calculation was carried out using the upper shield flux at point A of Fig. 8-4. This technique was successfully used in the study of the lower axial shield (Ref. 8-11).

For the present study, the 10 neutron energy groups used in the DOT II calculations were expanded to an equivalent 24-neutron-group spectrum at point A of Fig. 8-4. This spectrum was in turn used as the source for one-dimensional 1DFX (Ref. 8-12) 39-group neutron-coupled gamma ray transport calculations through a slab composed of the liner and 50 cm of concrete. The maximum calculated gamma ray heating rate in the concrete, about 0.5 MW/cm^3, occurred in the zone adjacent to the liner. This value is conservative by a factor of four and hence poses no problems for the study.

8.1.4. Conclusions

Results of the preliminary analysis of the revised upper axial shield indicate that

1. The design is conservative by a factor of about seven relative to stainless steel.

2. The high-temperature gas-cooled reactor (HTGR) liner steel (A-537B) must be used for the GCFR liner with an 85°F (47.2°C) NDTS. Near the coolant inlet ducts the liner is marginal, requiring additional shielding.

3. Gamma ray heating of the concrete does not appear to be a problem.

8.2. GRID PLATE SHIELDING

8.2.1. Candidate Shielding Material Assessment

A location proposed for irradiation of candidate grid plate shielding material specimens was evaluated to determine if the environment is sufficiently representative of GCFR conditions. The location is 390 mm below the

core bottom of an EBR-II F-5 subassembly at location 4B2, and an EBR-II residence time of 420 full-power days was assumed. It was determined that the E > 0.1 MeV fluence exposure would be about a factor of two higher for the irradiation sample than for the actual grid plate shielding.

The shielding effectiveness of the candidate materials $ZrH_{1.6}$, B_4C, and beryllium were compared, and the effectiveness of using B_4C in conjunction with the moderating materials $ZrH_{1.6}$ or beryllium was also examined. The parameter of interest is the relative damage response as a function of shield thickness, D(X), defined by the relation

$$D(X) = \frac{\sum_{g=1}^{G} \phi_g(x) G_g}{N} \quad , \tag{8-1}$$

where G_g is the average damage response function for the g^{th} broad group [the upper-bound damage function for 5% UE in stainless steel 316 irradiated at 399°C (Ref. 8-7) was used in the calculations]; $\phi_g(x)$ is the group g absolute flux at distance x through the shield; and N is an arbitrary normalization factor. Therefore, the value D(X) represents the relative effectiveness of reducing the absolute flux in addition to reducing the damaging effectiveness of the spectrum.

A series of one-dimensional calculations for the various candidate materials was carried out for D(X). The results indicate that B_4C is a somewhat more effective shielding material than beryllium or beryllium + B_4C, and $Zr_{1.6}$ or $ZrH_{1.6}$ + B_4C is more effective than any combination of B_4C and beryllium.

The two-dimensional complexity of the grid plate shielding problem precluded the extrapolation of the results to predict the effect of different shielding materials on the grid plate shielding requirements, which affects the fuel assembly length. However, as indicated in Ref. 8-5, using $ZrH_{1.6}$

in conjunction with B_4C in the grid plate shielding results in a fuel assembly which is 4 cm shorter than that obtained with B_4C shielding alone.

The primary conclusions of this study were

1. Streaming considerably reduces the relative advantages of the different materials.

2. The choice of grid plate shielding material is dictated by material performance, cost, and experience rather than shielding effectiveness.

The B_4C shielding is currently considered preferable since a great deal of applicable irradiation data is available.

8.2.2. Grid Plate Gamma Ray Heating

Detailed gamma heating distributions for the grid plate calculated at ORNL were provided to GA as input for grid plate structural performance evaluations. The calculations assumed

1. Homogenized grid plate shield region.
2. Homogenized grid plate.
3. Beginning-of-life core and blankets.

The maximum (core center line) gamma heating rates were 210 and 16.6 mW/cm^3 at the bottom and top of the grid plate, respectively.

8.2.3. Requirements for the Grid Plate Shielding Design Confirmation Experiment

During this quarter, a report summarizing experiment objectives and requirements was written (Ref. 8-13). The potential impact of rod streaming was reviewed in order to put the problem into perspective with regard to providing adequate design margins vis-a-vis performance of design confirmation

experiments. It was recommended that the conduct of the experiment be contingent upon the preanalyses providing confidence that the stated experimental objectives can be met. The results of the rod streaming experiment, completed in FY-76, together with analytical results are sufficient to conservatively bound the rod streaming effect as a factor of two or three increase in neutron-induced damage to the grid plate. An upper-bound margin of two or three is acceptable, though undesirable owing to cost implications.

8.3. EQUIVALENT FISSION FLUENCE FOR DAMAGE TO GRAPHITE FOR GCFR RADIAL SHIELD

ASTM Designation E525-74 recommends that the neutron flux and fluence for the correlation of radiation damage to graphite be reported in terms of the "equivalent fission fluence for damage in graphite," Φ_G, defined as

$$\Phi_G = \frac{\int_0^\infty \int_{t_1}^{t_2} \sigma_s(E)p(E)\phi(E,t)dtdE}{\int_0^\infty \sigma_s(E)p(E)\chi(E)dE \Big/ \int_0^\infty \chi(E)dE} , \qquad (8\text{-}2)$$

where $\phi(E,t)$ = absolute neutron flux,

$\sigma_s(E)$ = carbon scattering cross section,

$p(E)$ = atom displacement weighting function based on the Thompson and Wright model (Ref. 8-14),

$\chi(E)$ = fission spectrum,

$t_2 - t_1$ = exposure time at flux level $\phi(E,t)$.

The denominator of Eq. 8-2 is given by Ref. 8-15 as 720×10^{-24} displacements per atom (dpa) per unit fluence in the fission spectrum χ. The numerator is the dpa in the fluence $\phi x(t_2 - t_1)$. Therefore, Φ_G physically represents the fluence in the fission spectrum χ which results in the same dpa as the spectrum and fluence of interest.

Equation 8-2 was evaluated for graphite in the 300-Mw(e) demonstration plant radial shield at the level of the core midplane; the largest exposure to shielding graphite occurs near the inner surface of the inner radial shield at the core midplane level. Fine-group graphite atom displacement cross sections (i.e., $\sigma_s p$ in Eq. 8-2) based on the Ref. 8-14 weighting function p were collapsed to nine broad groups above 2.38 eV using a GGC-5 (Ref. 8-17) generated spectrum for the two-row thorium blanket. The neutron flux was obtained from an existing 1DFX (Ref. 8-18) calculation which assumed a beginning-of-life, three-enrichment-zone core and a two-region thorium blanket (Ref. 8-16). Each radial blanket region corresponded to a blanket row and included the U-233 density averaged over equilibrium cycles 3 and 4.

Table 8-3 presents the details fo the dpa and Φ_G calculation for graphite located at the innermost region of the inner radial shield. Note that the exposure over 30 yr of plant operation at 0.8 capacity results in 50.2 dpa, and the 2.0×10^{23} total fluence exposure corresponds to a 6.97×10^{22} fluence exposure in the fission spectrum χ (Fig. 8-5 is a plot of Φ_G through a radial traverse of the radial shield at the core midplane level). This exposure either exceeds the exposure for which graphite irradiation data are available or is in an exposure range in which irradiation-induced graphite expansion is large. Therefore, it is concluded that inner radial shield graphite must be designed for replacement.

8.4. SOURCE SENSITIVITY ANALYSIS PROGRAM

An auxiliary computer program, Source Sensitivity (SOS), was written to perform analyses of the sensitivity of ex-core or in-core detector response to the core and blanket source distribution. The relevant equation (Ref. 8-16) is

$$\left\langle Q, \Phi^{+} \right\rangle = \left\langle \sigma_d, \Phi \right\rangle \quad , \tag{8-3}$$

where Q = distributed fission source from a forward eigenvalue calculation,

Φ = forward flux from the forward calculation,

TABLE 8-3
CALCULATION OF DISPLACEMENTS PER ATOM AND EQUIVALENT FISSION FLUENCE FOR DAMAGE TO GRAPHITE[a] LOCATED AT THE INNERMOST SURFACE OF THE INNER RADIAL SHIELD

Group g	Lower Energy of Group g (eV)	Fluence (30 yr at 0.8 capacity) (n/cm^2)	Displacement Cross Section $(\sigma_{sp})_g$ (barns)	Displacements Per Atom
1	6.72+06	1.43+20	604	0.09
2	3.01+06	1.39+21	811	1.13
3	1.00+06	7.08+21	708	5.01
4	2.47+05	2.86+22	702	20.1
5	5.25+04	4.95+22	382	18.9
6	1.17+04	4.16+22	102	4.25
7	1.23+03	3.64+22	20.4	0.74
8	6.14+01	1.77+22	3.6	0.06
9	2.38+00	8.26+21	0.07	∿0
10	0.00+00	9.32+21	∿0	∿0
Total		2.00+23		50.2

[a] Φ_G = 50.2 dpa/720 x 10^{-24} dpa/n-cm^2 = 6.97 x 10^{22} n/cm^2.

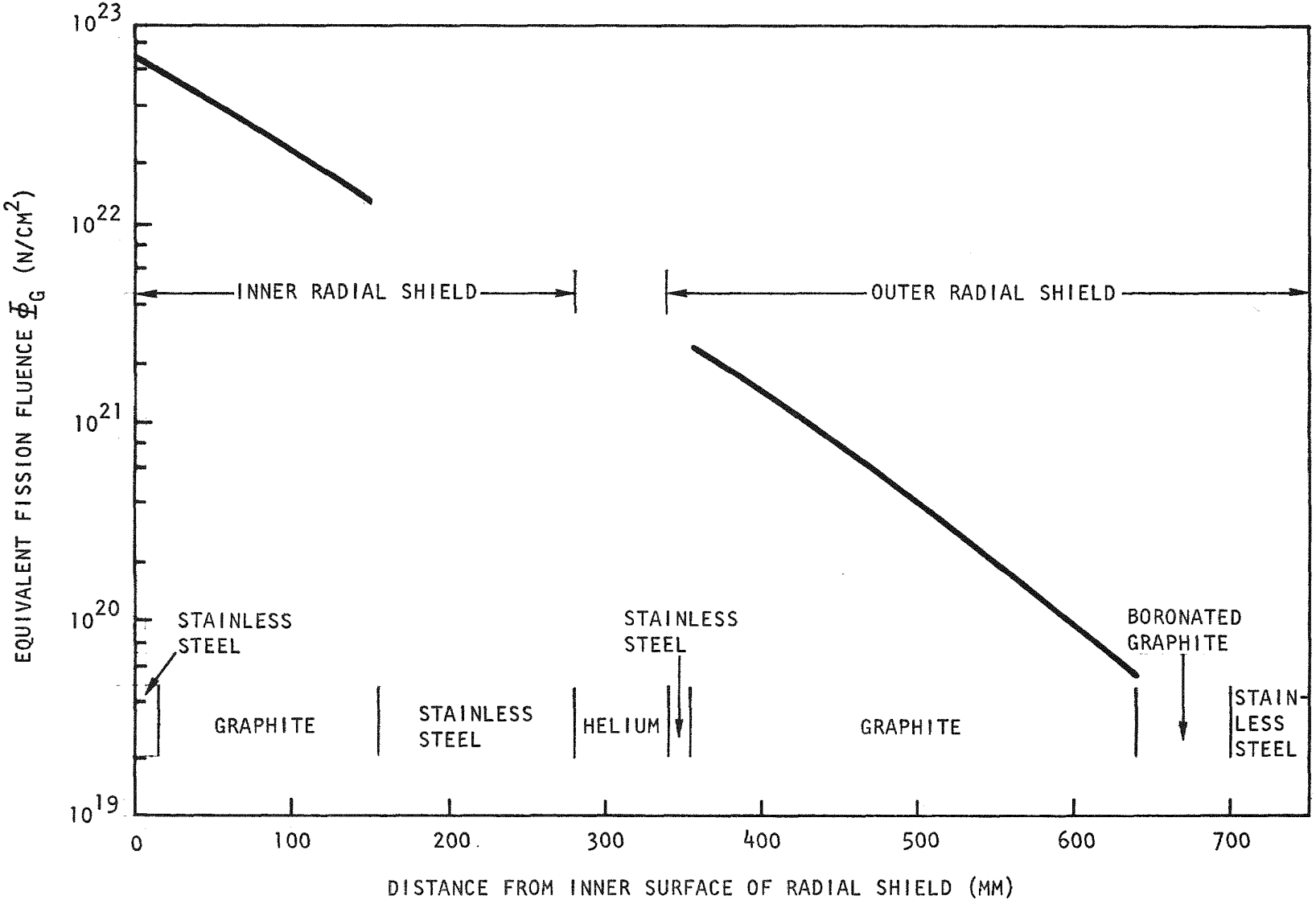

Fig. 8-5. Equivalent fission fluence for damage to graphite through a boronated 300-MW(e) GCFR radial shield

σ_d = response function of interest,

Φ^+ = adjoint flux for the adjoint source σ_d,

and $\langle\ \rangle$ designates integration over all phase space. The SOS program solves Eq. 8-3 for the contribution to the detector response due to fission in interval i, R_i. For an isotropic fission source, R_i is evaluated as

$$R_i = \sum_{g=1}^{G} \left\{ \chi_g \, U^+_{g,i} V_i \left[\sum_{g=1}^{G} (\nu\Sigma_f)_{g,i} U_{g,i} \right] \right\} , \qquad (8\text{-}4)$$

where χ = fission spectrum,

U = scalar forward flux,

U^+ = scalar adjoint flux,

V = interval volume,

ν = neutrons per fission,

Σ_f = fission cross section,

g = group mesh point,

i = space interval mesh point.

The response function σ_d is completely arbitrary. The SOS code will be used to determine (1) the change of flux monitor (fission chambers located in the PCRV) signal due to changes in core and blanket power distribution and (2) the sensitivity of grid plate damage to the core and blanket axial source distribution; the grid plate damage is sensitive to the blanket power distribution, which changes significantly during burnup owing to the buildup of fissile material. Accurate calculation of grid plate damage requires that the axial blanket plutonium distribution be defined reasonably well.

REFERENCES

8-1. Rouse, C. A., D. R. Mathews, and P. K. Koch, "Gas-Cooled Fast Breeder Reactor Shielding Benchmark Calculation," ERDA Report GA-A14236, General Atomic, January 1977.

8-2. Mynatt, F. R., "DOT Two-Dimensional Discrete Ordinates Transport Code," Oak Ridge National Laboratory Report ORNL-CCC-89, K1694, October 1969.

8-3. Broido, J. H., "Grid Plate Shielding Design Configuration Experiment," General Atomic, unpublished data.

8-4. "Gas-Cooled Fast Breeder Reactor Quarterly Progress Report for the Period May 1, 1976 Through July 31, 1976," ERDA Report GA-A13975, General Atomic, August 31, 1976.

8-5. Perkins, R. G., and R. J. Cerbone, "Physics Design of the 300-MW(e) Gas-Cooled Fast Breeder Reactor Demonstration Plant Grid Plate Shielding," ERDA Report GA-A14124, General Atomic, September 1976.

8-6. McElroy, W. N., R. L. Simons, and D. G. Doran, "Damage Function Analysis," USAEC Report HEDL-SA-755, Hanford Engineering Development Laboratory, October 21, 1974.

8-7. Nuclear Systems Materials Handbook, v. I, II, Hanford Engineering Development Laboratory (TID-26666).

8-8. McElroy, W. N., R. E. Dahl, Jr., and C. Z. Serpan, Jr., "Damage Functions and Data Correlation," Nucl. Appl. Technol. 7, 561 (1969).

8-9. Nagel, M., and R. J. Cerbone, "Neutron-Coupled Gamma-Ray Cross Section Requirements for Gas-Cooled Fast Breeder Reactors," USAEC Report GA-A13329, General Atomic, March 12, 1975.

8-10. Cerbone, R. J., et al., "Shielding Analysis of the 300-MW(e) GCFR, A Topical Report Summarizing the Shielding Physics Analysis Performed During Fiscal Year 1975," ERDA Report GA-A13558, General Atomic, August 12, 1975.

8-11. "Gas-Cooled Fast Breeder Reactor Quarterly Progress Report for the Period February 1, 1976 Through April 30, 1976," ERDA Report GA-A13868, General Atomic, May 31, 1976.

8-12. Archibald, R., K. D. Lathrop, and D. Mathews, "1DFX - A Revised Version of the 1DF (DTF-IV) SN Transport Theory Code," Gulf General Atomic Report Gulf-GA-B10820, September 27, 1971.

8-13. Perkins, R. G., and R. J. Cerbone, "Grid Plate Shielding Design Confirmation Experiment - 'Grid Plate Shielding Design Confirmation Experiment Test Requirements,'" General Atomic, unpublished data.

8-14. Thompson, M. W., and S. B. Wright, "A New Damage Function for Predicting the Effect of Reactor Irradiation on Graphite in Different Neutron Spectra," J. Nucl. Mater. 16 146-154 (1965).

8-15. Genthon, J. P., "Les Travaux Du Sous-Groupe 'Dommages D'Irradiation Du Groupe De Travail D'Euratom Sur La Dosimetrie En Réacteur De Recherche," Nucl. Eng. Design 33 7-9 (1975).

8-16. Bell, G. I., and S. Glasstone, Nuclear Reactor Theory, Van Nostrand Reinhold, New York, 1970.

8-17. Mathews, D. R., et al., "GGC-5, A Computer Program For Calculating Neutron Spectra and Group Constants," Gulf General Atomic Report GA-8871, September 27, 1971.

8-18. "Gas-Cooled Fast Breeder Reactor Quarterly Progress Report for the Period August 1, 1975 Through October 31, 1975," ERDA Report GA-A13766, General Atomic, January 5, 1976.

9. SYSTEMS ENGINEERING (189a No. 00585)

9.1. CORE THERMAL-HYDRAULIC PERFORMANCE

9.1.1. Power Distribution

The GACOOL program (Ref. 9-1) was modified to accept a chopped cosine power distribution in the active core region, a parabolic power distribution in the axial blanket, and a nonsymmetric power distribution function in the radial blanket. This work was performed in accordance with the GACOOL/nuclear analysis interface subtask and provides a new dimension to core thermal-hydraulic analysis performed with GACOOL without losing the original capability of the program to accept general numerical power distribution functions for the core. This work was necessary to establish a common basis for the GACOOL/CALIOP (Ref. 9-2) comparison study.

9.1.2. GACOOL/CALIOP Comparison Study

In order to check the analytical approach used in GACOOL and gain confidence in its operation, the GACOOL and CALIOP programs were compared. Certain inconsistencies in the results of the two computer programs became apparent during the early stages of the study, and an effort to resolve these inconsistencies resulted in a major overhaul of GACOOL, with the elimination and/or addition of several subroutines. Although the general approach of the two codes to core thermal-hydraulic analysis is different, the calculation of pressure drop is identical. In calculating pressure drop and midwall cladding temperatures, GACOOL proceeds along the fuel rod, starting from the top end of the upper axial blanket and using average gas properties for elemental segments along the fuel rod.

Comparison of the results obtained by the two programs for the most recent GCFR core design shows excellent agreement of the calculated pressure drops. The flow rates and temperature rise through each channel, however, are somewhat different; GACOOL predicts a slightly smaller (about 1%) flow rate to achieve the same midwall cladding temperature, which in turn results in an approximately 1% higher temperature rise across the channels. The effect of this difference on overall reactor (core plus radial blankets) performance is a core outlet temperature which is a few degrees higher than that predicted by CALIOP. The cause of this rather small difference can be traced to the use by CALIOP of a closed-form approach for evaluating midwall cladding temperature. The COBRA program (Ref. 9-3) was also used as a second source of comparison for evaluating the accuracy of GACOOL, and it was found that the pressure drop and heat transfer analysis results of COBRA agree with the GACOOL results, confirming the consistency of the analytical approach used in GACOOL.

9.1.3. GACOOL/CALIOP Interface

Because GACOOL is a core performance program, it can be used as a realistic core model for a wide range of operating conditions for the life of the GCFR core. GACOOL is relatively fast and requires only a modest computer storage location, but it is dependent on CALIOP for detailed core geometric information. Transfer of these data from CALIOP to GACOOL required a long and tedious effort and familiarity with both programs. In order to minimize this effort, a new capability was added to CALIOP for punching data cards for GACOOL use. This reduced the time lag between obtaining a core design from CALIOP and starting GACOOL to only a few minutes compared with several hours. This change was also important in that new changes in CALIOP would not affect GACOOL. This was made possible by transferring major geometric data such as hydraulic diameter and free flow area instead of recalculating these parameters in GACOOL. A large number of repetitive core geometry calculations within GACOOL have also been eliminated.

9.1.4. GACOOL/Nuclear Analysis Interface

The general method of providing core physics data has been investigated. This method affects GACOOL since it provides three-dimensional time-dependent power distribution data. This nuclear analysis data bank is ideal for GACOOL use.

9.1.5. Reactor Outlet Temperature Increase by Axial Enrichment Zoning

Axial enrichment zoning has been proposed to increase the reactor outlet temperature for a given maximum midcladding temperature. The power distribution for a two-zone axial enrichment scheme was calculated assuming that the ratio of enrichments for the two zones is 1.7 (Fig. 9-1). The dotted curve in Fig. 9-1 shows the power distribution calculated by assuming an unchanged neutron flux distribution; this is a reasonable approximation to the correct distribution. As a first approximation, the average enrichment required for the axially varied loading is the same as that for a constant loading.

The CALIOP program was adapted to study three-zone axial enrichment patterns assuming that the neutron flux distribution is the same as that for constant axial loading. For a given set of enrichment ratios (maximum to minimum and intermediate to minimum), the code selects the axial zone lengths so that the maximum midcladding temperature is reached in each zone. A separate program was written to search for (1) the optimum intermediate to minimum concentration for a given maximum to minimum and (2) the overall optimum combination. The correct maximum rod rating and overall maximum to average fuel power are also calculated.

The overall optimum three-zone enrichment pattern results in enrichments in the ratio of 2.5/1.5/1.0. The resulting temperature increase of 19°C is 59% of the maximum attainable by a loading giving a constant fuel surface temperature. This case resulted in a large increase in fuel maximum to average flux (from 1.412 to 2.140), which would result in a proportionate decrease in fuel lifetime for a given limiting irradiation.

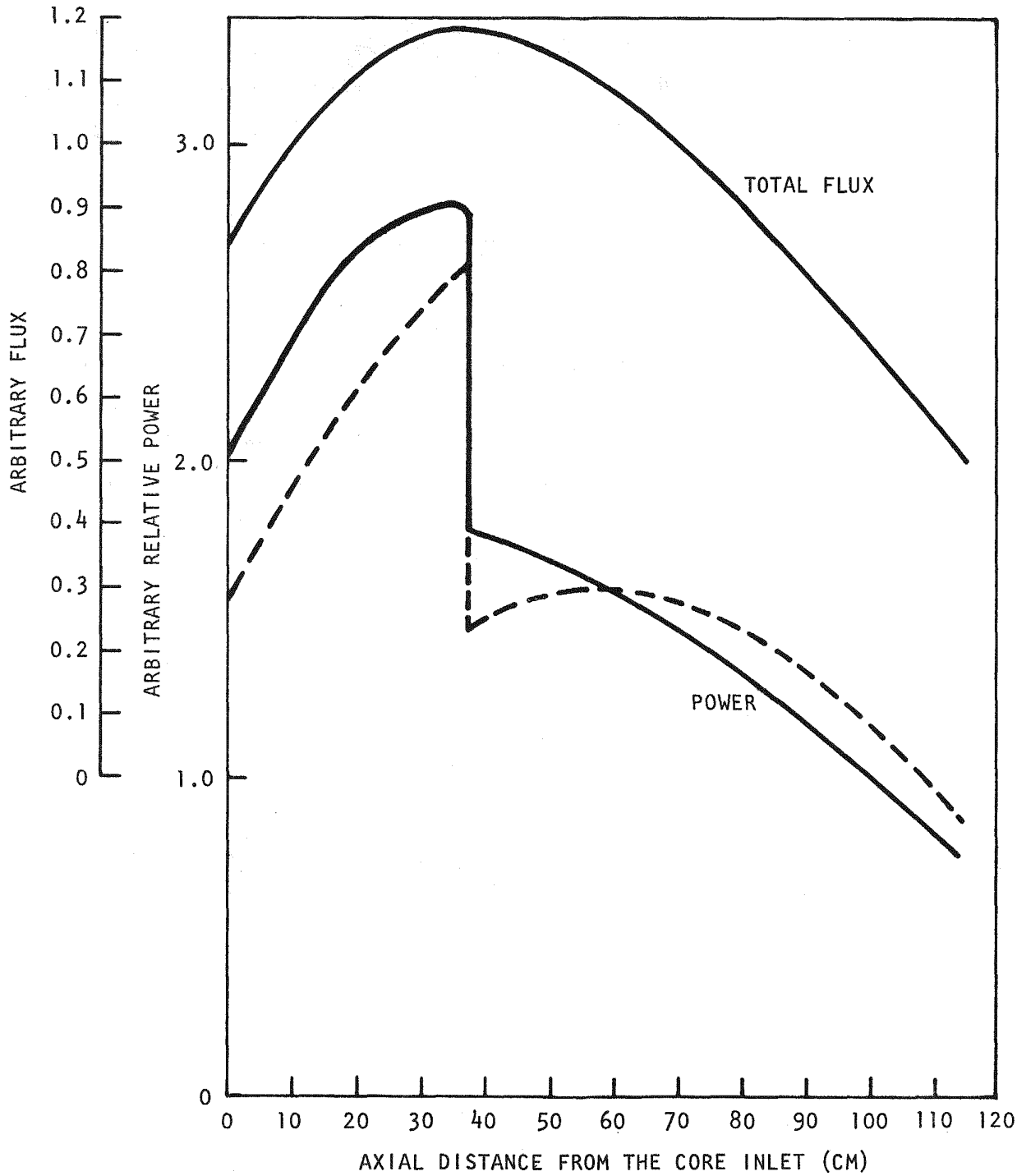

Fig. 9-1. 300-MW(e) revised low-ΔP core with axial power shaping

Figure 9-2 shows temperature increase as a function of maximum to minimum enrichment for three-zone patterns in which the intermediate enrichment is optimized. It is indicated that a considerable fraction of the maximum temperature increase can be attained with lower enrichment ratios and lower fuel maximum to average flux ratios. For example, at a maximum to minimum enrichment ratio of 1.5 and a flux maximum to average of 1.68, the temperature increase is 14.4°C, or 74% of the maximum attainable by three-zone axial enrichment.

9.2. SYSTEMS INTEGRATION

During this quarter, work on the systems integration subtask concentrated on the preparation of a GCFR system integration plan. This plan is scheduled to be completed and submitted to ERDA on September 30, 1977. A partial draft of the plan has been prepared for preliminary review and comment, and the proposed contents of the plan are as follows:

1. Introduction
2. Summary
3. System Integration Objectives
4. System Integration Approach
   - 4.1. Organizational Approach
   - 4.2. System Requirements Identification
   - 4.3. Design Integration and Control
   - 4.4. Verification of Design Adequacy
   - 4.5. Test Programs Integration
5. Key Issue Resolution

9.3. DOCUMENTATION MANAGEMENT

The purpose of this subtask is to develop and implement effective documentation management. In the course of this activity, general design descriptions of NSS systems and the overall demonstration plant will be prepared and collected in a design book.

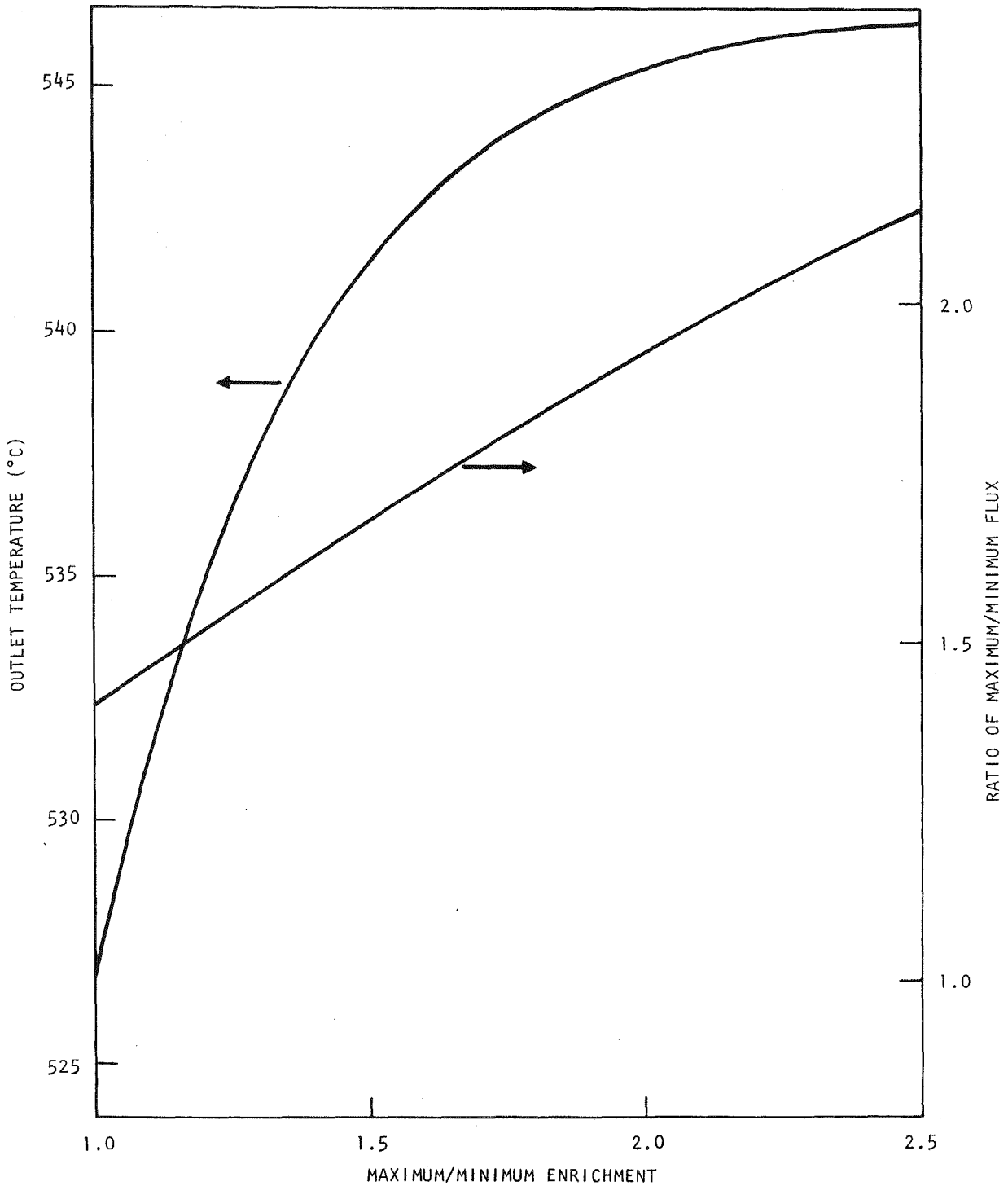

Fig. 9-2. Outlet temperature vs degree of axial enrichment zoning

During this quarter, a presentation on documentation management and configuration control was made to ERDA representatives. The purpose of the presentation was to review the plans being developed for the Program Definition and Licensing Phase (PDLP). The following items were discussed:

1. Documentation management (design book, document tree, document procedures).

2. Configuration control (identification, description, change control, traceability).

An updated version (issue B) of the engineering document tree for the PDLP was finalized and distributed. This updated version was reviewed by engineering organizations which did not participate in the original issue of the document tree. In addition, by mutual agreement between GA and ERDA, submittal of the schedule for the documents on the engineering document tree was deferred pending clarification of the overall schedule for the PDLP. The impact of this deferment was judged to be minimal inasmuch as approximately 50% of the documents on the tree (the design criteria) were previously scheduled during the conceptual design phase. An outline of the design book was prepared and distributed. This outline describes the purpose, contents, responsibilities, and format of the book and its relationship to other documents. Representative design data were selected (primarily from Ref. 9-4) for the purpose of assembling a preliminary draft of the design book.

During the next quarter, work will continue on the engineering document tree and the design book. The document tree activity will mostly be routine maintenance, such as additions, deletions, title changes, etc. Work on the design book will include the development of suitable formats and a detailed table of contents.

REFERENCES

9-1. Medwid, W. A., "GACOOL -- A Computer Program for Gas-Cooled Fast Breeder Reactor Core Thermal-Hydraulic Performance Analysis," General Atomic, unpublished data.

9-2. Thompson, W. I., "CALIOP -- A Multichannel Design Code for Gas-Cooled Fast Reactors," General Atomic, unpublished data.

9-3. Rowe, D. S., "COBRA IIIc: A Digital Computer Program for Steady State and Transient Thermal-Hydraulic Analysis of Rod Bundle Nuclear Fuel Elements, "Battelle Northwest Laboratory Report BNWL-1695, March 1973.

9-4. "300-MW(e) Gas-Cooled Fast Breeder Reactor Demonstration Plant," General Atomic Report GA-A13045, July 15, 1974.

10. COMPONENT DEVELOPMENT (189a No. 00586)

10.1. REACTOR VESSEL

The scope of this subtask is to ensure that the design of the PCRV and related components which contribute to the integrity of the pressure boundary is satisfactory and to test critical component configurations to make certain that they attain the design objectives. This subtask will demonstrate by analyses and tests that the PCRV and its penetrations and closures meet the design criteria, and it will also provide assurance that (1) the design of the thermal barrier satisfactorily protects the liner and PCRV from the effects of high temperatures and (2) the flow restrictors for the large penetrations can be developed to limit the flow of helium from the primary coolant systems to acceptable levels in the event of structural failure of a penetration or closure component.

Work accomplished during the previous quarter consisted of preparing various PCRV configurations for review. One set of configurations was prepared for a PCRV with a steam generator and a helium circulator in the same cavity and another for a PCRV with a steam generator and a reverse flow helium circulator in separate cavities. The latter configuration caused the PCRV to have a larger diameter and, thus, increased costs. Therefore, it was decided to use the first configuration and revise it to include a reverse flow circulator. A new set of PCRV configurations showing two arrangements for introducing the primary coolant into the circulator inlet plenum was prepared. The first arrangement introduced the coolant via a duct through the center of the steam generator, and the second used a bypass duct from the steam generator. The latter configuration was chosen as the basis for a study of steam generators with and without resuperheat. The feasibility of fabricating and constructing [in accordance with the ASME Boiler and Pressure Vessel Code (Ref. 10-1)] the prototype configuration for the reactor cavity closure shown in Fig. 10-1 was studied and confirmed.

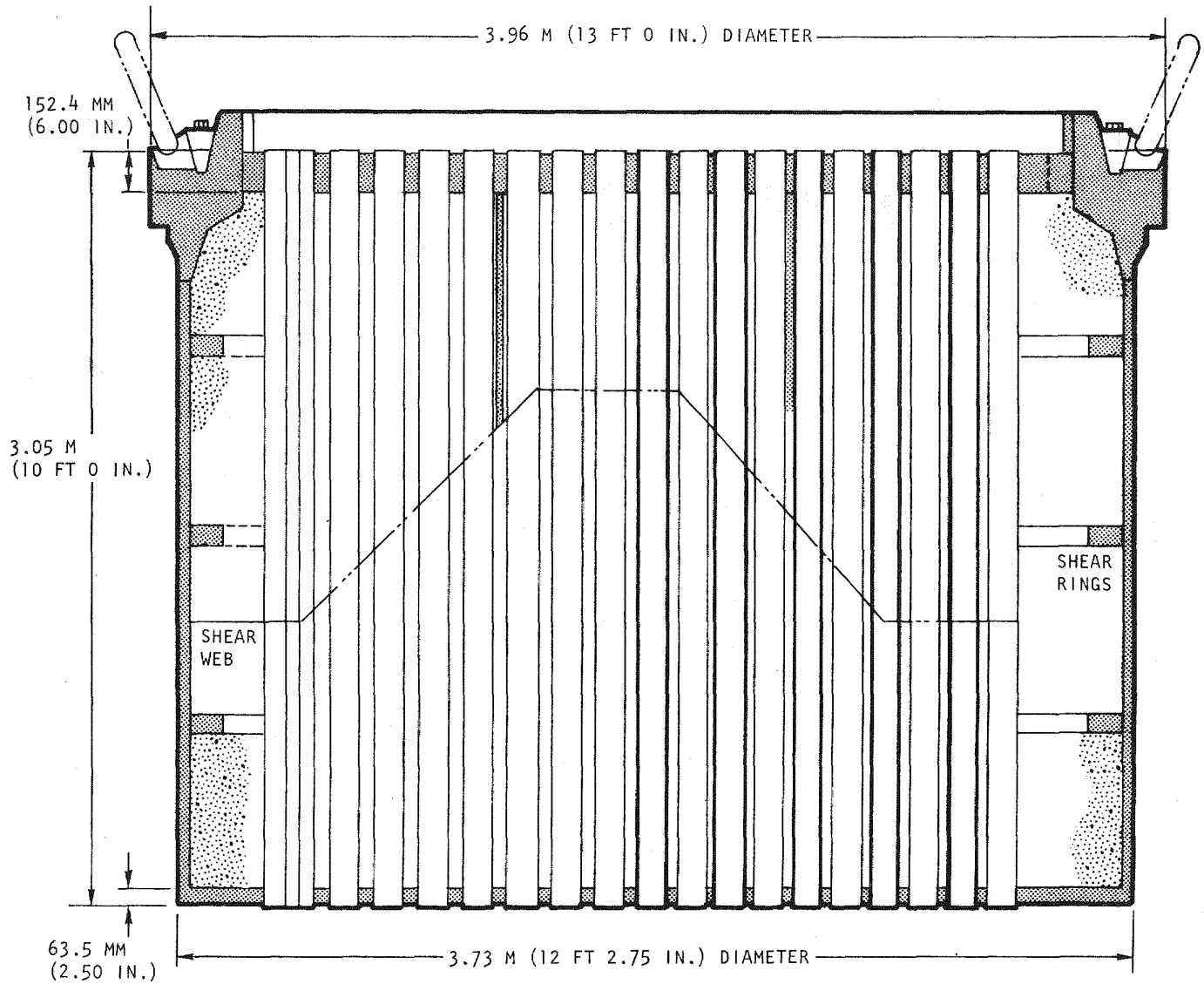

Fig. 10-1. Prototype configuration of reactor cavity closure

Representatives of GA and ORNL met during the last quarter to coordinate the closure testing program being conducted by ORNL, and drawings for the 1/15-scale model of the reactor cavity closure, shown in Fig. 10-1, were presented by ORNL for review. The question of whether the testing fixture for the 1/4-scale model should be a steel forging or a prestressed concrete vessel was discussed, and agreements were reached on providing information for the 1/4-scale model testing, closure holddown system, review of the drawings for the 1/15-scale model of the reactor cavity closure, and instrumentation for testing of the 1/15-scale model of the reactor core cavity closure. General Atomic was informed by ORNL that the microconcrete had been cast for the 1/15-scale model of the steam generator cavity closure (Fig. 10-2) and structural testing would start as soon as the concrete was cured. A logic diagram, work breakdown structure, and schedule for thermal barrier activities were drafted, design efforts continued in support of PCRV configuration studies, and the thermal barrier design criterion was drafted.

During this quarter, a cost comparison study was conducted for two PCRV configurations having steam generators with and without resuperheaters. The PCRV configurations were based on having the centrally supported steam generators in the same cavity as the reverse flow helium circulators and introducing the primary coolant into the circulator inlet plenum by a bypass duct through the PCRV concrete leading from the bottom of the steam generator. The first PCRV configuration (C-2) contains a steam generator without resuperheater (Fig. 10-3); the second configuration (C-3) contains a steam generator with resuperheater (Fig. 10-4). Sizing calculations were made for each configuration to determine the PCRV diameters, and calculations were made to determine the quantity of the tendons required. Views have been made to establish the routing of the ducts and the placement of the tendons, and the task of establishing the differential cost between the two PCRV designs has been initiated. To assist in this effort, a list of materials was prepared for each design, giving the quantities required for each PCRV component, such as concrete, rebar, tendons, liners, thermal barriers, and prestressing channels.

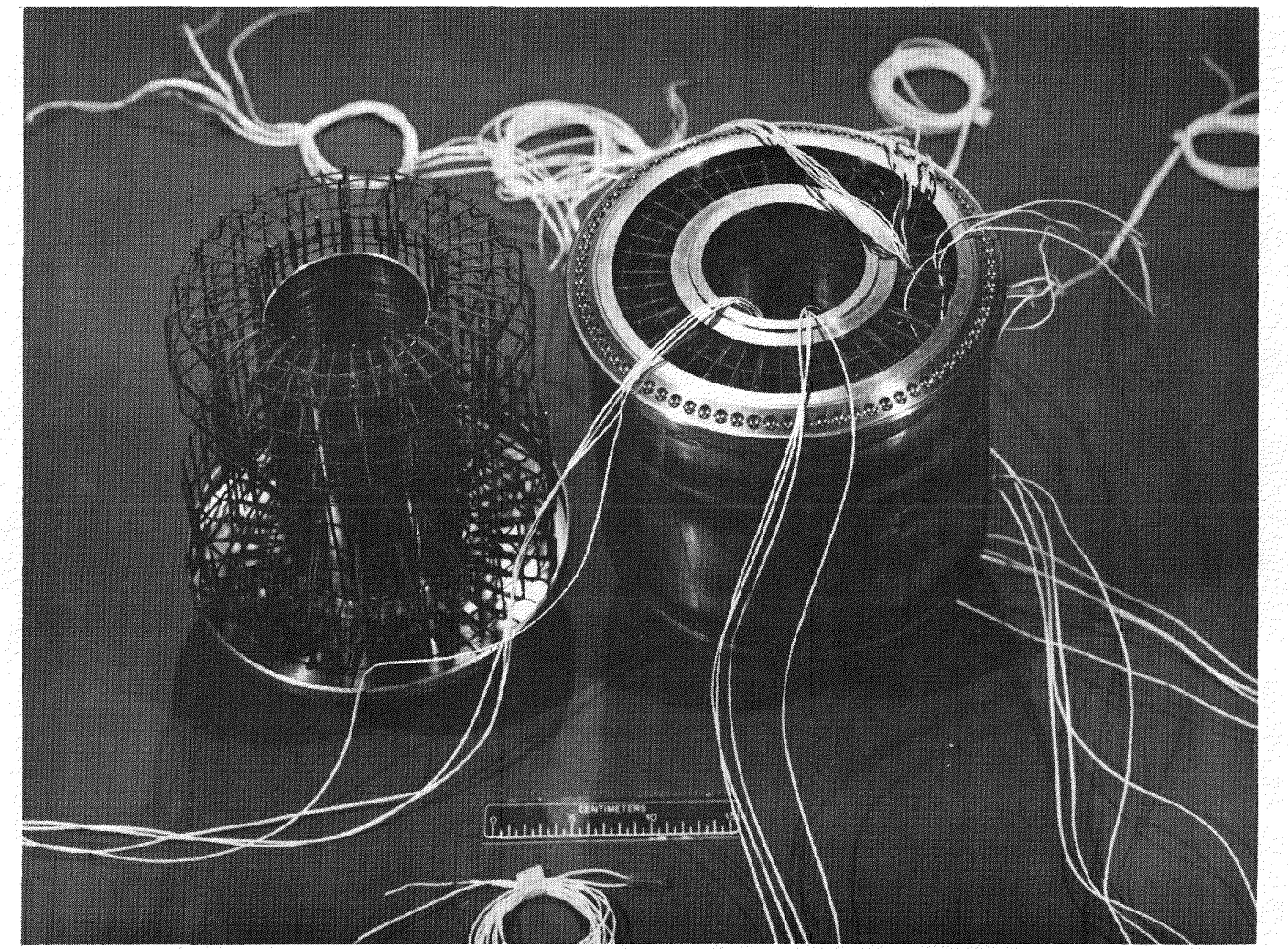

Fig. 10-2. 1/15-scale fabricated model of steam generator closure

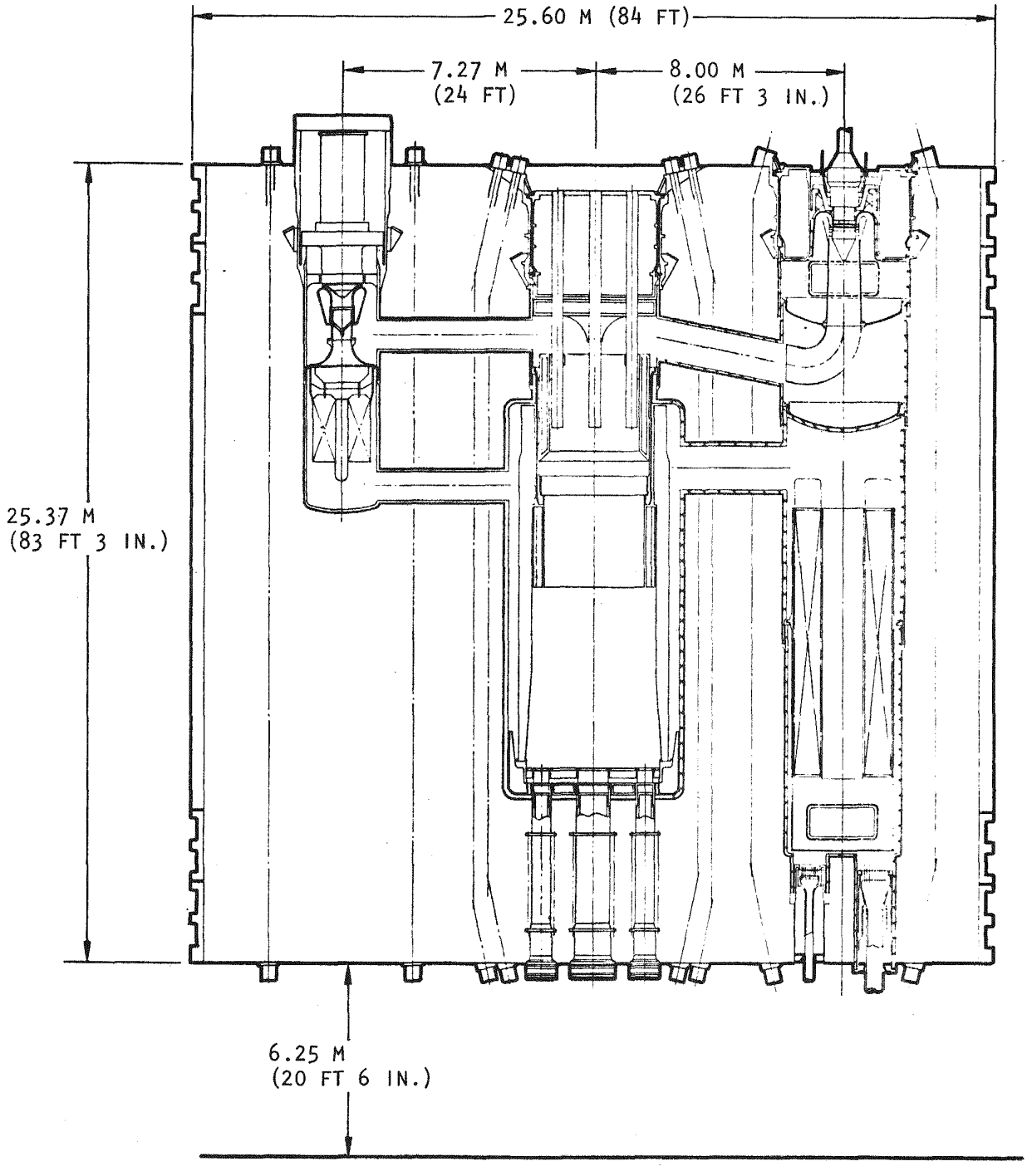

Fig. 10-3. PCRV configuration C-2 (with nonresuperheat steam generator)

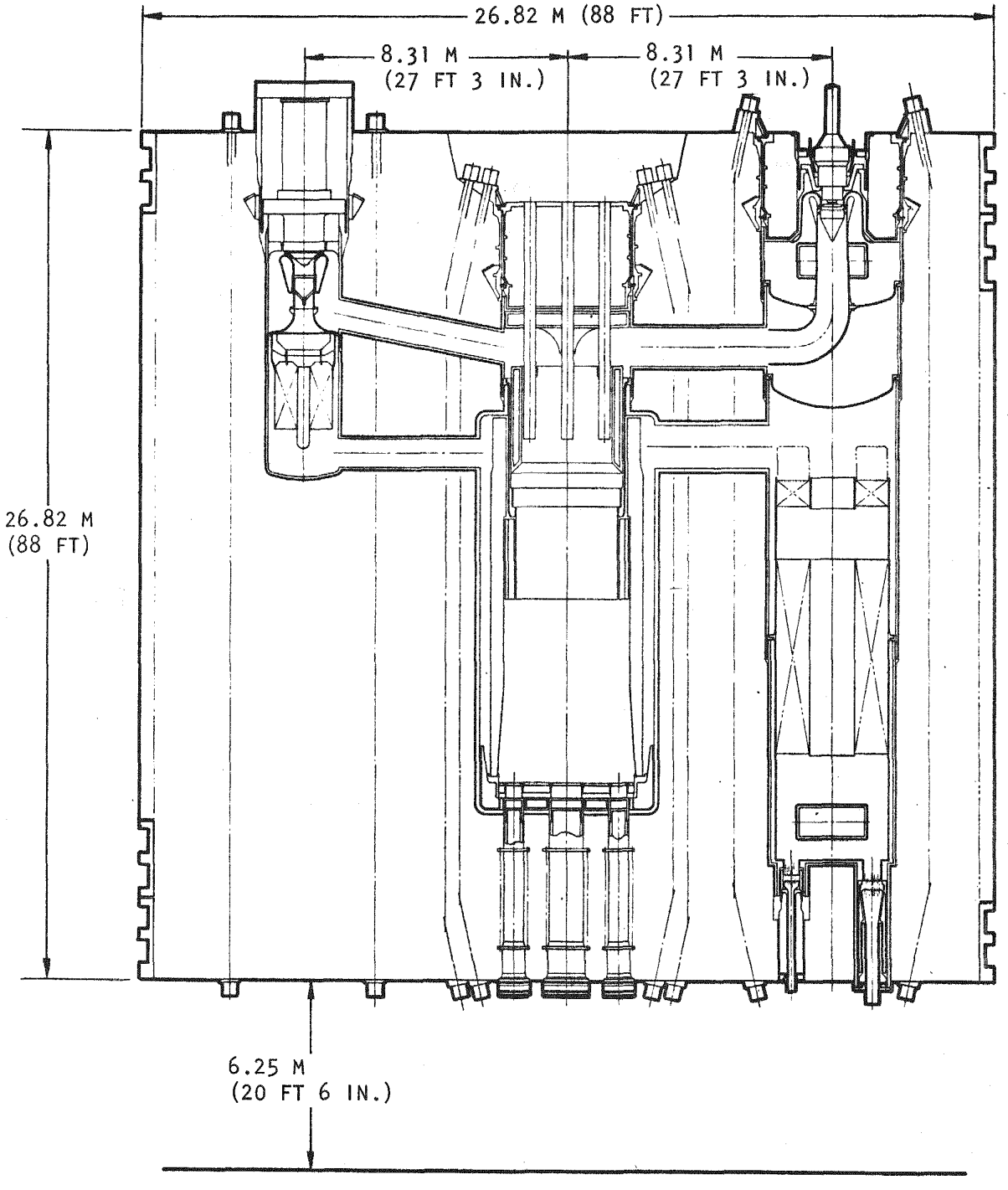

Fig. 10-4. PCRV configuration C-3 (with resuperheat steam generator)

design/layout studies were made for the lower main reactor cavity region and lower steam generator penetrations.

10.2. CONTROL AND LOCKING MECHANISMS

During this quarter, work continued on alternate mechanism concepts for supporting and locking core assemblies to the grid plate. Reference 10-5 describes the basic design philosophy and guidelines being followed for this study. The design objectives are as follows:

1. Each core assembly shall be retained by a separate locking mechanism located at the grid plate elevation.

2. The locking mechanism shall be actuated by an externally introduced servicing machine at reactor shutdown.

3. The locking mechanism shall support the core assembly in the upward direction to counteract weight and coolant flow pressure forces and provide vertical and horizontal restraint against vibration and seismic forces.

4. In addition to the primary locking function, the locking mechanism shall provide a secondary and independent backup locking feature.

5. The locking mechanism shall be adaptable to an instrument tree arrangement for leading thermocouples to the gas outlet flow region of the core assembly.

Figure 10-5 shows a core assembly locking principle considered in this study. Attachment of the core assembly to the grid plate is performed by a removable and replaceable mechanism which is approximately 194 mm

Testing of PCRV closure models is being conducted at ORNL, which has manufactured the component parts of the 1/15-scale model reactor cavity closure with the penetrations for drive mechanisms for each individual core assembly. Since GA is investigating alternate designs for the reactor core cavity closure, ORNL has been requested to suspend work on the closure until an alternate design has been selected. A GA representative witnessed the pressure testing program for the 1/15-scale model of the steam generator. The tests were performed for the elastic and inelastic stress and deflection ranges with overpressurization to structural failure. Ten pressure cycles were made, taking the pressure from 0 to 10.07 MPa (1460 psig) maximum cavity pressure (MCP) in steps of 2.07 MPa (300 psi) and then depressurizing. Recordings were made of the readings for the seven strain gauges and displacement gauges at each step in pressure, and the instrument readings were closely duplicated for each of the cycles. The overpressurization test was conducted with the pressure being applied in increments of 3.45 MPa (500 psig). At a pressure of 75.8 MPa (11,000 psig) ($\sim$7 MCP), the testing was suspended, with the model showing no structural distress. A report on this testing is being prepared by ORNL.

PCRV design documentation (Refs. 10-2, 10-3) were finalized, and the thermal barrier logic diagram and RECS information were reviewed and incorporated into the PCRV logic diagram. The thermal barrier design criterion (Ref. 10-4) was reviewed and issued.

In an effort to reassess the development plan for thermal barrier testing, a preliminary analysis of the hot duct pressure distribution and its effect on permeation flow and heat transfer was initiated. Pressure distributions were calculated for ducts with and without a thermal shield (a circular duct which keeps flow from impinging on the cover plates). The absence of the thermal shield causes an increase of $\sim$7% in the amount of heat transferred, and elimination of the thermal shield, especially without HTGR-type hot streaking, appears promising. However, a more extensive analysis and probably a test of this configuration will be required in order to confirm the elimination of the thermal shield. Thermal barrier

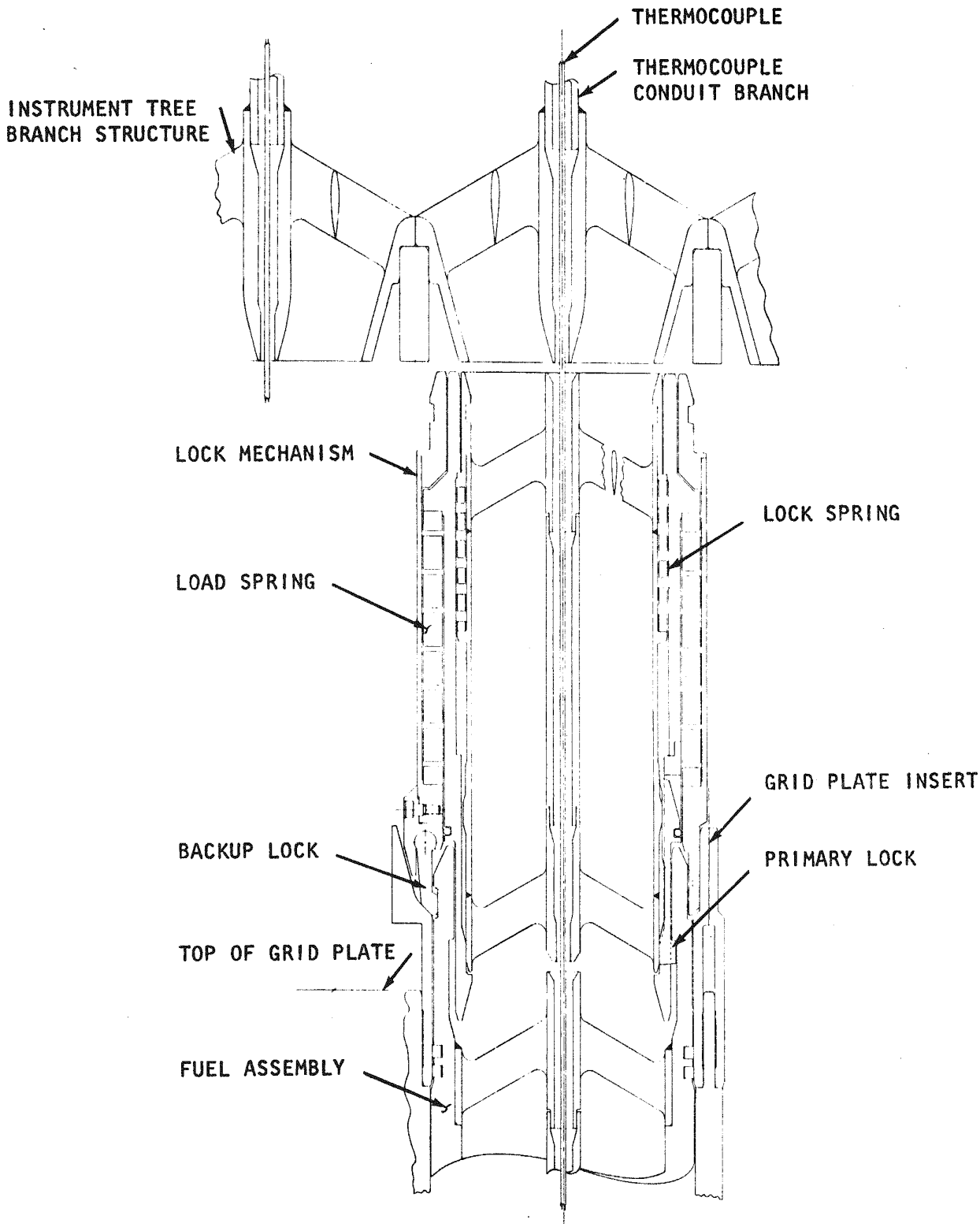

Fig. 10-5. Fuel assembly locking mechanism

(7.6 in.) in diameter and 424 mm (16.7 in.) long. The operating principles of the locking mechanism are as follows:

1. Upward retention force is supplied by a spring which is preloaded to counteract downward separating forces and a substantial overload margin which provides required clamping action against vibration and seismic forces.

2. Reaction to the upward tension force is transmitted downward through the outer cylindrical member to the top of the grid plate.

3. The gripping fingers engaging the core assembly are retained in the locked position by the innermost sleeve. This locking sleeve is spring loaded in the locked direction; gravity and flow forces act in the same direction.

4. The secondary or backup lock function is provided through pawls which transmit the preload reaction force into a radial engagement with an external gripping ledge of the core assembly.

Figure 10-5 also illustrates the proposed method of routing thermocouple leads into the fuel assembly. The portion of the instrument tree structure above the locking mechanism is the termination of the thermocouple conduit branches above the flow guide nozzles. A conduit extension in the locking mechanism guides the thermocouple lead into a mating passage in the core assembly. To provide access to the locking mechanisms during refueling, the instrument trees are raised to give unobstructed clearance for the lock actuation machine. Thermocouple leads are withdrawn prior to raising the instrument trees. Figure 10-6 is an elevation view through the upper reactor plenum and PCRV; a typical arrangement of instrument trees is shown. One instrument tree is located at the center and six others are evenly distributed near the outer boundary of the core. The central instrument tree is raised to provide clearance for the lock actuation machine. The tubular trunk of the instrument tree provides the entry path for the lock actuation machine.

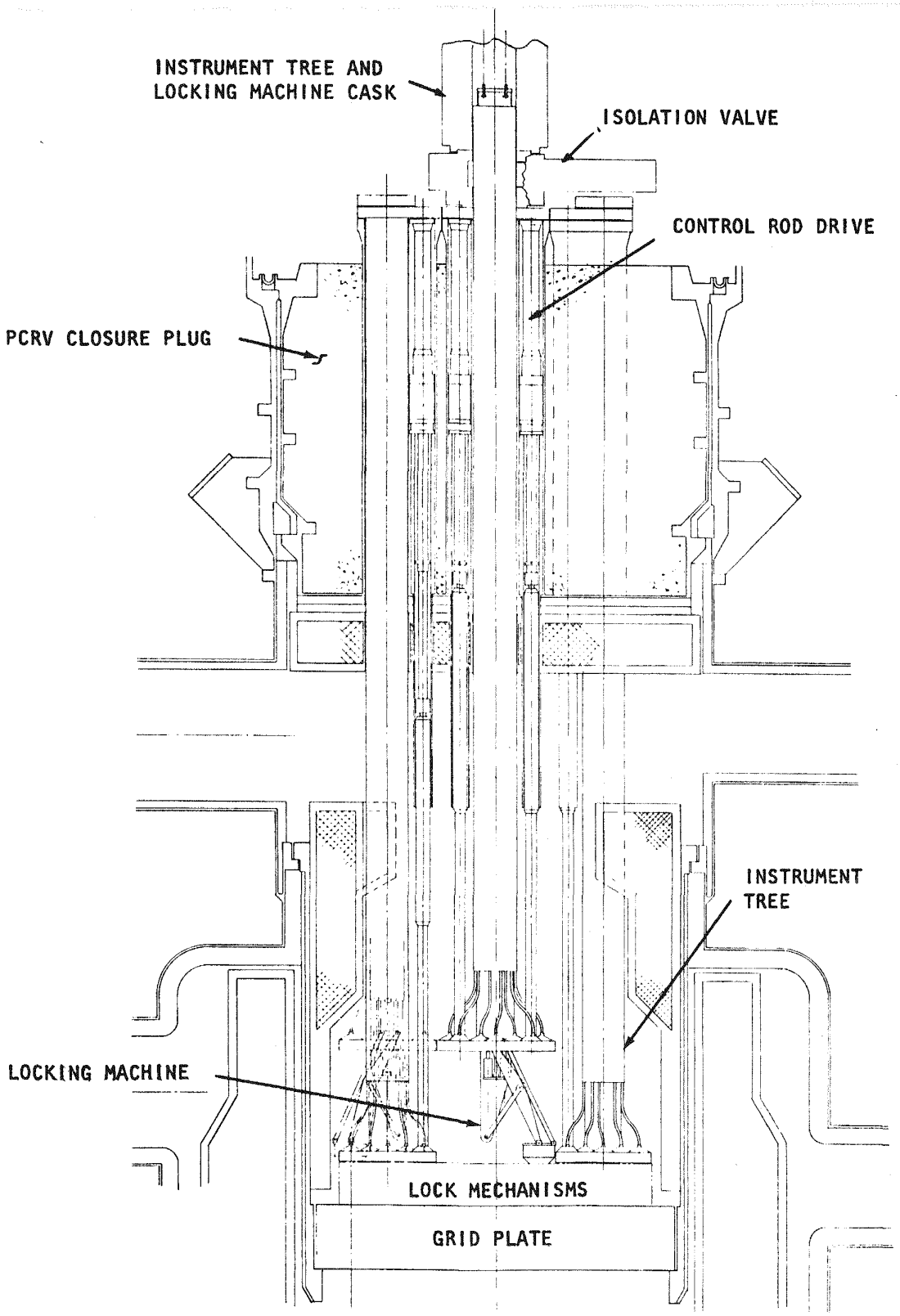

Fig. 10-6. Instrument tree and locking machine elevation

10.3. FUEL HANDLING DEVELOPMENT

During this quarter, the in-vessel fuel handling machine conceptual layouts were updated, implementing the major improvements described in Ref. 10-5. These improvements were primarily concerned with the revised concept of utilizing the fuel transfer machine (FTM) for dropped fuel assembly recovery using an interchangeable manipulator. This manipulator would be in modular form and attached to the FTM in place of the lifting mechanism module, which is normally used for refueling purposes. The conceptual design layout effort included a development of a plenum service machine (PSM) manipulator arm and fuel assembly grapple mechanism.

A major effort was made to finalize a study on methods of refueling from below the core without any penetrations through the PCRV bottom head directly below the core region. Four schemes were considered; the basic differences between the various schemes are in the path of transit taken by a fuel assembly between the reactor service building and the core, based on the position of the refueling penetration through the reactor vessel. These schemes are

1. Scheme 1: side entry, bottom removal.

2. Scheme 2: side entry from outside PCRV.

3. Scheme 3: side entry, vertical transfer machine through top.

4. Scheme 4: vertical entry and vertical transfer machine through top.

Scheme 1 avoids penetrating the PCRV outside diameter and its circumferential prestressing bands. A fuel assemlby is lowered to a receiving position below the core, turned from a vertical to a horizontal attitude, and moved through a hole in the internal vessel side wall. The fuel assembly is turned back into a vertical attitude for subsequent downward

removal through a penetration in the bottom of the PCRV. Since the PCRV outer wall does not have a penetration through which the handling machine can be removed, service is limited.

In scheme 2, there is a large, radial, horizontal, tunnel-like penetration through the PCRV side wall with a consequent interruption of the circumferential prestressing bands. The fuel handling machine would be housed in this tunnel and would move inward to a position under the core, where it would have to remove, orient, and pivot a fuel assembly to enable subsequent removal of the assembly from the PCRV. This scheme may have some structural advantages since the containment building height might be reduced, and the higher elevation of the horizontal refueling penetration reduces the excavation required for the spent fuel storage pool.

Scheme 3 utilizes a vertical fuel transfer machine which enters from above, through one of three holes or passages alongside the core boundary. This machine functions exactly as the reference design FTM by transferring a fuel assembly from underneath the core to a removal machine below the core. The removal machine is quite similar to that required for scheme 2, and in fact, the identical entry through the PCRV as that described for scheme 2 would also be required for scheme 3.

For scheme 4, a vertical FTM is passed down through the core center; this requires the omission of seven fuel assemblies. The FTM transfers a fuel assembly from underneath the core to a position just outside the core, where the fuel assembly may be withdrawn from above through a vertical hole. This scheme involves additional equipment on top of the PCRV, but complexity inside the reactor is significantly reduced. In addition, this unconventional scheme requires additional fuel assemblies at the edge of the core to compensate for the seven central assemblies; however, this is not expected to noticeably alter the diameter of the top closure plug.

10.4. CORE SUPPORT STRUCTURE

The purpose of this subtask is to ensure the availability of the structural analysis methods and materials mechanical behavior required to assess the structural integrity of the GCFR core support structure under all anticipated operational and safety-related loading conditions in the GCFR environment. Work accomplished during the last quarter included development of a proposed criterion for the maximum reactivity change due to loss of the pressure in the core and in the event of a safe shutdown earthquake (SSE). Analytical expressions for the deflection and moment in the grid plate under thermal or radiation swelling loads have been derived. The derivation assumes that the load is linear through the thickness and is an arbitrary axisymmetric function of the radius with a simply supported edge condition.

During this quarter, the design criterion for the GCFR core support structure has been reviewed and is in the process of being approved. A meeting was held with Westinghouse to review the Clinch River breeder reactor (CRBR) core support design, and some recommendations on GCFR core support were obtained.

10.4.1. Seismic Structural Analysis of the GCFR Core Support Structure With the Effects of Core Assemblies

A detailed work scope for the seismic structural analysis of the GCFR core support structure including the effect of core assemblies has been written. The object of the analysis is to determine the ligament stress and motion of the core support structure and core assemblies. Two methods, analytical and finite element, will be used, and the results must be within an acceptable engineering range.

10.4.2. Thermal Analysis of the Grid Plate

During this quarter, thermal analysis of the grid plate for steady-state normal operating conditions at 100% power has been initiated. The

purpose of the analysis is to predict the grid plate radial and axial temperature distributions and provide input for grid plate thermal stress analysis. Detailed grid plate gamma heating distributions in the radial and axial directions have been received from ORNL and are being used in the thermal analysis.

10.5. REACTOR SHIELDING ASSEMBLIES

The purpose of this task is to develop analytical methods and experimental programs to evaluate the reference design of the reactor shields. This evaluation considers heating and cooling of the shields, materials evaluation, seismic effects, need for flow tests, and structural analysis. The evaluation also includes alternate shield configurations as necessary to develop a satisfactory design.

During the previous quarter, shield configuration studies were performed to determine the method of support for the outer radial wraparound preshield and lower shield assembly. During this quarter, plant layout criteria drawings for upper, lower, and radial shielding have been completed and are in review. Weight calculations for the present shielding design were also performed to provide the necessary information required for the plant layout criteria. A preliminary hydrodynamic analysis was performed to determine the pressure drop characteristics of the new outer radial shield support configuration. This analysis indicates that the pressure losses are excessive; thus, design changes are required. A study was initiated to assess the PCRV and bottom shield modifications necessary to accommodate containment of molten material in order to accomplish the postulated post-accident fuel containment (PAFC). A meeting was held between GA and ANL to establish design criteria for the PAFC.

10.6. MAIN CIRCULATOR, VALVE AND SERVICE SYSTEM

The purpose of this subtask is to develop the helium circulator, its service system, and the main loop isolation valve to demonstrate performance and reliability by testing under anticipated operating conditions. The overall objective for FY 77 is to initiate predesign and performance analysis

of the circulator configuration, service system, and loop isolation valve. Requirements for the circulator subcomponents will be established and preliminary design layouts made. Service system requirements and system diagrams will be prepared, and a conceptual design of the main loop isolation valve will be completed. Work has been initiated on the conceptual and preliminary design of the helium circulator and service system.

10.6.1. Circulator Design and Performance Analysis

A layout of the reverse flow circulator (Ref. 10-5) installed in the PCRV steam generator cavity closure plug was completed. In this design (Figs. 10-7, 10-8), it is necessary to place the circulator support flanges within the concrete closure plug in order to obtain a sufficient diffuser length before the outlet gases are turned prior to entering the cross duct to the core. The inlet plenum to the circulator is isolated from the steam generator and the circulator exit duct by two pressure barrier plates across the steam generator cavity. This design provides for improved seals, improved installation of the circulator exit duct (which also contains the main valve), and reduced turning diffuser exit losses. The diffuser and main valve are installed separately, prior to installation of the circulator, and can remain in the PCRV if the circulator needs to be removed for service.

As reported in Ref. 10-5, consideration was given to a proposal to establish the design point for the demonstration plant at 107% power to account for 5% overpower for the valves "wide open" condition plus 2% overpower for control and instrument steam measurement uncertainties. A conceptual design was developed for a single-stage axial flow circulator with a design point based on 107% power and a pressure rise of 345 kPa (50 psia). The detailed design parameters are shown in Table 10-1.

It appears possible to optimize the blade parameters and the combined overall effect on the helium compressor and steam turbine to obtain a single-stage circulator design which will satisfy the required operating conditions. The operating conditions for the drive turbine for this design

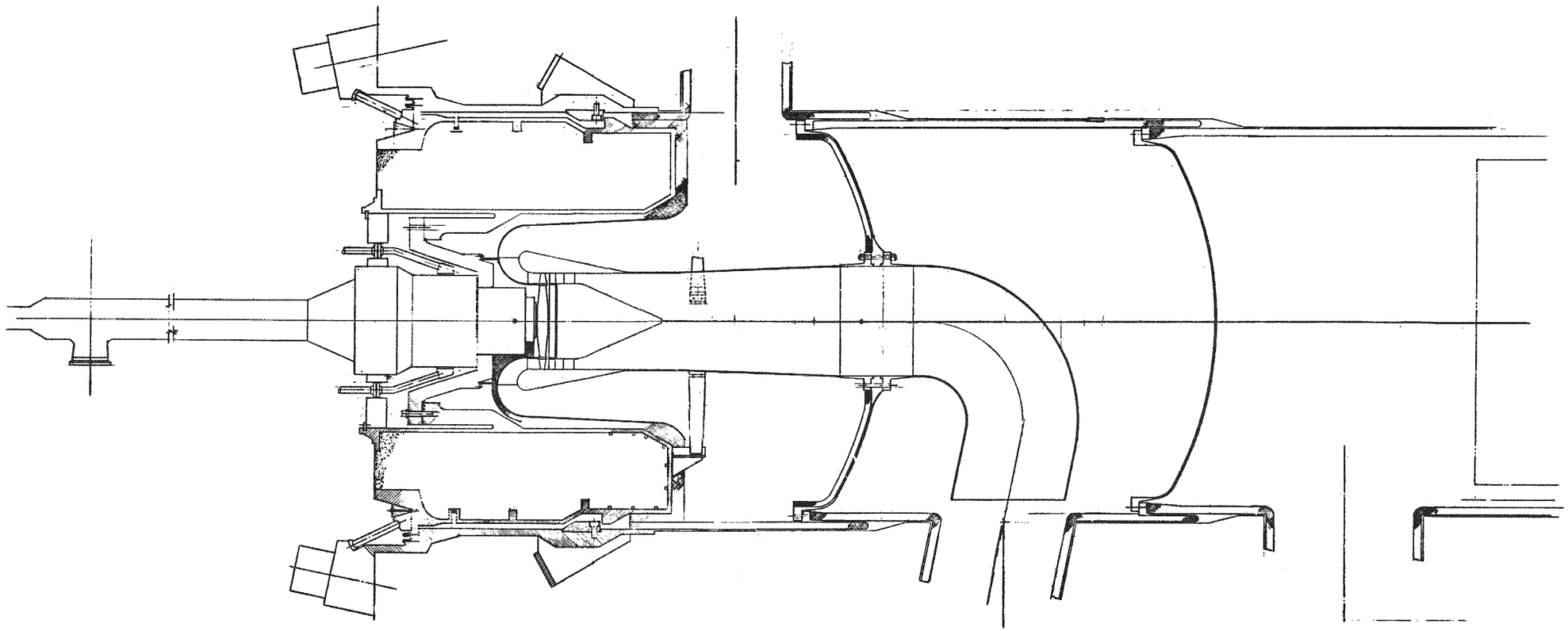

Fig. 10-7. Installation of circulator in PCRV

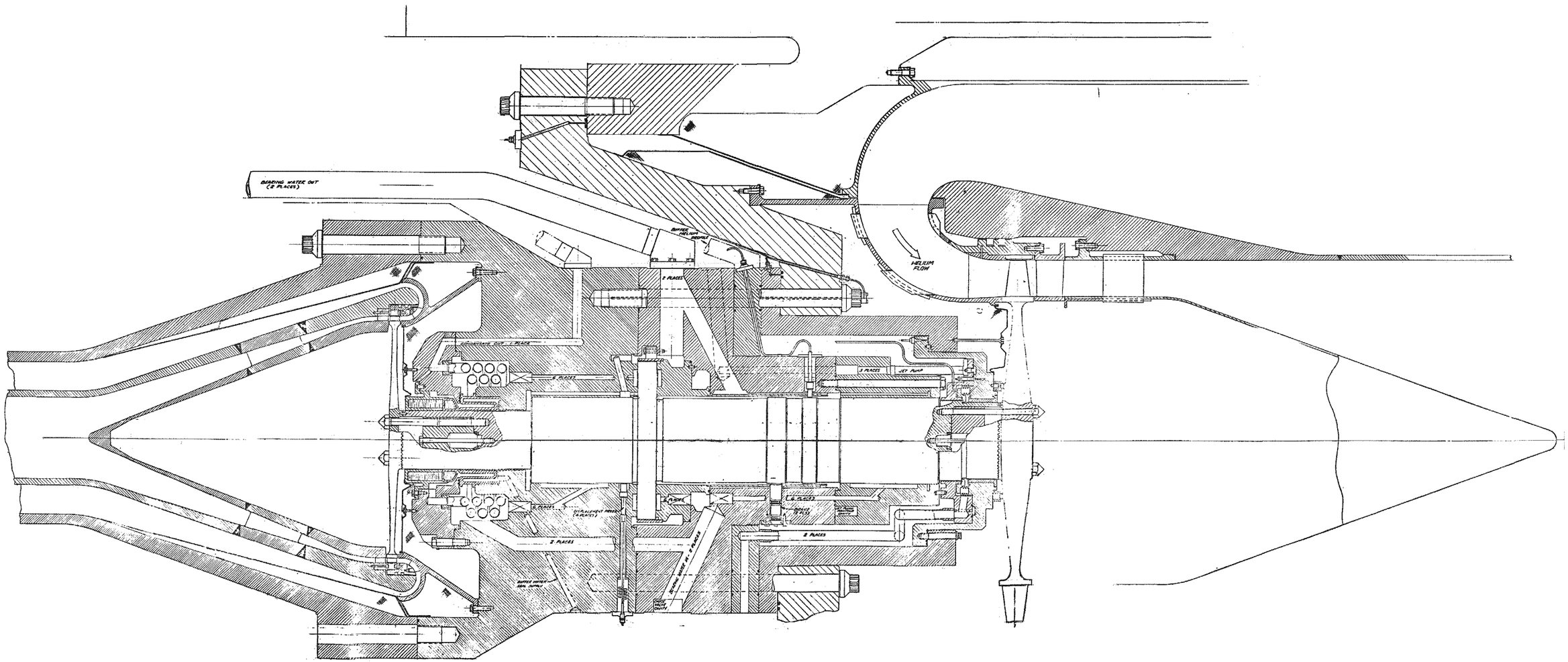

Fig. 10-8. Layout of circulator

TABLE 10-1
OPERATING CONDITIONS FOR LOW-POWER MAIN CIRCULATORS

	Case						
	0	1	2	3	4	5	6
Helium							
Reactor power (%)	107	100	100	100	100	100	100
Flow rate [kg/s (lb/s)]	322 (709)	291 (642)	268 (592)	242 (533)	290 (639)	263 (581)	257 (567)
Pressure rise [MPa (psi)]	0.35 (50)	0.29 (42)	0.26 (38)	0.25 (36)	0.26 (38)	0.23 (34)	0.23 (34)
Outlet temperature [°C (°F)]	349 (660)	346 (655)	318 (604)	290 (555)	346 (655)	318 (604)	349 (660)
Inlet pressure [MPa (psi)]	8.65 (1255)	8.62 (1250)	8.62 (1250)	8.62 (1250)	10.07 (1461)	10.13 (1469)	8.62 (1250)
Speed (rpm)	8400	7550	6750	6275	6730	6300	6720
Horsepower [kW (1000 HP)]	21.3 (28.5)	14.6 (19.6)	11.2 (15.0)	9.3 (12.5)	13.0 (17.4)	10.6 (14.2)	10.4 (14.0)
Blade stress ratio	1.0	0.80	0.64	0.55	0.75	0.56	0.50
Steam							
Flow rate [kg/s (lb/s)]	136 (300)	125 (275)	118 (261)	116 (256)	122 (269)	116 (256)	134 (294)
Inlet pressure [Mpa (psi)]	19.2 (2780)	19.2 (2780)	12.3 (1780)	12.3 (1780)	19.2 (2780)	12.3 (1780)	13.1 (1900)
Inlet temperature [°C (°F)]	507 (944)	507 (944)	506 (943)	506 (943)	507 (944)	506 (943)	506 (943)
Outlet pressure [Mpa (psi)]	9.2 (1327)	11.1 (1608)	8.2 (1196)	8.6 (1251)	11.6 (1675)	8.6 (1244)	10.0 (1430)
Δh [1000 J/kg-K (Btu/lb-°F)]	280 (67)	218 (52)	172 (41)	151 (36)	197 (47)	163 (39)	138 (33)
Mach No.	0.96	0.83	0.74	0.69	0.78	0.71	0.67
Blade height [mm (in.)]	12 (0.47)	11 (0.43)	18 (0.72)	17 (0.69)	11 (0.42)	17 (0.69)	20 (0.78)
Aspect ratio	0.42	0.45	0.66	0.65	0.40	0.65	0.55

are close to the upper limit for a single-stage turbine. Compressor aerodynamic performance was less critical than drive turbine design, but it also approached the upper limit for a single-stage machine. The most critical parameters in the design of the circulator were stress levels in the blade root attachments to the disk, size of the disk and shaft, bearing speed, and required bearing water pressures. Although preliminary analysis indicated that this design met all performance and design requirements, several parameters were operating at the limits of the state-of-the-art technology, and therefore it may be difficult to demonstrate predicted performance and reliability.

A number of changes were identified to provide greater confidence in the design of the single-stage circulator; these changes are being evaluated. One of the changes, increasing the primary helium pressure 10%, will reduce the ΔP requirements. Reduction of the core inlet temperature and the helium flow rate is also being studied as part of the thermal-hydraulic analysis of the primary loop system. This would lower the ΔP requirements, circulator horsepower, and steam pressures and result in a better matched compressor and drive turbine.

Subsequent to a review of the plant operating conditions and equipment design margins, it was concluded that the design point for NSS equipment, including the circulator, should be established for 100% reactor power. The NSS output at this level would provide the potential for the turbogenerator to operate up to 105% power with the valves wide open. These reduced requirements would lower the system pressure drop from 395 to 290 kPa (50 to 42 psi), which in turn would improve the blade parameters on the compressor and turbine sections of the circulator (Table 10-1). In order to evaluate the overall effect of other possible changes in system requirements (such as lower ΔP, higher system pressure, and lower core inlet temperature) on the circulator, the six cases presented in Table 10-1 were investigated to establish system parameters which would improve a single-stage circulator, even if the changes might result in degradation of the overall reactor cycle efficiency. Additional optimization studies will be made to establish overall plant design parameters.

In all the cases shown in Table 10-1, the system pressure drop was lowered in order to improve the blade operating parameters on the compressor and turbine. A lower ΔP alone is insufficient to obtain desirable blade parameters. However, combination of lower ΔP and lower core inlet temperature gives an improved turbine blade aspect ratio and blade height, a lower nozzle Mach number, and lower blade stresses. Increased primary system pressure is not a sufficient improvement in itself but is highly desirable in combination with lower core inlet temperature because of lower flow rates, helium ΔP, and blade stresses and improved turbine blade height and aspect ratio.

The steam pressures for these cases were chosen to give a turbine steam exit pressure which is close to the PCRV pressure at the design point. This results in the minimum axial thrust loads on the circulator shaft. In choosing the final operating conditions, it is desirable to operate at circulator turbine steam exit pressures which are always below helium inlet pressure. This eliminates the necessity for a buffer steam/water seal in the circulator, which is presently required with the high-pressure steam design.

Cases 3, 5, and 6 are the most desirable for the design of the single-stage circulator. However, other considerations such as plant efficiency and steam generator size and cost must be optimized in conjunction with the circulator parameters. Circulator qualification testing and requirements for the hot flow test of the reactor prior to plant start-up must also be considered, and the greatest similarity possible must be maintained between GCFR demonstration plant equipment and system technology and that for the commercial plant.

An alternative to the single-stage circulator improvements presented in Table 10-1 is a two-stage compressor and a two-stage turbine. A two-stage drive turbine for the circulator would have a more conservative blade design, and a two-stage circulator compressor would solve any blade root stress problems associated with any future increase in helium pressure rise requirements. Preliminary analysis also indicates that a two-stage compressor

and a two-stage drive turbine on a common shaft should be capable of meeting any anticipated design and performance requirements for the larger commercial plant. The circulator speed would be reduced to 6000 rpm compared with 8400 rpm of the current reference design. The lower speed will make it easier to obtain the required first critical speed margins above design speed. Work is continuing on a two-stage circulator design.

10.6.2. Alternate Circulator Design Studies

Because of the large steam flow requirements for qualification testing of the series flow circulator at full power and hot flow testing in the reactor prior to reactor start-up, it may be desirable to use an alternate circulator drive mechanism or system. An electric motor drive or a multi-stage, lower-pressure steam turbine drive similar to the types used for feedwater pumps might have merits. For instance, an electric motor drive would permit full-power, non-nuclear hot flow testing without the necessity to generate high-pressure steam. However, the compatibility of the motor and the compressor relative to performance flexibility, control, and safety (particularly with respect to maintenance of continuous cooling in the event of a design basis depressurization accident with loss of off-site power) requires evaluation. Similarly, a series or parallel flow multistage external drive turbine connected to the circulator compressor could be used with steam from the steam generator or extraction steam from the main turbine. For full-flow preoperational testing, the steam would be supplied by auxiliary boilers.

Studies are presently being performed to establish the consequences of the alternate drive systems listed below. These designs are being investigated for vertical and horizontal orientations.

1. An external drive turbine with two-stage axial flow in series with the main turbine and driving a two-stage axial flow compressor. A better aerodynamic matching of the turbine and compressor appears possible with this arrangement. It also seems adaptable to a wide

range of operating conditions and offers a number of alternative test facilities and hot flow test options.

2. An electric-motor-driven circulator with a single-stage radial flow compressor. This requires the development of a 20,000-hp electric motor with a maximum speed of 3,600 rpm. Conceptual drawings of this arrangement showing the general size and relationship of the components have been completed, and submerged and external drive motor arrangements are being studied.

3. A commercial multistage external turbine drive. A two-stage axial flow (6000 rpm) or a single-stage radial flow compressor (3600 rpm) could be used with this type of drive. About 20% of the main steam is diverted to the circulator drive turbine. Conceptual layouts are being prepared.

4. A low-pressure steam, parallel flow multistage turbine supplied with steam from the intermediate pressure stage of the main turbine to drive a 6000-rpm axial flow compressor. An electric pony motor is required in case of accidental steam loss to the circulator.

The design chosen will be applied to the demonstration plant and the larger commercial plant.

10.6.3. GCFR Circulator Criteria Committee

A GCFR Circulator Criteria Committee has been formed to review the criteria, requirements, and overall design philosophy for the main helium circulator. The committee has been requested to prepare a list of safety and operational criteria for the circulator and to draft a hot flow preoperational test program for the 300-MW(e) plant. A number of meetings have been held to discuss the HTGR lead plant vibration assessment program and the GCFR circulator test power level. Recommendations for hot flow test requirements have been completed and are in review.

10.6.4. Main Circulator Service System

Preliminary design work is continuing on the main circulator service system, but progress is still being delayed because of changes in the main circulator configuration and system requirements. The design calls for bearing water to be supplied to the main circulator bearings by two multistage centrifugal pumps, each with a power of about 350 kW (475 hp), operating in parallel. For diversity, one pump will be driven by steam and the other by an electric motor. Both pumps may have to be continuously operated to avoid a circulator trip if one of the pumps fails. An additional 1-min supply of bearing water will be stored in accumulators for use during the circulator shutdown sequence in case the normal bearing water supplies are interrupted. Because there will be two pumps, the use of feedwater as a backup bearing water system, which has caused several circulator trips and water ingress at the Fort St. Vrain HTGR, will not be used for the GCFR. The circulator shaft sealing system will be similar to that of the HTGR with the addition of a high-pressure buffer water seal for the steam end. Water for the seal will come from the high-pressure bearing water supply. A low-pressure separator to remove helium from the bearing shaft seal drain water and a dryer for removing water vapor from the buffer helium will also be used. A piping and instrumentation diagram for the service system is being prepared.

10.7. STEAM GENERATOR

The purpose of this subtask is to design and develop a steam generator which meets the operational, performance, and safety requirements of the GCFR. The scope of work for this year includes the conceptual design of a first-of-a-kind steam generator by (1) optimization of the tube geometry for performance, cost, and boiling stability; (2) structural and stress analysis of tubing, tube sheets, and tube supports (thermal growth studies will be initiated); and (3) preliminary vibration analysis for the chosen tube geometry and support system.

10.7.1. Thermal Hydraulics

Steam generators without a resuperheater and using 2-1/4 Cr - 1 Mo steel were designed for the proposed 107% power cycle conditions. Because of the increased thermal duty, the higher helium and water flow rates, and the lower inlet helium temperature, the steam generators require more tubes in parallel and a greater bundle length and surface area for the same frontal area. Several frontal areas were investigated to obtain a range of bundle lengths. As part of the tube geometry study, steam generators without a resuperheater were sized using 3.17/2.54 cm (1.25/1.00 in.) diameter tubes instead of the presently used 2.54/1.90 cm (1.00/0.75 in.) diameter tubes for the 107% capacity condition. The steam generators with the larger-diameter tubes require significantly fewer tubes in parallel and have a somewhat greater bundle length and surface area and a smaller fraction of the overall water-side pressure drop in the economizer than the steam generators with the smaller-diameter tubes. More detailed comparison of steam generators using the two tube size combinations will be made. As a result of the 107% power cycle study of the steam generator and circulator, it was agreed that the design point for NSS equipment should be established at 100%. Application of additional margins will be determined for components as dictated by safety requirements.

As part of an overall cycle study directed toward identification of conditions resulting in reduced helium circulator power requirements (see Section 10.6), steam generators were sized for two cycles which utilized a 13.1-MPa (1900-psia) [instead of 20-MPa (2900-psia)] steam exit pressure. The required surface area was sensitive to the helium inlet temperature [533° or 521°C (991° or 970°F)], with the higher temperature resulting in a much lower surface area.

As part of the effort to update the steam generator development plan, some specific aspects of helical coil boiling behavior were investigated. At 100% power, the temperature increase at the inside tube wall at critical heat flux varies from about 4.4°C (8°F) at a steam quality of 0.90 to about

6.7°C (12°F) at a steam quality of 0.10. Since critical heat flux is likely to occur over a range of steam qualities, the very wide span above was used, and the inside tube wall temperature increases were consequences of the change from nucleate to film boiling. The virtually constant tube temperature increases result from the film boiling coefficient and the heat flux increasing with steam quality.

An initial study of steam generator thermal characteristics at the nominal 2% steam flow conditions following a turbine trip was made; steady-state conditions 4 min after trip were assumed. For given helium flow and temperature conditions, the nominal 2% steam flow produced superheated steam (at essentially helium inlet temperature) at the exit, with all heat transfer effected in a portion of the economizer and no heat transfer elsewhere in the steam generator. Although the exit steam temperature was the same at 2% flow and 100% flow, the temperature distribution along the bundle was considerably changed and should be evaluated for stress and structural effects. Preliminary analysis indicates that at 2% flow, the combination of very low heat flux and very low flow results in an inside tube wall temperature increase at the onset of critical heat flux which is much larger [approximately 53°F (29.4°C)] than that which occurs at the 100% power and flow condition. Based on this, the tube wall temperature fluctuations at 2% flow and the associated thermal stresses are expected to exceed those existing at 100% flow. Evaluation of a low-flow boiling stability test section consisting of a coil within a coil (water flowing inside the tube, helium flowing in the annulus) as a possible alternate to the present HTGR test section in the Carmen 2 (CEA) test loop indicates that such a geometry can satisfy thermal and overall test requirements.

10.7.2. Resuperheat/Nonresuperheat Design and Cost Study

Assembly and detail drawings were completed for the steam generator designs with and without a resuperheater, and the general arrangements for the two designs are shown in Figs. 10-9 and 10-10. These drawings were prepared for the design and cost study initiated during the last quarter. The

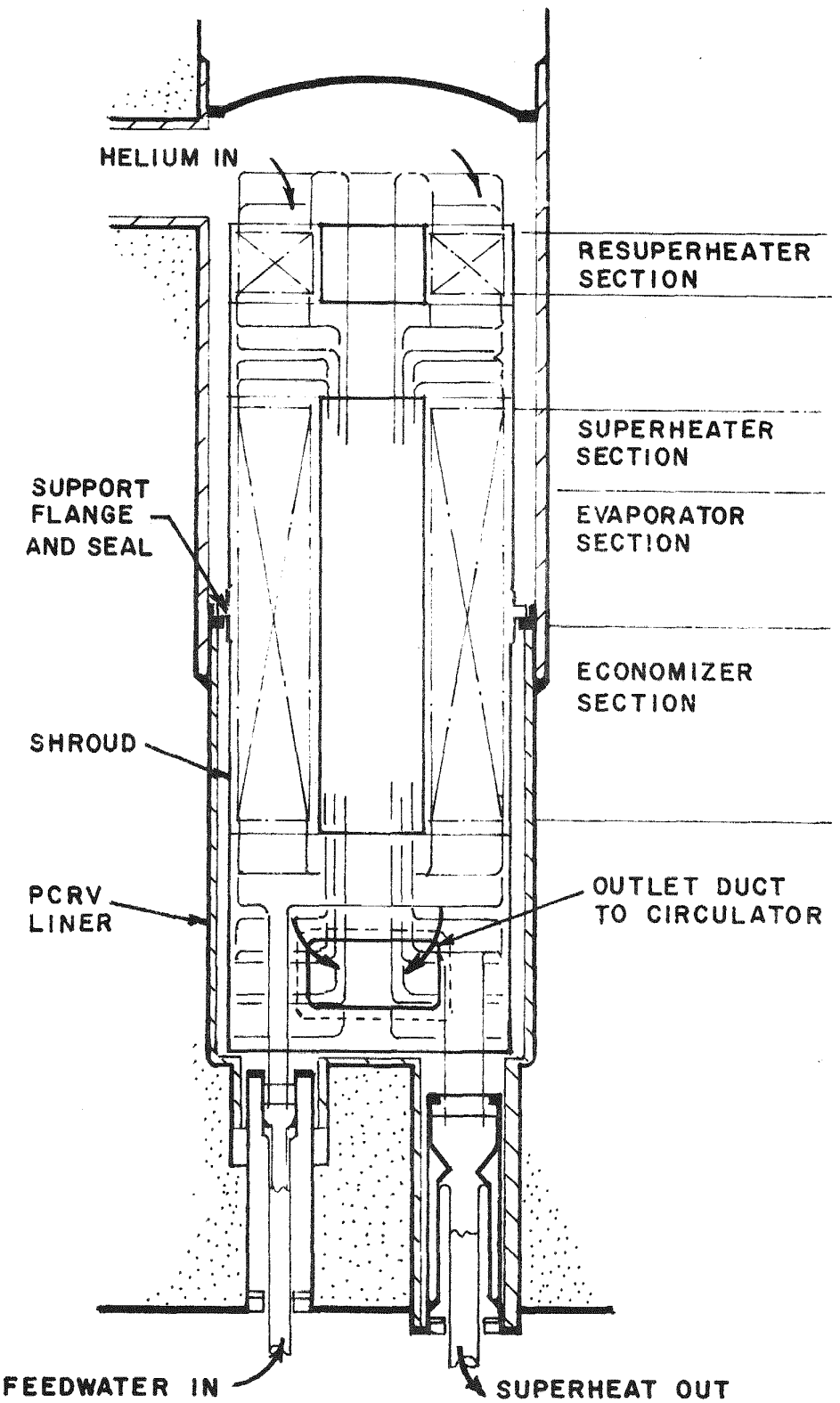

Fig. 10-9. Steam generator with resuperheater

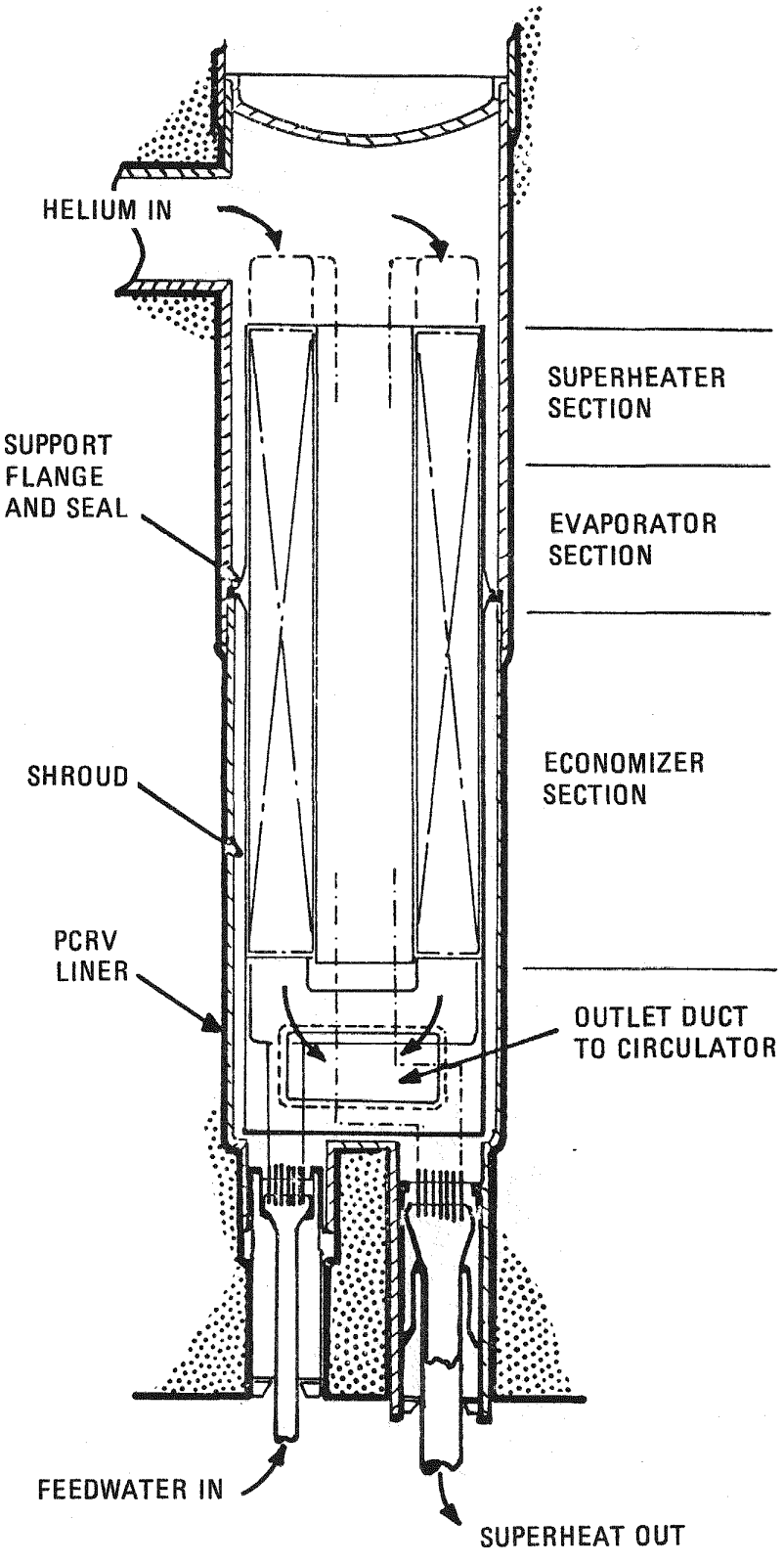

Fig. 10-10. Steam generator without resuperheater

design characteristics and conditions from which these two designs were developed are summarized in Table 10-2. All pressure-retaining components and load-bearing members were sized in accordance with the applicable sections of the ASME Boiler and Pressure Vessel Code, Section III (Ref. 10-6). Several design improvements and additions have been incorporated into these designs. The general arrangement with a resuperheater is shown in Fig. 10-9. This design incorporates a center-supported module, and the unit is a once-through, uphill-boiling, counterflow helical bundle configuration. Hot helium enters the component from the top, flows downward through the resuperheater and main bundle, and leaves the steam generator cavity via a duct in the PCRV. Superheat and resuperheat IN and OUT leads are routed within the central section of the steam generator module, and four penetrations for feedwater, superheat, resuperheat IN, and resuperheat OUT are located in the bottom of the steam generator cavity.

The general arrangement of the nonresuperheater design is shown in Fig. 10-10. The main helical coil bundle consists of an economizer-evaporator-superheater section and is centrally supported. This unit is also a once-through, uphill-boiling counterflow configuration. Helium enters the bundle from the top, flows downward, and exits from the steam generator cavity via a duct within the PCRV. Two penetrations (feedwater and superheater) are located in the bottom of the steam generator cavity. Elimination of the resuperheater results in considerable simplification by avoiding the resuperheater bundle, resuperheat lead tubes, and associated tube sheet penetrations. The outer shroud diameter is reduced, less expansion space is required for lead tubes below the bundle, and the overall length of the steam generator is reduced, thereby permitting corresponding reductions in the PCRV cavity dimensions and ultimately the size of the PCRV. By eliminating the resuperheater, the overall length of the steam generator is reduced from 17.6 to 15.8 m (57 ft 9 in. to 52 ft 6 in.), and the outer shroud diameter is reduced from 3.6 to 3.3 m (11 ft 9 in. to 10 ft 9 in.).

Table 10-3 compares the significant design characteristics of the two designs. The number of tubes, welds, subheaders, and tube lengths and weights associated with each steam generator configuration are presented.

TABLE 10-2
STEAM GENERATOR DESIGNS

Frontal Area [m^2 (ft^2)]	Surface Area [m^2 (ft^2)]	Total Bundle Length[a] [m (ft)]	No. of Tubes, Resuperheater/ Main Bundle	Bundle Helium ΔP [MPa (psi)]	Type
10.5 (113.0)	3,176 (34,166)	5.76 (18.9)	360/230	0.016 (2.3)	With resuperheater[b]
8.6 (92.0)	2,926 (31,485)	6.52 (21.4)	360/225	0.026 (3.8)	
6.6 (71.4)	2,685 (28,885)	7.92 (26.0)	360/222	0.043 (6.3)	
6.6 (71.4)	2,707 (29,128)	8.10 (26.6)	295	0.045 (6.6)	Without resuperheater[c]

(a) Does not include space between resuperheater and main bundle.

(b) With resuperheater: helium temperature in = 544°C (1011°F), out = 342°C (648°F); water temperature in = 208°C (406°F), out = 496°C/468°C (925°F/875°F); helium flow rate = 0.96 x 10^6 kg/hr (2.12 x 10^6 lb/hr); water flow rate = 3.9 x 10^5 kg/hr (8.53 x 10^5 lb/hr); water pressure drop = 1.79 MPa (260 psi).

(c) Without resuperheater: helium temperature in = 544°C (1011°F), out = 344°C (651°F); water temperature in = 208°C (406°F), out = 513°C (955°F); helium flow rate = 0.98 x 10^6 kg/hr (2.17 x 10^6 lb/hr); water flow rate = 4.3 x 10^5 kg/hr (9.46 x 10^5 lb/hr); water pressure drop = 1.79 MPa (260 psi).

TABLE 10-3
DESIGN CHARACTERISTICS OF THE RESUPERHEATER AND NONRESUPERHEATER STEAM GENERATORS[a]

	Nonresuperheater	Resuperheater
No. of tubes		
Evaporator-economizer-resuperheater	295	222
Resuperheater	--	360
No. of welds		
Evaporator-economizer-resuperheater	10,915	11,988
Resuperheater	--	19,440
No. of subheaders		
Evaporator-economizer-resuperheater, feedwater	--	--
Evaporator-economizer-resuperheater, superheat (2:1)	--	111
Resuperheater in (3:1)	--	120
Resuperheater out (3:1)	--	120
Total tube bundle length (including leads [m (ft)]		
Evaporator-economizer-resuperheater	129,000 (5,000)	119,000 (391,000)
Resuperheater	--	28,000 (92,000)
Weight [metric tons (tons)]		
Tubes (total)	74 (81.4)	81.5 (89.7)
Other components	70.5 (77.6)	83.2 (91.5)
Steam generator (total)	144.5 (159.0)	164.7 (181.2)

[a]Material is 2-1/4 Cr - 1 Mo.

The nonresuperheater system does not require subheaders, and consequently the number of welds is greatly reduced; this substantially simplifies the system and improves its reliability. The tube material used for the comparison was 2-1/4 Cr - 1 Mo [25.4 mm (1 in.) and 19.0 mm (0.75 in.) diameters]. The weight of the nonresuperheater steam generator is about 18.2 tonnes (20 tons) less than that of a steam generator with a resuperheater. In the course of this study, attention was given to fabrication of individual components. A parallel study was prepared to define the assembly sequence for each of the designs.

A detailed review of the current HTGR reference steam generator design (Mark IIB) was completed, and applicable design features were incorporated into the GCFR designs. As a direct result of this review, the tube sheet arrangement was substantially revised. The primary reason for this revision was to provide for in-service inspection of specified primary containment welds. This redesign required larger tube sheet penetrations within the PCRV. The steam generator with a resuperheater requires four tube sheet penetrations for the feedwater, superheat, and resuperheat IN and OUT. The minimum diameter for the tube bundle is dictated by the diameters of the four tube sheet penetrations.

Cost comparisons showed that the nonresuperheater steam generator hardware, shipping, and installation costs for the three units are approximately $\$4 \times 10^6$ lower than the costs for the resuperheater version. Development cost differences between the two designs are considered to be negligible since the low-flow stability tests are only made on the main bundle. Helium inlet flow tests will have essentially the same scope with or without the resuperheater. The reduction in steam generator engineering design and in architect-engineer indirect costs was estimated to be approximately $\$2 \times 10^6$. Although this study shows the clear design and cost advantage of the nonresuperheater steam generator, a decision on the configuration will be made after completion of the performance and cost evaluation of the steam-to-steam reheat study presently being made in conjunction with the main turbine study.

10.8. AUXILIARY CIRCULATOR, VALVE AND SERVICE SYSTEM

The general objectives of this task are (1) to prepare and issue a core auxiliary cooling system (CACS) component development plan document and (2) to develop CACS components which meet reliability and safety criteria by testing under anticipated operating conditions.

During this quarter, the CACS development plan was completed (Ref. 10-7). The overall CACS development program consists of six phases: (1) preparation of a CACS design criteria document under private funding; (2) performance of CACS design optimization studies; (3) development of component design criteria under private funding; (4) achievement of design and performance analysis; (5) performance of component design verification tests; and (6) accomplishment of preoperational start-up testing in the demonstration plant. Reference 10-7 describes only the component design verification tests (phase 5) for the major components, including the auxiliary circulator and its drive motor, the core auxiliary heat exchanger (CAHE), and the auxiliary loop isolation valve. The CACS conceptual and preliminary design analysis to be carried out in phase 4 will be reviewed and approved before the actual subcomponent and component verification tests are conducted.

As part of the CACS design optimization, application to the GCFR of a preliminary conceptual design study of the bottom-fed CAHE with a bayonet straight-tube design is being conducted using the revised NUSIZE code (Ref. 10-8). The constraint in this study is to limit the heat duty, helium flow frontal area, and pressure drop across the heat exchanger to the same values as those for the helical tube bundle CAHE design for the GCFR 300-MW(e) demonstration plant (see Ref. 10-9). The straight-tube bundle is substantially longer and more complex because of the lowering of the cross duct in the PCRV. This study will be continued in order to compare the bottom-fed bayonet straight-tube bundle with the top-fed helical-tube bundle CAHE design.

The preliminary scope of the design optimization study of the CACS equipment for the NSS core auxiliary cooling water system has been examined,

and an increased effort will be made to produce sufficient data for proceeding with the preliminary design of the CACS critical components. A commitment has been made to evaluate the reliability of the auxiliary loop isolation valve, and a design package showing the mechanical details of the valve and a detailed valve development plan are being prepared. The valve will be the first component to be evaluated under the newly instituted Engineering Reliability/Integration Program. The results of the reliability study will be used in discussions with the Nuclear Regulatory Commission (NRC) to determine the licensability of the valve.

10.9. HELIUM PROCESSING COMPONENTS

A scoping review of the HTGR helium processing system has been made to identify the similarities and differences between the component design and technology for the large HTGR lead plant and the GCFR. Because of the absence of system requirements for the GCFR helium processing system, this review is preliminary. The processing components subtask has been rescheduled for FY 78, at which time the system requirements input will have been developed.

REFERENCES

10-1. "ASME Boiler and Pressure Vessel Code," (ASME 111/2).

10-2. "Prestressed Concrete Reactor Vessel (PCRV)," General Atomic, unpublished data.

10-3. "PCRV Cavity Liners and Closures," General Atomic, unpublished data.

10-4. "PCRV Thermal Barrier," General Atomic, unpublished data.

10-5. "Gas-Cooled Fast Breeder Reactor Quarterly Progress Report for the Period November 1, 1976 Through January 31, 1977," ERDA Report GA-A14240, General Atomic, February 1977.

10-6. "ASME Boiler and Pressure Vessel Code," Section III, 1974 edition (ASME 111/2).

10-7. Khoe, J. H., "Core Auxiliary Cooling System Component Development Plan," ERDA Report GA-A14109, General Atomic, March 1977.

10-8. Swanson, L. L., "GEN-SIZE, A Once-Through Steam Generator Design Code," General Dynamics, General Atomic Division, unpublished data, March 1966.

10-9. "300-MW(e) Gas-Cooled Fast Breeder Reactor Demonstration Plant," General Atomic Report GA-A13045, July 15, 1974.

11. PLANT DYNAMICS (189a No. 00638)

11.1. CONTROL SYSTEMS

The development plan for the GCFR plant control systems is nearing completion; this plan is a greatly expanded version of Ref. 11-1. References 11-2 and 11-3 have been used as guides in the preparation of the current plan, particularly for structuring the tasks. There are two major development areas in the plan: reactor and plant control systems and computer applications to plant control. The first area provides the framework for orderly development of the plant control systems required for the safe and efficient operation of the plant. Design and analysis methods will be compiled and evaluated for use in this development. Models and simulations will be generated and used to solve the control problems and to verify the solutions. The control system performance requirements will be established based on the control needs of the plant and the simulation analyses of plant dynamic characteristics. In addition, interfaces of the system with other plant systems, the operator, plant operational procedures, and off-site conditions will be defined and appropriate requirements prepared.

Conceptual control system designs will be generated and evaluated, and the need for and applicability of advanced control methods (e.g., noninteracting, optimal, and adaptive methods) will be analyzed. Following these evaluations, reference designs for the control systems will be selected, and extensive analyses with more detailed simulations will be performed to determined loop interactions, parameter sensitivities, and component requirements. Test procedures and evaluation techniques will be devised for in-plant testing of the control systems, and control system and plant failure modes will be examined to establish the effects on overall plant safety and to determine the potential for using the plant control systems to mitigate the effects of failures.

The second major development area deals with the incorporation of computers (primarily digital) into the plant control systems. This work will draw heavily upon the extensive research being done in the LMFBR program. A conceptual design of a digital control system will be developed and analyzed, and if the evaluation is favorable, the design will be considered the reference design for the GCFR plant control systems, and additional development work will be performed.

11.2. SEISMIC ENGINEERING

11.2.1. Development Plan

Work is in progress to prepare an integrated GCFR seismic development plan; a preliminary plan will be drafted in FY 77 and completed in FY 78. The objectives of the development plan are (1) to outline a seismic engineering program for the GCFR; (2) to establish the interfaces with component design activities; (3) to estimate associated schedules and costs; and (4) to establish seismic design criteria for the core, core support structure, and shielding.

The seismic engineering work will provide analyses of safety-related behavior involving modes of failure and responses, and the major factor considered will be the mechanical loading induced by earthquakes. An effort will be made to identify accidents, and a structural analysis will be performed to define safety concerns.

The development plan will coordinate the seismic engineering work for the GCFR. The design concept for a 300-MW(e) GCFR demonstration plant developed by GA will be used as the reference design (Ref. 11-4). With the exception of the core, core support structure, and shielding, the seismic technology of the HTGR will be applied to the design of GCFR structures and equipment. The seismic technology of the LMFBR will also be utilized for the seismic design of the GCFR core, core support structure, and shielding, but owing to the unique nature of these components, an independent development program will also be required.

The tasks are divided into four groups:

1. Provision of a general seismic model of the GCFR.
2. Development of special analytical methods and computer programs.
3. Development of seismic test programs.
4. Preparation of cost, manpower, and schedule estimates.

11.2.1.1. General Seismic Model of the GCFR. Seismic excitation of the NSS systems for the analysis, design, and verification of their adequacy when subjected to earthquake loadings is specified at two levels: (1) the operating basis earthquake (OBE) and (2) the SSE (Ref. 11-5). The input motion to the overall plant is specified by horizontal and vertical ground response spectra shown in Figs. 1 and 2 of Ref. 11-5. The designated shapes of the spectra and the horizontal acceleration determine the input motion. Using the seismological data, the maximum values of the ground accelerations will be determined for OBE and SSE conditions. All numerical results presented in Ref. 11-5 are for 1 g of horizontal excitation. To obtain information on the 300-MW(e) plant, the values of the design response spectra must be multiplied by the proper scale factors. These scale factors will be determined based on the seismological survey.

The seismology of a site is based on regional studies, a detailed review of the available literature (including published and unpublished reports and maps) and the interpretation of aerial photographic data, remote sensing surveys, mineralogical studies, and subsurface investigations conducted at the site.

According to requirements, response spectra and time-history analyses will be performed. Artificial time histories of 12-s duration, whose response spectra are the U.S. Atomic Energy Commission (USAEC) design response spectra, provide the input to the time-history analyses.

Figure 11-1 shows the flow diagram for obtaining the general seismic model of the GCFR. The overall seismic model of the GCFR will be formulated

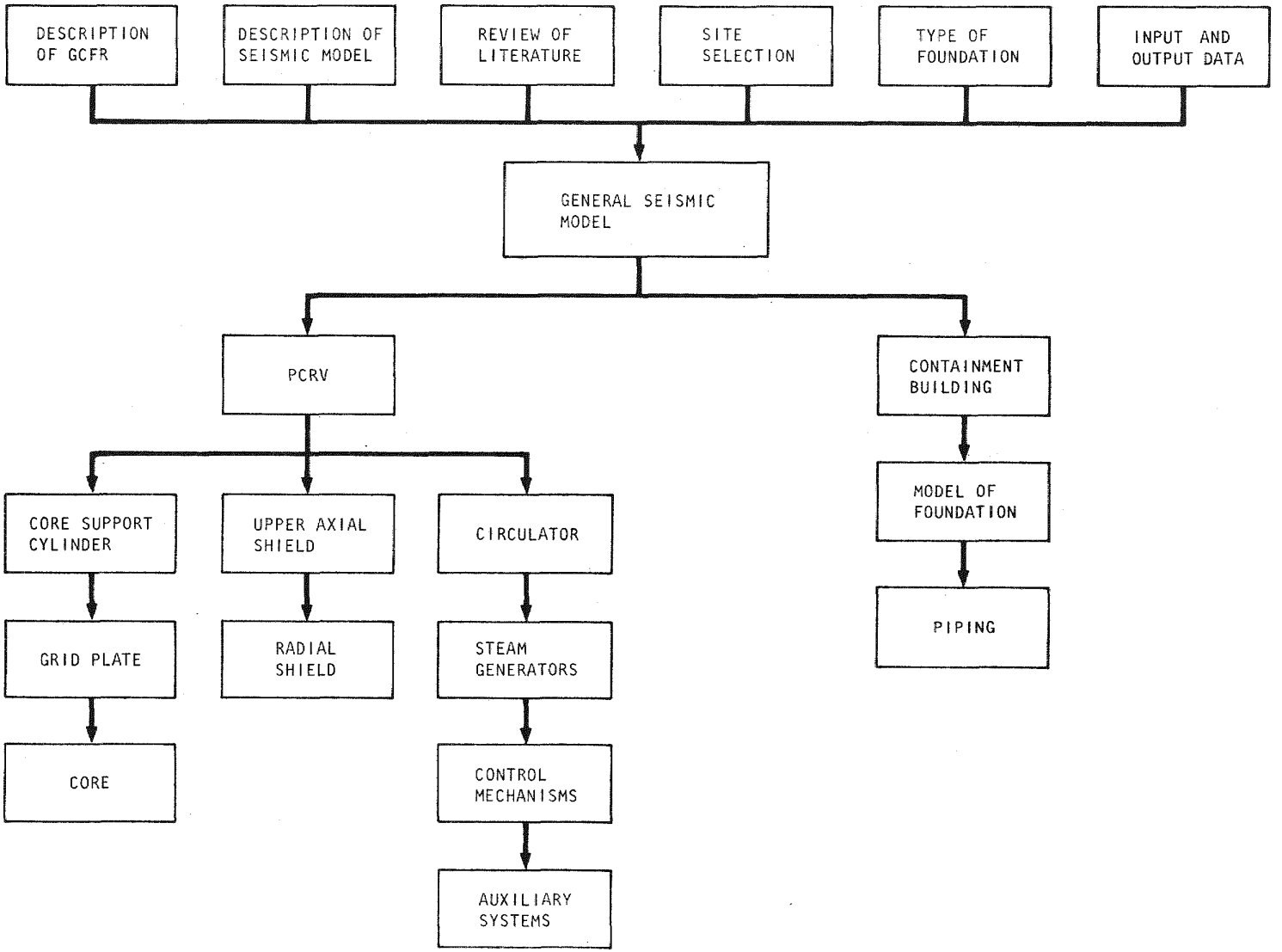

Fig. 11-1. Flow diagram for obtaining general seismic model of the GCFR

as a linear spring-mass model with 80 mass points and interconnecting elastic springs. All major components of the GCFR will be included in this model: (1) soil foundation; (2) containment building; (3) PCRV; (4) core support cylinder; (5) grid plate; (6) core; (7) radial and upper axial shields; (8) circulator; (9) steam generator; and (10) control mechanisms. The auxiliary system and piping will be optional. The output of this computer program will be the amplitudes, accelerations, forces, and stresses of each component. Some of these results will be directly used by the component designers, and other results will be applied to the detailed seismic analyses of special seismic programs.

11.2.1.2. Special Analytical Methods and Related Computer Codes. Available technical information on the HTGR, LMFBR, and pressurized water reactor (PWR) is being reviewed for its application to the GCFR. However, there are certain problems specific to the GCFR design:

1. Seismic analysis of the core, grid plate, and support structures.
2. Seismic analysis of the steam generators.
3. Seismic analysis of control mechanisms.

Since the core support structure is completely different from that of the LMFBR or any other reactor, seismic analysis requires an independent development program. This effort is divided into six parts:

1. Determination of the free vibration of the fresh core and grid plate by combined analytical and finite-element methods.

2. Study of the seismic excitation of the fresh core and grid plate by combined analytical and finite-element methods.

3. Investigation of the effect of the core support cylinder on the vibration of the combined core and grid plate.

4. Examination of the free vibration of the core and grid plate, including the effects of swelling and thermal bowing, by analytical methods.

5. Study of the seismic excitation of the combined core, grid plate, and core support cylinder, including the effects of swelling and thermal bowing, by combined analytical and finite-element methods.

6. Determination of dynamic loads, stresses, and impacts in the ducts of the core assemblies and prediction of core reactivity.

11.2.1.3. Seismic Test Programs for the GCFR. The seismic test programs required to ensure the reliability of the GCFR design or to support and verify the analytical techniques and computer programs are discussed. In some cases, the seismic development tests will be full scale, and in other cases, dynamic scale models will be applied. Available technical information from the HTGR, LMFBR, and PWR programs will be fully utilized.

The test program for the core and core support structure is divided into five parts:

1. Seismic model test of the core and grid plate.

2. Model test of the combined core, grid plate, and core support cylinder.

3. Impact test of the fuel and blanket assemblies.

4. Fracture test of the simulated duct specimens.

5. Fracture test of the simulated grid plate specimens.

A 0.15-scale model of the core and grid plate was tested in FY 76; this test program is being continued in FY 77.

11.2.2. Extension of GCFR Core Support Structural Dynamics Model Test

The first phase of the GCFR core and core support structural dynamics 0.15-scale model test was completed, and the results are reported in Refs. 11-6 and 11-7. The second phase of the test program was resumed in January 1977. Detailed measurements of the mode shapes and frequencies of the core and grid plate from 20 to 25 Hz are in progress, and the data are being reduced and evaluated. The test model was excited in the horizontal and vertical directions, and the mode shapes were measured at 21 different locations on the core and grid plate.

11.3. FLOW AND ACOUSTIC VIBRATIONS

The effort during this quarter was mainly devoted to an evaluation of the fuel and blanket assembly locking mechanisms for flow-induced vibrations and the establishment of preoperational test requirements. The ongoing conceptual design studies for the 300-MW(e) GCFR demonstration plant have produced alternate ways of locking the fuel and blanket assemblies to the grid plate, resulting in changes in the component arrangement in the upper plenum cavity. In the reference design, 238 locking assemblies and 27 control rod drive assemblies were envisaged for locking the fuel, blanket, and control assemblies to the grid plate. This implies that 238 tubes approximately 90 mm in diameter and 27 tubes approximately 175 mm in diameter (all tubes being 8.53 m long and fixed at the top at the PCRV plug and the top of the grid plate) would traverse the upper plenum. An alternate design also used 27 control rod drive assemblies, but all fuel and blanket assembly locking mechanisms were eliminated.

The results of the studies indicated that vortex-induced vibrations could occur in the reference design layout at reduced power conditions as well as in the alternate design under normal operating loads. Under full-power conditions, no vortex-induced vibrations are expected for the 256-tube array of the reference design. It was also shown that with whirling caused by the interaction of flow fields around the tubes, unstable, large-amplitude vibrations can be expected for the outer layers

of the array. With the alternate design, only stable, small-amplitude vibrations are expected. Ways of suppressing vortex-induced vibrations have been examined.

Preoperational test requirements have been established for the flow-induced and acoustically induced vibration analysis. The preoperational test requirements depend on NRC requirements, the eventual requirements of the utility, the state of the art, and the analytical efforts in the preceding phases. All testing should have a confirmatory character and be limited in scope and should consist of at least (1) one-loop, full-mass flow tests at 320°C and 9 MPa with two-thirds of the dummy core blocked off to simulate the right core pressure drop and (2) a three-loop, partial-mass flow test. The operating conditions and experimental program have been specified.

REFERENCES

11-1. "Gas-Cooled Fast Breeder Reactor Demonstration Plant Development Program Plan," v. II, Gulf General Atomic Report Gulf-GA-A10788, September 20, 1972.

11-2. "Liquid Metal Fast Breeder Reactor Program Plan," v. 4, USAEC Report WASH-1104, August 1968.

11-3. "Liquid Metal Fast Breeder Reactor Program Plan," v. 4 (2nd ed.), USAEC Report WASH-1104, December 1972.

11-4. Simon, R. H., J. B. Dee, and W. I. Morita, "Gas-Cooled Fast Breeder Reactor Demonstration Plant," in Proceedings of the American Nuclear Society Topical Meeting on Gas-Cooled Reactors: HTGR and GCFBR, Gatlinburg, Tennessee, May 7-10, 1974, p. 336 (CONF-740501).

11-5. "Design Response Spectra for Seismic Design of Nuclear Power Plants," USAEC Regulatory Guide 1 60, Revision 1, December 1973.

11-6. "Gas-Cooled Fast Breeder Reactor Quarterly Progress Report for the Period August 1, 1976 Through October 31, 1976," ERDA Report GA-A14112, General Atomic, November 1976.

11-7. "Gas-Cooled Fast Breeder Reactor Quarterly Progress Report for the Period November 1, 1976 Through January 31, 1977, ERDA Report GA-A14240, General Atomic, February 1977.

12. REACTOR SAFETY, ENVIRONMENT, AND RISK ANALYSIS (189a No. 00589)

The purpose of this task is to investigate the safety characteristics of the GCFR. A liaison and coordination subtask integrates the ERDA-sponsored GCFR safety work at GA and the national laboratories into a national GCFR safety program which is responsive to the need for GCFR safety research. A GCFR Safety Program Plan is being developed to define the safety research needed for the demonstration plant and the longer-term GCFR commercialization program. Safety research at GA includes probabilistic accident analysis, accident consequence analysis, radiological and environmental analyses, and postaccident fuel containment (PAFC) analyses.

Logical probabilistic methods are employed to determine the probabilities associated with various accident initiation and progression sequences and to identify potential design modifications which would help reduce risks. The thermal behavior of the fuel assembly duct walls under conditions of loss of shutdown heat removal is being analyzed to determine the heat-up and melting sequence of the cladding, duct walls, and fuel, because duct wall melting has been identified as an important phenomenon influencing the accident sequence. PAFC analyses are being performed to assess the capability of the current design and to identify potential modifications which could improve the molten fuel containment capability. The behavior of fuel aerosols in the PCRV and the containment is being investigated, with the initial objective of defining the level of detail which is required or desirable for analysis of aerosol behavior following low-probability accidents leading to core damage. A methodology for integrating reliability considerations into the GCFR engineering effort at the system, subsystem, and component levels is being developed for trial use on a selected system, with the objective of determining the optional use of reliability engineering methods in the GCFR.

12.1. REACTOR SAFETY PROGRAM COORDINATION

Coordination of the safety analysis programs at GA, ANL, and EG&G, Idaho, was continued and provides the means by which a cooperative safety analysis effort in support of GCFR development is maintained. A joint GA/ANL review meeting was held to assess the status of GCFR safety analysis for severe accidents leading to core melting. Extensive adaptation and use of LMFBR safety technology over the past three years has advanced the status of core disruptive accident analyses in the GCFR to a level comparable to that of the LMFBR. The extent of fuel vaporization predicted in a loss of flow accident with failure to scram is comparable to LMFBR accidents if an adiabatic expansion to the containment back pressure is assumed. However, because of the high coolant pressure and the fact that system pressure can only be slowly reduced, it is expected that future analyses of heat losses during the fuel expansion phase will significantly reduce the extent of fuel vaporization in GCFR core disruptive accidents. The work energy potential of core disruptive accidents is calculated to be very low because of the inherently low efficiency of transmitting work energy through the helium coolant to the primary coolant system boundary. For the 300-MW(e) GCFR demonstration plant, the ANL calculated work energy potential of <10 MWs (Ref. 12-1) is far below the minimum work energy absorption potential in the PCRV of 4000 MWs determined by the Naval Ordinance Laboratory (Ref. 12-2).

In response to a request by ERDA, development of a GCFR safety program plan has been initiated. The safety program plan will identify current GCFR safety research and development status and define the safety research and development program, including the associated schedules and funding requirements necessary for the demonstration plant and the longer-term GCFR commercialization effort. The safety program plan will contain three major sections:

1. Definition studies will identify the probabilistic accident analyses and system reliability analyses necessary for classifying GCFR

abnormal operating conditions into the upset, emergency, faulted, and beyond design basis accident categories.

2. The system safety technology portion will identify the safety research and development required to analyze, predict, and verify plant performance during anticipated, upset, emergency, and faulted plant conditions. The major objective of system safety technology research and development is to define the safety limits for each accident category and develop the technology for providing analytical and experimental assurance that all plant conditions meet the safety limits.

3. The core accident technology portion will identify the analytical and experimental safety research and development required to analyse and predict the consequences of low-probability accidents which exceed the safety limit and lead to core damage. The major objective of core accident technology research and development is to demonstrate that the primary system containment features provide an adequate safety margin for low-probability accidents. In order to meet this objective, the safety program plan will identify the analytical development required to predict the consequences of core melt and core disruptive accidents and the safety tests necessary to support and verify the analytical models.

12.2. PROBABILISTIC ACCIDENT AND RISK ANALYSIS

12.2.1. Introduction

Accident initiation and progression analysis (AIPA) techniques developed in FY 74 (Ref. 12-3) are being applied to the probabilistic analysis of potential accident sequences leading to low-probability, high-consequence outcomes. The consequences of these sequences are also under study at ANL and at GA under other subtasks. The objective of this work is to assess the risks of these accident chains in the GCFR.

During FY 77, the analysis effort is concentrating on two areas which have been shown by previous work to be significant in affecting GCFR risks. The first area involves the development of a more detailed probabilistic analysis of GCFR residual heat removal (RHR) systems; the second area involves the development and assessment of containment event trees for the GCFR.

12.2.2. Residual Heat Removal Reliability Analysis

During FY 77, a more detailed probabilistic analysis of GCFR RHR systems is being performed to further identify the level of achievement of the current design and to consider potential design improvements. Forced-convection shutdown cooling is achieved in the GCFR by using two separate RHR systems, each of which has multiple loops for redundancy. The normal operational RHR system utilizes steam-driven main circulators, main cooling loops, and portions of the normal steam power conversion system components. A diverse backup safety RHR system is provided by the CACS, which utilizes electric-motor-driven circulators and pressurized water loops which exhaust heat to the atmosphere. Electrical power for the continued operation of these RHR systems is provided from either off-site or redundant on-site emergency diesel supplies. Reliability models are being developed to qualitatively represent and quantify GCFR main loop, CACS, and electrical power system operation as necessary to provide RHR. Three types of key initiating events are being considered to enable a greater level of detail to be achieved in the RHR analysis effort. These events are transients (including loss of off-site power), depressurization (hole size ≤ 30 cm^2), and earthquakes (greater than or equal to the design basis earthquake).

During the previous quarter, qualitative models representing the various phases of main loop cooling were completed. During this quarter, qualitative models representing CACS and electrical power system operation were completed. These models include detailed reliability block diagrams which describe the components of the RHR systems as well as the interfaces with systems not explicitly part of the RHR function. Figure 12-1 presents

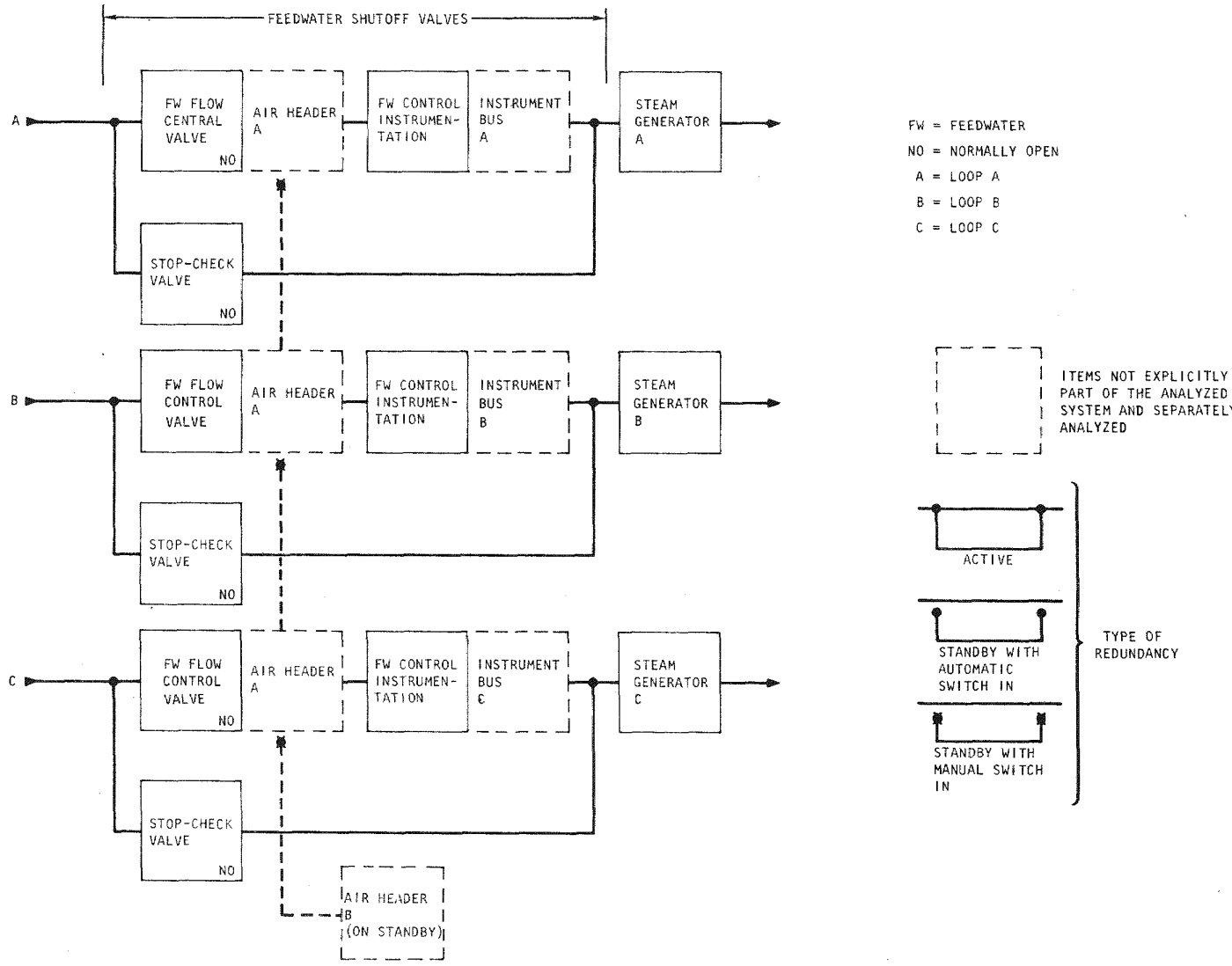

Fig. 12-1. Portion of the reliability functional block diagram for main loop RHR

a portion of such a reliability block diagram for main loop RHR and shows that for this portion of the system, each of the three main loops is independent except for a control air supply. The air supply is indicated by a common air header A "on-line" and a header B "on standby." The instrument bus supplies to the feedwater control instrumentation are independent, and the stop-check valve and feedwater control valve are in "active redundancy" with each other since both must fail to cause loop failure.

Failure modes and effects analyses (FMEA) which search for single "active" or "passive" system failures are being prepared to complement these reliability block diagrams. The effects of potential common mode failures of redundant components within the system are also being identified, and the models are being quantified with failure data developed under the gas-cooled reactor reliability data bank task (Section 15). A summary report detailing the above work is being prepared and is scheduled for completion during the next quarter.

12.2.3. Containment Event Tree Analysis

During FY 77, the accident sequence analysis work performed in previous years (Ref. 12-4) is being supplemented by the probabilistic analysis of sequences leading from a loss of coolable core geometry through containment release to the public. During this quarter, the effects of various phenomena associated with a postulated core meltdown were examined to determine the likelihood of secondary containment shell rupture. The CONTEMPT-G computer code (Ref. 12-5) is being employed to model the transient pressure and temperature response of the GCFR containment following release of helium and gaseous and volatile fission products from the PCRV. Phenomena being modeled include the potential effect of the reaction of oxide fuel, stainless steel, and fused silica with graphite in the lower shield, producing noncondensable carbon monoxide gas (Ref. 12-6). If the PCRV liner fails, decomposition of the concrete and containment base slab may generate additional noncondensable CO_2 gas. As the concrete heats up, water is driven off in the form of steam, which may rise through the melt

and react with molten steel to produce flammable H_2 gas. These products of concrete decomposition are also considered in the analysis. The analysis, which will be completed during the next quarter, indicate that even for the most conservative assumptions, the containment would not approach failure pressure or temperature limits before 24 hr.

12.3. ACCIDENT CONSEQUENCE ANALYSIS

12.3.1. Introduction

The consequences of low-probability accident sequences leading to core damage are investigated under this subtask to determine the expected behavior of the GCFR core and the performance of its activity barriers in mitigating the potential release of activity from the containment. During FY 76, analyses were performed to determine the assembly duct wall heat-up and melting sequence relative to fuel heat-up during a loss of decay heat removal accident. During this quarter, analyses of thermal bowing of declad fuel rods and the effect of bowing on heat transfer to the duct wall and induced stress distributions were completed. Fission and breeding product activity inventories in the GCFR core are being calculated, and several aerosol analysis codes have been received and are being made operational.

12.3.2. Loss of Decay Heat Removal Accident Analysis

A complete loss of all forced circulation in the shut-down reactor leads to monotonic heat-up of the core, resulting in initial cladding melting near the core axial midplane. Molten cladding drains toward the lower axial blanket and is expected to refreeze in the lower blanket region. Intensive heat transfer from the outermost declad fuel to the duct wall leads to initial duct melting at the duct midflat. Duct melting progresses sideward to the duct corner as well as axially away from the core midplane. The lateral temperature gradients which are induced in the outermost rows of fuel rods owing to heat losses to the duct wall cause the declad fuel rods to bow, and thermal stresses are induced.

12.3.3. Fuel Rod Bowing and Thermal Stresses

The results of previous fuel rod bowing analyses (Refs. 12-7, 12-8) show a tightening up of the rod bundle toward the assembly center. Bundle tightening is significantly influenced by the boundary condition at the core - upper blanket interface and by the rod-to-rod spacing. As a result of the two-dimensional temperature distribution, thermal stresses are produced in the fuel rods concurrent with bowing, and additional stresses are induced owing to interference forces exerted on the rods.

The axial normal stresses generated in the fuel rods at the time of duct melting have been analyzed for the rods located along a traverse to the duct midflat and along a traverse to the duct corner. These traverses are shown in Fig. 12-2. The largest temperature gradients in the transverse direction exist at the time of duct melting, during the loss of decay heat removal accident sequence. At this time, the cladding and grid spacers have melted over the core length such that the fuel rods are laterally unsupported over the core length. The temperature distribution in a fuel rod is approximated as a linear function across the rod and a cosine function in the axial direction. Support of the fuel rods at the core - lower axial blanket interface is assumed to be fixed owing to the refrozen cladding. At the core - upper blanket interface, three boundary conditions are considered: namely fixed, pinned, and free. For the fixed and pinned upper boundary conditions, thermal stresses are produced in the fuel rods; for the free upper boundary condition, no thermal stresses are developed. Furthermore, in the case of fixed-pinned or fixed-free connections, there are additional stresses induced in the fuel rods as a result of either rod-to-rod interference or deflection restraint provided by the duct wall at the free ends of the fuel rods (Ref. 12-8). These stresses have been calculated using standard formulas for flexure of one-dimensional narrow beams and have been superimposed on the thermal stresses corresponding to the cases with fixed-pinned or fixed-free connections to obtain the combined stresses developed in the fuel rods. The combined stresses produced in the fuel rods are shown in Figs. 12-3 through 12-5. These stresses are at a maximum at the

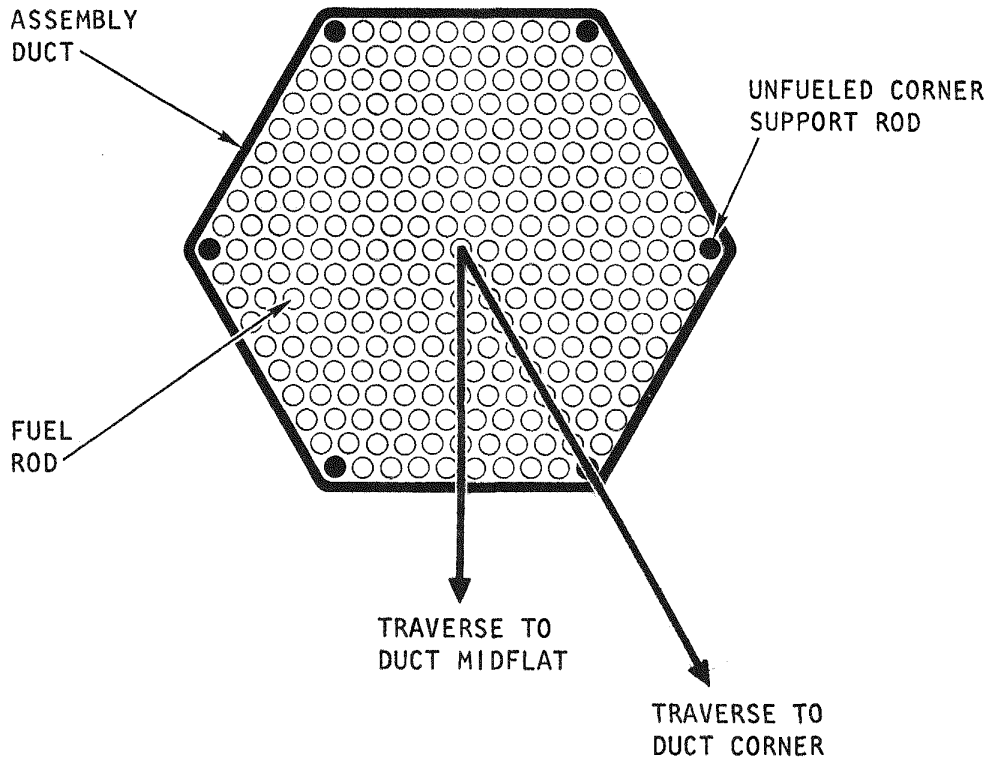

Fig. 12-2. Fuel assembly cross section

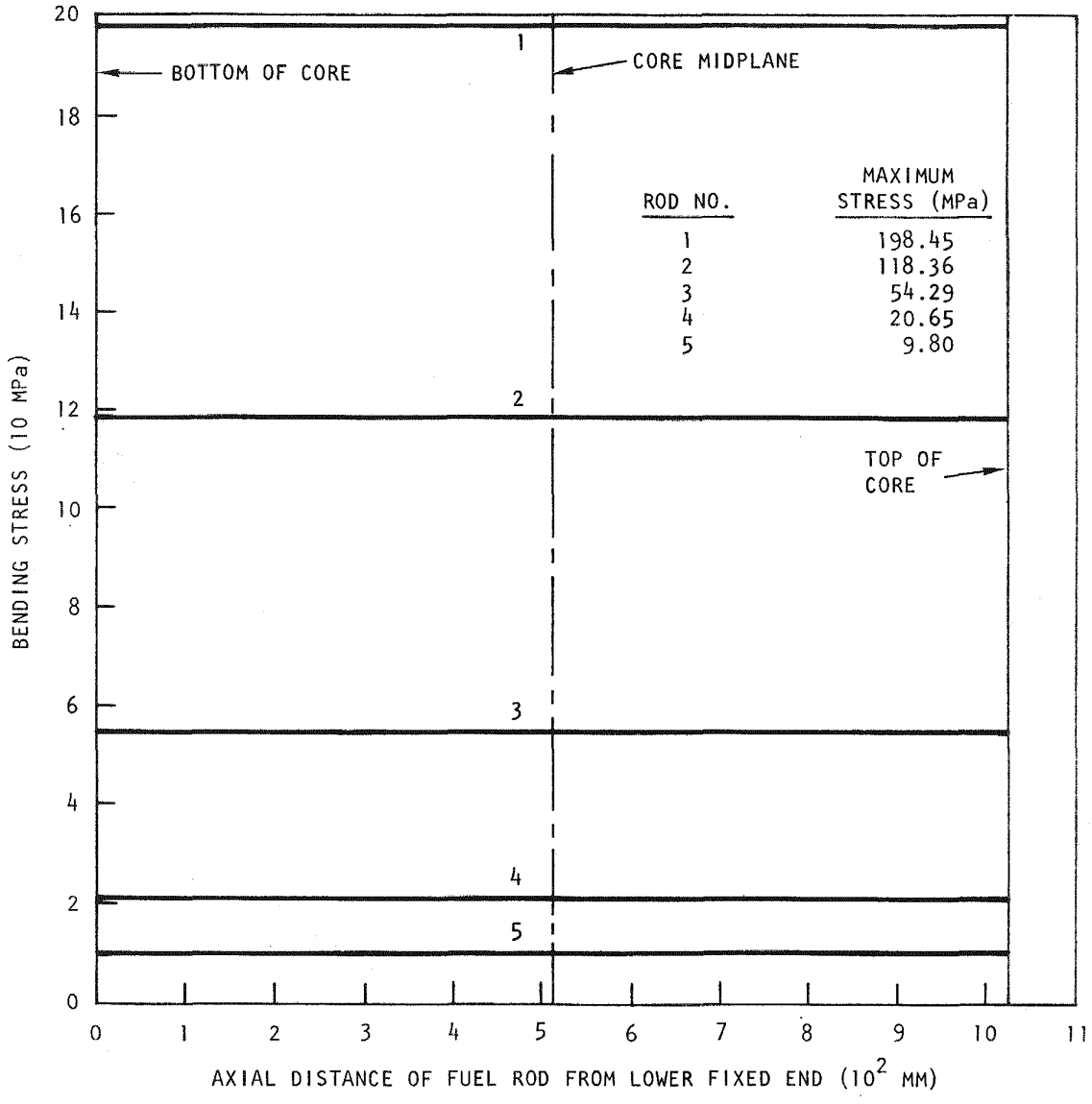

Fig. 12-3. Thermal bending stress in the axial direction of the fuel rod along a traverse to the duct midflat at the time of duct melting; end supports are fixed-fixed

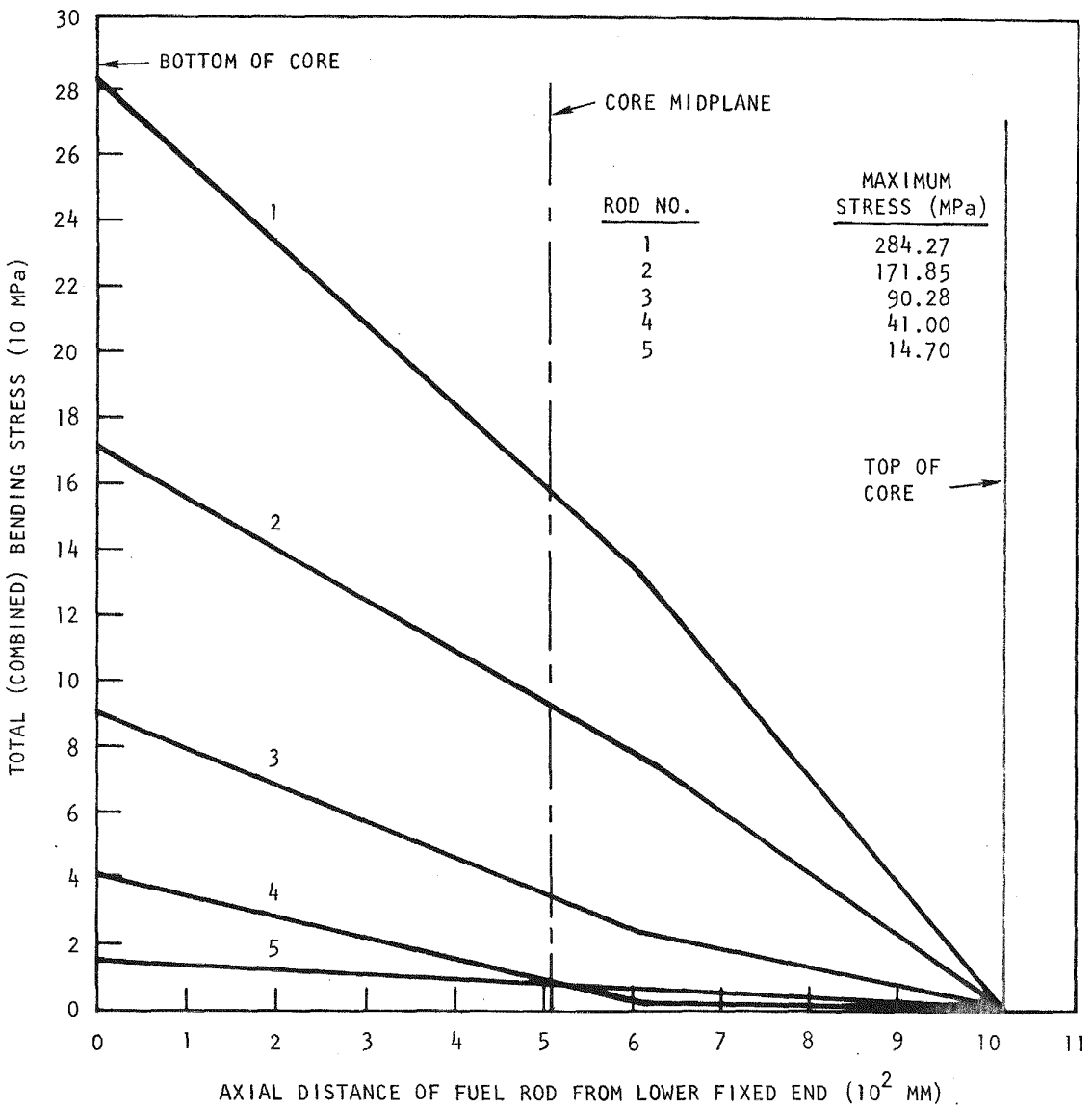

Fig. 12-4. Total bending stress in the axial direction of the fuel rod along a traverse to the duct midflat at the time of duct melting; end supports are fixed-pinned

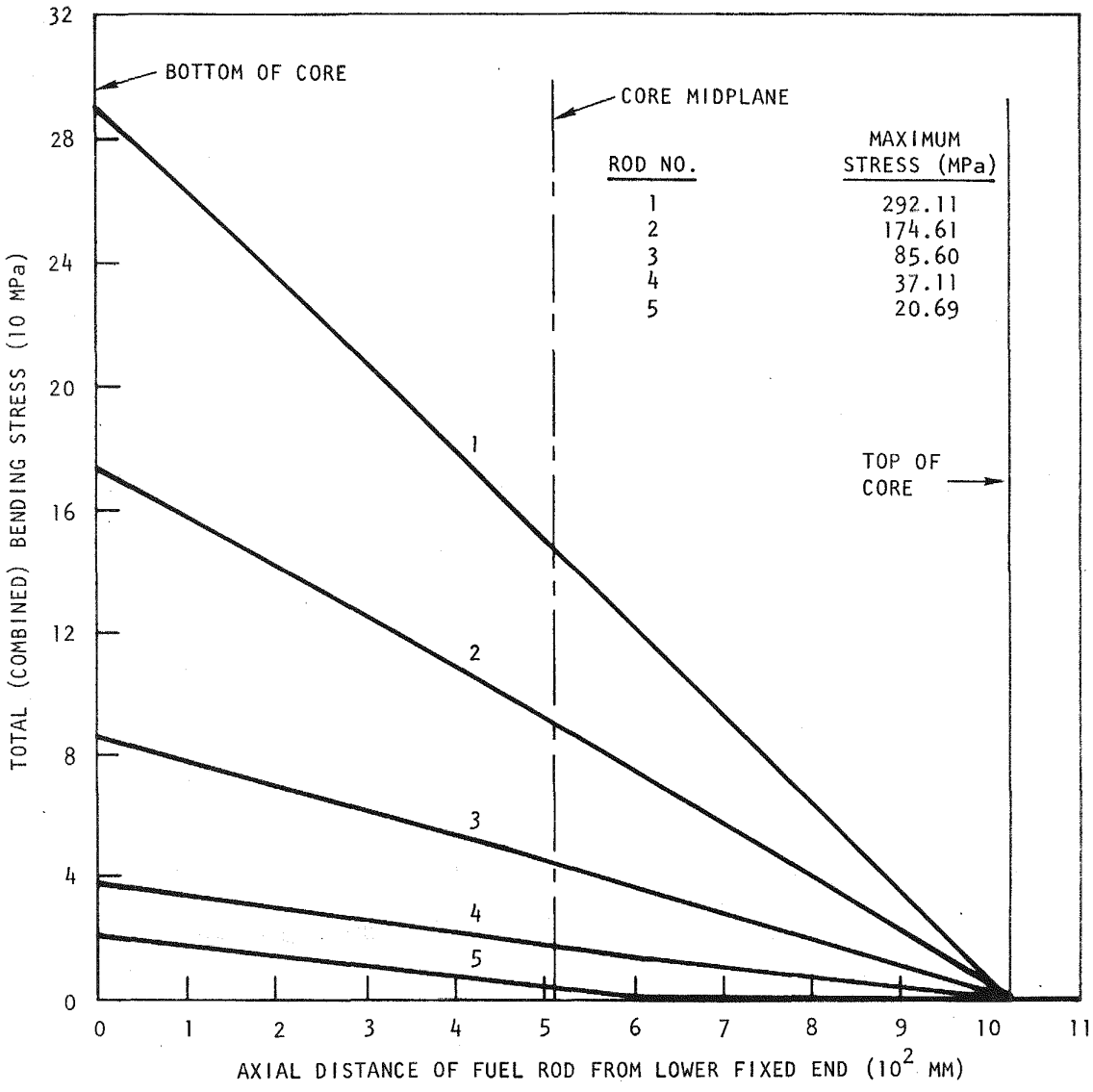

Fig. 12-5. Total bending stress in the axial direction of the fuel rod along a traverse to the duct midflat at the time of duct melting; end supports are fixed-free

outermost fibers of the declad fuel rod, i.e., on the surface of the fuel rod. The normal surface stresses (maximum stresses) are plotted as a function of the axial coordinate, originating at the lower fixed end of the fuel rod. The largest surface stresses are tabulated, and the rods are numbered from the duct toward the assembly center. The stresses produced in the fuel rods are significantly influenced by the choice of upper boundary support.

The thermal stress distribution in the fuel rods for a fixed end support at the top of the core with no interference between rods is given in Fig. 12-3. This boundary support would be approached if the restraining moment from the unmelted cladding in the upper axial blanket were large and the pellet bonding strong. There are no externally induced forces exerted on the fuel rods for this case since there is no interference between rods (Ref. 12-6). Because of symmetrical boundary conditions, the constraining moments at the end supports are equal, and therefore the resulting stresses are constant over the length of the fuel rod.

A weak restraining moment by the unmelted cladding in the upper axial blanket is simulated by a pinned connection at the top. The combined maximum stress profiles for the fuel rods, with the rods pinned at the core - upper blanket interface, are shown in Fig. 12-4. The moment in the fuel rod varies linearly with the axial coordinate of the rod. The maximum moment occurs at the lower fixed end of the fuel rod and approaches zero at the upper pinned end. Therefore, the maximum stresses occur at the lower end of the fuel rods.

If bonding of fuel pellets is weak near the top of the core, the fuel rods could become detached at the core - upper blanket interface as a result of bowing-induced stresses. Such a condition is simulated by a free upper boundary support. In this case, the maximum stresses produced in the fuel rods include the stresses induced by deflection restraint by the duct wall at the free upper end and rod-to-rod interference. The resulting stress profiles are shown in Fig. 12-5. The maximum peak stresses occur at the lower end of the fuel rods.

For comparison, thermal, induced, and combined maximum stresses are given in Table 12-1 for the three types of end supports. The volumetric average temperatures of the fuel rods and the fracture strength of unirradiated mixed oxide fuel (UO_2-20 wt % PuO_2) evaluated at the volumetric average temperatures of the fuel rods are also listed. The fuel rods located along a traverse to the duct midflat experience the largest maximum stresses, and the fuel rods located along a traverse to the duct corner also develop high stresses. The outer two rows of fuel rods in the central assembly experience peak stresses on the rod surface which exceed the fracture strength of the fuel evaluated at the volumetric average temperatures of the fuel rods. Since the average temperature of these fuel rods is in the range 1400° to 1800°C, failure of the fuel rods is likely to occur in either a brittle fashion by rapid growth of minute cracks in the material or a semibrittle manner with some plastic deformation prior to failure. The bending stress in tension is of importance since the fracture strength of ceramics such as $(U,Pu)O_2$ is an order of magnitude lower in tension than in compression. Furthermore, the fracture strength of sintered fuel pellet stacks is expected to be lower than that of a solid fuel rod.

It is concluded that as a result of adverse temperature conditions existing in the fuel rods during a loss of decay heat removal accident, high stresses are developed in the fuel rods located in the outer two rows of the central fuel assembly. In addition, the fuel rods in the outermost row or in the outer two rows of the central fuel assembly develop stresses which exceed the fracture strength of the fuel. The possible reduction in the residual stresses due to primary creep has not been taken into account in the analysis for lack of empirical correlations and experimental data in the primary creep region for the mixed oxide fuel.

To further support and substantiate the conclusions drawn from this study, the following observations and recommendations are made:

1. A few loss of flow tests (Ref. 12-8) have indicated that the declad, sintered pellet stacks would fuse together and maintain an integral

TABLE 12-1
STRESSES GENERATED IN THE FUEL RODS DUE TO THERMAL BOWING, ROD-TO-ROD INTERFERENCE, AND DEFLECTION RESTRAINT BY THE DUCT WALL FOR RODS LOCATED ALONG A TRAVERSE TO THE DUCT MIDFLAT AT THE TIME OF DUCT MELTING

Rod No.	Volumetric Average Temperature (°C)	Fracture Strength[a] σ_f (MPa)	Stresses at Location of Maximum Total Stress						
			Fixed-Fixed End Supports	Fixed-Pinned End Supports			Fixed-Free End Supports		
			Maximum Thermal Stress (MPa)	Thermal Stress (MPa)	Induced Stress Due to Rod-to-Rod Interference (MPa)	Combined Maximum Stress (MPa)	Induced Stress Due to Deflection Restraint At Free End By Duct Wall (MPa)	Induced Stress Due to Rod-to-Rod Interference (MPa)	Combined Maximum Stress (MPa)
1	1488.59	131.34	198.45	297.68	-13.41	284.27	294.94	-2.82	292.12
2	1745.87	146.52	118.36	177.54	-5.69	171.85	170.54	4.07	174.61
3	1891.98	155.14	54.29	81.43	8.85	90.28	71.55	14.04	85.59
4	1967.78	159.62	20.65	30.98	10.02	41.00	18.58	18.53	37.11
5	1997.65	161.38	9.80	14.70	0.0	14.70	0.0	20.69	20.69

[a] $\sigma_f = 27.4 + 0.059T$ (K).

rod geometry until the onset of melting. However, this evidence is not conclusive, and further verification of this behavior is needed.

2. The strength characteristics of bonded fuel pellet stacks are also not known, although out-of-pile, direct electric heating experiments at ANL are expected to yield information on the bending strength of bonded fuel pellet stacks. This information is vital for determining the validity of the analysis.

3. Primary creep data are needed to determine whether the creep is significant enough to relieve a portion of or all the residual stresses in the fuel rods.

4. If the primary creep rate is not significant, the failure and propagation of failure of the remaining rods which may be induced by the failure of the outermost rows of rods in the fuel assembly will have to be investigated.

5. Relocation of fractured pieces of fuel within the fuel assembly depends largely on the core geometry prevailing during the time of fuel failure. The effect of potential fuel distribution on subcriticality shall be assessed.

12.3.4. Radiological Analysis

Preparation for a preliminary analysis of fuel aerosol behavior in the GCFR has been continued, and the applicability of the analytical methods and test data of the LMFBR aerosol program to GCFR conditions is being reviewed. Three aerosol codes developed under the LMFBR program have been received and are being converted to the GA UNIVAC 1110 computer system. The HAARM-2 code (Ref. 12-9) is an extension of the HAA-3 code (Ref. 12-10) developed by Atomics International (AI). The current version of HAARM-2, which is sponsored by the NRC Reactor Safety Research Division, has been received

from HEDL. The PARDISEKO-III code (Ref. 12-11) has been developed by KFK in Germany and has been successfully tested against the HAARM-2 code; however, it appears to require extensive computer time. A current version of the code has been received from ORNL. The GALP code (Ref. 12-12) is being developed by General Electric (GE) for the analysis of aerosol behavior in pipe flow. This code has been set up on the GA computer, and a sample problem has been successfully executed. It is expected that this code will have primary application to the analysis of aerosol behavior in the GCFR primary system inside the PCRV and in the PCRV relief valve train.

The primary difference between GCFR aerosol conditions and LMFBR conditions appears to be in the high-pressure behavior environment in the PCRV and the elevated temperatures in the primary system. The applicability of LMFBR codes to GCFR conditions will be investigated prior to extended use of these codes. Some possible code modifications may be identified as a result of this assessment.

12.4. POSTACCIDENT FUEL CONTAINMENT

A study on downward heat removal considering chemical reactions between the graphite, core, and shielding materials was reported in Ref. 12-6. Previous analyses did not consider the heat of reaction (endothermic) in the thermal model, and thus the results were conservative. During this quarter, a more detailed model was prepared which included the oxide fuel - graphite chemical reactions in the heat transfer calculations; i.e., reaction heat absorption was treated as a heat sink at the oxide fuel - graphite interface. Cases with and without cooling have been studied.

12.4.1. Chemical Reactions Between Oxide Fuel and Graphite

Experimental investigations of chemical reactions between a UO_2 - stainless steel mixture and graphite are reported in Ref. 12-13; however, most of the results are qualitative. The input for the present analysis is mainly based on the experimental results of Ref. 12-14, in which only

the UO_2 - graphite reaction was investigated, and no participation of steel was assumed. According to the experimental findings of Ref. 12-14, only a UC layer is formed between the UO_2-graphite interface for temperatures less than 2000°C, whereas UC and UC_2 layers are present for an interface temperature greater than 2000°C. The mean thickness of the carbide layers versus the square root of time is shown in Fig. 12-6 (from Ref. 12-14).

The rate of reaction heat absorbed during the chemical reactions may be obtained by using information from Ref. 12-15:

$$H_r = 7.74 \times 10^8 \text{ J/kg-mole (UC or } UC_2) \quad .$$

Based on a UC density of 13,600 kg/m^3, a UC_2 density of 11,700 kg/m^3, and a reactor cavity floor area of 23.64 m^2, the reaction heat may be expressed as joules per unit thickness of the carbide product, or

$$H_r = 9.96 \times 10^8 \text{ J/mm-UC} \quad ,$$

$$= 8.18 \times 10^8 \text{ J/mm-}UC_2 \quad .$$

According to Ref. 12-13, with the participation of stainless steel, the chemical product is the mixed carbide $UFeC_2$ which has a melting temperature of 2000°C. Therefore, in the present analysis, the UO_2-graphite reaction is considered to be diffusion controlled for interface temperatures less than 2000°C, and a bare reaction rate (without accumulation of the carbide products) is used when the products are molten. The quantity of carbon monoxide generation in kilograms can be found from the amount of carbide formed, i.e., carbon monoxide generation = 72.0 x mm of UC formed and 59.0 x mm of UC_2 formed.

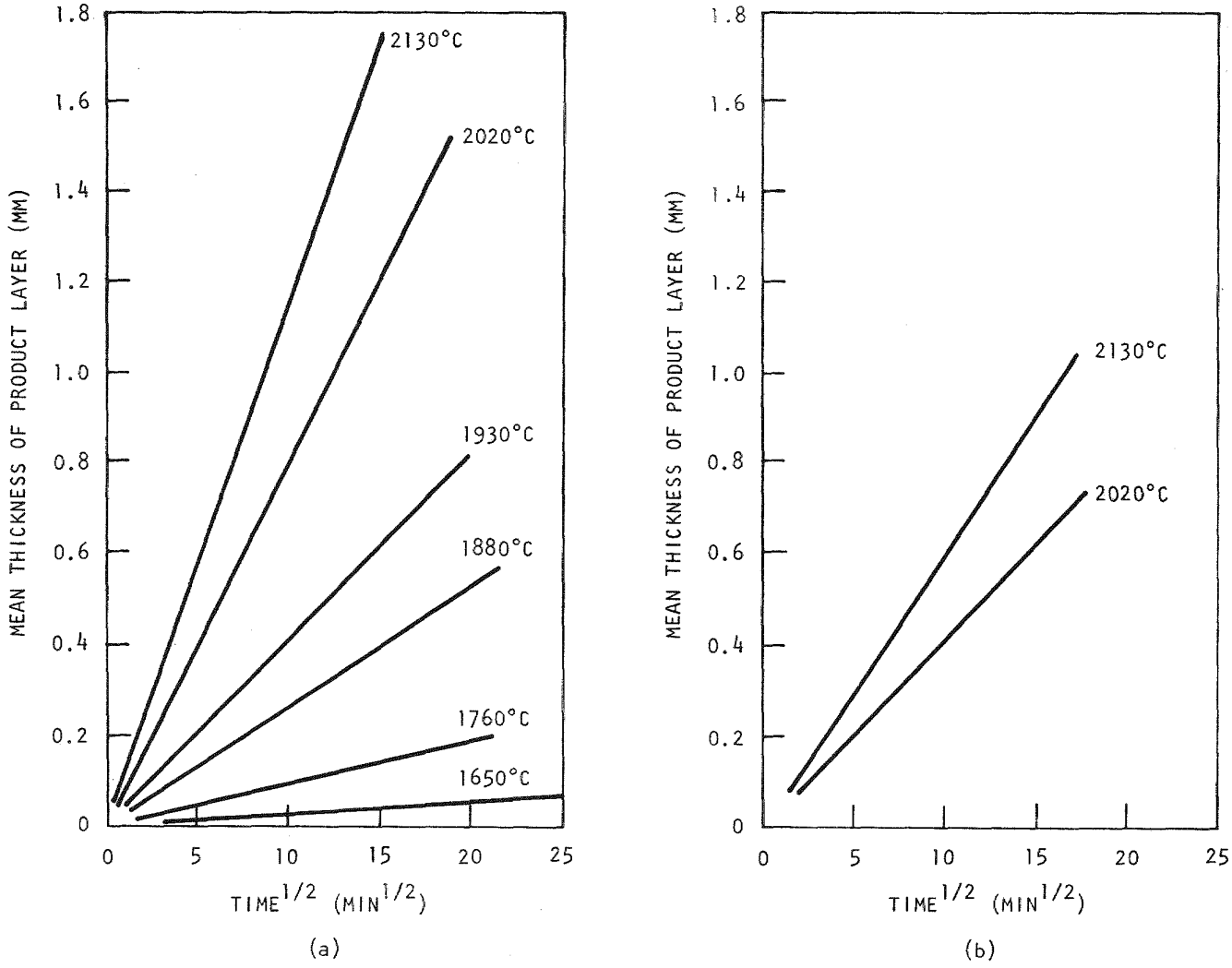

Fig. 12-6. Mean thickness of uranium carbide layer vs square root of time: (a) formation of UC, (b) formation of UC_2

12.4.2. Debris Layer Models

The computational model for the analysis is shown in Fig. 12-7. Three debris layer models were studied:

1. In model A, chemical reactions are completed early in the transient analysis, and debris layers are represented by a homogeneous layer of the chemical products.

2. In model B, chemical reactions proceed at a slow rate, and debris layers contain a homogeneous mixture of UO_2 and stainless steel.

3. In model C, flotation of stainless steel (from the lower shield above the graphite layer) is completed early. A layer of stainless steel overlays a layer of UO_2.

For each of the above models, the core debris resulting from a full core meltdown was assumed. In the transient process, the thickness of the graphite layer is reduced according to the percentage of completion of the chemical reaction.

12.4.3. Carbon Monoxide Generation for the Case Without Cooling

Heat transfer calculations were made for the three different models with the conservative assumption of no external cooling to maximize the reaction rate. The results are shown in Table 12-2. Model C, with stainless steel overlaying UO_2, is the most conservative: the time to reach liner melting is the shortest, and the carbon monoxide generation is the greatest at any instant during the transient process. The UO_2-graphite chemical reaction is 8% complete at the time of liner melting and 26% complete at the end of 24 hr. Three-quarters of the downward-flowing decay heat is absorbed by chemical reactions at the end of 24 hr. This indicates that the effects of chemical reactions are important in heat transfer calculations. For all three models, the quantity of carbon monoxide in the containment is far below the flammability limit.

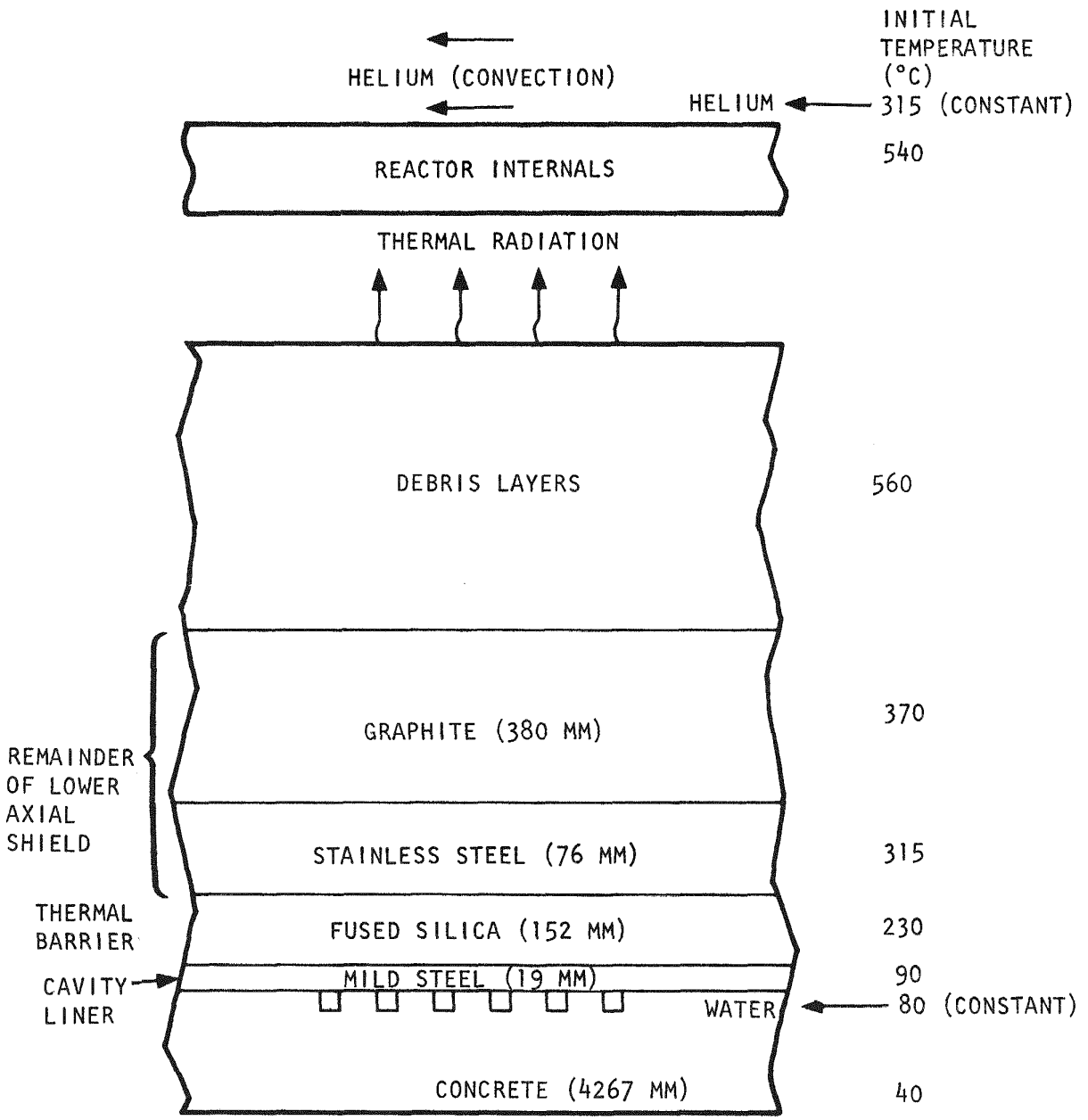

Fig. 12-7. Computational model for the analysis with material interactions

TABLE 12-2
CARBON MONOXIDE GENERATION FOR DIFFERENT DEBRIS LAYER MODELS WITHOUT COOLING

	Model[a]		
	A	B	C
Time to reach liner melting (hr)	15.5	20	14
At time of liner melting (no cooling)			
Carbon monoxide generation (kg)	403	468	835
Percentage of completion	3.9	4.5	8
Ratio of reaction heat/ downward heat	0.34	0.38	0.39
At end of 24 hr			
Carbon monoxide generation (kg)	1308	1108	2736
Percentage of completion	12.5	11	26
Ratio of reaction heat/ downward heat	0.63	0.56	0.74
Carbon monoxide in containment[b] (%)	1.8	1.6	3.8
Molten fuel temperature (°C)	2112	2905	2805

[a] Model A is a mixture of carbide products; B is a mixture of UO_2 and stainless steel; and C is stainless steel overlaying UO_2.

[b] Flammability limit of carbon monoxide in air is about 11% (Ref. 12-16).

12.4.4. CO Generation for the Case With Cooling

Heat transfer calculations were also made for conditions in which helium cooling and cavity liner cooling are available. Only model C was studied, but the thermal barrier thickness was allowed to vary. The results are given in Table 12-3. It can be seen that with liner cooling, the cavity liner temperatures are quite low so that liner buckling can be avoided. For the case of a 153-mm thermal barrier, the UO_2-graphite chemical reaction may reach 60% completion, but for a 51-mm and a 25.5-mm thermal barrier, only 9% and 1.5% completion, respectively, will be reached. The carbon monoxide concentration in the containment for the 153-mm thermal barrier will reach 8%, which is close to the flammability limit for carbon monoxide in air at 11% (Ref. 12-16). Therefore, in order to avoid the combustion hazard, either a thinner thermal barrier or a protective layer above the graphite, such as a layer of boron nitride, can be adopted.

12.5. LICENSING SUPPORT AND INTEGRATION

As part of the licensing support activity, the CRBR licensing proceedings are being monitored in order to obtain guidance on NRC positions with respect to core disruptive accidents in fast reactors. The CRBR plant safety margin licensing requirements and the types of analyses needed to establish compliance with these requirements are being evaluated to provide direction for the scope of the analyses necessary for beyond design basis accidents for the GCFR demonstration plant. Efforts are being directed toward a resumption of the GCFR prelicensing review by the NRC and the Advisory Committee on Reactor Safety (ACRS). Although resumption of the NRC review is currently limited by manpower, it appears that a resumption of the ACRS review may proceed in the near future. Preparations have been made for an ACRS subcommittee hearing in June which will concentrate on the progress of the design and safety-related aspects of the GCFR demonstration plant since completion of the initial review in 1974.

TABLE 12-3
CARBON MONOXIDE GENERATION WITH COOLING FOR
DIFFERENT THERMAL BARRIER THICKNESSES

	Thermal Barrier Thickness		
	153 mm	51 mm	25.5 mm
Maximum cavity liner temperature (°C)	143 (at 29 hr)	175 (at 21 hr)	192 (at 15 hr)
Maximum percentage of completion of chemical reaction (%)	60 (at 90 hr)	9 (at 40 hr)	1.5 (at 25 hr)
Carbon monoxide in containment (%)	8	1.2	0.21

12.6. ENGINEERING RELIABILITY INTEGRATION

12.6.1. Introduction

During the first quarter of FY 77, a new subtask was initiated in response to an ERDA request to investigate analytical methods for predicting the reliability of new components and/or systems. The major objective under this subtask is to identify the methods to be used in integrating reliability considerations into the GCFR engineering effort. A secondary objective is to begin applying these methods to a selected safety-related system and component.

12.6.2. Methods Identification

In line with meeting the objectives for FY 77, a survey of reliability programs has been completed by EG&G (Ref. 12-17). This survey focuses on three of the most widely used reliability standards, MIL-STD-785A, NPC-250-1, and RDT F2-9T. These standards originated in the Department of Defense, The National Aeronautics and Space Administration, and ERDA, respectively. The standards were reviewed to identify the requirements common to all three. The survey describes the benefits, costs, and problems experienced in the implementation of reliability programs. Recommendations made by EG&G for a GCFR reliability program include the following:

1. The design engineer should do his own failure mode and effects analysis.

2. The methods used in the reliability program should be as simple as possible.

3. Suppliers of components should be required to provide data which support the assumption of reliability as well as the functional ability of the equipment.

12.6.3. Sample System and Component Methods Application

During this quarter, the auxiliary loop cooling system and auxiliary loop isolation valve were selected as the safety-related system and component, respectively, to be studied. The lack of a natural-convection capability or passive heat sink in the GCFR makes the reliability of RHR a key safety issue. The auxiliary loop cooling system provides the safety residual heat removal capability for the GCFR following all accident conditions. The auxiliary loop isolation valve was selected because it is an uncoded component for which a probabilistic approach may be of direct benefit. It is a relatively simple device whose interactions with other systems are fairly well understood. The similarity of the GCFR auxiliary loop isolation valve and the HTGR auxiliary loop isolation valve may permit the use of historical data on valve operation from the Fort St. Vrain HTGR in the evaluation of the methods developed under this subtask.

REFERENCES

12-1. "Gas-Cooled Fast Reactor Core Disruption Accidents," Argonne National Laboratory Report ANL/RAS/GCFR-76-1, November 1976.

12-2. "Preapplication Safety Evaluation of the Gas Cooled Fast Breeder Reactor," USAEC Project 456, August 1, 1974.

12-3. "GCR Accident Initiation and Progression Analysis - Progress Report for the Period February 1 Through June 30, 1974," USAEC Report GA-A13094, General Atomic, October 8, 1974.

12-4. Kelley, A. P., Jr., "Gas-Cooled Fast Breeder Reactor Accident Initiation and Progression Analysis Progress Report for the Period July 1, 1975 Through June 30, 1976," ERDA Report GA-A14079, March 1977.

12-5. Houghton, W. J., and L. L. Turner, "Operation of the CONTEMPT-G Containment Analysis Program on the Univac 1108 Computer," General Atomic Report GA-A12692 (Supplement A), February 8, 1974.

12-6. "Gas-Cooled Fast Breeder Reactor Quarterly Progress Report for the Period November 1, 1976 Through January 31, 1977," ERDA Report GA-A14240, February 1977.

12-7. "Gas-Cooled Fast Breeder Reactor Quarterly Progress Report for the Period August 1, 1976 Through October 31, 1976," ERDA Report GA-A14112, General Atomic, November 1976.

12-8. Spencer, B. W., et al., "Summary and Evaluation of R-Series Loss-of-Flow Safety Tests in TREAT," in Proceedings of ANS/ENS International Meeting on Fast Reactor Safety and Related Physics, October 1976.

12-9. Reed, L. D., and J. A. Gieseke, "HAARM-2 Users Manual," Battelle Memorial Institute Report BMI-X-665, 1975.

12-10. Hubner, R. S., E. V. Vaughan, and L. Banmash, "HAA-3 User Report," Atomics International Report AI-AEC-13038, 1973.

12-11. Jordan, H., W. Schikarski, and H. Wild, "Nuclear Aerosols in Enclosed Systems," EURFNR-1227, 1974.

12-12. Huang, T. C., "Review and Development of Aerosol Analytical Methods," ERDA Report GEAP-14147, General Electric, September 1976.

12-13. Peehs, M., et al., "Experimental Investigation on the Compatibility of a SNR-Type Corium with Graphite," Paper Presented at the International Meeting on Fast Reactor Safety and Related Physics, Chicago, Illinois, October 1976.

12-14. Craven, B., and E. R. McCartney, "Studies of Reactions Between Uranium Dioxide and Graphite," J. Am. Ceram. Soc. 44, 12-15 (1961).

12-15. Wicks, C. E., and F. E. Block, "Thermodynamic Properties of 65 Elements - Their Oxides, Halides, Carbides, and Nitrides," Bureau of Mines Bulletin 605, 1963.

12-16. Bone, W. A., D. M. Newitt, and C. M. Smith, "Gaseous Combustion at High Pressures, Part IX: The Influence of Pressure Upon the 'Explosion Limits' of Inflammable Gas-Air, etc., Mixtures," Proc. Royal Soc. (London), Ser. A 117, 553 (1928).

12-17. Navetto, C. J., and M. E. Stewart, "A Survey of Reliability Programs," EG&G Report RE-S-77-12, March 1977.

13. GCFR SAFETY TEST PROGRAM (189a No. 00588)

It is the responsibility of GA to coordinate the National GCFR Safety Test Program; GA will review and direct the program so that it is responsive to safety test needs and identifies new test needs for which test plans must be proposed and implemented on a time scale which is consistent with GCFR program needs.

13.1. GRIST-2 PROGRAM

The GRIST Program is being developed by ERDA, ANL, EG&G, and GA as a follow-on to analytical and experimental programs being conducted under the LMFBR and GCFR programs. The objective of the GRIST program is to go beyond design basis accidents and, in particular, to investigate the behavior of melted cladding and fuel. The GCFR Safety Program Review Committee has reached the consensus that GCFR fuel tests in a transient facility are needed to investigate fuel behavior during unprotected loss of flow and reactivity insertion transients. Acting on this recommendation, ERDA has directed that work commence on a transient GCFR test facility.

The GRIST-2 loop system is in the conceptual design phase, and test train development has been initiated at ANL. During this quarter, the GRIST-2 loop system requirements for the conceptual design phase were finalized and issued by EG&G (Ref. 13-1).

In response to ERDA Nuclear Research and Applications Division requests for inclusion of GRIST-2 program requirements in the SAREF program, the ERDA Reactor Development and Demonstration Division has requested definition of the GRIST-2 requirements for the SAREF program in two specific areas: (1) the transient reactor test facility (TREAT) upgrade and (2) the support facilities [hot fuel examination facility (HFEF), test train assembly

facility, transport facilities, etc.). Preparation of these documents is in progress and their submission to the SAREF office is planned for June.

The GRIST-2 program organization and organizational responsibilities were discussed by representatives of GA, EG&G, ANL, and ERDA; Fig. 13-1 presents an outline of GRIST-2 program organization and responsibilities, and Fig. 13-2 indicates the major hardware interfaces. GA is responsible for direction of the overall GRIST-2 program, and it shall be guided by the objective that the program develop an experimental core safety technology basis which serves the objectives of the GCFR program and is consistent with the GCFR development schedule. GA will develop a GRIST program management plan; an overall program schedule; program objectives, criteria, and requirements; and a safety test program plan. GA is also responsible for the design and fabrication of test fuel rods and test bundle grid spacers, including the test fuel rod preirradiation program. Fuel rod preirradiation will provide information on in-pile GCFR fuel rod performance under pressure-equalized conditions.

EG&G is responsible for the design, fabrication, installation, and operational checkout of the GRIST-2 loop system and in-pile tube, including loop-related control and data acquisition systems. EG&G will also perform major system maintenance and train TREAT personnel in loop system operation; this includes development of operating manuals and safety envelope analysis reports. EG&G will also verify loop system readiness prior to a test and evaluate loop system performance following a test.

ANL is the designated GRIST-2 experimenter and is therefore responsible for all aspects of test train development, fabrication, and instrumentation. For each test, ANL is responsible for test planning, specification, safety analysis, pre- and post-test analyses, postirradiation examination, and test evaluation. GRIST program planning will proceed on the assumption that the TREAT operations group is responsible for operation during a TREAT test and routine maintenance of the GRIST loop system. The TREAT operations group is also responsible for assembly and disassembly of GRIST equipment at the TREAT reactor top.

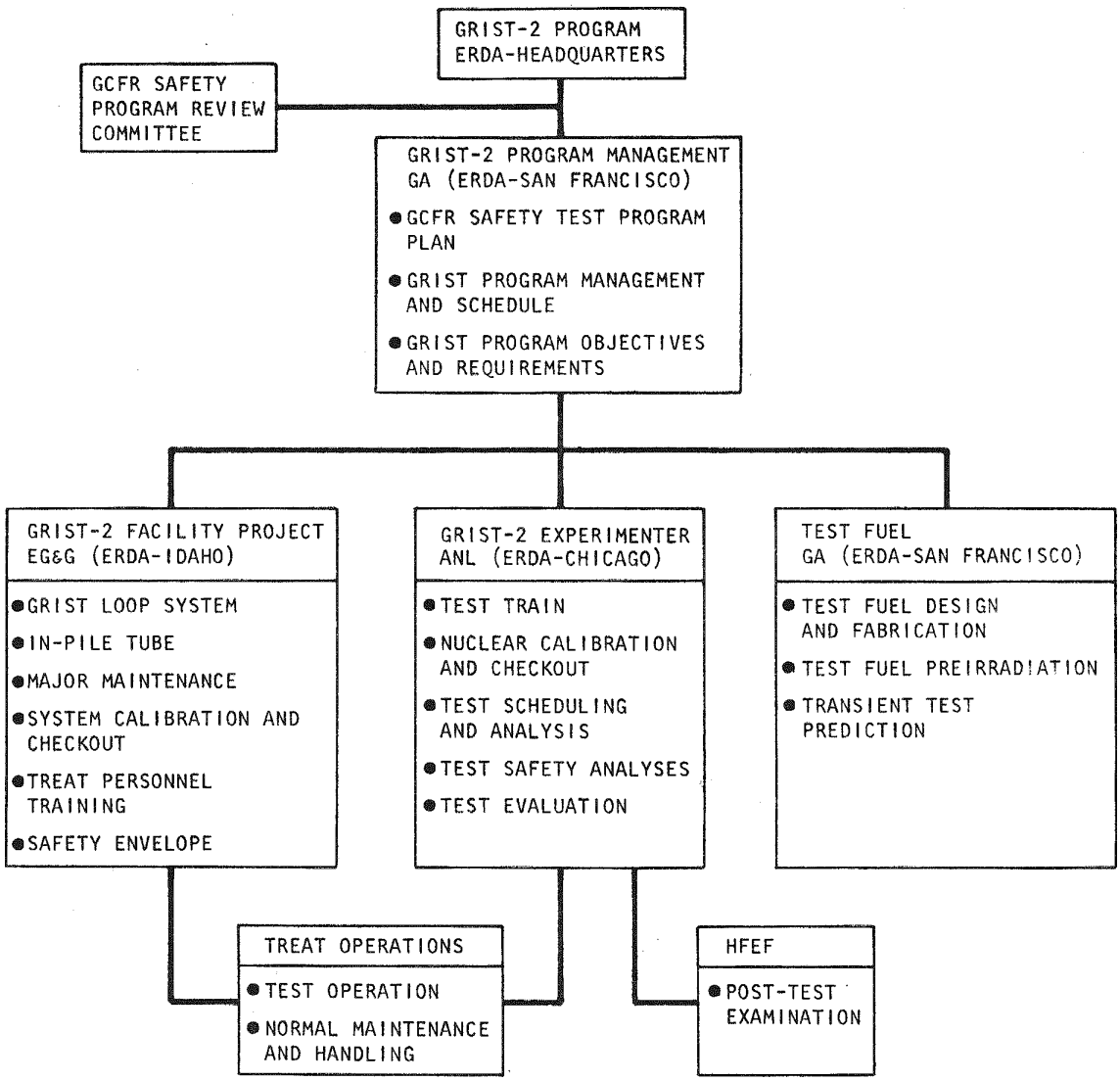

Fig. 13-1. GRIST program organization and responsibilities

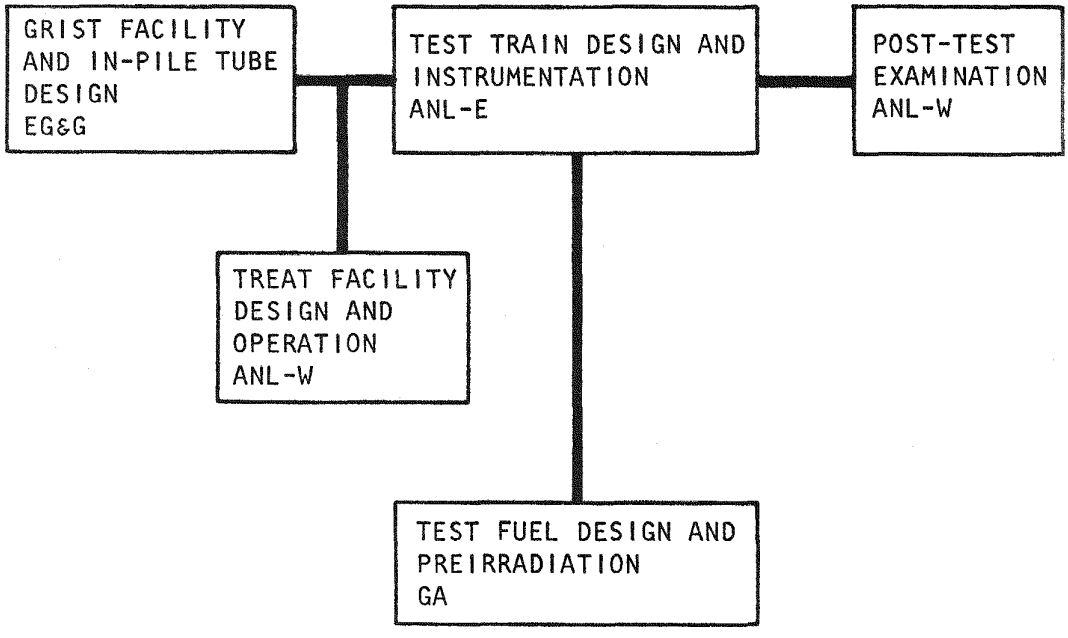

Fig. 13-2. GRIST program equipment interfaces

13.2. DUCT MELTING AND FALLAWAY TEST PROGRAM

During this quarter, duct melting and fallaway test (DMFT) program objectives, criteria, and requirements were completed and issued for external review. It is anticipated that several test program alternatives will be considered as a result of the review.

REFERENCE

13-1. "GRIST-2 Facility Project Objectives and Requirements Document - Revised February 22, 1977," EG&G Technical Report PG-G-77-001, March 8, 1977.

14. GCFR NUCLEAR ISLAND DESIGN (189a No. 00615)

14.1. GENERAL ARRANGEMENT AND SYSTEMS

The purpose of this subtask is to provide the general arrangement of the nuclear island so that the feasibility of several nuclear island concepts can be established together with the major dimensions of the buildings. The preliminary plant arrangement sketches were reviewed by the GCFR Utility Program Review Committee following internal review at GA. The comments of the committee were favorable, and GA is proceeding on the basis of the proposed arrangement. More detailed arrangements have not been prepared because key technical decisions have been delayed by the curtailed budget, the need for resolution of design differences with the German groups, and the evaluation of the impact of safety requirements on the CRBR plant by the NRC. These delays have forced the architect-engineer contract to slip.

Informal contacts were made with Bechtel Corporation, Brown & Root, Stone & Webster, and United Engineers & Constructors to determine what information was required from GA to permit them to start conceptual design work, a cost estimate, and a construction schedule for the nuclear island.

The proposed division of design responsibility for the demonstration plant is as follows:

1. NSS: GA.
2. Nuclear island: selected architect-engineer.
3. Turbine plant and auxiliaries: owner-operator.

The nuclear island has been defined to include the systems and structures listed in Table 14-1.

TABLE 14-1
NUCLEAR ISLAND SYSTEMS AND STRUCTURES

System	Number
Helium storage system	2400
Nitrogen system	2500
Service water system	4200
Reactor plant cooling water system	4600
Core auxiliary cooling water system	4700
Spent fuel storage pool cooling water system	4800
Decontamination system	6100
Radioactive liquid waste system	6200
Radioactive solid waste system	6500
Containment building heating, ventilation, and air conditioning	7300
Instrument air system[a]	8200
Communication system[a]	8300
Hydraulic power systems[b]	8600
Auxiliary service system	8700
Piping[c]	9100
Electrical system[c]	9200
Insulation[c]	9300
Painting[c]	9400
Construction testing equipment[c]	9800
Start-up equipment[c]	9900
Structures	
Containment building[d]	
Reactor service building[d]	
Plant control building[d,e]	
Helium storage building	
Radioactive waste building	
Penetration building[d]	
Service water cooling tower[d] and pump house[d]	

[a] The owner-operator is responsible for portions of these systems within the turbine plant buildings.

TABLE 14-1 (Continued)

(b) It is anticipated that there will be more than one hydraulic power system module. The architect-engineer will be responsible for module servicing valves in their systems.

(c) These systems are included in the architect-engineer and owner-operator scope of responsibility.

(d) Seismic Category I structure.

(e) The owner-operator is responsible for the layout of the main control room.

14.2. STRUCTURAL DESIGN

The purposes of this subtask are to perform the necessary design of NSS equipment, participate in the layout of the equipment in the containment, and take part in the support efforts required for assuring the feasibility of the nuclear island.

Equipment and component lists were compiled for the NSS, and the equipment and components were itemized according to system; these lists will be submitted to the cognizant engineers for coordination.

Nuclear Services Corporation submitted its report on the analysis and design of the containment equipment opening for the 300-MW(e) GCFR (Ref. 14-1). This report, which is in review, indicates that it is feasible to locate the equipment opening in the haunch of the containment building without special reinforcement around the penetration. The concrete hub around the opening will not be excessive and can be reinforced with standard rebar.

A cost study to determine the difference in costs of the NSS with and without a resuperheater was completed by the HTGR Cost Development staff (Ref. 14-2). The cost estimation for the nuclear island considered the steel containment building and the concrete confinement building. The size of the buildings was determined by the diameter and height of the PCRV, and there were two PCRV sizes: one with a resuperheater and the other without. Sketches of each design were made, and calculations were run to determine the amount of steel and concrete required in the containment/confinement. A Pullman-Kellogg cost study report of the main steam piping (Ref. 14-3) was reviewed for comparison with the present design. The designs were similar, and the Pullman-Kellogg estimate with minor additions was used for the cost evaluation.

REFERENCES

14-1. Tang, C. C., "Analysis and Design of Containment Equipment Opening for 300-MW Gas-Cooled Fast Reactor," Nuclear Services Report GUL02-05, January 21, 1977.

14-2. Sonn, D. L., "Cost Trend Study, Resuperheater Versus Nonresuperheater," General Atomic, unpublished data.

14-3. Madadi, R., "300-MW GCFR Resuperheater Piping Study for General Atomic," Pullman-Kellogg Report 5231-01, September 27, 1976.

15. GAS-COOLED REACTOR RELIABILITY DATA BANK (189a No. 00617)

The functions of the data bank are to obtain, supply, and store reliability data estimates in support of the probabilistic accident analysis performed under the GCFR and HTGR probabilistic accident and risk analysis tasks.

15.1. GCFR CRITICAL DATA NEEDS

As a result of preliminary probabilistic risk studies on the GCFR, a list of components and subsystems which require reliability data for quantification of RHR system reliability has been generated. During this quarter, reliability data for this list were collected from over 20 different sources and tabulated in a draft summary table which is presently being reviewed. The component list is divided into two groups: (1) electrical and mechanical components and systems considered to be generic equipment in nuclear and fossil-fired power plants and other industries (principally secondary steam cycle equipment); (2) components and systems unique to gas-cooled reactors for which generic data assignments may be inappropriate. Reliability data for the first group of components are available from many sources, but better sources of nuclear power plant risk assessment data are Refs. 15-1 through 15-7 because of their large data base and updating. Reliability data for the second group are more difficult to obtain and in many cases must be analyzed for their applicability to gas-cooled reactor conditions and designs.

Detailed British reliability data on gas isolation valves, gas circulators, feedwater pumps, and auxiliary boilers were received from Systems Reliability Service (SRS), and draft tabulations for unique and generic components were developed. Current data bank activities for the LMFBR program were also discussed, and the British data were combined with other information

from various sources, including Refs. 15-1 through 15-7, to determine component failure rates. The draft tabulations are in review on a trial use basis. The preliminary form of these tabulations is similar to that in Ref. 15-1, Table III-1, which catagorizes the reliability data estimates from each source for each component and failure mode of interest. The failure rate medians and ranges can then be combined with repair and test interval information to calculate the system unavailabilities.

15.2. COMMON MODE FAILURE DATA

The other data required for GCFR evaluations is information on common mode or dependent system failures. These data must be compared with normal operating data so that effective β factors (Ref. 15-8) can be determined for each redundant system. A continuing review of data and operating experience with the equipment categories listed in Table 4-3 of Ref. 15-8 is in progress; other equipment categories are also being examined.

15.3. DOCUMENTATION OF RELIABILITY DATA

Information from several data sources is maintained by the data bank, which requires updating as new information is received. Sources such as Refs. 15-3, 15-5, and 15-7 provide periodically updated reports on equipment failures and nuclear power plant operating experience. These sources also supply material used to review and update reliability data estimates as operating experience in nuclear power plants increases. These documents are stored by the data bank for reference. In addition, a notebook containing calculations leading from raw data sources to failure rate estimates for each component and failure mode is being maintained.

REFERENCES

15-1. "Reactor Safety - An Assessment of Accident Risks in U.S. Commercial Nuclear Plants," U.S. Nuclear Regulatory Commission Report WASH-1400 (NUREG-75/014), October 1975.

15-2. "Equipment Availability, Fossil, Component Cause Code Summary Report 1973," Edison Electric Institute, 1974.

15-3. "Operating Units Status Report, Licensed Operating Reactors: Data for Decisions," Nuclear Regulatory Commission Monthly Publication (NUREG-0020-1 to 12, 1976).

15-4. "Summaries of Failure Rate Data," v. 1 and 2, Government-Industry Data Exchange Program, GIDEP Operations Center, Corona, California, August 1975, October 1976.

15-5. "Nuclear Plant Reliability Data System 1975 Annual Reports of System and Component Reliability," Southwest Research Institute, San Antonio, Texas, August 1976.

15-6. "Failure Data Handbook for Nuclear Power Facilities," v. I, II, Liquid Metal Engineering Center Memo 69-7, August 1969.

15-7. "Nuclear Power Experience," published by B. J. Verna, Encino, California, on a monthly basis.

15-8. "HTGR Accident Initiation and Progression Analysis Status Report," v. II, ERDA Report GA-A13617, General Atomic, October 1975.